EPSC2018

TP2 abstracts

13 Sep 2018 15:36:00

EPSC Abstracts
Vol. 12, EPSC2018-1, 2018
European Planetary Science Congress 2018

Soil Evaporation on Mars by Magnetic Dipole-Dipole Interactions between Magnetic Clusters

Francisco J. Arias[a*]
[a] *Department of Fluid Mechanics, University of Catalonia, ESEIAAT C/ Colom 11, 08222 Barcelona, Spain*
(Dated: April 3, 2018)

Magnetic dipole-dipole interaction on the surface of Mars and its significance with regard to saltation is discussed. It is shown that dipolar magnetic collisions between magnetized clusters o aggregates on Mars could potentially eject soil particles from the surface with heights around of 1 cm or thereabouts depending of the size of the soil particle and with a maximum effectiveness around of 100 ?m diameter. The magnetic dipolar mechanism could operate in concert with the wind to trigger dust storms specially when the stress forces exerted by the air are only enough to roll soil particles (reptation) but high enough to induce the approaching of magnetic clusters to a critical distance where attractive interaction between dipoles can overcome the frictional forces opposing the motion and then igniting saltation. Utilizing a simplified physical model, analytical expressions for the maximum height as function of the diameter of the soil particle was derived. .

Keywords. *Aeolian transport, Saltation, Loss of river deltas,Martian dust cycle*

I. INTRODUCTION

The object of this work was a first assessment on a new mechanism for aeolian transport on the surface of Mars which can contribute to the ejection of grain and dust particles. The proposed mechanism is driven by magnetic dipole-dipole collisions between magnetized grains of the Martial soil enabling dust and grains to hop erratically over the surface with ballistic trajectories where can emigrate transported by the Martian winds or igniting saltation. Dipole-dipole magnetic collisions seems an unavoidable consequence on the surface of Mars. In fact, since the early times of the Viking missions to Mars (1976) and the Mars pathfinder mission (1977) it was well established that the martian soil and dust is magnetic. More recently, according with the NASA´s Mars Exploration Rover Spirit, almost all dust particles in the Martian atmosphere are magnetic and containing the strong magnetic mineral magnetite (Fe_3O_4), [1]. As a result, magnetic dipole-dipole interactions with the formation of magnetic aggregates and clusters is an unavoidable phenomena, in fact, there is a great deal to try to avoid such an interactions, [2].

II. METHODS

A. assumptions

The difficult which arose when attempting to analyze the proposed mechanism, lie in the complexity of the dynamic problem which in addition with the substantial uncertainties in the magnitude of several parameters not known with high precision today allows only a first theoretical assessment. The simplifying assumptions utilized in the analysis and a short discussion of their validity follows:

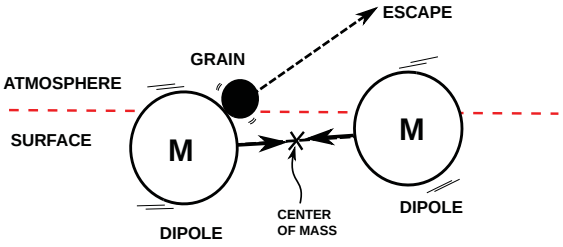

FIG. 1: Saltation induced process by magnetic interaction between two dipoles

(a) Only a single knock-on collision is considered. Therefore, neither multiple dipole collisions with a given grain particle or slowing dow with media is considered. Calculation using elastic scattering laws shows this to be an reasoned assumption.

(b) Both dipoles have the same magnetization with the

*Corresponding author: Tel.: +93 73 98 666; Electronic address: frarias@mf.upc.edu

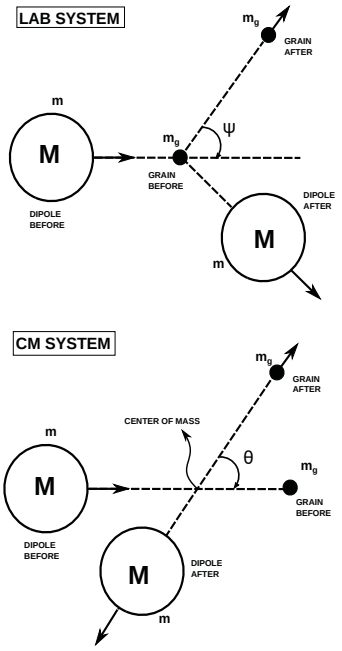

FIG. 2: Grain particle elastic scattering in laboratory (LAB) and center of mass (CM) systems.

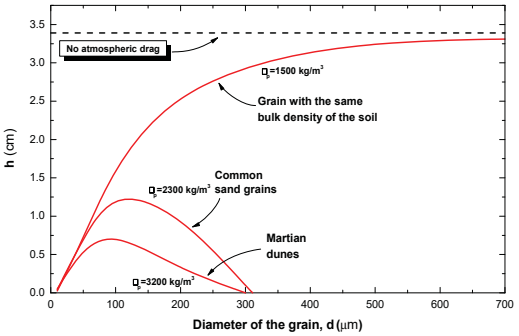

FIG. 3: The maximum height attained by a grain ejected from the surface by collision with a dipole as function of the diameter of the grain

same diameters. Due to the multiplicity of possibilities, it seems that the most representative would be to assume that magnetic agglomeration and growth of magnetic clusters is more or less homogeneous and then in average each magnetic aggregate has the same magnetization and the same size.

B. analysis

The actual situation from our generalized model is shown in Fig. 1. In this, two dipoles located at the surface are being accelerated each other to their center of mass located in between. This situation occurs when both dipoles are close enough to overcome the rolling drag force opposing the motion, and this may be ignited by the action of typical Martian winds which although insufficient for direct entrainment of grains into the atmosphere by air shear, however strong enough for moving sands and then renewing the soil from consolidate magnetic big clusters and promoting the formation of new ones and grain pilling up. Now, during its accelerated travel to the center of mass, the dipole can eventually hit some grain and the exchanging momentum as depicted in Fig. 1. The energized grain can then escape the surface.

With this rather simple picture we can infer some the-

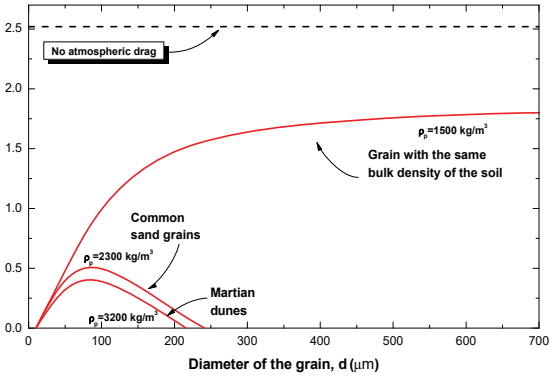

FIG. 4: The most probable height attained by a grain ejected from the surface by collision with a dipole as function of the diameter of the grain

oretical estimations of the proposed mechanism.
To begin with, let us analyze the minimum density of dipoles required to develop a continuous dipole-dipole interaction on the surface of Mars. This can be made as follows:

First, the magnetic force between two aligned dipoles with the same magnetization M and the same diameter d_p (according with our simplifying assumptions) and separated by a distance r is given by, [2],

$$F_m = \frac{\mu_o \pi M^2}{24} \frac{d_p^6}{r^4} \tag{1}$$

On the other hand, if the dipoles are separated by a distance r, then the density of particles per unit of area N may be roughly calculated as $N \approx \frac{1}{r^2}$ particles per unit of area, and then, Eq.(1) may be rewritten as

$$F_m \approx \frac{\mu_o \pi M^2 d_p^6 N^2}{24} \tag{2}$$

On the surface this force must be balanced by the rolling friction force given by

$$F_f = \frac{\rho_p \pi d_p^3 g c_d}{6} \tag{3}$$

where ρ_p is the density of the dipole (mass per unit of volume), g is gravity, and c_d the rolling friction factor. By equating Eq.(5) and Eq.(3) we obtain that the critical density required for magnetic agglomeration yields

$$N_c = \frac{2}{M} \sqrt{\frac{\rho_p g c_d}{\pi \mu_o d_p^3}} \tag{4}$$

Likewise, the critical distance r_c in which magnetic dipolar interaction overcomes frictional opposing forces is given by $N_c \approx \frac{1}{r_c^2}$ which yields

$$r_c = \left[\frac{\mu_o M^2 d_p^3}{4 \rho_p g c_d} \right]^{\frac{1}{4}} \tag{5}$$

• Discussion

Although the magnetization of particles on Mars is not known with high precision, nevertheless it has been estimated around $\approx 3 \times 10^4$A/m [3]; the density of the grain of soil around 3.2×10^3 kg/m^3 and Martian particles with diameters 600 μm , [4]; $g = 3.711$ m/s^2; $\mu_o = 4\pi \times 10^{-7}$ H·m, assuming a conservative large rolling drag factor around $c_d = 1.0$, with these values one obtains $N_c \approx 25$ particles per cm^2. This represent a critical distance around of $\approx 2000 \mu$m for particles with diameter 600 μm.

C. momentum considerations

In previous section it was assessed if the conditions for magnetic clustering and growth were satisfied in terms of the minimum critical density required. It was found that at the surface the dipole-dipole activity is a process highly probably.

In this section we will analyze what will be the fate of the particle of dust wince is knocked out by the dipole up to finally "escape" or is absorbed by the media.

To begin with, the kinetic energy E_g which can gain the grain after the collision with a dipole with kinetic energy E_m is given in the LAB system by, [5]

$$\frac{E_g}{E_m} = \frac{4 m_g m}{(m_g + m)^2} \cos^2 \psi \tag{6}$$

where m_g and m are the mass of the target grain and the dipole, respectively; ψ is the angle through which m_g is deflected in the LAB system. The mass of the dipole could be more or less the same than the grain, however, a more conservative assumption (reducing the kinetic energy of the ejected grain) is to assume that because the magnetic agglomeration, dipoles they growth forming clusters heavier than grains, i.e., $m \gg m_g$ and then Eq.(6) simplifies as

$$\frac{E_g}{E_m} \approx 4 \cos^2 \psi \frac{m_g}{m} \tag{7}$$

The energy of the dipole E_m can be calculated taking into account that each dipole is approaching each other towards their center of mass. Because both dipoles were initially at rest, then the center of mass is always at rest and then the maximum kinetic energy which can be transported by a dipole will be a half of the total kinetic energy of the two dipole system (approaching each other with the same velocity towards their center of mass). Therefore, the kinetic energy of a single dipole is given by

$$E_m = \frac{\mu_o \pi M^2}{144} \frac{d_p^6}{r^3} \tag{8}$$

and the maximum energy of the dipole at the moment of collision with the dust particle will occur when when $r \to d_p$, i.e., just before the collision with the other dipole at the center of mass, therefore, Eq.(9) simplifies as

$$E_m \approx \frac{\mu_o \pi M^2 d_p^3}{144} \tag{9}$$

Inserting the above equation into Eq.(10), the maximum kinetic energy E_{max} gained by the grain target with $\cos^2 \psi = 1$, yields

$$E_{max} = \frac{\mu_o \pi M^2 d_p^3}{36} \frac{m_g}{m} \tag{10}$$

Taking into account that $m = \frac{\rho_p \pi d_p^3}{6}$, Eq.(10) becomes

$$E_{max} = \frac{\mu_o M^2 m_g}{6 \rho_p} \tag{11}$$

D. The maximum height

Once the grain is ejected from the surface after the collision with the dipole, the maximum altitude attained if atmospheric drag is neglected is given by the total conversion of the initial kinetic energy of the grain i.e., E_{max} into gravitational potential energy, $m_g g h$, yielding

$$h = \frac{\mu_o M^2}{6\rho_p g} \tag{12}$$

A more accurate calculation implies considering the atmospheric drag force. This force may be approximated by using the Stokes law assuming a viscous uniform drag, and creeping motion in the vertical-direction. This is justified if we consider that Reynolds number are expected to be no higher than 100 or thereabouts, Almeida et al. (2008). Therefore, the momentum equation is given by

$$m_g \ddot{h} = -m_g g - 3\pi\eta d\dot{h} \tag{13}$$

where $\ddot{h}$ and $\dot{h}$ are the vertical acceleration and velocity of the grain at time t, respectively; η is the dynamic viscosity of the atmosphere; and d the diameter of the grain. Considering the initial condition $\dot{h}(t=0) = \sqrt{\frac{2E_{max}}{m_g}}$, Eq.(13) is easily solved and yields

$$h(t) = -\frac{m_g g t}{3\pi\eta d} + \frac{m_g}{3\pi\eta d}\left[\sqrt{\frac{2E_{max}}{m_g}} + \frac{m_g g}{3\pi\eta d}\right]\left[1 - e^{-\frac{3\pi\eta d t}{m_g}}\right] \tag{14}$$

and considering Eq.(11) and $m_d = \frac{\pi\rho_d d_d^3}{6}$ where ρ is the density of the grain which may be assumed equal than the dipole, i.e., $\rho \approx \rho_p$, Eq.(14) becomes

$$h(t) = -\frac{\rho_p g d^2 t}{18\eta} + \frac{\rho_p d^2}{18\eta}\left[\sqrt{\frac{\mu_o M^2}{3\rho_p}} + \frac{\rho_p g d^2}{18\eta}\right]\left[1 - e^{-\frac{18\eta t}{\rho_p d^2}}\right] \tag{15}$$

E. The most probable height

Eq.(15) was a derivation for the maximum height attained by a grain ejected after collision with a dipole, and in doing so, it was assumed that the grain is ejected in a straight vertical angle and then without horizontal compound. Nevertheless, the most probably situation is that dipole-dipole collisions occur in the horizontal plane, and then the grain must be ejected with a certain probabilistic angle following the mechanics of elastic scattering. To begin with, let us consider the collision of the grain with the dipole in the Lab system as well as the Center of Mass system as depicted in Fig. 2. Experiments indicate that the scattering between particles with energies lower than MeV, are spherically symmetric, i.e. isotropic, in the center of mass (**CM**) system, [6]. In other words, it appears from experiments that all values of $\cos\theta$ from -1 to $+1$ are equally probably.

The relationship between θ i.e., the angle through which m and m_g is deflected in the **CM** system and the angle ψ though which m_g is deflected in the **LAB** system, is given by [5]

$$\psi = \frac{\pi}{2} - \frac{\theta}{2} \tag{16}$$

Therefore, if scattering is spherically symmetric in θ, it will also be so in ψ.

The average cosine of the scattering angle ψ -in the **Lab** system, is given by

$$\bar{\beta} = \frac{\int_0^\pi \cos\psi d\Omega}{\int_0^\pi d\Omega} \tag{17}$$

where $d\Omega$ is an element of solid angle. Taking into account that $d\Omega = 2\pi\sin\theta d\theta$ and the relationship between angles at the Lab and Cm systems given by Eq.(16) it is found that

$$\bar{\beta} = \frac{2}{3} \tag{18}$$

and then the most probably height $h^*(t)$ is given by

$$h^*(t) = -\frac{\rho_p g d^2 t}{18\eta} + \frac{\rho_p d^2}{18\eta}\left[\sqrt{\frac{\mu_o M^2(1-\bar{\beta}^2)}{3\rho_p}} + \frac{\rho_p g d^2}{18\eta}\right] \times \left[1 - e^{-\frac{18\eta t}{\rho_p d^2}}\right] \tag{19}$$

and considering Eq.(18) becomes

$$h^*(t) = -\frac{\rho_p g d^2 t}{18\eta} + \frac{\rho_p d^2}{18\eta}\left[\sqrt{\frac{5\mu_o M^2}{27\rho_p}} + \frac{\rho_p g d^2}{18\eta}\right]\left[1 - e^{-\frac{18\eta t}{\rho_p d^2}}\right] \tag{20}$$

III. RESULTS

A. Analysis

In order to obtain some idea of the shape of the curve predicted by Eq.(15) and Eq.(20) for the maximum and the most probably height, respectively, we assume some values of the parameters: The magnetization of particles on Mars is not known with high precision, but has been

estimated up to a $\approx 3 \times 10^4$A/m [3]; $g = 3.711$ m/s^2; $\mu_o = 4\pi \times 10^{-7}$ H·m; particle densities can be found as low as $\rho_p = 2300$ kg/m^3 for common sands White (1979) up to $\rho_p = 3200$ kg/m^3 for typical Martian dunes [4]. The dynamic viscosity of the Martian atmosphere can be calculated as function of temperature T, using the Suterland´s formula, [7]

$$\eta = \eta_o \left[\frac{T_o + C}{T + C}\right] \left(\frac{T}{T_o}\right)^{\frac{3}{2}} \tag{21}$$

where for CO_2 we have $\eta_o = 1.48 \times 10^{-5}$ kg/ms, $C = 240$, and $T_o = 293.15$ K. Therefore for the range of temperatures on the surface of Mars a representative $\eta_o = 1.0 \times 10^{-5}$ kg/ms is assumed. The resulting curves are shown in Fig. 3 and Fig. 4 for the maximum and most probably height, respectively., and considering typical densities for sands of Mars. Also the possibility that some grains share the same density than the bulk density of the soil -which can be as low as $\rho_p = 1500$ kg/m^3 or less, [8] is plotted. It is seen that for typical sands the attainable height could be around 0.5-to.1.5 cm and with a maximum efficiency fo grains with diameters $\approx 100\mu$ m. The case for grain with densities close to the bulk density of the soil (which implies porosities around 60% ,[8] shows that an asymptotic height ≈ 3.3 cm is attained.

IV. DISCUSSION AND CONCLUSIONS

A new type of particle ejection mechanism driven by magnetic dipole-dipole collisions on the surface of Mars was investigated. The preliminary results are showing that grain of soil could be ejected after the collision with energetic dipoles up to a maximum height between ≈ 0.7 cm to ≈ 1.2 cm for Martian dunes and common sands, respectively, and with the most probable height around 0.5 cm and with a diameter of the grain around 100 μm. The mechanism can works in a cooperative way with the wind to trigger dust storms. In fact, even when the stress forces exerted by the air are only enough to roll the particle around the point of contact with the surface (reptation), however, this soft wind can induce the approaching of dipoles and then promoting dipole-dipole collisions which by the mentioned momentum exchange with the surrounding grains can ignite saltation.

NOMENCLATURE

c = rolling drag coefficient
d = diameter of the particle
E = energy
F = force
g = gravity
h = height
m = mass
M = magnetization
N = number of particles per unit of area
r = distance between dipoles
T = temperature
z = altitude

Greek symbols

$\bar{\beta}$ average cosine of the angle ψ
μ_o permittivity of free-space
η dynamic viscosity
ρ density of the particle
ψ angle of deflection in the LAB system
θ angle of deflection in the CM system
Ω solid angle

subscripts symbols

c critical
f friction
g grain
m magnetic
p particle
1 before collision
2 after collision

ACKNOWLEDGEMENTS

This research was supported by the Spanish Ministry of Economy and Competitiveness under fellowship grant Ramon y Cajal: RYC-2013-13459.

V. REFERENCES

[1] Bertelsen P., et al. (2004). Magnetic Properties Experiments on the Mars Exploration Rover Spirit at Gusev Crater. Science, 305, Issue 5685, pp. 827-829.
[2] Rosensweig, R.E. (1985). Ferrohydrodynamics. Cambridge University Press-Dover Publications.
[3] Madsen, M. B., et al. (2003). Magnetic Properties Experiments on the Mars Exploration Rover mission, J. Geophys. Res., 108, 8069
[4] Almeida, M. P., E. J. R. Parteli, J. S. Andrade Jr., and H. J. Herrmann (2008), Giant saltation on Mars, Proc. Nation. Acad. Sci., 105, 17, 6222-6226, doi:10.1073/pnas.0800202105.
[5] Marion J.B., Thornton S.T., (1988). Classical Dynamics of Particles & Systems. Thrid edition, HBJ, Publishers, ISBN: 0-15-507640-X.
[6] Glasstone S., (1955). Principles of Nuclear Reactor Engi-

neering. D Van Nostrand Comapny, Inc.
[7] Parteli E.J.R., Herrmann H.J. (2007). Dune formation on the present Mars. Phys. Rev. E 76, 041307.
[8] Benton C. Clark III, et al (1977). The Viking X Ray Fluorescence Experiment: Analytical methods and early results. J. Geophys. Res., 82,4577-4594.

EPSC Abstracts
Vol. 12, EPSC2018-14, 2018
European Planetary Science Congress 2018

Seasonal Variations in SEB Components over Gale crater

Vidhya Ganesh Rangarajan (1) and Mili Ghosh (2).

(1) Dept of Civil Engineering, IIT Guwahati (2) Birla Institute of Technology, Mesra, Ranchi (vidhyaganeshr@iitg.ernet.in)

Abstract

The surface energy budget (SEB) is a comprehensive strategy to understand the thermal behaviour of a planetary surface. Knowledge of the surface radiative transfer helps us understand near surface thermal environments. There are various methods and numerical models to partially compute energy budgets. The best methods for efficient calculation of each SEB component are assimilated and an attempt is made to enhance computational accuracy using in situ rover observational data from MSL Curiosity. The variations of each of these components are analyzed on a seasonal timescale and ground heat storage is indirectly calculated, whose computation, otherwise, is difficult.

1. Introduction

The study of energy interactions at the Martian surface and sub-surface determines the near-surface thermal environment and therefore presents a significant role in understanding its habitability and major physical processes [1]. The SEB is based on the law of conservation of energy and is given by Eqn.1

$$(1 - A)S\downarrow + L\downarrow = L\uparrow + H + \lambda E + G \quad (1)$$

where, A is the albedo of the surface, S↓ is the downwelling short-wave radiation, L↓ is the downwelling longwave radiation, L↑ is the upwelling longwave radiation, H is the sensible heat flux, λE is the latent heat flux and G is the heat exchange by conduction into ground. The terms on the LHS correspond to the forcing terms and those on the RHS correspond to the response terms of the radiative transfer. It is to be noted that many models have been developed to calculate components of the surface energy budget [2,3,4]. However, the variation of these components on a seasonal timescale is yet to be determined. Seasonal studies of SEB components can give us an idea of the microclimates and the nature of each season on Mars. In the present research, an attempt is made to study this variation and understand the factors influencing the same. It is to be noted that seasons in the southern hemisphere are studied here. Similar analogies can be derived for corresponding northern hemisphere seasons.

2. Datasets

Ground Temperature Sensor (GTS), Air Temperature Sensor (ATS) and Pressure Sensor (PS) data from Rover Environment Monitoring Station (REMS) onboard MSL Curiosity were used in this study. The time of study was chosen based on two factors – solar longitude and the movement of the rover. In order for the study to provide an efficient representation of each season, the sols are so chosen so that they lie in the mid (second month) of each three-month season period wherein peak characteristics of each season are experienced. As a result, sols 108, 110, 112, 234, 251, 270, 440, 441, 443, 610, 620 and 631 were chosen. The rover was in Point Lake, Yellowknife Bay, Cooperstown and Mt. Remarkable respectively during the chosen dates [5].

3. Methodology

Downwelling shortwave radiation was computed using the radiative transfer model developed by [6] wherein the albedo was varied from 0.20 to 0.25 in the model, a satisfactory approximation of the range of albedo values for dry land. The diurnal values of atmospheric dust opacity for the twelve sols under study were obtained from the Mars Climate Database v5.2 (MCD) [7]. The downwelling longwave radiation components were also obtained from MCD. The upwelling longwave radiations were calculated by applying Stefan-Boltzmann law on surface temperature measurements made by the GTS. The emissivity was varied from 0.9 to 1.0 to calculate

minimum and maximum values of L↑ [4]. The sensible heat flux was calculated using Eqn. 2.

$$H = K^2 C_p u \rho_a f(R_b) \frac{(T_g - T_a)}{\ln^2\left(\frac{z_a}{z_0}\right)} \quad (2)$$

where H is the sensible heat flux, ρ_a is the atmospheric density computed from the surface pressure, C_p is the specific heat of CO_2 at constant pressure (≈736 J kg^{-1} K^{-1}), T_g is the GTS recorded surface temperature, T_a is the ATS measured atmospheric temperature, K is the von Karman constant, Z_a is the height at which atmospheric temperature and wind speed 'u' are recorded (= 1.6m), Z_0 is the surface roughness and $f(R_b)$ is a function of Bulk Richardson number R_b which is used to incorporate effect of wind turbulence [8]. The surface roughness length was assumed to vary from 0.5cm to 1.5cm based on TES measurements at Gale crater [9]. Maximum and minimum values of sensible heat flux were obtained when the absolute difference of (Tg – Ta), surface roughness Z_0 and wind speed u were maximum and minimum respectively. A simple rearrangement of the surface energy budget equation would result in ground heat flux calculation if all other components are computed.

4. Results and Discussions

The Martian surface energy budget follows a pattern similar to that of Earth, being significantly dominated by the downwelling shortwave and upwelling longwave radiations (Fig 1). Sensible heat and downwelling longwave radiations contribute very less to the budget unlike that of Earth where their contribution is at least an order higher. This could be essentially due to the absence of a relatively denser atmosphere on Mars that decreases the degree of atmospheric absorption and thereby magnitude of atmospheric emitted longwave radiation. Global planetary temperatures too do not experience drastic changes as much of the upwelling longwave radiations emitted from the surface go back to space without much atmospheric intervention. Table 1 shows the maximum and minimum values obtained for the SEB components during the 12 sols chosen for study.

Spring is the shortest but hottest season of the Martian year. It experiences the highest magnitude of surface energy fluxes. Average maximum surface and atmospheric temperatures range around 285 K and 260 K respectively. Spring also experiences the highest diurnal variation in temperatures, roughly around 90 K. Mars is closer to the Sun for most parts of spring when compared to that of summer, thereby causing the atmosphere to emit the highest magnitude of longwave radiation. Spring also marks the onset of global wide dust storms and is the most affected season due to dust absorption, with almost 34% of solar insolation getting trapped in the atmosphere.

Southern summers are at least 10 sols longer than spring. Surface temperatures rise up to around 275 K, almost 5 to 10 K lesser than spring. The diurnal variation of temperature is comparatively lesser in summer i.e. of the order of 75 K. the effect of global wide dust storms gradually recede through the summer and the winds thereby become less turbulent. The percent dust absorption is roughly around 32%, a tad lower than that of spring. With decrease in concentration of dust particles as represented by the lower dust optical depth, the longwave radiation emitted by the atmosphere also reduces and hence, summer has a lower downwelling longwave radiation than that of spring. But, lower surface temperatures create an imbalance between solar insolation and emitted surface longwave radiation, thereby allowing greater flux to be stored as ground heat.

Table 1 Maximum and minimum values of SEB components for the 12 sols

Season	Sol	L↑ (W/m²)		L↓ (W/m²)	(1-A) S↓ (W/m²)		H (W/m²)	
		Max	Min		Max	Min	Max	Min
Spring	108	388	64	65	450	0	45	-23
	110	387	65	66	444	0	44	-24
	112	389	63	66	447	0	44	-23
Summer	234	328	73	47	436	0	42	-16
	251	330	72	48	434	0	37	-15
	270	310	75	48	438	0	34	-16
Autumn	440	247	63	33	349	0	34	-12
	441	254	62	33	347	0	36	-13
	443	249	63	33	346	0	38	-15
Winter	610	276	41	30	340	0	31	-25
	620	284	39	31	347	0	34	-26
	631	291	49	32	356	0	33	-20

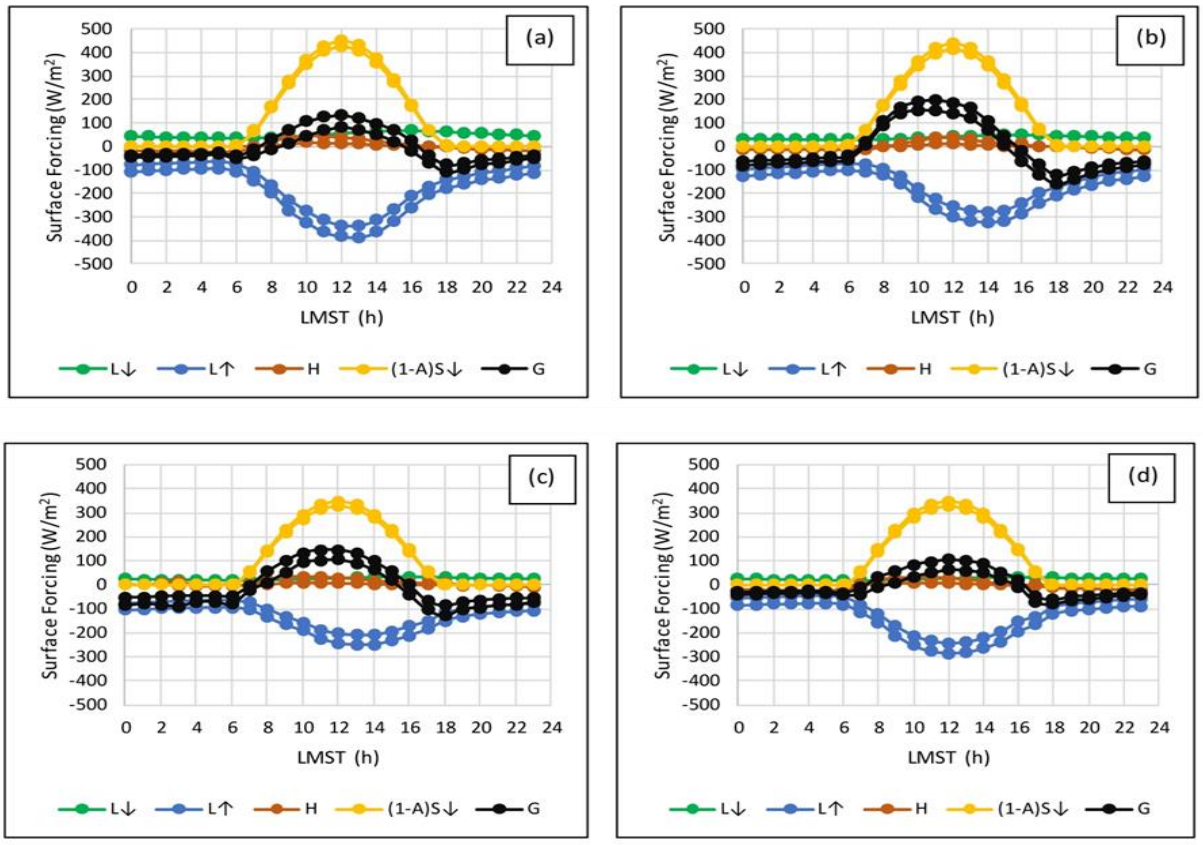

Fig 1 Surface forcing in (a) Spring (b) Summer (c) Autumn (d) Winter

Autumn forms the longest season of the Martian year, and the surface temperatures reach a maximum of around 255 K at noon. Autumn also experiences the least diurnal variation in ground temperature roughly around 60 K. The aphelion tends to occur in late autumn and it is seen that the Mars – Sun distance tends to be larger for most part of autumn than winter. This results in autumn experiencing the least upwelling longwave radiation. However, an irregularity in sensible heat flux variation is seen at night time.

Winter experiences the least diurnal insolation period and is least affected by dust. Temperatures can go as low as 177 K and as high as 265 K., thereby showing an increased diurnal variation of temperature. It is to be noted that Martian atmospheric conditions do not vary much and are somewhat stable in the autumn and winter months, as determined by similar magnitudes of surface energy budget components. Since the magnitudes of all fluxes are low, the resulting ground heat storage is also low.

From this study, it can be inferred that rover missions, landing in the southern hemisphere must be scheduled in such a way that the rover lands towards the end of winter and begins its science activity from the onset of spring as this would enable optimum solar power utilization and uninterrupted science activity by the rover as spring and summer are found to experience greatest solar insolation in a Martian year. Studies of geothermal heat and ground conduction could be undertaken during summer as it reports the highest magnitudes of ground heat storage. It is to be noted that spring and summer however are the maximum dust affected seasons in the Martian southern hemisphere. Hence, additional arrangements for dust cleaning the solar panels in the rovers need to be made in order to achieve maximum power utilization. The mission scheduling of MSL Curiosity is well-planned and can be followed for future Mars missions. Provisions may also be made for an alternative source of power during the autumn and winter seasons like utilization of nuclear power in the form of radio-isotope thermoelectric generators (RTGs) which have implemented by NASA to power

25 different US space crafts including the Viking landers [10]. This is essential because the latter seasons constitute to more than 65% of the Martian year in the southern hemisphere. So, if complete utilization of these two seasons can be made, the mission would become highly efficient and would result in greater science study of the Martian surface.

Acknowledgements

The authors thank NASA PDS Geosciences Node for providing us with Curiosity REMS data and Mars Climate Database v5.2 for providing us with dust optical depth values to calculate the SEB components. The authors also acknowledge the support from ISRO to conduct this research. Immense help provided by Dr. German Martinez during the course of this work is also highly acknowledged.

References

[1] Bonan, Gordon, (2002), Surface Energy Fluxes, Ecological Climatology: Concepts and Applications, First Edition, Cambridge University Press, pp. 209-247.

[2] Vicente-Retortillo, Á., Valero, F., Vázquez, L., Martínez, G.M., (2015), A model to calculate solar radiation fluxes on the Martian surface, Journal of Space Weather and Space Climate 5, A33. doi:10.1051/swsc/2015035

[3] Savijärvi and Määttänen., (2010). Boundary-layer simulations for the Mars Phoenix lander site, Quarterly Journal of the Royal Meteorological Society 136, 1497–1505, doi:10.1002/qj.650

[4] Martínez, G.M., Rennó, N., Fischer, E., Borlina, C.S., Hallet, B., de la Torre Juárez, M., Vasavada, A.R., Ramos, M., Hamilton, V., Gomez-Elvira, J., Haberle, R.M., (2014). Surface energy budget and thermal inertia at Gale Crater: Calculations from ground-based measurements, Journal of Geophysical Research: Planets 119, 1822–1838. doi:10.1002/2014JE004618.

[5] Curiosity Drive Log (http://curiosityrover.com /tracking /drivelog.html).

[6] Haberle, Robert. M., McKay, C.P., Pollack, J.B., Gwynne, O.E., Atkinson, H.D., Appelbaum, J., Landis, G.A., Zurek, Richard. W., Flood, D.J., (1993), Atmospheric effects on utility of solar power on Mars, NASA Technical Reports, NASA Ames Research Center, 845-885.

[7] Madeleine, J. B., Forget, F., Millour, E., Montabone, L., Wolff, M. J, (2011), Revisiting the radiative impact of dust on Mars using the LMD Global Climate Model, Journal of Geophysical Research, 116, Issue E11, doi:10.1029/2011JE00385.5

[8] Sutton, Jordan. L., Leovy, C. B., Tillman, J. E., (1978), Diurnal Variations of the Martian surface layer: Meteorological parameters during the first 45 sols at two Viking lander sites, Journal of Atmospheric Sciences, Vol 35, pp. 2346-2355.

[9] Hébrard, E., Listowski, C., Coll, P., Marticorena, B., Bergametti, G., Määttänen, A., Montmessin, F., Forget, F., 2012. An aerodynamic roughness length map derived from extended Martian rock abundance data. Journal of Geophysical Research: Planets 117, pp.01-26. doi:10.1029/2011JE003942.

[10] Fraser et al., (2004), Fuel cell power system options for Mars rovers, Proceedings of the 2nd International Conference on Green Propellants for Space Propulsion, Italy.

EPSC Abstracts
Vol. 12, EPSC2018-18, 2018
European Planetary Science Congress 2018

Model of the Crustal Magnetic Field in the Martian Aurora Zone

Chuxin Chen
presenting author **Chuxin Chen**
School of earth and space sciences, University of science and technology of China, Hefei, China (chuxin@ustc.edu.cn)

Abstract

It is well known that aurorae are prominent on planets with a global magnetic field and occur where open magnetic field lines converge. The UV spectrometer used for investigating the characteristics of the atmosphere of Mars (SPICAM) on board the Mars Express made the first observation of auroral-type emission in the cusp region of the strong crustal magnetic field on Mars and found that the arc of the Martian aurora zone is very narrow in width, which obviously differs from that of other planets. Based on the observation, we put forward a model of a crustal magnetic field on the Martian aurora zone through the morphology of Martian aurorae. In the model, equivalent currents are proposed; the topology and magnitude of the magnetic field generated by these equivalent currents are consistent with that of the crustal magnetic field in the Martian aurora zone. The morphology of the Martian aurora zone generated through the model matches well with the observations made by the Mars Express orbiter.

EPSC Abstracts
Vol. 12, EPSC2018-51, 2018
European Planetary Science Congress 2018

Seasonal changes of near-surface relative humidity on Mars

Bernadett Pál (1), **Ákos Kereszturi** (1), Francois Forget (2)
(1) Research Centre for Astronomy and Earth Sciences, Hungary (pal.bernadett@csfk.mta.hu)
(2) LMD, Institut Pierre Simon Laplace Université Paris 6, BP 99, 4 place Jussieu, 75005 Paris, FRANCE

Abstract

The seasonal changes of relative humidity on Mars near the surface calculated from the output of LMDZ GCM are presented.

1. Introduction

Mars has been of key importance in the search for extraterrestrial life for decades now. During its geological history there were most likely times, when the planet had lakes, rivers, even oceans [1], however mainly because of its lack thick of atmosphere and general dryness, water cannot exist as a liquid in large volumes nowadays. Based on recent results, liquid water might emerge on microscopic scale on the surface of hygroscopic materials [2] if the environmental factors (e.g. relative humidity, temperature) are favourable [3]. To understand the possibility of deliquescence on the planet, it is important to examine the global variations of relative humidity near the surface.

2. Methods

We investigated the seasonal changes in relative humidity (RH) first by modelling approach using the output from LMDZ GCM detailed in [4], which is the second generation of the climate model developed in the LMD described in [5, 6], then with the measurements from the MGS TES. From these two different datasets we calculated the RH described below. In this abstract we only present the findings from GCM. To examine the annual variations of RH we chose four specific locations of the Mars on its route around the Sun. To mark the time of a year on Mars, we used solar longitude (Ls), Northern spring equinox at Ls = 0°, Ls = 90° at the Northern summer solstice, Ls = 180° at the Northern autumn equinox and Ls = 270° for the Northern winter solstice.

2.1. Calculations from GCM

To get the **relative humidity** values the saturation water vapor volume mixing ratio (WVVMR) needed to be calculated. This can be done with the following equation:

$$\mathrm{Q_{sat}} = \frac{100}{\mathrm{P}} \cdot 10^{2.07023 - 0.00320991 \cdot \mathrm{T} - \frac{2484.896}{\mathrm{T}} + 3.56654 \cdot \log(\mathrm{T})} \quad (1)$$

where P is the surface pressure, T is the surface temperature. To calculate the RH directly above the regolith, the WVVMR was assumed to be well mixed between the first two altitude layers of the model, the first being at approximately 4 m, and the second at approximately 23 m above sea level. Using this assumption the WVVMR at the surface ($\mathrm{Q_0}$) is equal to those at the first level. Such, the RH can be calculated as:

$$\mathrm{RH} = \frac{\mathrm{Q_0}}{\mathrm{Q_{sat}}} \quad (2)$$

3. Results

In this section the GCM calculated RH values are shown for the four chosen times (LS 0°, 90°, 180° and 270°), first with local time changing by longitude. This is to illustrate the differences between day and night and to see how it changes throughout a Martian year. Next we demonstrate figures with times unchanged with geographical longitude, where it is 2 am LT everywhere. This local time was selected, because the TES measured at roughly 2 am and 2 pm everywhere and by modelling for the same local times it allows us to see global trends and variations coming from two different methods, thus giving us the full picture in a greater detail. On these figures we can examine the seasonal changes excluding daily variations.

On Figure 1. we can see, that the region east from Alba Patera (AP) and Tharsis (T) seems to show elevated RH values during all seasons during evening hours. Arabia Terra (AT) is also 2-3 orders of magnitude more wet, than its surroundings, especially during northern spring and autumn. At the time of northern

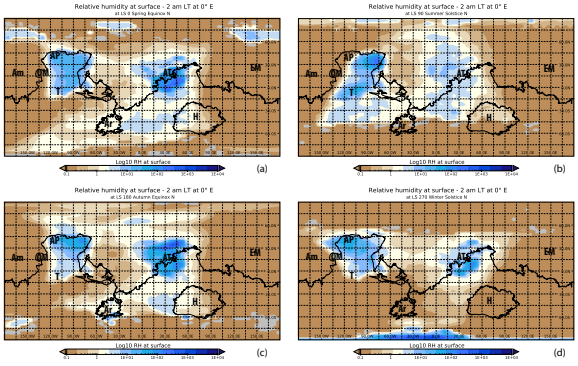

Figure 1: RH values directly above the surface calculated from GCM modelled data at the time of northern spring equinox (a), northern spring solstice (b), northern autumn equinox (c) and northern winter solstice (d), 2 am local time at 0° E.

summer, it's RH is still 1 order of magnitude higher, than the neighboring area, but it is less significantly more humid, than during the other three seasons. It is interesting to notice, that the zone between 60° W - 15° W is rather dry, despite that it is 10 pm - 12 am LT there at the figure.

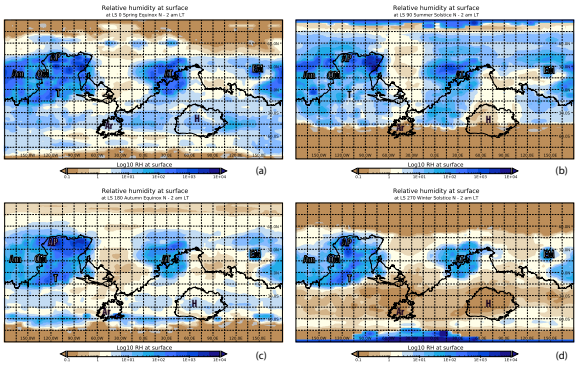

Figure 2: RH values directly above the surface calculated from GCM modelled data at the time of northern spring equinox (a), northern summer solstice (b), northern autumn equinox (c) and northern winter solstice (d), 2 am local time globally.

On Figure 2. we can see the snapshots, where it is 2 am LT everywhere on the planet. During all seasons on the GCM model result three distinct areas appear as oversaturated regions, the first zone being encircled by Amazonis (Am), Alba Patera (AP) and Tharsis (T); the second around Arabia Terra (AT); and the third is the region around Elysium Mons (EM). They are the least defined during the time of northern summer solstice, during this time the regions south from Tharsis (T), Amazonis (Am) and Arabia Terra (AT) stretch further down south, with similar RH values, thus there is no well-defined edge present to the wet zones. The three zones are visible the most clearly during northern winter, at which time their RH values are 2-3 magnitudes of order higher, than the rest of the planet surface.

4. Summary and Conclusions

The northern spring and autumn show quite similar characteristics on both types of figures (maximum RH, overall global pattern of the location of elevated RH values), however during spring the northern polar region seems rather dry compared to autumn. There is also a band between 30° S and 55-60° S, what seems more wet, than it's vicinity. The differences are more apparent between the northern summer and winter seasons, with the northern hemisphere being more wet during northern summer, and parts of the southern hemisphere during northern winter. Further results will be presented at the EPSC meeting.

Acknowledgements

This work was supported by the COOP-NN-116927 project of NKFIH, the EXODRILTECH (4000119270) project of ESA and the two STSM (39045 and 39178) TD1308 - Origins and evolution of life on Earth and in the Universe (ORIGINS) action of the COST European Cooperation in Science & Technology.

References

[1] McKay, C. P., Davis, W. L.: Icarus, Vol. 90, pp. 214 - 221, 1991.

[2] Nikolakakos, G., Whiteway, J. A..: Icarus, Vol. 308, pp. 221 - 229, 2018.

[3] Pál, B. and Kereszturi, Á.: Icarus, Vol. 282, pp. 84 - 92, 2017.

[4] Hourdin, F., et al.: Climate Dynamics, Vol. 27, pp. 787 - 813, 2006.

[5] Sadourny, R., Laval, K.: Berger A., Nicolis C. (eds) New perspectives in climate modeling. Elsevier, Amsterdam, 1984.

[6] Forget, F. et al.: J. Geophys. Res., Vol. 104, pp. 24155 - 24176, 1999.

EPSC Abstracts
Vol. 12, EPSC2018-68, 2018
European Planetary Science Congress 2018

The Banded Terrain on the Hellas Basin Floor, Mars: Gravity-driven flow not Supported by New Observations

Hannes Bernhardt (1,2), Mikhail Ivanov (3), Dennis Reiss (1), Harald Hiesinger (1), Ernst Hauber (4), Jaclyn D. Clark (2) (1) Westfälische Wilhelms-Universität, Institut für Planetologie, Münster, Germany (2) Arizona State University, School of Earth and Space Exploration, Tempe, AZ, USA (3) Vernadsky Institute, Russian Academy of Sciences, Moscow, Russia (4) Institut für Planeten- forschung, Deutsches Zentrum für Luft- und Raumfahrt, Berlin, Germany (h.bernhardt@asu.edu)

Abstract

We performed comprehensive, statistical geomorphologic analyses of the banded terrain, a ~30,000 km² area on the northwestern Hellas basin floor characterized by a Dm- to km-scale pattern of curvilinear troughs. The texture pattern does neither conform to topography nor exhibits regional (> 10s of km-scale) arrangements. Due to its association with glaciofluvial landforms (potential eskers and sandur plains) we tentatively propose a formation of the banded terrain as viscous till that was deformed by glacial overburden pressure.

1. Introduction

The western Hellas basin floor on Mars (Fig. 1 inlet) hosts a complex landscape containing several unique land- forms in close geographic association, e.g., the "honey- comb" and "banded" (or "taffy pull") terrains [e.g., 1-4]. Recent investigations concluded the honeycomb terrain to be truncated diapirs, possibly of salt or ice [3,5]. However, while periglacial features have been observed on the enigmatic banded terrain [1,3,6], its nature, formation, and thus its implications for the geologic, as well as climatic history of the Hellas basin remain largely unknown.

2. Data and methods

In order to resolve the textures of the banded and honeycomb terrains over their entire ex- tents, we produced a 1:175,000 photogeologic map encompassing an area of ~159,700 km² between 50°E 33.4°S and 61.3°E 44.3°S on the west-northwestern Hellas basin floor. The mapping process was carried out on a purpose-built, seamless CTX [e.g., 7] mosaic alongside version 12 of the THEMIS-IR Day Global Mosaic [8] and the global MOLA DEM [9]. Local-scale observations, including multi-temporal investigations, were made using HiRISE [10] as well as MOC-NA [11] images. Based on the CTX mosaic and MOLA DTM, we also performed a grid mapping (2x2 km grid size) of the entire banded terrain to assess its relation to local slopes (Fig. 1).

3. Observations

The characteristics of the banded terrain have been described in detail by [1,3,4]. In our map it covers over 30,000 km² and is subdivided into two subtypes. The creviced type (light blue/grey) is a smooth surface dissected by curvilinear troughs ("inter-bands" [1]). The ridged type (navy blue) has a rougher surface and shows the same general texture, but produced by ridges with the same dimensions as the troughs. In some locations, ridged type areas appear to superpose creviced type areas. Individual bands appear to interact in both, brittle and duc- tile manners (e.g., HiRISE PSP_008269_1395 showing one band "breaking" through another, causing slab rotation). Comparisons of MOC-NA with HiRISE images taken up to 14 years apart show no discernible change within the banded terrain (e.g., collapse by de-volatilization). The banded terrain superposes the honeycomb terrain (e.g., partially filling several honeycomb cells) as well as the hummocky, more elevated interior formation of the Hellas basin. Along its transition to the lower "Hellas Planitia trough" in the northwestern basin, the material of the interior formation appears as elongate mesas embayed by banded terrain. In many locations, band orientations are aligned to the mesas, or terminate on one side and continue on the other. Several large crater ejecta (e.g., Beloha crater) superpose the banded terrain. In certain locations, e.g., at 57,66°E 35,67°S, ejecta appears to be dissected by bands of the underlying banded terrain (e.g., north of Kufstein crater). According to our grid mapping (Fig. 1) the orientation of bands does not seem to correlate with the local slope. All grid box categories (Fig. 1 inlets) are nearly equally abundant

and distributed randomly, except within the honeycomb cells (circular arrangements dominant) and in the northernmost extents (lobate/slope-perpendicular arrangements dominant). In general, the banded terrain occurs across an elevation spectrum of almost 2 km, from -7667 m up to -5548 m. Within this spectrum, the creviced type follows a quasi-Gaussian distribution, whereas the ridged type occurs mostly below ~ -7,000 m.

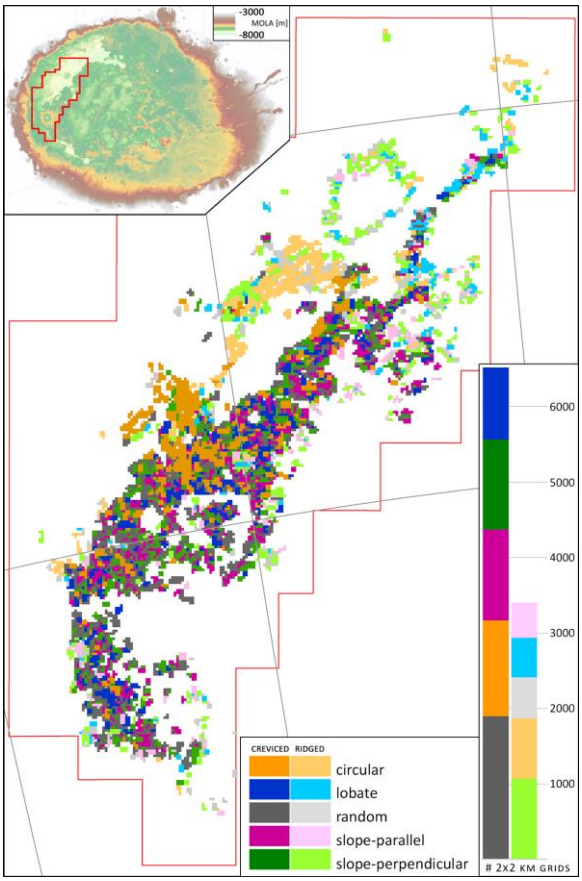

Figure 1: Grid mapping (2x2 km grid size) covering the entire banded terrain (light and navy blue units in (A)). The inlets show the different categories (defined by the banded terrain's relation to the local slope) assigned to grid boxes, as well as their respective abundances, i.e., number of grid boxes (cumulative bar chart). The inlet in the upper left shows the map's location on a color-coded MOLA view of the Hellas basin floor.

4. Discussion and conclusions

Based on previous [1,3,6,12] and new observations, it is highly unlikely that the banded terrain is the surface expression of a deeply rooted unit (e.g., truncated layers displaced by ductile de- formation during honeycomb formation [13-15]). Instead, the banded terrain seems to be a relatively thin, draping unit that experienced intense, mostly ductile, deformation at relatively shallow depths or at the surface. This viscous behavior, as well as the occurrence of periglacial landforms (e.g., thermokarst-like depressions) [1,3,6], imply a high volatile content in the past. However, its generally elevated thermal inertia (based on THEMIS), along with outcrops and small ejecta containing up to decameter-scale blocks [12], indicate that the banded terrain has since been compacted/cemented and desiccated, probably by katabatic winds. Such winds were suggested to be pervasive in this area [16,17] and likely cause ongoing deflation. Hence, we interpret the ridged type of the banded terrain as degraded version of the creviced type, with the ridges being clastic dikes of material that once filled the crevices. This is in agreement with the ridged type predominantly occurring in the lowest elevations of the unit's extent, where deflation is expected to be more intense [3,17]. Contrary to a previous assessment [1], our observations (band orientations not correlating with the local slopes of modern topography) do not support gravity-driven flow as the source of deformation that resulted in today's banded terrain. Instead, our investigation implies numerous, small- scale, slope-independent stress fields (<10s of km) of different orientations. These stress fields must have sufficed not only to deform the banded terrain, but also to deform superposing crater ejecta in certain locations (e.g., at 57,66°E 35,67°S). Furthermore, as no regional pattern (>10s of km) can be identified within the banded terrain, we suggest that large-scale, regional stress fields had little or no effect on its deformation. "Band hierarchies", i.e., bands overlapping or apparently breaking through each other, indicate multiple phases of deformation, possibly at different strain rates. One possible yet inconclusive formation model for the banded terrain might be a wet-based, subglacial environment, in which ductile material was deformed in stress fields caused by the ice overburden pressure. This pressure acted in conjunction with bed topography as well as zones of variable surging and basal decoupling, resulting in various different strain rates and band arrangements.

References: [1] Diot, X. et al. (2015) JGR: Planets, 120(12), 2258–2276. [2] Bernhardt et al., (2016) Icarus, 265, 407-442. [3] Bernhardt et al., (2016) JGR: Planets, 121, 714-738. [4] Voelker at al. (2017) PSS, 145, 49-70. [5] Weiss and Head (2017) Icarus, 284, 249-263. [6] Diot et al. (2014) PSS, 101, 118-134. [7] Malin, M. C. et al. (2007) JGR, 112(E5), E05S04. [8] Edwards et al. (2011) JGR: Planets, 116, E10008 . [9] Smith, M. D. et al. (2001) JGR, 106(E10), 23689. [10] McEwen, A. S. (2007) JGR, 112, E05S02. [11] Malin, M. C., & Edgett, K. S. (2010) The Mars Journal, 5, 1–60. [12] Diot, X. (2015) PSS, 121, 36–52. [13] Moore and Wilhelms (2001) Icarus 154, 258-276. [14] Mangold and Allemand (2003) Int. Conf. Mars#3047. [15] Kite et al., (2009) LPSC#1249. [16] Siili, T. (1999) PSS, 47(8–9), 951–970. [17] Howard et al. (2012) LPSC#1105.

EPSC Abstracts
Vol. 12, EPSC2018-101, 2018
European Planetary Science Congress 2018

Terrestrial Saharan analogues to examine the groundwater origin of theater-headed valleys on Mars

Abotalib. Z. Abotalib (1,2) and Essam Heggy **(**1,3)

(1) University of Southern California, Los Angeles, USA, (2) Department of Geological Applications, NARSS, Egypt, (3) Jet Propulsion Laboratory, Pasadena, USA (afarag@usc.edu)

Abstract: Understanding the mechanism of formation of fluvial landforms on Mars, is essential for a proper assessment of its paleoclimatic and current hydrologic conditions. The origin of Martian theater-headed valleys (THV) has long been a subject of debate with several hypotheses including groundwater sapping, mega-flooding, lava flows, and landslides. We explore herein the similarities in geometry, geomorphological and geological associations between THV in the Sahara and in Ius Chasma to support a common groundwater sapping origin. Evidence include: (1) similar morphometric characteristics including theater-like heads, stubby looking geometry, propagation along fractures and occurrence along rock walls; (2) similar geomorphological settings including very low upslope contributing areas compare to minimum eroded volumes, lack of well-developed stream networks, widespread distribution along escarpments and absence of flood deposits; and (3) similar geological associations such as occurrence in highly faulted areas and association with hydrated salts in the form of layers and or veins. These findings support the hypothesis that long-lasting groundwater processes may have contributed to the formation of these valleys on Mars rather than intensive short-lived processes.

1. **Introduction:** The original groundwater sapping hypothesis is challenged by the capability of springs to cut canyons into massive rocks and alternatively mega-floods and landslides were suggested [1]. On Earth however, widespread THV cutting through the carbonate plateaus in the Sahara are confirmed to be of long-lasting groundwater processes based on recent isotopic, geochemical and hydrogeological evidences [2]. Herein, we constraint the geomorphological, lithological and textural characteristics of THV in the Eastern Sahara as a limited analog to the THV in Ius Chasma using field-supported structural and textural mapping derived from ALOS PalSAR, Landsat-8 scenes and similar settings on Mars using, MOLA and HRSC images.

2. Geomorphological similarities: THV in the Sahara and in Ius Chasma have similar morphometric characteristics (Fig. 1; insets) including theatre-like heads, stubby looking geometry, propagation along fractures and occurrence along rock walls. Additionally, THV in both areas occur along plateau escarpments with regional gradients sloping away from the THV locations (Fig. 1). This setting results in minimizing the contribution of the surface runoff to the THV locations. We derived a new geomorphological index by dividing the upslope contributing area by the minimum eroded volume across different THV in Ius Chasma and in the Sahara and then compared these values with THV of confirmed surface runoff origin such as Box and Blind canyons that cut through the Snake River Plain in Idaho, USA [1]. The results (Fig. 2) show that Box and Blind canyons have high index values that are up to seven orders of magnitude higher than those of the Saharan and Martian THV. This significant difference supports a groundwater sapping origin of THV in Ius Chasma.

3. Similar geological associations: THV in the Sahara and in Ius Chasma occur in areas with high structural control [2, 3]. In addition to the propagation of THV along fracture sets, faults provide vertical conduits for artesian upward discharge of groundwater from deep aquifers to the surface and leading to cliff sapping and evolution of the THV [2]. Moreover, hydrated sulfates (such as gypsum) are commonly reported from the sidewalls and the foothills in association with Saharan and Martian [4] THV (Fig. 3). The relatively recent sediments (younger than 2.9 Gy) on Mars also support a groundwater origin of these features. Additionally, MSL Curiosity rover images indicate abundant distribution of calcium sulfate veins [5] in

the sedimentary deposits similar to those reported from the Sahara (Fig. 3).

4. Discussion and Conclusions: Similarity in morphology and geological associations between Saharan and Martian THV suggest a common origin by groundwater sapping from deep aquifers along faults. Rock disintegration by groundwater-related salt weathering could have played a key role in carving the THV.

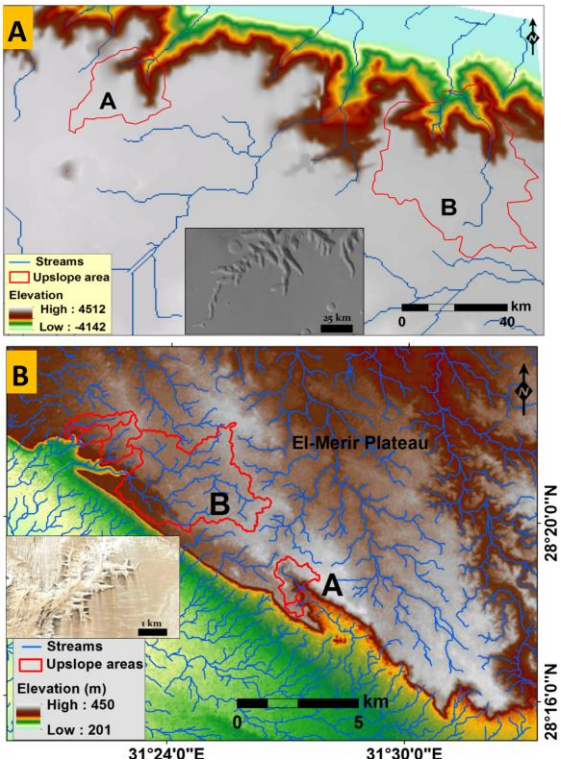

Figure 1: Stream networks superimposed on (A) MOLA DEM of THV in Ius Chasma and (B) PalSAR DEM in El-Merir Plateau showing minimal contribution from surface runoff. Insets are HRSC and Geoeye-1 images of THV examples.

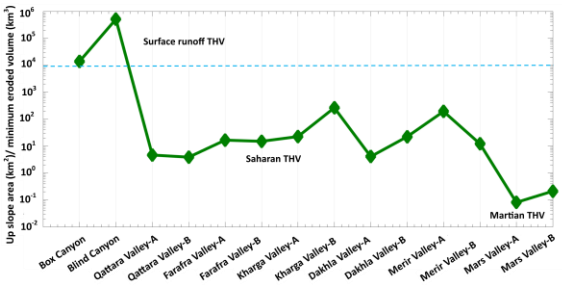

Figure 2: Geomophological index showing the low index values of Martian and Saharan THV compare to those formed by surface runoff in the Snake River Plain, USA.

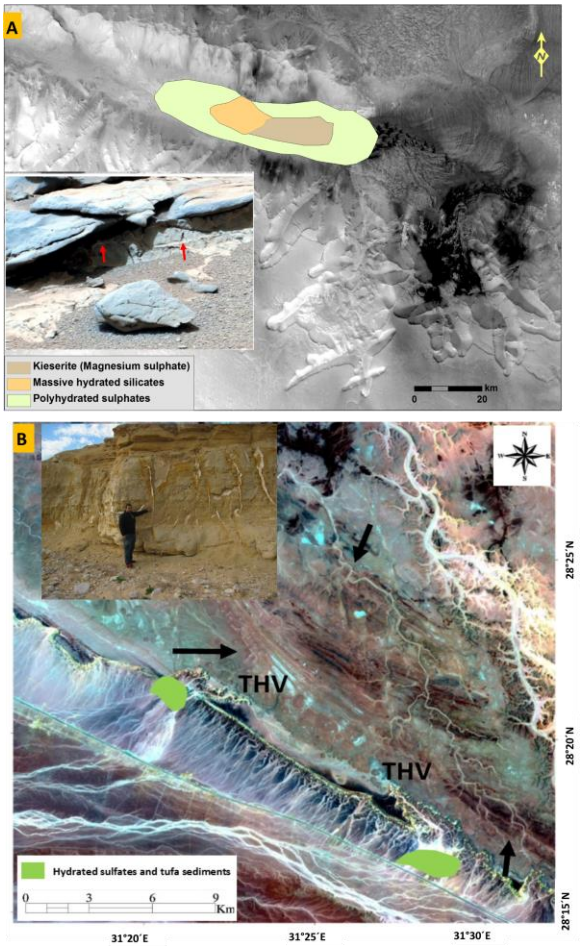

Figure 3. Association of hydrated sulfates with the locations of THV in Ius Chasma [HRSC image] (A) and El-Merir Plateau [Landsat-8 image] (B). Insets are NavCam image of the MSL Curiosity rover in Yellowknife Bay, Gale crater and field photo in El-Merir Plateau, Egypt showing abundant gypsum veins cutting through sedimentary successions. The salt veins that are cutting through different stratigraphic units suggest a groundwater-related origin and high activity of salt weathering along the rocky materials.

Acknowledgements: This work is funded by NASA Planetary Geology and Geophysics award NNX15AV76G.

References

[1] Lamb, M. et al. (2008), Science 320, 740-744, [2] Abotalib, A. et al. (2016), Earth-science reviews 156, 108-136, [3] Montgomery, D. et al. (2009), GSA Bulletin 121, 117-133, [4] Roach, L. et al. (2010), Icarus 206, 253-268, [5] Nachon, M. et al. (2014), Journal of Geophysical Research: Planets 119, 1991-2016.

EPSC Abstracts
Vol. 12, EPSC2018-149, 2018
European Planetary Science Congress 2018

The Penetration of Solar Radiation into Carbon Dioxide Ice and Snow

H. E. Chinnery[1], A. Hagermann[2], E. Kaufmann[2], S. R. Lewis[1].
(1) School of Physical Sciences, The Open University, Milton Keynes, UK. (2) Department of Biological and Environmental Sciences, University of Stirling, Stirling, UK. (Hannah.chinnery@open.ac.uk)

Abstract

The depth to which solar radiation can penetrate through ice is important for understanding surface-atmosphere interactions across the surface of Mars. Related phenomena include cryoventing of CO_2 which creates dendritic troughs in the polar regions, and gully formation in the absence of liquid water. New light intensity measurements for calculating the e-folding scale, otherwise known as the absorption scale length, or penetration depth, of CO_2 slab ice are presented here, providing improved constraints on this parameter, which is vital for thermal models of the seasonal polar caps. In addition to this, the e-folding scale of both carbon dioxide snow and water snow has been measured, which has applications for modeling the volatile budget across the Martian surface.

1. Introduction

Icy surfaces behave differently to rocky or regolith-covered surfaces in response to irradiation because visible light can penetrate partially into the subsurface. Ices are transparent or translucent to visible and shorter wavelengths of light, while opaque in the infrared, which makes a solid state greenhouse effect possible [1]. This can result in significant differences in the shallow subsurface temperature profile when compared to rocky surfaces. Of particular significance for modeling the solid-state greenhouse effect is the e-folding scale of the ice. The e-folding scales of CO_2 slab ice [2], CO_2 snow and H_2O snow for the cumulative wavelength range 300 to 1,100 nm have been constrained. These are vital parameters in heat transfer models for the Martian surface, enabling us to better understand surface-atmosphere interactions at Mars' polar caps.

The permanent polar caps on Mars primarily consist of water ice. These are stable year round at both the northern and southern poles. However, as temperatures drop during autumn, CO_2 begins to condense out of the atmosphere at high latitudes to form the seasonal polar cap, containing around 25% of the atmospheric CO_2 at its maximum extent [3]. This can occur as both direct condensation or as precipitation: snow [4]. Whilst measurements have been made previously for water snow, e.g. [5, 6], no measurements for CO_2 snow have been published. Furthermore, there are several differences in sample preparation and experimental methodology in these previous studies which are considered during result analysis. With optical properties quite different to water ice, this could affect the thermal regime of the surface and shallow subsurface in these regions. Additionally, a widespread CO_2 frost cycle is now known to occur, with nighttime frosts frequently observed through to low latitudes [7]. As the presence of solid CO_2, either as slab ice or as snow/frost deposits, is widespread across the surface of Mars, having accurate models to describe how solar irradiation interacts with surface CO_2 ice could further our understanding of some of the unique surface processes observed today.

Such phenomena include active gully formation on mid-latitude slopes without the presence of liquid water [8]; spider formations in the Cryptic region in the south, which occur in consistent locations every spring [9]; and seasonal furrows in the northern hemisphere, which are similar to those in the south but tend to be smaller and ephemeral, occurring in different locations each year due to shifting sand dunes [10].

2. Methodology

Slab ice samples were prepared by condensing CO_2 directly from the gas phase within a pressure vessel cooled by liquid nitrogen. This forms large CO_2 ice blocks, which were then cut to size and polished smooth prior to experiment commencement [2].

CO_2 snow was made by decompression directly from a liquid CO_2 cylinder. The snow was sieved to <1 mm grain size, and stored in liquid nitrogen until use. This minimised sintering and contamination by water frost. Water snow was made by spraying deionised

water into a dewar of liquid nitrogen, which was then sieved and stored in sealed containers at -85°C to avoid sintering of the samples.

Both the snow and slab ice experiments were undertaken in an argon-filled chamber, which was first cooled with liquid nitrogen. This both reduced the sublimation rate of the CO_2 ice, and minimised water frost deposition on both the sample and the glass plate the sample is held on.

3. Results

Table 1 E-folding scale results based on the minimum, maximum and mean light intensity measurements for each sample of CO_2 slab ice.

Sample No.	E-Folding Scale, ζ (mm)		
	Min Intensity	Max Intensity	Mean Intensity
1	40.00	28.57	32.58
2	43.48	30.30	33.33
3	35.71	58.82	47.62
4	35.71	71.43	47.62

The e-folding scale calculated using minimum light intensity measurements for samples 1 and 2 is higher than that calculated using the maximum data (see Table 1). This is due to the fact that these samples started out more opaque or 'milky', and so light penetration was lower than in the other samples. As measurements commenced, the minimum amount of light able to penetrate through the sample increased steadily. However, additional cracks would reduce the maximum light intensity, and so the rate of increase in light penetration was slower than that for the minimum results. In contrast, samples 3 and 4 were much more transparent at the beginning, and so any cracks forming would affect the minimum and maximum readings more equally than in samples 1 and 2. Consequently, we have more confidence in the results obtained from samples 3 and 4.

It is reasonable to give an e-folding scale value of ζ = 35.7 mm ± 7.7 mm for cracked, higher albedo CO_2 ice; for perfectly smooth, unblemished slab ice ζ = 65.1 mm ± 6.3 mm would be more applicable. However, we would urge caution with using the highest estimations of the e-folding scale, for in reality, any thermal variations, such as the diurnal insolation cycle, are likely to cause thermal cracking of the CO_2 slab ice. In addition, the e-folding scales of H_2O and CO_2 snow were calculated from light intensity measurements to give mean value of ζ = 11 mm ± 2 mm for both types of snow. Given the estimated errors, the e-folding scales can be considered identical. This suggests that light propagation through translucent ices at the grain sizes measured ($\leqslant$ 1mm) is determined by the number of scattering surfaces rather than the specific material's optical properties.

We therefore recommend the use of 47.6 mm for modelling 'normal' CO_2 slab ice conditions on Mars, and 11 mm for snow or frost.

Acknowledgements

This work was funded by STFC under grant no. ST/N50421X/1, with additional support from grant no. ST/L000776/1.

References

[1] Matson, D. L., & Brown, B. H. Solid-state greenhouses and their implications for icy satellites. Icarus, 77(1), 67–81, 1989.

[2] Chinnery, H. E., Hagermann, A., Kaufmann, E., Lewis, S. R. The penetration of solar radiation into carbon dioxide ice. J. of Geophys. Res. Planets, Vol. 123, 2018.

[3] Tillman, J. E., N. C. Johnson, P. Guttorp, and D. B. Percival, The Martian annual atmospheric pressure cycle: Years without great dust storms, J. Geophys. Res., Vol. 98, 10963–10971, 1993.

[4] Mount, C. P., and T. N. Titus, Evolution of Mars' northern polar seasonal CO_2 deposits: Variations in surface brightness and bulk density, J. Geophys. Res. Planets, Vol. 120, 1252–1266. 2015.

[5] Kaufmann, E. and Hagermann, A. Penetration of solar radiation into pure and Mars-dust contaminated snow. Icarus, 252: 144-149, 2016.

[6] France, J.L., King, M.D. and MacArthur, A., 2010. A photohabitable zone in the Martian snowpack? A laboratory and radiative-transfer study of dusty water–ice snow. Icarus, Vol. 207(1): 133-139

[7] Piqueux, S., Kleinböhl, A., Hayne, P. O., Heavens, N. G., Kass, D. M., McCleese, D. J., Schofield, J T., Shirley, J. H. Discovery of a widespread low-latitude diurnal CO_2 frost cycle on Mars. J. Geophys. Res. Planets, Vol. 121, 2016.

[8] Diniega, S., Hansen, C. J., McElwaine, J. N., Hugenholtz, C. H., Dundas, C. M., McEwen, A. S., & Bourke, M. C. A new dry hypothesis for the formation of Martian linear gullies. Icarus, Vol. 225(1), 526–537, 2013.

[9] Kieffer, H. H. Cold jets in the Martian polar caps. J. Geophys. Res., Vol. 112, 2007.

[10] Bourke, M., & Cranford, A. Seasonal formation of furrows on polar dunes, Fifth Mars Polar Science Conference: 6059, 2011.

EPSC Abstracts
Vol. 12, EPSC2018-183, 2018
European Planetary Science Congress 2018

Subsurface Volatile Deposition on Mars

N. Patel (1), A. Hagermann (2), S.R. Lewis (1), E. Kaufmann (2), M. Balme (1)
(1) The Open University, UK (2) University of Stirling, UK (narissa.patel@open.ac.uk)

Abstract

We have modelled the transport of heat in the martian regolith, taking into account the change in thermal properties caused by an increase in water ice content. Under these conditions we have found that the addition of water ice allows for increased ice formation at depth, rather than under the assumption that thermal properties are unchanged. This is important because it will affect estimates of global subsurface volatile deposition.

1. Introduction

Present day observations on Mars have shown water ice is present at the poles and within the subsurface [1]. At both poles, there is a water ice cap overlain by a carbon dioxide ice cap, due to the lower temperatures required for carbon dioxide to freeze [1]. Both polar caps have a permanent and seasonal component, with the CO_2 ice layer reducing in size during the summer in each hemisphere [1]. Within the subsurface at lower latitudes, water ice has been observed by the Phoenix lander [2] and exposed at cliff faces [3]. The depth to the water ice table has been shown to increase with decreasing latitude [1]. However, the global distribution has also been shown to vary over time with the obliquity cycle and to a smaller extent with the eccentricity and precession cycles [4, 5]. In order to study the effect of the obliquity cycle, the UK version of the Mars Global Circulation Model (GCM) [6, 7] is coupled with an updated regolith model which is presented here.

2. Theory

Subsurface volatile deposition is heavily dependent on the thermal properties of the subsurface [8], primarily variations in thermal conductivity (k), density (ρ) and specific heat (c).

Studies of thermal inertia [8] have shown that variations in thermal conductivity have a more significant effect on heat conduction than the volumetric specific heat (ρc), because the value of thermal conductivity can vary by around two orders of magnitude. Previous studies of thermal conductivity in martian regolith have shown that it is a complex function of many factors, including composition, bulk porosity, the shape and size of the grains, gas pressure within pores and temperature [9, 10].

Alongside these factors, the addition of water ice has also been shown to significantly increase the thermal conductivity of the bulk regolith [10, 11], affecting heat conduction and thus impacting the stability of ice within the subsurface. Experiments [11] and models [10, 12] show that thermal conductivity increases rapidly and non-linearly with ice content. Consequently, the effect of increasing ice content on thermal conductivity is not well understood. Here, we present a regolith model that uses the Hertz factor to determine the effect of water ice content, as suggested previously for porous water ices [13], which will be coupled with the Mars GCM [6, 7].

3. Regolith Model

The regolith model is an updated version of the 1D thermal model of [5] with an improved method for determining thermal conductivity throughout the porous regolith. The model determines the distribution of water between the vapour, adsorbate and ice phases, and the distribution with depth of each of these phases at a single location, given surface temperatures and geothermal heat flux as the upper and lower boundary conditions, respectively.

The thermal conductivity in the model varies with depth and ice content, as shown in Figure 1, as well as temperature. The variation in thermal conductivity of the regolith with depth is based on the model described in [9], and the variation in thermal conductivity of water ice with temperature is based on the model described in [14]. The increase in thermal conductivity with ice content is calculated using the Hertz factor for contact area, assuming that ice grows at sinter necks between two spherical grains.

The geothermal heat flux value is currently assumed

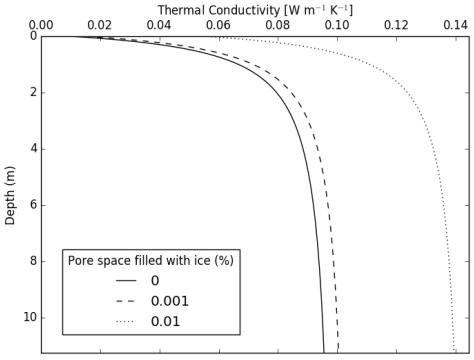

Figure 1: Thermal conductivity with depth for a regolith with a porosity of 47%. The solid line represents the thermal conductivity for a regolith containing no ice, and the dashed lines represent the effect of the addition of ice into the pore space.

to be constant and is based on previous studies [15]. However, the HP^3 instrument on the InSight lander, which is due to arrive in November 2018, will make the first surface heat flux measurements on Mars. These measurements will be used as the geothermal flux boundary at the base of the thermal model.

4. Summary and Future Work

We found that the addition of water ice increases ice stability at depth and this is so far like [10]. We plan to extend this model by performing global simulations at different obliquities to investigate the resulting change in ice distribution.

Acknowledgements

This research is funded via an STFC PhD Studentship to HEC.

References

[1] Mellon, M.T., Jakosky, B.M.: Geographic Variations in the Thermal and Diffusive Stability of Ground Ice on Mars, JGR: Planets, Vol. 98, E2, pp. 3345-3364, 1993.

[2] Cull, S., Arvidson, R.E., Mellon, M.T., Skemer, P., Shaw, A., Morris, R.V.,: Compositions of subsurface ices at the Mars Phoenix landing site, Geophysical Research Letters, Vol. 37, 24, 2010.

[3] Dundas, C.M., Bramson, A.M., Ojha, L., Wray, J.J., Mellon, M.T., Byrne, S., McEwen, A.S., Putzig, N.E., Viola, D., Sutton, S., Clark, E., Holt, J.W.: Exposed subsurface ice sheets in the Martian mid-latitudes, Science, Vol. 359, 6372, pp. 199-201, 2018.

[4] Newman, C.E. and Lewis, S.R. and Read, P.L.: The atmospheric circulation and dust activity in different orbital epochs on Mars, Icarus, Vol. 174, pp. 135–160, 2005.

[5] Steele, L.J. and Balme, M.R. and Lewis, S.R.: Regolith-atmosphere exchange of water in Mars' recent past, Icarus, Vol. 284 Supplement C, pp. 233-248, 2017.

[6] Forget, F., Hourdin, F., Fournier, R., Hourdin, C., Talagrand, O., Collins, M., Lewis, S.R., Read, P.L. and Huot, J.: Improved General Circulation Models of the Martian Atmosphere from the Surface to Above 80 km, JGR: Planets, Vol. 104, pp. 24155-24175, 1999.

[7] Millour, E., Forget, F., Spiga, A., Navarro, T., Madeleine, J.B., Montabone, L., Pottier, A., Lefèvre, F., Montmessin, F., Chaufray, J.Y. and others: The Mars Climate Database (MCD version 5.2), EPSC 2015, Vol. 10, pp. 438, 2015.

[8] Palluconi, F.D., Kieffer, H.H.: Thermal Inertia Mapping of Mars from 60^oS to 60^oN, Icarus, Vol. 45, 2, pp. 415-426, 1981.

[9] Grott, M., Helbert, J., Nadalini, R: Thermal Structure of Martian Soil and the Measurability of the Planetary Heat Flow, JGR: Planets, Vol. 112, E9, 2007.

[10] Piqueux, S., Christensen, P.R.: Temperature-dependent thermal inertia of homogeneous Martian regolith, JGR: Planets, Vol. 116, E7, 2011.

[11] Siegler, M., Aharonson, O., Carey, E., Choukroun, M., Hudson, T., Schorghofer, N., Xu, S.: Measurements of thermal properties of icy Mars regolith analogs, JGR: Planets, Vol. 117, E3, 2012.

[12] Mellon, M.T., Jakosky, B.M., Postawko, S.E.: The Persistence of Equatorial Ground Ice on Mars, JGR: Planets, Vol. 102, E8, pp. 19357-19369, 1997.

[13] Kossacki, K.J., Kömle, N.I., Kargl, G., Steiner, G.: The influence of grain sintering on the thermoconductivity of porous ice, Planetary and Space Science, Vol. 42, 5, pp. 383-389, 1994.

[14] Kinger, J.: Some consequences of a phase transition of water ice on the heat balance of comet nuclei, Icarus, Vol. 47, pp. 320-324, 1982.

[15] Soto, A., Mischna, M., Schneider, T., Lee, C. and Richardson, M.: Martian Atmospheric Collapse: Idealized GCM studies, Icarus, Vol. 250 Supplement C, pp. 553-569, 2015.

EPSC Abstracts
Vol. 12, EPSC2018-192, 2018
European Planetary Science Congress 2018

Preferred orientations of Martian rock cracks through radiative transfer and geometric analyses

Christina L Smith and John E. Moores
Centre for Earth, Space Science and Engineering, York University, Toronto, Canada (chrsmith@yorku.ca)

Abstract

This abstract presents a study of rock crack orientation preferences across Mars stemming from differential insolation of v-shaped rock cracks of a variety of relative depths. This work uses a new extended radiative transfer model of Mars covering the 200-1000nm wavelength range at 10° intervals in Ls and planetary latitude. The outputs of this code are used as input to an original geometric algorithm to determine the most illuminated orientations of cracks as a function of position and season.

1. Introduction

Preferred orientations of rocks exist on Earth and have also been reported along the traverse of Mars Exploration Rover A (MER A, "Spirit", [1]). On Earth it was shown [3] that preferred orientations could be due to differential insolation received by the cracks due to self-shielding by their own geometry. This abstract extends this work to Mars to identify whether differential insolation could also play a role in detected Martian preferred orientations.

2. RT and Geometric algorithms

In this work, we use a combination of a radiative transfer code (Doubling and Adding, D&A, [2]) and an original geometric algorithm. The Martian atmosphere is modelled using the former code by extending the UV model of [4] so it covers the wavelength range 200-1000nm. The atmosphere was modelled for entire sols at 10° increments in planetary latitude and solar longitude. The geometric algorithm models the cracks as v-shaped and ranging from depth:width ratios of 1:1 to 4:1 with 10 degree increments in rotation clockwise from north. We identify the preferred orientations as those that receive the most energy, in contrast to works carried out on Earth, as moisture would require sufficient insolation to melt and thus be mobilised.

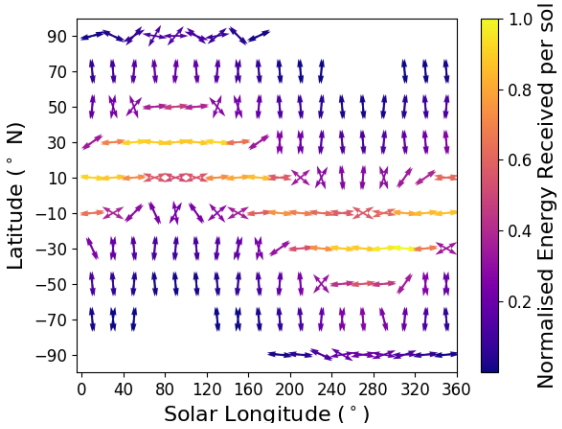

Figure 1: Primary and secondary orientations at 20° intervals in Ls (abscissa) and planetary latitude (ordinate). Colours indicate the relative amount of energy received by the bottom third of the cracks

3. Whole Mars results

Across Mars, depending upon the latitude and Ls of a particular position, we identify three primary modes: an E-W mode most prominent around the equator, a N-S mode, most prominent at higher latitudes, and a cross-mode (NE-SW/NW-SE) which appears at the interface between the two other modes and becomes more significant for deeper cracks. The primary and secondary orientations of cracks with dimensions 2:1:5 (depth:width:length) is shown in Fig. 1. These, for ease of viewing, are shown only at every 20° in Ls and planetary latitude - for the full figure we refer you to [5].

With increasing crack depth in comparison to crack width, we observe a decrease in the region of E-W mode dominance, and an associated increase in the width of the region where cross-modes are dominant. There is a slight increase in the size of the region where N-S modes are dominant, but this is a much less

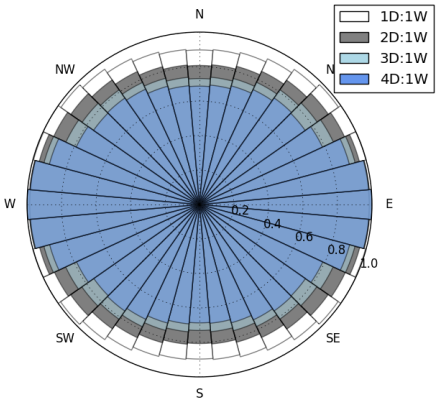

(a) No minimum energy threshold.

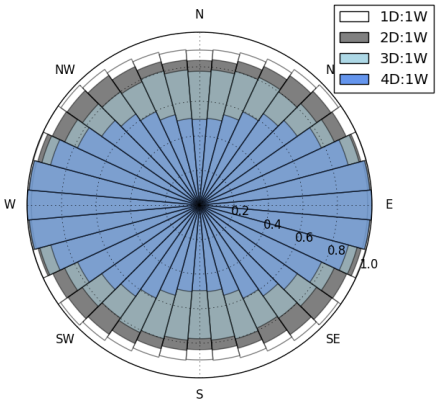

(b) With minimum energy threshold.

Figure 2: Normalised insolation received by cracks with depth:width:length ratios of 1:1:5 and 4:1:5 at -10° N over the whole Martian year.

significant effect than with the cross-mode region.

4. Spirit Site

Spirit's landing site (Gusev Crater) is found at -14.7° N, 175.5°E. Using our Full Mars Model, extracted at the nearest grid point, shows differential insolation would result in a general E-W mode for shallow cracks, leading up to a cross-mode for the deepest cracks, as shown in Fig. 2(a). Requiring a minimum threshold of energy to allow cracks to propagate in a given direction (equal to the amount of energy required to melt a 0.5mm layer of water ice) increases the prominence of the cross mode and reduces the offset from North of the primary cross mode's orientation (Fig. 2(b)).

[1] report preferred orientations of $46° \pm 20°$ (offset from North). The cross modes of our results in the NE-SW direction are in agreement with the upper limit of [1], but in order to get only one of these two modes visible, crack growth would need to be diurnally restricted.

References

[1] M.-C. Eppes, A. Willis, J. Molaro, S. Abernathy, and B. Zhou. Cracks in Martian boulders exhibit preferred orientations that point to solar-induced thermal stress. *Nature Communications*, 6:6712, Mar. 2015.

[2] C. A. Griffith, L. Doose, M. G. Tomasko, P. F. Penteado, and C. See. Radiative transfer analyses of Titan's tropical atmosphere. *Icarus* , 218:975–988, Apr. 2012.

[3] J. E. Moores, J. D. Pelletier, and P. H. Smith. Crack propagation by differential insolation on desert surface clasts. *Geomorphology*, 102:472–481, Dec. 2008.

[4] J. E. Moores, C. L. Smith, and A. C. Schuerger. UV production of methane from surface and sedimenting IDPs on Mars in light of REMS data and with insights for TGO. *Planet. Space Sci.* , 147:48–60, Nov. 2017.

[5] C. L. Smith and J. E. Moores. Geometric shielding of surface rocks on Mars. submitted to Icarus, 2018.

EPSC Abstracts
Vol. 12, EPSC2018-225-1, 2018
European Planetary Science Congress 2018

Stereo-topographic mapping of the Stratigraphy of Mars' South Polar Layered Deposits

P. Becerra (1), M.M. Sori (2), N. Thomas (1), A. Pommerol (1), M. Almeida (1), S. Tulyakov (3), A. Ivanov (3,4), E. Simioni (5), G. Cremonese (5), and The CaSSIS Team.
(1) Physikalisches Institut, Universität Bern, Bern, Switzerland (2) University of Arizona, Tucson, AZ, USA (3) École polytechnique fédérale de Lausanne, Lausanne, Switzerland (4) Space Center, Skolkovo Institute of Technology, Moscow, Russia (5) INAF, Osservatorio Astronomico di Padova, Padova, Italy

Abstract

We correlate exposures of SPLD beds in different locations using stereo data from MRO's HiRISE and from TGO's CaSSIS instrument.

1. Introduction

The Polar Layered Deposits (PLD) of Mars are km-thick deposits of stratified H_2O ice and dust, observable remotely because of exposures of their inner structure in scarps at their margins and spiral troughs throughout [1]. Observations of these exposures in the north PLD [2] support the theory that this stratigraphic record is influenced by climate variations forced by Mars' insolation history [3–5].

The southern deposits (SPLD; Fig. 1a), which appear to be at least an order of magnitude older than the NPLD [6,7], have exposed strata that are thicker, darker, and more eroded than in the north [8–10]. In addition, the prospect of tying a climate record to the SPLD is hindered by the solutions for Mars' past orbital evolution becoming chaotic earlier than ~20 Ma [4], younger than the estimated SPLD surface age. These problems have resulted in fewer studies of the SPLD in comparison to its northern counterpart.

Here, we map SPLD stratigraphy at high resolution using HiRISE Digital Terrain Models (DTMs; Fig. 1b) and the first stereo-images taken by TGO's CaSSIS [11], which although not able to view the southernmost latitudes, can observe the northern margin of the SPLD (130ºE – 220ºE; Fig. 1a). This region likely represents a separate stratigraphic unit, which CaSSIS will be able to extensively study in stereo; the first science phase passes have already acquired observations of bed exposures in UL (Fig. 1c). We search for dominant periodicities in the stratigraphy, and attempt to correlate exposures in different regions of the SPLD to determine if a consistent climate signal is recorded throughout [12].

2. Methods

We use data analysis methods similar to those used for the NPLD by [2]. The dataset (Fig. 1) consists of 8 HiRISE-based DTMs [13] of bed exposures spread out across the SPLD, and approximately 12 CaSSIS stereo pairs (most are planned for the imaging cycles in the next month), at least two of which will be available for analysis by the time of the conference. At the time of writing, these methods have been applied to the HiRISE data, and will be applied to the available CaSSIS data before EPSC. As in [2], we extract local slope (at the vertical resolution of the DTMs, ~1m for HiRISE, ~8 m for CaSSIS), and bed protrusion (a property explained in [12], which is a proxy for resistance to erosion) from the DTMs. Five individual linear profiles taken ~10 m apart along strike (~ 30 m for CaSSIS) are averaged to minimize noise due to smaller-scale effects (Fig. 1c). Fig. 2 shows average protrusion profiles for each HiRISE study site.

We visually compare topographic profiles through the different SPLD sites (e.g. Fig. 2) and we use dynamic time warping (DTW) to quantitatively correlate profiles from different sites. The DTW method tunes a function to another to test for a possible high covariance between the two (here, depth is a proxy for time) and has been validated for use in Mars' PLD [14].

We search for periodicities in the continuous linear profiles using Wavelet Analysis [2]. The wavelet power spectra (WPS) reveal any dominant periodic forcing frequencies in the data, providing another tool for correlating strata from different sites and informing future investigations into the putative orbitally-forced deposition of the SPLD.

3. Results: HiRISE

Protrusion profiles for 7 of the 8 HiRISE sites are shown in Fig 2. The exposure at site S1 does not overlap in elevation range with any other site and thus is not shown. However, a lack of elevation overlap does not necessarily imply no correlation, as accumulation rates can vary widely over the PLD [2].

Results from wavelet analysis seem consistent with the general picture in Fig. 2 (example WPS for S0 are shown in Fig. 3). S3 and S6 have similar

dominant wavelengths in protrusion (22 m and 14 m) and slope. The lower 5 sites have larger dominant wavelengths in protrusion (S0 = 72 m, S4 = 102 m, S5 = 47 m, S2 = 34 m, S7 = 135 m), and in slope. Additionally, DTW correlation results (not shown here) suggest a similar structure. We hypothesize that the three sets of profiles correspond to three different accumulation periods. A 3-sequence structure was suggested before by [9]. This study correlated exposures of similar units based on morphology, but a quantitative correlation is still missing.

The WPS also suggest that at least regional climate signals exist in the SPLD, but the exposure stratigraphy of the SPLD appears more complex and less consistent than that found in the NPLD. Ongoing radar analysis suggests these difficulties may also exist in beds that are not exposed at the surface [15].

4. Future Work

An expanded dataset of DTMs will significantly improve our work, as was the case for the NPLD. We have targeted numerous new areas in the SPLD for DTM creation. In particular, extensive CaSSIS coverage of Ultima Lingula (UL) - where we only have one HiRISE DTM - will help define whether UL represents an entirely different stratigraphic unit, or if it can be correlated to the Promethei Lingula Layer sequence (PLL) of [9], and will provide the most detailed stratigraphic mapping of the region do date. Additionally, there is also only one HiRISE DTM in the highest areas of the SPLD (S1), so we have also targeted this area for HiRISE DTM production to obtain a complete picture of the accumulation history of the SPLD.

Further in the future, we plan to statistically compare the dominant wavelengths in the stratigraphy to the possible orbital scenarios before 20 Ma proposed by [4]. As was done for the north by [2], and for equatorial deposits by [16], we will compare the average ratios of wavelengths in the stratigraphic data to that of the possible oscillations of the average insolation [3].

5. Figures

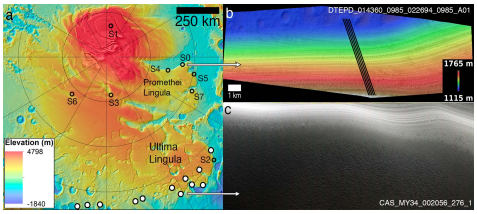

Fig. 1. (a) MOLA map of the SPLD with study sites indicated. Labeled open circles = HiRISE DTMs. White-filled circles = Planned/Executed CaSSIS Stereo. (b) HiRISE DTM of site S0 with profiles drawn (c) 1st CaSSIS color stereo pair of the UL margin. Filters: NIR-RED-PAN [11]. Location shown by arrow.

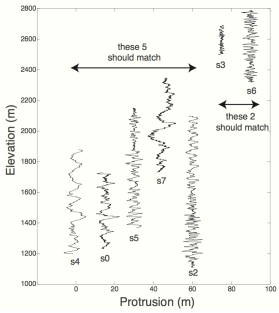

Fig. 2. Average protrusion profiles from HiRISE DTMs as a function of elevation for 7 sites in the SPLD. Profiles are offset in increments of 15 m on the x-axis for better visibility.

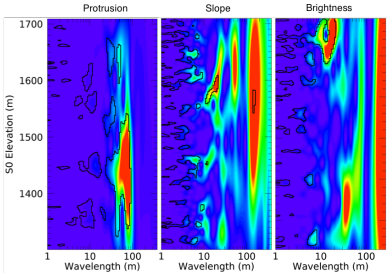

Fig. 3. Wavelet Power Spectra of the protrusion, slope, and brightness profiles of site S0. Warmer colors indicate higher power. Black lines are contours denoting the 95% confidence level over red noise (see [2] for details).

Acknowledgements

The authors wish to thank the TGO/CaSSIS spacecraft and instrument engineering teams for the successful completion of the instrument. CaSSIS is a project of the University of Bern and funded through the Swiss Space Office via ESA's PRODEX programme. The instrument hardware development was also supported by the Italian Space Agency (ASI) (ASI-INAF agreement no. I/018/12/0), INAF/Astronomical Observatory of Padova, and the Space Research Center (CBK) in Warsaw. Support from SGF (Budapest), the University of Arizona and NASA are also gratefully acknowledged. The authors also thank the HiRISE Science and Operations team for the acquisition of the images and the production of the DTMs.

References

[1] Byrne et al. *Ann. Rev. Earth Planet. Sci.* (2009) [2] Becerra et al. *GRL* (2017) [3] Laskar et al. *Science* (2002) [4] Laskar et al. *Icarus* (2004) [5] Hvidberg et al. *Icarus* (2012) [6] Herkenhoff et al. *Icarus* (2000) [7] Koutnik et al. *JGR* (2002) [8] Byrne and Ivanov, *JGR* (2004) [9] Milkovich and Plaut, *JGR* (2008) [10] Limaye et al. *JGR* (2012) [11] Thomas et al. *Space Sci. Rev.* (2017) [12] Becerra et al. *JGR* (2016) [13] Kirk et al. *JGR* (2008) [14] Sori et al. *Icarus* (2014) [15] Whitten et al. *AGU* (2017) [16] Lewis et al. *Science* (2008).

EPSC Abstracts
Vol. 12, EPSC2018-245-1, 2018
European Planetary Science Congress 2018

Gully activity in Sisyphi Cavi, Mars

Jan Raack (1), Susan J. Conway (2), Meven Philippe (2), Thomas Heyer (1), Dennis Reiss (1) and Harald Hiesinger (1)
(1) Institut für Planetologie, Westfälische Wilhelms-Universität Münster, Germany, (2) Laboratoire de Planétologie et Géodynamique, Université de Nantes, France (jan.raack@uni-muenster.de)

1. Introduction

We present preliminary results of our study regarding recent gullies and their ongoing activity/modification within the Sisyphi Cavi region on Mars. Recent studies have shown gully activity in this region [1, 2], in which Raack et al. [1] proposed a potential formation process for one active gully: dry flows of sandy/dusty material over a sublimating translucent seasonal CO_2 slab ice.

In the same region numerous dark spots [3, 4] and dark flows [5, 6] can be found on dunes as well as on slopes of the pits during spring. It is thought that this activity is most likely triggered by basal sublimation of seasonal CO_2 ice followed by degassing through small cracks in the ice crust, carrying darker sand and dust to the surface [4]. On sloping surfaces, these lofted materials can move downslope leading to dark flows [5, 6]. The morphological similarity between dark flows within a gully in the northern region of Sisyphi Cavi [1] and the dark spots and flows in the same region during spring leads us to the hypothesis of a similar formation mechanism. Furthermore, dark flows have also been proposed to form via jets through the CO_2 ice slab [6, 7]; comparable to the proposed formation mechanism for the active gully [1].

By extending our survey area to the whole Sisyphi Cavi we want to test our hypothesis that the near-polar gullies and the dark spots and flows have similar formation mechanisms.

2. Methods

2.1 Study Region

Sisyphi Cavi is a pitted terrain in the south polar region of Mars. Our study region (20°W to 10°E and 66° to 76°S) comprises all of the pits of Sisyphi Cavi (Figure 1). The steep slopes of numerous pits hold several recent gullies with ongoing present-day activity [1, 2]. Within the pits and on the slopes of the pits, numerous dark spots and dark flows can be observed in spring. The depth of the pits is up to ~1 km [1]. It is proposed that the pits were formed by the basal melting of volatile rich material by subglacial volcanos [8]. During southern winter the complete region is covered in centimeter to decimeter thick seasonal CO_2 slab ice with contaminations of H_2O and dust [1].

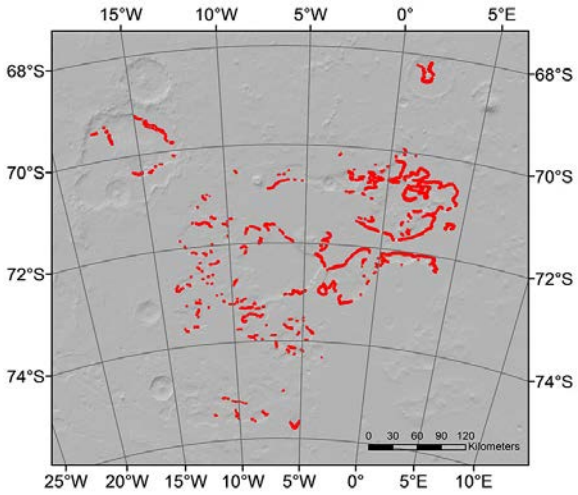

Figure 1: Preliminary map, showing gullies and gully-like structures within Sisyphi Cavi based on CTX images. Background MGS MOLA DEM hillshaded relief.

2.2 Proposed working plan

Here the presented work is preliminary and ongoing, we will:

1) Map all of the gullies in the Sisyphi Cavi region and analyze their orientation and slope angles (if suitable data are available) based on CTX images (preliminary results shown in Figure 1), and MOLA/HRSC/CTX elevation data.
2) Identify the activity of gullies over the last few martian years (MY) based on HiRISE images. This work will be carried out with the Multi-Temporal Database of Planetary Image Data (MUTED) [9, 10]. Activity will

be then narrowed down to the smallest time range for each MY.

3) Identify and map the dark flows and dark spots in the region.
4) Investigate identified activity in detail with spectral and thermal datasets to identify possible triggering mechanisms of the dark flows inside and outside gullies.

2.3 Data

Our mapping of gullies is based on CTX images. Until now for our preliminary results we have used numerous single CTX images, but for the final study it is planned to use a part of the global CTX-Mosaic by Dickson et al. [11]. We will also use all of the 479 HiRISE images which are available in our study region for detailed analysis. For the identification of current activity of our observed geomorphological features, MUTED [9, 10] is a perfect tool to not only identify the multi temporal coverage of HiRISE images, but also for the search for adequate thermal and spectral datasets. Based on MUTED, 345 HiRISE images have a multi temporal coverage in this region.

3. Results of recent studies

As described shortly in the introduction, in 2015 a previous study about present-day activity of one specific gully (1.44°E, 68.54°S) within the Sisyphi Cavi region was published [1]. This detailed work comprised a multi-temporal analysis of the gully on the basis of 36 HiRISE images, as well as spectral data acquired by CRISM and OMEGA and thermal datasets acquired by TES [1]. The active gully has very similar dimensions, slope angle and orientation to the adjacent gullies. Therefore activity of only one gully was difficult to explain. The multi-temporal part of this study showed that activity occurred between solar longitudes (L_S) ~218° and ~226° in MY 29-31 [1]. At this time of year surface temperatures rise rapidly and CO_2 and H_2O surface frost sublimate. Spectral modelling has shown that the annual surface frost is translucent CO_2 slab ice with H_2O contamination [1]. Raack et al. [1] proposed that dry material was eroded due to the sublimation of the seasonal slab ice at the steep slopes of the gully apron and channel and accumulated within the gully channel, which was still covered with ice. The ongoing sublimation of this ice triggered the movement of this dry material on top of the ice down the gully to the apron. Such a mechanism was previously proposed by [12].

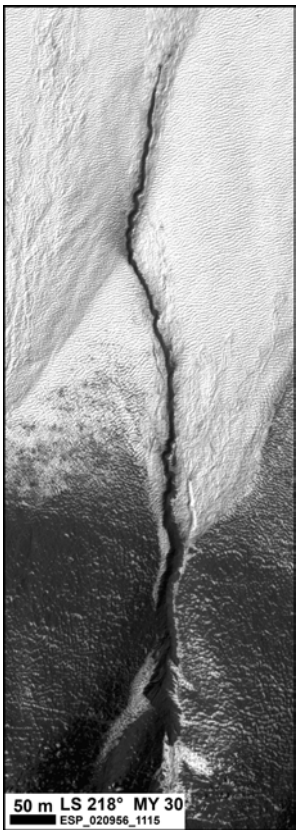

Figure 2: Active gully in Sisyphi Cavi. A dark flow is visible during spring within the gully alcove and channel. The dark material flows over the apron and new deposits are visible later in the spring. North is up, flow direction is from south to north. Modified after [1].

4. Preliminary results

During our preliminary study we have identified activity within additional gully channels, which are comparable to the activity identified by Raack et al. [1]. Furthermore, activity occurs at the same time as the appearance of dark spots and flows on dunes, which supports our working hypothesis that a similar formation mechanism forms both features.

5. References

[1] Raack, J. et al. (2015) Icarus 251, 226-243.
[2] Dundas, C.M., Diniega, S., McEwen, A.S. (2015) Icarus, 251, 244-263.
[3] Cantor, B., Malin, M., Edgett, K.S. (2002) JGR 107, E3, 5014.
[4] Piqueux, S., Byrne, S., Richardson, M.I. (2003) JGR 108, E8, 5084.
[5] Kereszturi, A. et al. (2009) Icarus 201, 492-503.
[6] Gardin, E. et al. (2010) JGR 115, E06016.
[7] Pilorget, C., Forget, F. (2016) Nat. Geosci. 9, 65-69.
[8] Ghatan, G.J., Head, J.W. (2002) JGR 107, E7, 5048.
[9] Erkeling, G. et al. (2016) PSS 125, 43-61.
[10] Heyer, T. et al. (2018) PSS, accepted.
[11] Dickson, J.L. et al. (2018) LPSC, 2480.
[12] Cedillo-Flores, Y. et al. (2011) GRL 38, L21202.

EPSC Abstracts
Vol. 12, EPSC2018-252, 2018
European Planetary Science Congress 2018

Experimental investigation of sand transport mechanisms by boiling liquid water under Mars-like conditions and potential implications for martian gullies and RSL

C. Herny (1), J. Raack (2,3), S. J. Conway (4) S. Carpy (4), T. Colleu-Banse (4) and M. R. Patel (2,5)
(1) Physikalisches Institut, Universität Bern, Sidlerstrasse 5, 3012 Bern, Switzerland (clemence.herny@space.unibe.ch), (2) School of Physical Sciences, Faculty of Science, Technology, Engineering & Mathematics, The Open University, Walton Hall, Milton Keynes MK7 6AA, UK, (3) Westfälische Wilhelms-Universität, Institut für Planetologie, Münster, Germany, (4) Laboratoire de Planétologie et Géodynamique - UMR CNRS 6112, Université de Nantes, 2 rue de la Houssinière - BP 92208, 44322 Nantes Cedex 3, France, (5) Space Science and Technology Department, STFC Rutherford Appleton Laboratory, Harwell Campus, Didcot OX11 0QX, Oxfordshire, UK.

Abstract

Active flow processes are currently ongoing at the surface of Mars, for example within gullies or RSL (Recuring Slope Lineae). One possible candidate involved in their formation and current activity is liquid water [1,2], but under current martian conditions liquid water is transient and can only be present in limited amounts [3]. However the surface temperature can locally exceed the melting point [4,5] on present-day Mars, leading to rapid boiling of liquid water. So far, little attention has been paid to the role of boiling in sediment transport processes. Recent study has highlighted that boiling water can drive unusual transport mechanisms leading to an enhanced transportation volume [6]. In our work [7,8] we conduct a series of experiments under low pressure to investigate the influence of both sand temperature (T_s) and water temperature (T_w) on the transport capacity of boiling liquid water under martian-like surface conditions. The experimental observations are then compared to physical laws. Results attest that among the two parameters, sand temperature is a driving parameter of sand transport by boiling water. This is enhanced at martian gravity.

1. Experimental set up and protocol

The experiments were performed under martian-like pressure (~9 mbar) in the Open University's Mars Simulation Chamber. The test bed was a rectangular tray, filled with a 5 cm thick layer of fine silica sand, set to an angle of 25° which is in the range of observed slope angles for martian gullies and RSL [2,5,7]. The water outlet was positioned at the top of the slope and controlled with a valve from outside. We performed experiments with 9 combinations of 3 different temperatures, 278 K, 288 K and 297 K for sand and water, respectively, which are consistent with temperatures measured at the surface of Mars [4,5]. Water was released for a duration of ~60 s with a mean flow rate of 11 m s^{-1}. We constantly monitored the sand temperature, water temperature, pressure, and humidity. The evolution of the test bed was recorded by cameras. We performed stereo-photogrammetry to produce digital elevation models and calculate the volumes of transported sand.

2. Experimental results

From observational data it is clear that the intensity of boiling was mainly driven by sand temperature while water temperature had only a minor influence. As sand temperature increases, the total volume of sand transported is increased by a factor of ~9 [7] while for different water temperatures it is rather constant (Fig. 1) [8]. The volume attributable to different transport mechanisms changed as the sand temperature increased. At T_s = 278 K, the majority of the sand is transported by overland flow while at $T_s \geq$ 288 K the majority is transported by mechanisms associated with boiling water, *i.e.* ejected pellets (sand-water mixture) and dry processes (including sand ejection and avalanches). We observe that the gas ejected by the boiling water is strong enough to create an air cushion at the bottom of pellets leading to their downslope levitation rather than rolling as observed at T_s = 278 K. Additionally, the produced gas is also able to eject single sand particles and drive dry avalanches. Water temperature plays a role in the duration of these dry processes which are longer at lower water temperature [8].

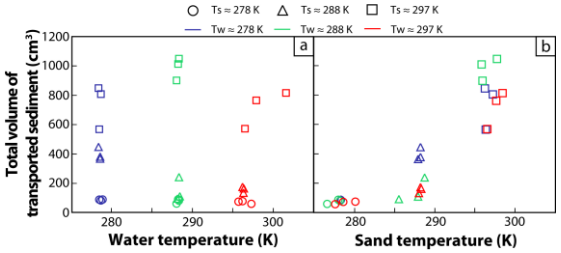

Figure 1: Transported sediment volume versus (**a**) water temperature and (**b**) sand temperature [8].

3. Transport mechanisms due to boiling and martian gravity scaling

Sand temperature is the main parameter controlling the boiling intensity because surface temperature drives the heat flux [9]. As liquid water is unstable it turns into gas and we observe single sand particle ejection and pellet levitation. In both cases the two forces in competition are the weight of the object and the force exerted by gas production. For sand ejection, we computed that for our experimental conditions and at T_s = 278 K grain ejection is very unlikely while at $T_s \geq 288$ K grains are ejected as observed in our experiments. If ejection does occur on Mars, the ballistic trajectory would be enhanced by a factor of 2.6 compared to Earth [8]. In addition, the increase of sand temperature leads to an increase in the duration of levitation of about several seconds and also a larger size range can potentially be lifted. We found that the levitation process under weaker Martian gravity is enhanced by a factor of ~7 and is able to transport larger objects for a longer time [7,8].

4. Conclusions

We find that sediment transport by boiling is characterised by grain ejection, granular avalanches and levitating pellets, which according to our scaling calculations are more effective transport processes under Martian gravity [7,8]. Among the two parameters tested, the sand temperature is the main driving parameter for transport via boiling while water temperature plays a minor role [8]. We highlight that if liquid water is present at the surface of Mars boiling could play an important role in understanding the recent changes in Martian gullies or RSL for which water is a candidate fluid [9]. It should not be neglected when analysing and modelling water flow features on Mars.

Acknowledgements

C. Herny and laboratory work was funded by Europlanet (Europlanet 2020 RI has received funding from the European Union's Horizon 2020 research and innovation program under grant agreement no. 654208). J. Raack was funded by a Horizon 2020 Marie Skłodowska-Curie Individual Fellowship (H2020-MSCA-IF-2014-657452). S.J. Conway was partially supported by the French Space Agency CNES. M.R. Patel was partly funded by the EU Europlanet programme (grant agreement no. 654208) and by the UK Space Agency/Science and Technology Facilities Council (ST/P001262/1).

References

[1] Malin and Edgett: Evidence for recent groundwater seepage and surface runoff on Mars, Science, Vol. 288, pp. 2330-2335, 2000.

[2] Conway S.J. and Balme M.R.: A novel topographic parameterization scheme indicates that Martian gullies display the signature of liquid water, EPSL, Vol. 454, pp. 36-45, 2016.

[3] Hecht M.H.: Metastability of liquid water on Mars, Icarus, Vol. 156, pp. 373-386, 2002.

[4] Haberle R. M. et al: On the possibility of liquid water on present-day Mars, JGR-Planets, Vol. 106, pp. 23317-23326, 2001.

[5] McEwen A. S. et al: Seasonal flows on warm Martian slopes, Science, 333, 740-743, 2011.

[6] Massé M. et al: Transport processes induced by metastable boiling water under Martian surface conditions, Nature Geoscience, Vol. 9, pp. 425-428, 2018.

[7] Raack J. et al: Water induced sediment levitation enhances down-slope transport on Mars, Nature Communication, Vol. 8, pp. 1151, 2017.

[8] Herny C. et al.: Downslope sediment transport by boiling liquid water under Mars-like conditions: experiments and potential implications for Martian gullies, GSL, Vol. 467, 2018.

[9] Diniega S. et al: A new dry hypothesis for the formation of Martian linear gullies, Icarus, Vol. 225, pp. 526-537, 2013.

EPSC Abstracts
Vol. 12, EPSC2018-257, 2018
European Planetary Science Congress 2018

Aeolian Transport in Coprates Chasma, Valles Marineris.

Sarah J. Boazman (1, 2), Peter M. Grindrod (1), Matthew R. Balme (3), Pieter Vermeesch (2) and Joel M. Davis (1)
[1]Dept. of Earth Sciences, Natural History Museum, London, UK, s.boazman@nhm.ac.uk. [2]Dept. of Earth Sciences, University College London, London, UK. [3]Dept. of Physical Sciences, Open University, Milton Keynes, UK.

Abstract

One of the most conspicuous active surface processes on Mars is aeolian transport (the movement of particles by wind), which has the potential to transport large volumes of sand across the martian surface, forming ripples and dunes of various morphology. In this study, we attempt to quantify the wind speeds occurring in Valles Marineris by measuring dune migration.

1. Introduction

Aeolian processes are the main agent of sediment transport on Mars. The wind is responsible for both the creation of landforms and erosion of the surface, thus shaping the martian landscape we see today. Aeolian landforms such as sand dunes, can aid our understanding of annual and seasonal climatic variations, such as changes in wind speed [1]. Dune fields on Mars have been observed to migrate, providing information about saltation [2, 3]. Although saltation is harder to initiate on Mars than Earth, because strong winds are rarer, once saltation is initiated, the sand flux is higher on Mars and so saltation is more easily maintained [4]. Saltation flux is one of the main controls on dune migration [5]. Migrating dunes illustrate that there are active winds occurring over the entire planet.

1.1 Study Site

Our study focuses on sand dunes in the equatorial region of Mars in the eastern part of Valles Marineris. The study site is the Coprates Chasma dune field (Figure 1), which lies within the southern Coprates Chasma trough, which is 4000m deep. The dune field is ~1 km in length and ~0.5 km width, covering an area 111km^2, and contains both barchanoid and longitudinal dunes.

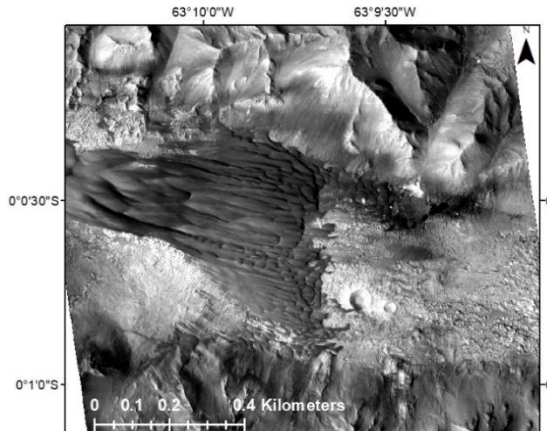

Figure 1. *CTX image F10_0396383_1658, showing the dune field at Coprates Chasma.*

2. Methods

We use a series of multi-temporal images from the Context Camera (CTX; 6 m/pixel [6]), with the Co-registration of Optically Sensed Images and Correlation (COSI-Corr) software package, [7] to measure the dune migration rates in the Coprates Chasma dune field over a 10 Earth year period (Figure 2). This should allow change across the dune field to be observed and a displacement rate to be calculated. Previous studies have used COSI-Corr with HiRise imagery due to the greater resolution; however, CTX has greater coverage in space and time, which is why CTX imagery has been chosen for our research.

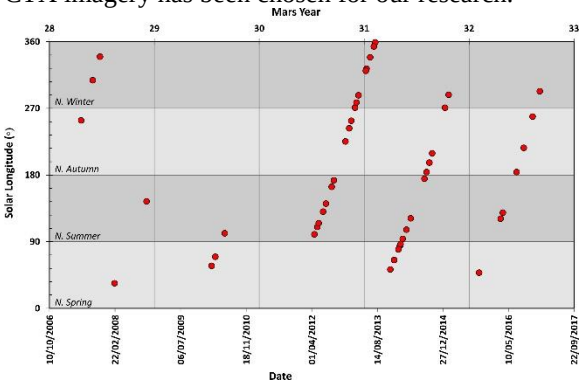

Figure 2*. CTX image coverage for our study area.*

2.1 Height and Dune Orientation Measurements

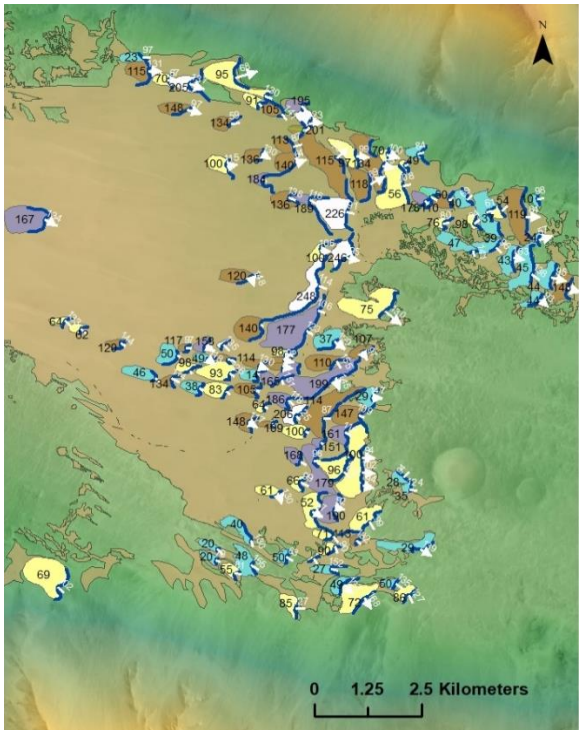

***Figure* 3**. *Outline of the dune field with the measured heights of individual dunes shown. Dunes are colour coded based on the height measurement. 0-50m blue, 51-100m yellow, 101-150m brown, 151-200 purple and 201-250m white. The white arrows show the orientation of the dune.*

Height measurements of the dunes have been taken to aid calculation of the sand flux that is occurring in this region. Dune heights in the dune field range from 10m to 248 m. These measurements were calculated from a CTX stereo-derived digital terrain model (DTM). We also measured the orientation of the dunes: the majority of the dune slipfaces have a south-east orientation (mean 113◦).

2.3 COSI-Corr

We have used CTX DTMs and orthorectified images in COSI-Corr to create preliminary displacement rate maps of the dune field. The images chosen cover a range of time scales (up to 10 years), to observe annual migration changes, as well as potential seasonal migration.

The displacement rate maps provide the measurements needed to calculate annual migration rate of the dunes. Previous studies have calculated annual migration rates on the order of 1-10 m/yr in Nilli Patera [2].

3. Summary and Future Work

We will use the displacement rate maps to measure dune migration in Coprates Chasma, which will then allow theoretical dune-forming wind speeds to be calculated. These results can then be compared to climate and atmosphere models to assess the wind regimes present in this area. This method can be applied to other areas in Valles Marineris to investigate the regional variations in the wind regimes. Furthermore, this method could be applied to bedform monitoring at future landing sites, providing an independent method of estimating wind speeds and sand fluxes, and which could then be used to assess their relative safety.

4. Acknowledgements

This work was supported by an STFC studentship (SB) and UK Space Agency grant ST/R002355/1 (PMG, JMD).

References

[1] Diniega, S. *et al.*: 'Our evolving understanding of aeolian bedforms, based on observation of dunes on different worlds', *Aeolian Research 26, 2016*.

[2]Bridges, N. T. *et al.:* Earth-like sand fluxes on Mars. *Nature,485,339-342* 2012

[3] Runyon, K. D., Bridges, N. T., Ayoub, F., Newman, C.E. & Quade, J. J. An integrated model for dune morphology and sand fluxes on Mars. *Earth Planet. Sci. Lett.* 457**,** 204–212, 2017.

[4] Fenton, L. K., Toigo, A. D. & Richardson, M. I. Aeolian processes in Proctor Crater on Mars: Mesoscale modeling of dune-forming winds.*J.Geophys.Res.E:Planets,110,1-18,* 2005.

[5] Kok, J. F. Difference in the wind speeds required for initiation versus continuation of sand transport on mars: Implications for dunes and dust storms. *Phys. Rev. Lett 104,* 2010.

[6] Malin, M. C. *et al.:* Context Camera Investigation on board the Mars Reconnaissance Orbiter, *J. Geophys. Res. E Planets* 112**,** 1–25, 2007.

[7] Leprince, S., Barbot, S., Ayoub, F. & Avouac, J. P. Automatic, Precise, Ortho-rectification and Coregistration for satellite Image Correlation, Application to Ground Deformation Measurement. *IEEE J. Geosci. Rem. Sens.* 45**,** 1529–1558, 2007.

EPSC Abstracts
Vol. 12, EPSC2018-260, 2018
European Planetary Science Congress 2018

Overview of recent ChemCam Findings after 2000 sols at Gale Crater, Mars

S. Schröder (1,2), R.C. Wiens (3), O. Gasnault (1), N. Mangold (4), J.R. Johnson (5), J. L'Haridon (4), J. Frydenvang (6), P.-Y. Meslin (1), A. Cousin (1), S. Maurice (1), and the ChemCam Team.
(1) Institut de Recherche en Astrophysique et Planétologie (IRAP), Toulouse, France. (2) Deutsches Zentrum für Luft- und Raumfahrt (DLR), Institut für optische Sensorsysteme (OS), Berlin, Germany. (3) Los Alamos National Laboratory (LANL), NM, USA. (4) Laboratoire de Planétologie et Géophysique de Nantes, Nantes, France. (5) Johns Hopkins University Applied Physics Laboratory, MD, USA. (6) Nat. History Museum – University of Copenhagen, Copenhagen, Denmark.
(Susanne.Schroeder [at] DLR.de)

Abstract

NASA's Mars Science Laboratory (MSL) rover Curiosity landed at Gale crater, Mars, in August 2012. Since then the rover has driven more than 19 km, and climbed 375 m, from the Bradbury landing site southwest over fluvio-deltaic strata, traversing the dark Bagnold Dunes, and is now ascending Mt. Sharp (formally Aeolis Mons). MSL carries aboard the first extraterrestrially employed LIBS (laser-induced breakdown spectroscopy) instrument ChemCam [1-3] that provides the elemental composition of rocks and soils. Here, we summarize the findings from lower Mt. Sharp, starting from Pahrump Hills to the current location of the rover at the Vera Rubin Ridge (VRR) with a focus on the geochemical stratigraphy as seen by ChemCam.

1. Introduction

ChemCam is composed of two instruments: a LIBS instrument for assessing the chemistry of targets in distances of up to 7 m and a Remote Micro-Imager (RMI) [4] that provides high resolution context images. ChemCam collects data nearly every sol, allowing variations in composition to be uniquely tracked at the submillimeter scale [3].

2. Recent Findings of ChemCam

With now over 2000 sols of the mission completed, more than 570,000 ChemCam LIBS spectra of soils and rocks have been recorded, analyzing over 2400 targets. Additionally, many ChemCam passive spectra (i.e. without lasing) have been recorded and analyzed [5-8]. The numerous analyses revealed the compositional diversity of the igneous rocks, the sedimentary rocks, and the diagenetic features.

2.1 Pahrump Hills and Marias Pass

On sol 750, MSL arrived at the light-toned layers of Pahrump Hills. The Pahrump outcrop corresponds to the first observed material at Mt. Sharp's base and is part of the Murray Formation, mainly constituted of mudstones [9]. It has been interpreted as an ancient lacustrine environment. The compositional diversity observed by ChemCam in the diagenetic features suggests a complex history of the sediments [10]. Its facies suggest a stronger alteration, with presence of minor F-bearing materials such as apatite, fluorite, and phyllosilicates [11]. The Stimson unit, which is unconformably overlying the Murray formation, is composed of eolian cross-bedded sandstones possibly evolved from ancient dunes. Both Murray and Stimson formations are highly enriched in SiO2 (>80 wt. %) locally at Marias Pass and Bridger Basin [9,12,13]. The Murray enrichment may be from a pulse of volcanic ash, as it contains tridymite, with subsequent mobilization to fractures in the Stimson.

Moreover, boron was detected in-situ for the first time on Mars by ChemCam at levels <0.05 wt.% in calcium sulfate filled fractures in the Murray mudstone and the Stimson sandstone as well as early in the mission at Yellowknife Bay [14].

2.2 Naukluft Plateau to Sutton Island

Ca-sulfate veins with Fe and Fe+Mg enrichment have been observed in the vicinity of the Naukluft Plateau and near the Old Soaker outcrop in the Sutton Island member implying changing pH and redox conditions in the groundwater [15].

Manganese and iron have shown strong increases with variable amounts of P and Mg in dark surface features [16]. These were found in several regions distributed ~160 m below the Vera Rubin Ridge, mostly in the Sutton Island member of the Murray formation. Mn oxide abundances have risen to >10 wt. % in some dark nodules and laminae. Iron, Mg, and P appear

correlated in high-P observations, with the highest values associated with vein-related inclusions. These findings provide additional evidence for the presence of a more shallow, oxidizing and weakly acidic to circumneutral lacustrine environment.

2.3 Vera Rubin Ridge (VRR)

On sol 1800, MSL arrived at the Vera Rubin Ridge, a ~6.5 km long and ~200 m wide topographic high [17] where relatively strong hematite signals were observed from orbit. ChemCam passive reflectance spectra and Mastcam multispectral data exhibited variable strengths of absorption bands near 535 nm and 860 nm along the traverse that corresponded well to the orbital maps. In ChemCam LIBS data no significantly increased Fe in the host rock was seen, but instead local high Fe detections (nearly pure FeO_T) associated with elongated and polygonal dark-toned clasts along light-toned Ca-sulfate veins were found [18]. These presumably diagenetic features showed lower abundances in all other major and minor elements suggesting a pure FeO mineral phase such as Fe-oxide. ChemCam passive reflectance spectra do not (or only weakly) show ferric absorptions associated with these features, contrasting with typical spectra associated with VRR host rocks.

2.4 Latest chemostratigraphy

The abundant data taken by the ChemCam instrument allows us to track changes in bedrock composition. Average bulk chemistry composition can be obtained by averaging all positions of a given target (ignoring locations on soil and diagenetic targets). Murray bedrock is enhanced in Si and alkali elements relative to usual Martian rocks while Ca is less abundant. Upon approach of the VRR, the Murray formation displayed increasing chemical index of alteration (CIA) that was anticorrelated with Ca, suggesting increasing weathering, especially leaching due to dissolution of either clinopyroxene or plagioclase [19]. These observations indicate weathering in an open system with liquid water, at or near the surface. The rover's cameras observed indications of periodic desiccation in the sediments, including putative mud cracks at Old Soaker at sol 1550 [20,21].

The VRR consists of laminated mudstones thought to be lacustrine in origin similar to the Murray formation and is interpreted as an individual group within the latter. The variation of the major and minor elements at the VRR does not extend the ranges defined by the previously investigated Murray bedrock and the absolute content is similar. However, relative differences between certain elements were found such as an increase in K in VRR but no corresponding increase in Na and a slightly increasing Al, resulting in a decreasing CIA in the VRR after the rising trend when approaching it. The observed reduced Li in the VRR could indicate lower clay content in the VRR and explain the higher erosional resistance [22].

Acknowledgements

This work was enabled by NASA's Mars Exploration Program, and by CNES in France. The team acknowledges JPL for developing and leading this successful mission and we thank the engineers and scientists who developed and operate the Curiosity rover and its instruments.

All Mars LIBS spectra and derived elemental compositions are available at *http://pds-geosciences.wustl.edu/missions/msl/chemcam.htm* and are described in > 40 peer-reviewed papers.

References

[1] Maurice S. et al. 2012. Space Sci. Rev. 170:95–166.
[2] Wiens R.C. et al. 2012. Space Sci. Rev. 170:167–227.
[3] Maurice S. et al. 2016. J. Anal. At. Spectrom. 31 :863.
[4] Le Mouélic S. et al. 2015. Icarus 249:93-107.
[5] Johnson J.R. et al. 2015. Icarus 249:74-92.
[6] Johnson, J.R. et al. 2016. Amer. Min., 101, 1501-14.
[7] Johnson, J.R. et al. 2017. JGR 122, 2655-2684.
[8] McConnochie T.H. et al. 2017. Icarus 307 :294-326.
[9] Grotzinger J. et al. 2015. Science, 350:625.
[10] Nachon M. 2017. Icarus 281 :121-136.
[11 Forni O. et al. 2016. LPSC XLVII #1990.
[12] Frydenvang J. et al. 2017. GRL 44:4716-4724.
[13] Morris R.V. et al. 2016. PNAS 113 26 :7071-7076.
[14] Gasda P.J. et al. 2017. GRL 44 : 8739-8748.
[15] L'Haridon J. et al. 2018. Icarus 311:69-86.
[16] Meslin P.-Y. et al. 2018. LPSC XLVIX #1447.
[17] Fraeman A.A. et al. 2018. LPSC XLVIX #1557.
[18] L'Haridon J. et al. 2018. LPSC XLVIX #1333.
[19] Mangold N. et al. 2017. LPSC XLVIII #1894 and submitted paper.
[20] Stein N. et al. 2017. Geology, doi:10.1130/G40005.1.
[21] Mangold N. et al. 2017. LPSC XLVIII #1908.
[22] Frydenvang J. et al. 2018. LPSC XLVIX #2310

EPSC Abstracts
Vol. 12, EPSC2018-269, 2018
European Planetary Science Congress 2018

Global properties of Martian Recurring Slope Lineae

Giovanni Munaretto (1), Maurizio Pajola (2), Gabriele Cremonese (2), Monica Lazzarin (1)

(1) Department of Physics and Astronomy "G. Galilei", University of Padova, Vicolo dell'Osservatorio 3, 35122 Padova, Italy (giovanni.munaretto.1@studenti.unipd.it), (2) INAF, Osservatorio Astronomico di Padova, Vicolo dell'Osservatorio 5, 35122, Padova, Italy.

Abstract

Recurring Slope Lineae (RSL) are narrow (0.5 – 5 m wide) dark features that source from bedrock outcrops and incrementally lengthen down warm, low albedo and low dust steep slopes [1]. Their activity starts in early local spring, when mid-afternoon temperatures are warm (≈ 250 K), ends in cold seasons, as temperatures drop, and recur every year in the same locations [1]. After their discovery by [1], the subsequent monitoring of Martian steep slopes has led to an increasing number of candidate and confirmed number of RSL sites, amounting to ~500 to date.

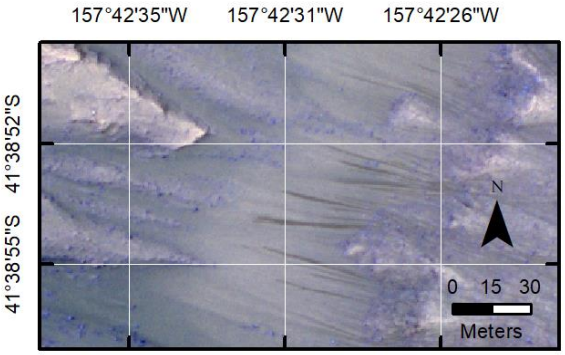

Fig. 1: RSL (dark lines) located in Palikir crater.

Most RSL have been identified in Valles Marineris (VM RSL, [1-4]), but they are also present in the southern mid latitudes (SML RSL) [5-7], in the equatorial highlands (EQ RSL) [1,2], as well as in Chryse and Acidalia Planitiae (CAP RSL) [8]. Multiple models have been proposed to explain their formation: the temperature dependence of RSL and their recurring darkening and fading suggested that a volatile may be involved in the process, such as freshwater or brines [1,5,8-11] although a distinct water spectral feature has not been observed yet [12,13]. Instead, the analysis of CRISM spectra at four sites showed a correlation between RSL activity and absorptions at 1.4, 1.9 and 3.0 μm wavelenghts attributed to the presence of hydrated salts, suggesting that a briny flow model is more likely [13]. According to such ''wet models'', RSL would form by melting of (briny) water ice during early spring that then would flow downslope darkening the regolith. Eventually, RSL would fade due to evaporation and decrease in temperatures. The main issue with these models is that the necessary volume of water required to supply RSL would be significant [3,14], while a clear water source has not been identified yet. To overcome this conundrum, other studies have proposed a formation mechanism based on dry granular flows [15], whose angle of repose is consistent with RSL slopes at many different sites. This scenario would imply a limited role for volatiles, but it hardly explains the annual recurrence and fading of RSL.

The aim of this work is to study the distributions of the global properties of all candidate and confirmed RSL, in order to provide a general picture of this phenomenon, hence framing the results from the detailed analysis of each single site. To do so, we collected all candidate and confirmed RSL sites present in literature [1-8] in a unique dataset. For each RSL location we extracted the MOLA elevation [16] and computed the local slope [17], TES thermal inertia [18], dust cover index [19], albedo [20] and IRTM rock abundance [21]. We then studied the distributions of such variables, identifying that the confirmed RSL sites occur in regions with MOLA elevation ranging from −5002 to 5088 meters, local slopes ranging from 0.09 to 36.66 degrees, daytime thermal inertia from 52 to 469 TIU (TIU is thermal inertia units, i.e. J m^{-2} $s^{-0.5}$ K^{-1}), nighttime thermal inertia from 171 to 2057 TIU, IRTM rock abundance from 2% to 25%, albedo from 0.09 to 0.24 and dust cover index from 0.95 to 0.99; the latter meaning that they have been found in almost dust-free regions of Mars.

As an example of the dataset we have, the daytime thermal inertia distribution of all confirmed and

candidate RSL sites is presented in Fig. 2A. The confirmed RSL sites have a thermal inertia ranging from 52 to 469 TIU, with a median of 224 TIU. When we extract both the VM RSL subset and the SML one we note that the VM RSL have a higher thermal inertia (median 268 TIU) with respect to those of the SML RSL (median 185 TIU), Fig. 2B and 2C; this behaviour is preserved even if we consider a larger sample with candidate RSL. Independently from the locations, all thermal inertia medians are above the dust thermophysical limit of 150 TIU [22], suggesting that most of the RSL do not generally occur on dusty surfaces.

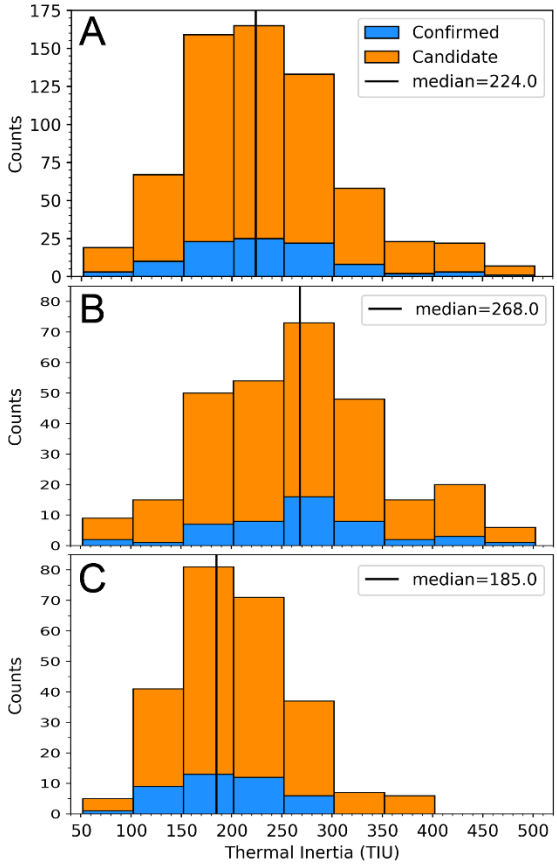

Fig. 2: A) Daytime Thermal Inertia (TI) distribution for all candidate (orange) and confirmed (blue) RSL and median of the *confirmed* distribution B) TI distribution for candidate and confirmed RSL in Valles Marines. C) TI distribution for candidate and confirmed RSL in southern mid latitudes.

By correlating all the considered variables, we propose new areas on Mars where RSLs have not been identified yet, but that have great potentiality to be discovered on HiRISE images in the near future.

Acknowledgments

The study has been supported by the Italian Space Agency (ASI-INAF agreement no.2017-03-17).

References

[1] McEwen, A.S. et al., 2011. Science 333, 740–743. [2] McEwen A. S. et al., 2014 Nat. Geosci., 7, 53-58. [3] Chojnacki, M. et al., 2016, J. Geophys. Res. Planets, 121, 1204–1231. [4] Stillman, D.E., et al, 2017a. Icarus, 285, 195–210. [5] Stillman, D.E. et al., 2014, Icarus, 233, 328–341. [6] Stillman, D.E, et al., 2018. Icarus, 302, 126-133. [7] Ojha, L. et al., 2014. Icarus 231, 365–376. [8] Stillman, D.E., et al., 2016. Icarus, 265, 125–138. [9] Chevrier, V.F., Rivera-Valentin, E.G., 2012. Geophys. Res. Lett. 39, L21202. [10] Levy, J.S., 2012. Icarus 219, 1–4. [11] Massé, M. et al., 2014, Planet. Space Sci. 92, 136–149. [12] Ojha, L.L. et al., 2013. Geophys. Res. Lett. 40. [13] Ojha, L. et al., 2015. Nature Geoscience 8, 829. [14] Grimm, R.E. et al., 2014. Icarus 233, 316–327. [15] Dundas, C. et al., 2017. 48th Lunar Planet. Sci. Conf., Mar 20-24. The Woodlands, TX, p. 2399. [16] Smith, D.E. et al., 2001. J. Geophys. Res. 106 (E10), 23689– 23722. [17] Burrough, P.A., McDonnell, R.A., 1998. Oxford University Press, New York. [18] Putzig, N. E., Mellon, M. T., 2007., Icarus, 191, 68-94. [19] Ruff, S. W., and P. R. Christensen, 2002. J. Geophys. Res., 107(E12), 5127. [20] Christensen, P.R. et al., 2001. J. Geophys. Res. 106 (E10), 23823–23871. [21] Christensen, P. R., 1986, Icarus, 68, 217-238. [22] Nowicki, S.A., Christensen, P.R., 2007. J. Geophys. Res. 112, E05007.

EPSC Abstracts
Vol. 12, EPSC2018-283-1, 2018
European Planetary Science Congress 2018

Estimates of Non-hydrostatic Stresses in the Martian Interior

Alexey Batov (1,2), Tamara Gudkova (2) and Vladimir Zharkov (2)
(1) V.A. Trapeznikov Institute of Control Sciences RAS, Russia (2) Schmidt Institute of Physics of the Earth RAS, Russia (batov@ipu.ru)

Abstract

We perform the stress field analysis of different zones on the surface and in the lithosphere of Mars in order to reveal the areas of maximum shear and extensional stresses as potential marsquakes' sources. Joint analysis of recent gravity and topography data truncated to degree 90 spherical harmonic in a frame of the static method is applied. The source of gravity anomalies is assumed to be the topographic loading and density anomalies at the crust-mantle boundary. Only non-equilibrium components of gravity and topography fields are considered: an outer surface of the hydrostatic equilibrium form of the planet is taken as a reference surface for topography and gravity field of Mars. Numerical calculations of extension-compression stresses and maximum shear stresses are carried out for an interior structure model of Mars having 150-300 km thick lithosphere, with a 1x1 arc-deg spherical grid and up to 1000 km depth.

1. Introduction

Studying of stress field in the Martian interior is of importance for forecasting seismic activity of the planet (for the seismic exploration of Mars). Discovery Program mission InSight (Interior Exploration using Seismic Investigations, Geodesy and Heat Transport) will place a single geophysical lander with a seismometer in Elysium Planitia on Mars to study its deep interior [1], as well as the international project of Russian Space Agency and European Space Agency suggesting seismic sounding of Mars is under preparation [3]. The estimates of global seismicity are reported in [2]. The youngest volcanic and tectonic features near Elysium Planitia are assumed to provide potential seismic sources. The purpose of this paper is to reveal areas of large shear and extension-compression stresses in the lithosphere of Mars as possible marsquakes' sources.

2. Method

Numerical simulation is based on a static approach (the loading factors technique or the Green's functions method) [4], [5], [7]. According to this method a planet is modelled as an elastic, self-gravitational spherical body. It is assumed, that deformations and stresses which obey Hooke's law are caused by the pressure of relief on the surface of the planet and anomalous density $\delta\rho(r, \theta, \varphi)$, distributed by a certain way in the crust and the mantle.

3. Interior structure model

As a benchmark real model for the planetary interior we use a trial model of Mars M_50 from [6] which satisfies currently available geophysical and geochemical data. The mean density of the crust is 2900 kg m^{-3}, the thickness of the crust is 50 km, the density contrast at the crust-mantle boundary is 360 kg m^{-3}.

4. Results

The results of modelling at depth 10 km are presented at figure 1.

The performed analysis shows that of particular importance are the areas beneath the impact ring basins, mascons Hellas Planitia and Argyre Planitia; the areas adjacent to the Tharsis rise Mare Acidalia and Arcadia Planitia; and huge canyon Valles Marineris. Beneath these regions, both the maximum shear stresses and the extensional stresses are quite high.

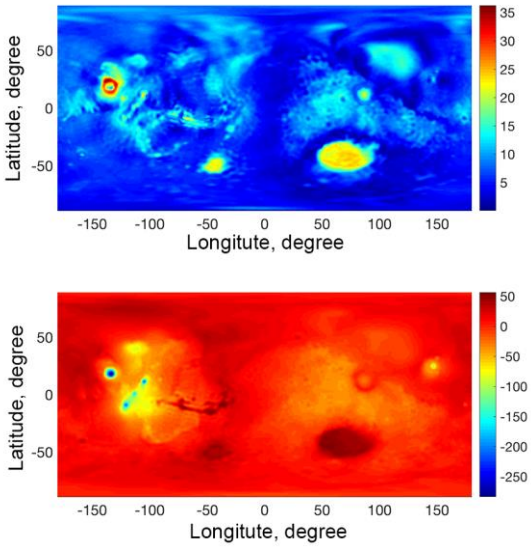

Figure 1: Non-hydrostatic shear stresses (up) and extension-compression stresses (down, extensional stresses are positive) at depth 10 km. Lithosphere 300 km.

5. Summary and Conclusions

High non-hydrostatic stresses may lead to relatively increased seismic activity for the above regions. The results could be of interest for the forthcoming seismic experiment on Mars. Investigation of areas of large stresses would be useful for further seismic events analyses.

Acknowledgements

The work was partly supported by Program 28 of Russian Academy of Sciences, the Russian Foundation for Basic Research, project no. 18-32-00875.

References

[1] Banerdt, W.B., Smrekar, S., Lognonné, P., Spohn, T., Asmar, S.W., Banfield, D., Boschi, L., Christensen, U., Dehant, V., Folkner, W., Giardini,D., Goetze, W., Golombek, M., Grott, M., Hudson, T., Johnson, C., Kargl, G., Kobayashi, N., Maki, J., Mimoun, D., Mocquet, A., Morgan, P., Panning, M., Pike, W.T., Tromp, J., van Zoest, T., Weber, R., Wieczorek, M.A., Garcia, R., Hurst, K. InSight: a discovery mission to explore the interior of Mars. In Proceedings of the 44th Lunar and Planetary Science Conference, p.1915, 2013.

[2] Knapmeyer M., Oberst J., Hauber E., Wählisch M., Deuchier C., Wagner R. Working models for special distribution and level of Mars' seismicity // J. Geophys. Res. E Planets, V. 111(11), P. 1-23, 2006.

[3] Manukin, A. B., Kalinnikov, I. I., Kalyuzhny, A. V., Andreev, O. N. High-sensitivity three-axis seismic accelerometer for measurements at the spacecraft and the planets of the solar system. In Proceedings of Solar System conference 7ms3, IKI RAN, 2016.

[4] Marchenkov, K.I., Lyubimov, V.M., Zharkov, V.N. Calculation of load factors for deeply buried density anomalies. Doklady Earth Science Sections 279, 14-16, 1984.

[5] Marchenkov, K.I., Zharkov, V.N. Stresses in the Venus crust and the topography of the mantle boundary. Sol. Astron. Lett. 16 (1), 77-81, 1989.

[6] Zharkov, V.N., Gudkova, T.V., Batov, A.V. On estimating the dissipative factor of the Martian interior. Sol. Syst. Res. 51, 6, 479-490, 2017.

[7] Zharkov, V.N. Marchenkov, K.I., Lyubimov, V.M. On long-waves shear stresses in the lithosphere and the mantle of Venus. Sol. Syst. Res., 20, 202-211, 1986.

EPSC Abstracts
Vol. 12, EPSC2018-294, 2018
European Planetary Science Congress 2018

Structural Mapping of the Inner Layered Deposits of the Crommelin Crater (Mars)

Dario Pesce (1), Riccardo Pozzobon (1), Matteo Massironi (1)

(1) Department of Geosciences, Università degli Studi di Padova, Italy, (2) INAF, Istituto Nazionale di Astrofisica e Planetologia Spaziali, Rome, Italy, (3) Department of Physical Science, The Open University, Milton Keynes, UK. (pesce.dario@gmail.com)

1. Introduction

Like many other impact craters within the Arabia Terra Region, on Mars, the Crommelin crater, located at 349.8° E and 5.1° N, displays a large central bulge and a well-preserved stratification (light albedo layered deposits) with some unusual landforms and structures that can be interpreted as fold sets, typical compressional structures often associated to diapiric rise on Earth [1]. It is possible to hypothesize that diapiric rise could have been responsible for central bulging on Crommelin crater and likely on other bulged craters on Arabia Terra.

This work, as part of the PLANMAP project, aim to realize a structural and geological map of the Crommelin crater area, estimating the extent of the deformation in the inner layered sequence of the crater, and finally to construct a 3D model of the basin showing the deformed deposits and the overall shape of the diapiric body underneath.

2. Data and methods

A high-resolution image dataset as well as DTMs were required to perform structural analysis, verifying strata dips and dip directions within the Crommelin crater floor and evaluate the presence of sequences of folds in the stratified deposits around the central bulge. In order to have an overall detailed view as well as good coverage of the study areas overlapping CTX images (6 m/px) were selected as pairs to produce stereo DTMs and orthorectified image mosaic. In addition, where available, HiRISE stereo images (0.25 m/px) were used. The DTMs were produced with Ames Stereo Pipeline and validated with the alignment on HRSC DTM (from DLR 100 m/px) and calibrating the heights according to MOLA topography (460 m/px) [2].

Analysis and mapping were conducted within ESRI's ArcGIS 10.3 environment, using T. Kneissl's Layer Tools extension [3].

3. Folded deposits

Several areas around Crommelin Craters bulge display clear stratification identified as ELD (Equatorial Layered Deposits) [4], suitable for analysis of strata dips and dip directions on DTMs. Within these deposits, folded stratigraphy were identified all around the central bulge.On the western and north-western sectors of the bulge a first sequence of folds was identified, with an approximate wavelength of ~1-2 km, displaying roughly concentric axial planes with an overall N-S orientation. The folds are symmetrical in the western area and become more asymmetric continuing to the north. The folds vergence is radial pointing outwards. The main sequence of folds seems probably perturbed by another less evident folding phase.

In the southern sector of the crater a second sequence of folds is highlighted by a series of elongated basin-like structures displaying a clear inwarddipping strat-

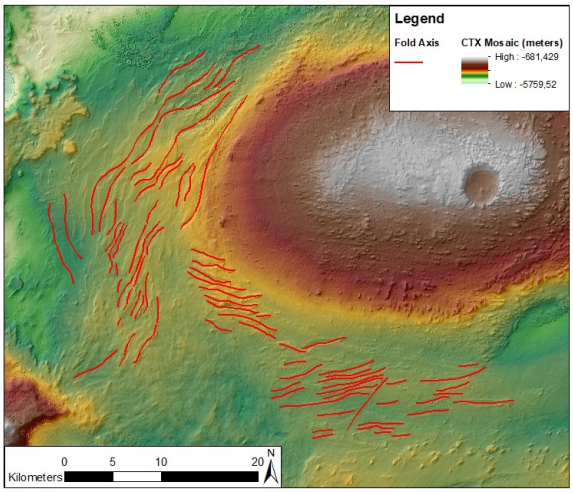

Figure 1: Overall view of the morphology of the central and south-west sector of the Crommelin crater. Red lines indicate inferred fold axes within the layered deposits around the strongly elliptical central bulge. CTX Mosaic (20 m/px).

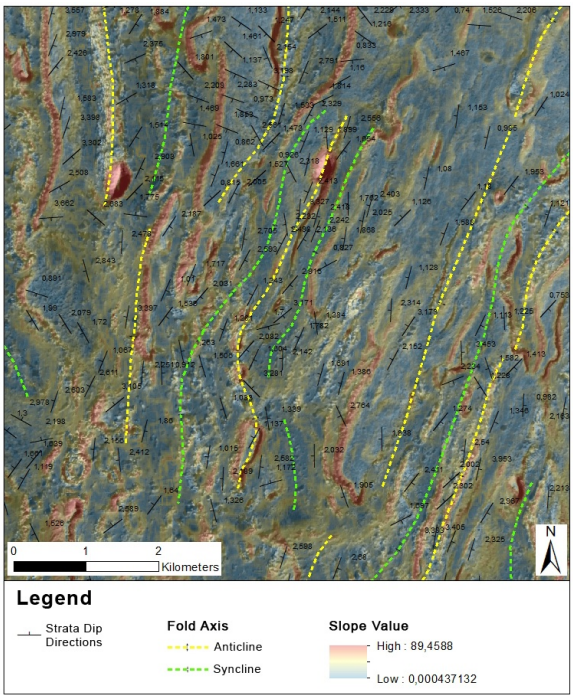

Figure 2: A detail of the western sector of the crater. The dotted lines indicate the axes of a fold sets (anticlines in yellow and synclines in green) inferred by the morphological contest and dip angles dip directions of the strata, measured on the CTX DTM and plottend in black with the dip angle highlighted. Orthorectified image mosaic with a slope layer overlaid in transparency.

ification with the dip angle progressively increasing towards the center of the basin. The approximate wavelength is kilometric and the axial planes are once again roughly concentric to the bulge but with an overall E-W orientation. Presumably, a second and more gentle folding phase overlaps the main one, with an axial orientation similar to that of the western area.The two main families of folds (the western set with N-S axes and the southern set with E-W axes) seem to insist respectively on two different units of the layered deposits, stratigraphically located one above the other and characterized by different morphological features.

4. Implications and future work

Several evidences suggest that crater's bulge may be hint for diapiric phenomenon. The uplift of the central section of the crater could easily have caused compressional stress on the surrounding rocks, leading to deformations that gave origin to fold sets. The trigger for the phenomenon could have been the impact cratering itself, having removed a rock mass volume that generated a differential lithostatic load favoring low density buried salt bodies to uprise [5].

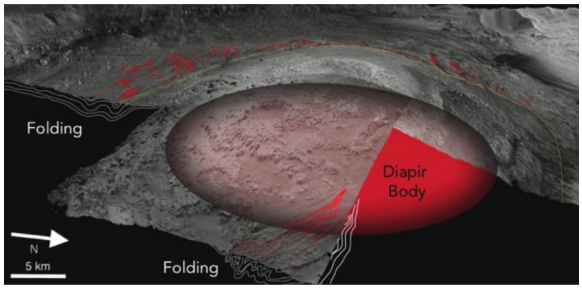

Figure 3: Perspective view and conceptual sketch of the diapiric body emplacement that likely caused bulging and folding. The diapir stays under the sedimentary layering coverage [5].

The folds setup suggests that the deformation could have occurred in more than one phases, influencing in a different way the various units that make up the inner layered deposits of the Crommelin crater.

The study will continue with a more in depth analysis of the deformation within the layered deposits as well as with a geological characterization of the deposits themselves, in order to create a structural and geological map of the Crommelin crater area and to produce a 3D model that will show the deformed deposits and the overall shape of the diapiric body underneath.

Acknowledgments

This research was supported by European Union's Horizon 2020 under grant agreement No 776276-PLANMAP.

References

[1] Dooley, T. P., et al., Inflation and deflation of deeply buried salt stocks during lateral shortening. J. Struct. Geol. 31, 582–600 (2009).

[2] Moratto, Z.M., et al., 2010. Ames Stereo Pipeline, NASA's Open Source Automated Stereogrammetry Software. In: Proceedings of the 41st Lunar and Planetary Institute Science Conference. Houston, Texas, #2364.

[3] T. Kneissl,et al., 2010. Measurement of strike and dip of geologic layers from remote sensing data – new software tool for ArcGIS. In: Proceedings of the 41st Lunar and Planetary Institute Science Conference. Houston, Texas, #1640.

[4] Hynek, B. Met al., 2002, Geologic setting and origin of Terra Meridiani hematite deposit on Mars: JGR: Planets, v. 107, no. E10, p. 18-11-18-14.

[5] R. Pozzobon, et al., 2015. Hints at diapirism in Arabia Terra bulged craters (Mars). In: European Planetary Science Congress Abstracts Vol. 10, EPSC2015-699, 2015.

EPSC Abstracts
Vol. 12, EPSC2018-339-1, 2018
European Planetary Science Congress 2018

Lobate features on Mars: a morphological and comparative study with dry and wet terrestrial analogues

Renaldo Gastineau (1), Susan Conway (1), Andreas Johnsson (2), Nicolas Mangold (1) and Peter M. Grindrod (3)
(1) CNRS, Laboratoire de Planétologie et Géodynamique, Nantes, France. (renaldo.gastineau@gmail.com)
(2) Department of Earth Sciences, University of Gothenburg, Gothenburg, Sweden.
(3) Department of Earth Sciences, The Natural History Museum, London, UK.

Abstract

If the small-scale lobes observed on Mars (Fig. 1) are the result of solifluction, their existence has important implications for our understanding of recent climate history, the distribution of thaw liquids and its geomorphic effects. We already know that these small-scale lobes are limited to sloping terrains, that they occur in craters which also host gullies and polygonal patterned ground and that they rise decimeters to few meters high [4,6]. In this study, we performed a comparative 3D morphometric analysis of the lobes on Mars and of terrestrial analogues to better understand their formation. We used data from High Resolution Imaging Science Experiment (HiRISE) camera in order to create Digital Terrain Models (DTMs). For the terrestrial analogues, we used DTMs and orthophotos of periglacial and desert environments on Earth.

1. Introduction

Small scale lobes (SSL) on Mars are landforms which have notable morphological similarities with terrestrial solifluction lobes (Fig. 1) [4]. SSL are limited to sloping terrain and mainly observed in the northern hemisphere. The southern hemisphere has more steep slopes [5], so the relative paucity of SSL is not clearly understood, but could be linked to hemispherical differences in surface properties [4]. Mid-latitude SSL have a pole-facing preference whereas high-latitude ones have an equator-facing preference [7].

2. Data and methodology

We used data from the HiRISE camera on the Mars Reconnaissance Orbiter at 25 cm/pixel. Using *Integrated Software for Imagers and Spectrometers (ISIS3)* and *Socet Set 5.6.0*, five DTMs at 1 m/pixel were made from HiRISE stereopairs. Six terrestrial analogues have been included in this study: Svalbard, Iceland, Sweden, Greenland, France and the Atacama Desert. The first five have solifluction lobes formed in periglacial environments and the last is a site where lobate forms are observed despite it being one of the driest places on Earth [2,3].

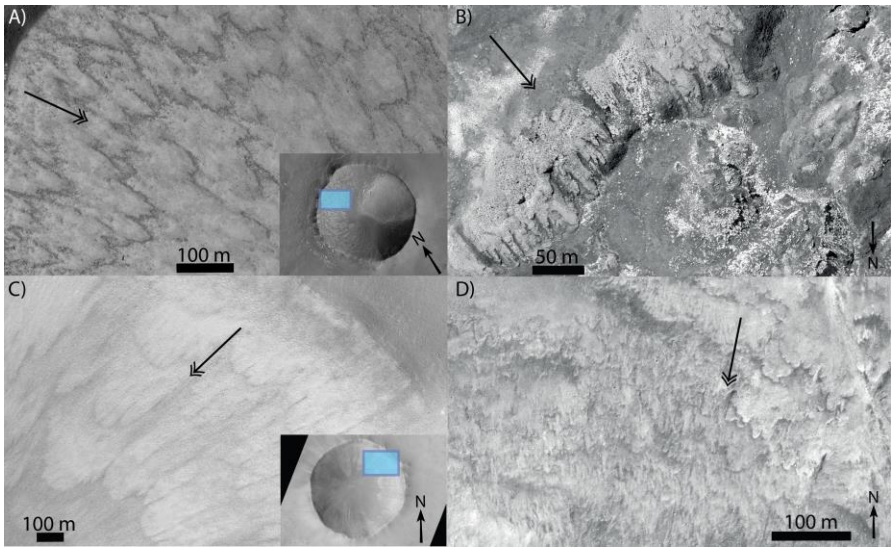

Figure 1: Examples of martian and terrestrial lobes. Double-headed arrows indicate the downslope direction. A) Sorted lobes in the northern hemisphere, in a 1-km-crater. B) Non-sorted lobes at Termignon in the Alps, France. C) Non-sorted lobes in a 4-km-crater. D) Non-sorted lobes located at Tindastóll, Iceland. Credit: NERC ARSF.

Terrestrial data comes from High Resolution Stereo Camera - AX (HRSC-AX), LIght Detection And Ranging (LIDAR), terrestrial scanner and Pléiades satellite imagery. Using *ArcMap 10.4.1*, we digitised the length and width of each lobe. Thus, slope, aspect, elevation or location of lobes along swath profiles could be derived.

3. Observations and results

To date we have analysed 4504 lobes, 1901 SSL on Mars and 2603 solifluction lobes on Earth. On Mars, SSL are observed on slopes ranging from ~10° to 37°, with a mean and median value of 25°. On Earth, solifluction lobes are found on slopes between 0 and 35°, the mean and median value are 14 and 16°, respectively (Fig. 2). For martian SSL, the width/length ratio appears to increase with decreasing slope. The same trend is apparent for the terrestrial solifluction lobes. On Earth, the W/L ratio of solifluction lobes have a maximum of ~15 for almost flat surfaces (Fig. 3). We are presently analysing the lobes from the Atacama Desert.

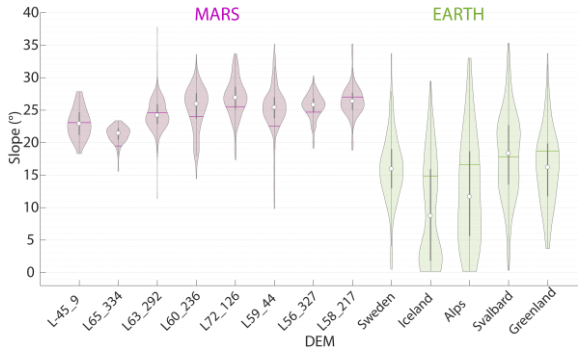

Figure 2: Violin plot of slope of lobes per site. White dots and horizontal lines represents mean and median values, respectively.

4. Discussion and conclusions

Previous work has concluded that SSL on Mars must be a result of solifluction, because they have similar plan-view morphology, slope-side setting and associated landforms to solifluction lobes on Earth [4]. However, our new 3D results shows martian SSL are restricted to high slopes, unlike terrestrial solifluction lobes (Fig. 2). This could be simply due to the lower gravity on Mars (1/3 of Earth gravity) meaning higher slopes are required to initiate creep. The fact that both datasets show the W/L ratio increases with decreasing slope, agrees with observed morphological transitions for solifluction lobes: from tongues to sheets with decreasing slope [e.g., 1]. Ongoing analysis of data from the lobes in the Atacama Desert, where the climate is thought to be more Mars-like will show whether this rare lobe-forming mechanism is a more appropriate analogue for martian SSL than solifluction.

Acknowledgements

This work was supported by the French Space Agency CNES.

References

[1] C.K. Ballantyne and C. Harris. The Periglaciation of Great Britain. CUP Archive, 1994. [2] J. D. Clarke, Geomorphology, vol. 73(1–2), 101–114, 2006. [3] J. J. Owen, et al., Geomorphology, 182, 157–172, 2013. [4] A. Johnsson, et al., Dynamic Mars, 2018. [5] M. Kreslavsky and J. Head, Geophysical Research Letters, 30 (15), 2003. [6] N. Matsuoka, et al., Permafrost and Periglacial Processes, 16(1), 99–113, 2005. [7] E. Nyström, EPSC Abstracts, 9 (EPSC2014-480–2), 2014.

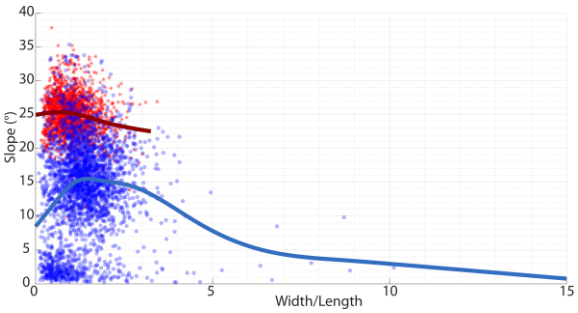

Figure 3: Plot of lobe width/length ratios as a function of mean slope. Blue and red dots represent terrestrial and martian data respectively. A spline for each dataset is also plotted.

EPSC Abstracts
Vol. 12, EPSC2018-346, 2018
European Planetary Science Congress 2018

Geomorphological Evidence of Local Presence of Ice-Rich Deposits in Terra Cimmeria, Mars

Solmaz Adeli (1), Ernst Hauber (1), Gregory G. Michael (2), Peter Fawdon (3), Isaac B. Smith (4), Ralf Jaumann (1,2)
(1) Deutsches Zentrum fuer Luft- und Raumfahrt (DLR), Institute of Planetary Research, Rutherfordstr. 2, 12489 Berlin, Germany (Solmaz.Adeli@dlr.de). (2) Freie Universität Berlin, Institute of Geological Sciences, Malteserstr. 74-100, 12249 Berlin, Germany. (3) Birkbeck, University of London, Malet St, London WC1E 7HX. (4) Planetary Science Institute, 1546 Cole Blvd Ste 120, Lakewood, Colorado, USA.

1. Introduction:

Evidence of shallow ground ice has been widely observed in the north and south mid-latitude regions of Mars such as: debris-covered glaciers [e.g., 1, 2]. There are also SHARAD observation [4] of ~70 m thick ice deposits in the mid-latitude regions. Global circulation models suggest that obliquity oscillations caused the mobilization of ice from polar regions and its re-deposition at lower latitudes [5, 6]. Although the obliquity variations are not predictable for periods more than 20 Ma ago [8], it is likely that the surface of Mars, during the Amazonian, has repeatedly undergone such climate changes leading to deposition and degradation of ice-rich material [e.g., 8, 9, 10]. This study describes well-preserved glacial-like deposits in Terra Cimmeria, which are defined here as valley fill deposits (VFD) (Fig. 1-a). They are located on the floor of a valley system which bears a record of Amazonian-aged fluvial and glacial processes [11].

2. Morphological characteristics:

Several deposits on the flat floors of S-N trending valleys south of Ariadnes Colles (34°S, 172°E) are characterized by (1) widths and lengths of a few kilometres, (2) convex-upward surface topography (Fig.1-b), and (3) pits and crevasses on their surfaces. These VFD are located a few tens of kilometres east of Tarq impact crater. Several of the VFDs are situated within the visible ejecta blanket of Tarq crater (Fig.1-a). The crater ejecta are observable on the surface and surrounding area of those VFDs. The VFDs have individual surface areas of a few km^2 to a few tens of km^2 (Fig1-b). In some cases they are located in the centre of the valley floor, whereas in other cases they cover the entire width of the host valley, indicating their post-valley formation. The valley width could reach up to a few kilometres, in some areas. Using a HiRISE DEM, we observed that one VFD has a thickness of ~30m. The latitude dependent mantle is also partly covering the VFD, and the surface of the VFD is exposed where the LDM has been degraded or sublimated.
The surfaces of VFD show only few impact craters with diameters equal or smaller than ~700m. Craters larger than 70m are mostly degraded, their rims show

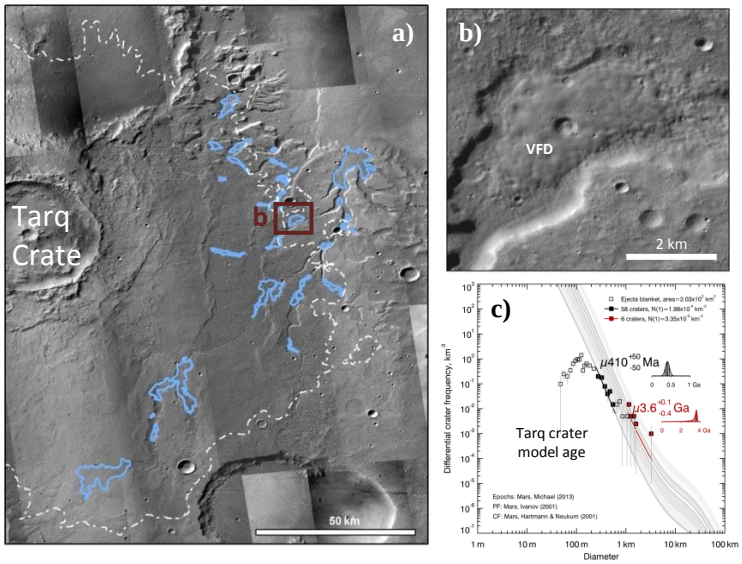

Fig. 1: a) An overview of the study area. The solid blue line represents the VFD locations. The dashed white line shows the Tarq Crater ejecta blanket. b) Zoom to one of the VFD, on the floor of a fluvial valley. c) Absolute model age corresponding to the ejecta blanket of Tarq crater. The data are plotted as a differential presentation of CSFD. μ is a function representing the uncertainty of calibration of the chronology model [3] (Epoch boundaries from [7]).

almost no positive relief (at CTX resolution) and they have flat floors. Where higher resolution data are available, we can observe linear features, cracks, and crevasses (lateral and transverse) on surface of VFD. Transverse crevasses may indicate tensile stress caused by viscous flow of the deposit. In several cases, in front of the VFD margins there is a zone up to ~3km of length, where the valley floor is covered by rough sediments. We interpret this rough zone as sediment accumulation similar to moraine-like material in front of a glacier. At the contact between the VFD and the valley walls, we observe several pits which most likely formed due to ice sublimation. These pits are aligned along the border of the VFD.

3. Absolute model age estimation: In order to understand the absolute model age (crater retention age) of the VFD, we analysed crater size-frequency distributions (CSFD) on CTX and HiRISE (where available) images using the method described in [3]. It should be noted here that there are uncertainties to derive a confident absolute model age of these deposits due the small area and small number of craters on VFD, in addition to the resurfacing phase(s) which may have most likely modified the crater morphology and their visible dimensions.

We suggest that the model age of the VFD surface is ~μ25 (±10) Ma, which corresponds to very late Amazonian (for μ definition see the Fig.1-c caption). The resurfacing event has roughly a recent age of ~μ3.4 (+2/-1) Ma and corresponds to late emplacement(s) of a thin layer of dust, airfall, and/or ice-rich material covering the VFD. In addition to the VFD, we also measured the CSFD on the ejecta blanket of Tarq crater, using a mosaic of CTX images. The result shows a model age of ~μ410 (±60) Ma for the impact crater (Fig.1-c), which corresponds to the end of the middle Amazonian, and a model age of ~μ3.6 (+0.1/-0.4) Ga for the base age.

4. Discussion: The VFD is characterized by a convex-upward shape, transverse crevasses, sublimation pits, and association with moraine-like deposits. These characteristics suggest that VFDs are ice-rich deposits with a thickness of a few tens of meters. The VFD was later partly covered by LDM which shows evidence of degradation, such as retreating boarders, sublimation pits, and scalloped depressions.

Our geomorphological observation suggests a link between the ejecta blanket of Tarq crater and the VFD distribution. It is, however, unclear whether the VFD formed 1) prior to the impact event, 2) contemporary to the impact, or 3) posterior to the impact and replacement of the ejecta blanket. In the first case, the emplacement of the ejecta blanket on a widespread ice layer would result in ice melt and mobilization into the valley. This case explains the VFD distribution but not the VFD model age. In the second case, the impact event may have occurred in ice-rich strata which, subsequently, have distributed a mixture of ejected material and ice, in other words, icy ejecta in the surrounding area. The ejected material deposited on the valley floor would have been preserved by the valley wall and therefore agrees with our interpretation. This case is consistent with the VFD distribution, our geomorphological observations, and a younger model age than the ejecta blanket. In the third case the VFD deposition may have taken place long after the Tarq impact event. This case is in agreement with our model age, but does not fully support our observations of their local distribution within the limits of the Tarq ejecta blanket and the fluvial valley. Therefore, the second scenario of impact into icy strata resulting in ice distribution in the area and ice deposits been preserved by the valley wall fits our geomorphological interpretations.

We conclude that the presence of ice-rich VFD provides local evidence of an episodic and multi-event process of ice emplacement in the mid-latitude regions of Mars during the Amazonian period.

5. Future work: Our next step is to look at the SHARAD radargrams of the VFD, aiming to observe the presence or lack of subsurface reflection. It should be noted here that the VFD covers a relatively small area which may not be in favour of a clear SHARAD observation. Additionally, the VFD location in a region with high relief (valley floor) may as well cause topographical clutter in a radargram.

References:

[1] Head, J.W., et al. (2003), *Nature*. *426*, p. 797-802. [2] Hubbard, B., et al. (2014), *The Cryosphere*. *8*(*6*), p. 2047-2061. [3] Michael, G.G., et al. (2016), *Icarus*. *277*, p. 279-285. [4] Stuurman, C.M., et al. (2016), *Geophysical Research Letters*. *43*(*18*), p. 9484-9491. [5] Forget, F., et al. (2006), *Science*. *311*, p. 368-371. [6] Madeleine, J.-B., et al. (2009), *Icarus*. *203*, p. 390-405. [7] Michael, G.G. (2013), *Icarus*. *226*(*1*), p. 885-890. [8] Laskar, J., et al. (2004), *Icarus*. *170*, p. 343-364. [9] Smith, I.B., et al. (2016), *Science*. *352*(*6289*), p. 1075-1078. [10] Head, J.W., et al. (2005), *Nature*. *434*, p. 346-351. [11] Adeli, S., et al. (2016), *Icarus*. *277*, p. 286-299.

EPSC Abstracts
Vol. 12, EPSC2018-365, 2018
European Planetary Science Congress 2018

Aqueous Alteration at Libya Montes Reveals Changing Geochemical Environments on Early Mars

D. Tirsch (1), J.L. Bishop (2), J.R.C. Voigt (1), L.L. Tornabene (3), G. Erkeling (4), and R. Jaumann (1,5)

(1) Institute of Planetary Research, German Aerospace Center (DLR), Berlin, Germany (Daniela.Tirsch@dlr.de). (2) Carl Sagan Center, The SETI Institute, USA. (3) University of Western Ontario, London, ON, Canada. (4) German National Library of Science and Technology (TIB), Hannover, Germany. (5) Institute of Geological Sciences, Freie Universitaet Berlin, Berlin, Germany.

Abstract

We analyze the emplacement chronology and aqueous alteration history of distinctive mineral assemblages and related geomorphic units near Hashir and Bradbury impact craters located within the Libya Montes. We use the morphology associated with specific mineral detections to extrapolate the possible extent of the units hosting these compositions. We characterize multiple units consistent with formation through volcanic, impact, hydrothermal, lacustrine, and evaporative processes. Altered pyroxene-bearing basement rocks are unconformably overlain by an olivine-rich unit, which is in turn covered by a pyroxene-bearing capping unit. Aqueously altered outcrops identified here include nontronite, saponite, beidellite, opal, and dolomite. See [1] for a comprehensive discussion.

1. Introduction

The Libya Montes region, located at the southern rim of the Isidis impact basin, is an excellent example of the diverse geological processes that have shaped this part of the Martian surface over time [e.g., 2, 3]. Evidence of fluvial, lacustrine, aeolian, volcanic, impact/basin-forming events and hydrothermal processes, which span most of the geologic time on Mars, can be found in close association with one another. These landforms at Libya Montes are related to both relatively unaltered materials and aqueously altered sedimentary deposits as well as local rocks. Libya Montes provides a geologically diverse setting with multiple spectral observations useful for deciphering the complex geological and aqueous alteration history of this region of Mars with high value for contributing to the global picture of the evolution and climatic history of the planet.

2. Methods

We derive our results from a spectro-morphological mapping project that combines spectral detections from CRISM imagery with geomorphology and topography from HRSC, CTX, and HiRISE data. CRISM compositional maps were prepared using parameters developed previously [4, 5]. Mapping was performed on the combined data sets in ArcGIS with a digitizing scale of 1:20,000. The mineralogical composition of the surface units was deduced from the color coding of the CRISM parameter products (mainly R: D2300, G: OLINDEX, B: LCPINDEX). CTX texture was used to interpret the unit's morphology and extent in places where CRISM data are not available.

3. Results and Discussion

We identified three distinct regional morphologic units (Fig. 1): The stratigraphically lowest unit is the pyroxene-bearing bedrock (Bpx) that represents the ancient Libya Montes highland massif. An olivine-rich layered unit (LUol) has been generally deposited in topographic lows of the Bpx unit where it embays the pre-existing Libya Montes terrain. This unit appears to be related to the banded olivine-rich unit detected at the Nili Fossae region, at Northeast Syrtis and the Isidis basin [1, 6, 7, 8]. This age of the LUol (3.77 Ga, [9]), its layer structure, as well as the fact that it appears to follow the topography are indicative of a flow and are consistent with a volcanic origin [1, 8,10] rather than an impact melt origin [7] (because it is too young to result from the Isidis impact). A recent study by [11] indicates that the unit decreases in thickness with distance from Nili Patera indicating that it might represent olivine-rich ash-fall deposits originating from Syrtis Major. A pyroxene-bearing caprock unit (Cpx) lies stratigraphically and topographically above the LUol unit. Due to its composition and appearance, we favor the interpretation of [7 and 8] that the caprock unit could be attributed to remnants of volcanic deposits generated from later stages of the evolution of the plume associated with Syrtis Major [12]. Since the LUol is always associated with the Cpx unit throughout our mapping region, they are most likely related to each other.

Various aqueous alteration minerals were identified in our study region (Fig. 1): Fe/Mg-smectites mostly crop out from the subsurface or are part of the walls of the ancient Libya Montes bedrock. Due to the widespread occurrence of these phyllosilicate-rich

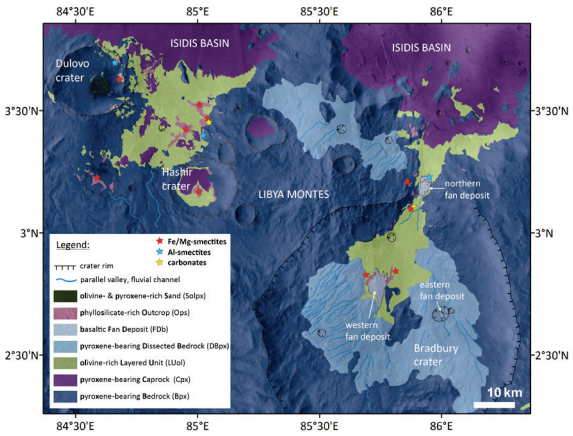

Fig. 1: Mapping of the Libya Montes study region as inferred from spectral and image data.

outcrops, local lacustrine processes, or igneous-induced hydrothermal processes are less likely formation mechanisms [13]. These phyllosilicates may have evolved instead from pervasive near surface alteration through impact-induced low-temperature hydrothermal processes in ancient bedrock material [14]. Al-smectites occur as isolated patches within the bedrock unit and along a discrete layer that crops out along the margins of a fan-shaped deposit. These sites are dominated by beidellite that is likely to have formed from low temperature hydrothermal alteration [15] or burial diagenesis of the bedrock materials at this site because beidellite forms at elevated temperatures [e.g., 9, 16, 17, 18]. Another smaller outcrop at the rear eastern margin of the same fan deposit (Fig. 2) is more consistent with opal. A further spectral signature of a thin bright layer along a nob in the middle of this smaller opal-bearing outcrop could be consistent with hydrated calcium chloride (Fig. 2). It shows absorption bands that are indicative of chloride salt minerals such as sinjarite. Whereas the beidellite at this fan delta might be allochtonous and could have been eroded from altered Libya Montes basement rocks, the opal-bearing deposit detected at the subaerial alluvial fan might have formed in situ through evaporative processes in a hydrothermal or lacustrine system in the course of the aqueous weathering of mafic rocks. The thin bright layer with the unusual spectral signatures attributed to Ca-chlorides reinforces an evaporative formation from brines.

Finally, we found dolomite intermixed with Fe/Mg-smectites that occurs in contact with olivine as it crops out from underneath the LUol. This mineral mixture appears to be the result of alteration of Noachian bedrock by neutral to slightly basic waters, which forms Fe/Mg-phyllosilicates and in some cases carbonates as well [9]. The composition of these altered rocks is likely affected by temperature and fluid chemistry at the time of alteration.

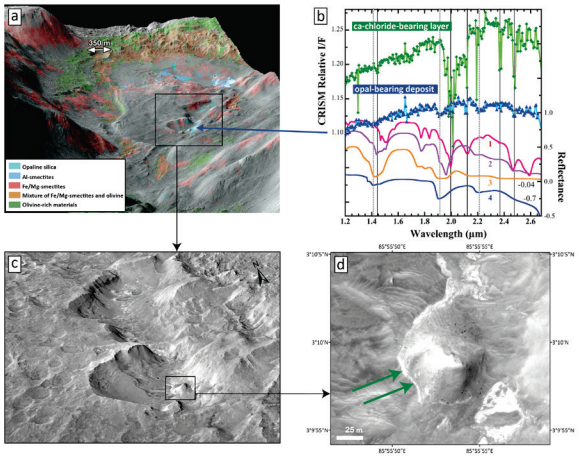

Fig. 2: Calcium-chloride detected within the opal-bearing outcrop located in the fan delta at the Bradbury region.

4. Summary and Conclusions

The diversity of mineral assemblages suggests that the nature of aqueous alteration at Libya Montes varied in space and time. This mineralogy together with geologic features shows a transition from Noachian aged impact-induced hydrothermal alteration and the alteration of Noachian bedrock by neutral to slightly basic waters via Hesperian aged volcanic emplacements and evaporative processes in lacustrine environments followed by Amazonian resurfacing in the form of aeolian erosion [1].

Acknowledgements: The work was supported by visiting scientist funding from the Helmholtz Foundation and Humboldt Foundation, NASA's Planetary Geology and Geophysics program and the NASA Astrobiology Institute. We acknowledge the efforts of the producers of the HiRISE DTMs namely Leocadie Feza Haguma, Sarah Mattson, and Joel Mueting.

References: [1] Tirsch, D., et al: Icarus, doi: 10.1016/j.icarus.2018.05.006, 2018. [2] Crumpler, L.S. & Tanaka, K.L.: JGR, 108, doi: 10.1029/2002JE002040, 2003. [3] Jaumann, R., et al.: EPSL, 294, 272-290, 2010. [4] Pelkey, S.M., et al.: JGR 112, doi: 10.1029/2006JE002831, 2007. [5] Viviano-Beck, C.E., et al.: JGR 119, 1403-1431, 2014. [6] Bramble, M.S., et al.: Icarus, 293, 66-93, 2017. [7] Mustard, J.F., et al: JGR, 112, doi: 10.1029/2006JE002834, 2007. [8] Tornabene, L.L., et al: JGR 113, doi: 10.1029/2007JE002988. [9] Bishop, J.L., et al: JGR 118, 487-513, 2013. [10] Hamilton, V.E. & Christensen, P.R.: Geology, 33, 433-436, 2005. [11] Kremer, C.H., et al: LPSC abstracts, p.1545, 2018. [12] Fawdon, P., et al.: JGR 120, 951-977, 2015. [13] Cannon, K.M., et al.: Nature, 552, 88, 2017. [14] Bishop, J.L., et al.: Nature Astronomy, doi: 10.1038/s41550-017-0377-9, 2018. [15] Grauby, O., et al: European Journal of Mineralogy, 5, 623-636, 1993. [16] Huertas, F.J., American Journal of Science, 300, 504-527, 2000. [17] Guisseau, D., et al.: American Mineralogist, 92, 1800-1813, 2007. [18] Bishop, J.L., et al.: Clays and Clay Minerals, 59, 378-399, 2011.

EPSC Abstracts
Vol. 12, EPSC2018-390, 2018
European Planetary Science Congress 2018

Subsurface Investigation over Elysium Planitia, Mars using SHARAD data

Si-Ting Xiong and Jan-Peter Muller
Imaging Group, Mullard Space Science Laboratory, Department of Space and Climate Physics, University College London. Holmbury St Mary, Dorking, Surrey, RH5 6NT, UK. (siting.xiong.14@ucl.ac.uk; j.muller@ucl.ac.uk)

Abstract

Elysium Planitia lies at the boundary between the southern highlands and northern plains. This region has been in the spotlight due to a discussion of whether its origins are fluvial or result from liquid lava. One explanation of its origin is that it was formed by fluvial processes and a frozen sea is buried under a thick dust cover. The other argument is that this region is formed by lava flows. Paleo-channels are claimed to have been found buried underground near Marte Vallis, east of the Western Elysium Basin. However, a comprehensive investigation of subsurface features in this region has not yet been carried out. In this study, we investigate subsurface features using Shallow RADar (SHARAD) radargrams covering this region with an automated pipeline. Secondly, we compare the location of subsurface features with surface images to assure that the extracted features from SHARAD data are from subsurface. According to this comparison, two buried craters are suspected to be identified among the extracted subsurface reflections.

1. Introduction

The Elysium region of Mars lies at the dichotomy boundary transition between the old, heavily cratered southern highlands and the younger northern plains. The region is dominated by compressional (wrinkle ridges), extensional (fractures) tectonic features and broad flat plains [1]. South of the Elysium rise, a broad flat basin was filled by a fluvial channel that originates at the westernmost fractures, the Cerberus Fossae, in Athabasca Valles. The channel is over 10 km wide, contains kilometre-scale streamlined islands and extends more than 300 km from Athabasca Valles to the basin. The Cerberus Fossae, is also proposed to be the fluvial source that carved Marte Vallis to the east [2]. The surface of this area is extremely young (less than 10 Ma old) while it is not uniform in age, as multiple events are testified by overlapping flows, presence of secondary craters and variations in crater density.

Several regions in the Elysium region of Mars have previously been investigated using SHARAD data. Balme et al. [1] discussed the typical terrain in the Western Elysium Planitia ("frozen sea" region) and mentioned that this typical terrain is not restricted to this region and can be traced to a much larger area. Morgan et al. [2] reconstructed paleo-channels in the east of Elysium Planitia, around the Marte Vallis. South of the main western Elysium basin, Alberti et al. [3] used a two-layer model to invert the dielectric constant over the Planitia region and Zephyria Planum (ZP), and found that the relative dielectric constant for the top most layer material is 3 in the ZP and about 3.6-3.8 over three other sites in the Planitia region. Pietro et al. [4] identified at least three main different fluvial units corresponding to three main wet phases and stratigraphic sequences pointing to several deposition-erosion cycles around Zephyria Planum.

Mars Advanced Radar for Subsurface and Ionosphere Sounding (MARSIS) [5] and SHARAD [6], are two complementary radar instruments which were launched to investigate the upper crust of Mars and search for subsurface features associated with water and ice. They are orbital sounding radar, that transmits low-frequency radar pulses and is capable of penetrating below the surface. The radar pulse is reflected from where there is a subsurface dielectric discontinuity. Compared to MARSIS, SHARAD has a higher range resolution (15 m vs 150 m for MARSIS) but shallower penetration depth (1 km vs 3 km for MARSIS in the Martian north pole).

In this study, an automated pipeline based on a Continuous Wavelet Transform (CWT) is applied for extracting subsurface layers from SHARAD data over the Elysium region of Mars, including the suspected frozen sea region and the region east in Marte Vallis.

2. Study site and dataset

In this study, we investigated the broad and flat plains in the Elysium region, including the main Western Elysium basin (Area A), Marte Vallis (Area C) and the

area between them (Area B). In these three study sites, 141, 189, 151 SHARAD radargrams are collected and processed, respectively for A, B & C.

3. Preliminary Results

We extract the subsurface reflections from the SHARAD data over area A, B and C independently using the proposed pipeline based on CWT [7] and then calculate their depths to the surface DTM. The depth map is shown in Figure 1, from which we can see there are two locations (indicated by red ellipses) which appear like buried craters or basins with deeper buried subsurface reflections than the surrounding reflections. These features have no surface manifestation in the High Resolution Stereo Camera (HRSC) imagery. The HRSC images in the red rectangle are shown in Figure 2.

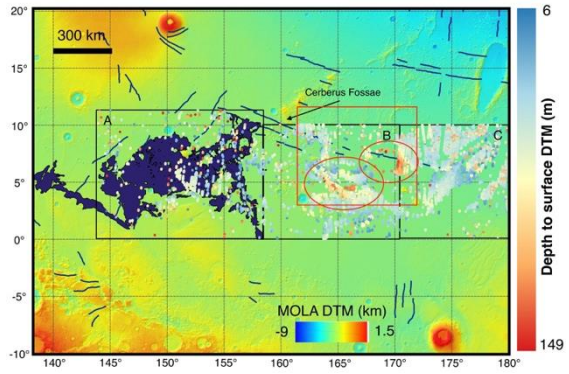

Figure 1: Study sites in Elysium Planitia region. Short dark blue lines are fractures. HRSC image of the red rectangle is shown in Figure 2.

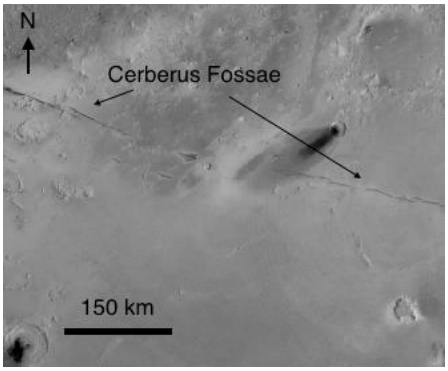

Figure 2: HRSC image (HD263_0000_ND3).

4. Discussion and Conclusions

In area A, there are not many subsurface reflections and their distribution follows no obvious pattern. East of the "frozen sea", more subsurface reflections can be found, such as in area B and C. The ellipse within area B indicates a feature which appears like a buried crater and a half-buried crater can be found next to it. The ellipse at the border of area B and C is over the east part of Ceberus Fossae, north of which there is a half-buried crater. We suspect that these two sites with deep buried subsurface layers are buried craters.

Acknowledgements

This work is jointly funded by the China Scholarship Council (CSC) and University College London (UCL) by providing a scholarship of Dean of MAPS prize to the first author.

References

[1] Cabrol, N.A. and Grin, E.A.: Lakes on Mars. Elsevier, 2010.

[2] Morgan, G.A., Campbell, B.A., Carter, L.M., Plaut, J.J. and Phillips, R.J.: 3D reconstruction of the source and scale of buried young flood channels on Mars, Science, Vol. 340, pp.607-610, 2013.

[3] Alberti, G., Castaldo, L., Orosei, R., Frigeri, A. and Cirillo, G.: Permittivity estimation over Mars by using SHARAD data: the Cerberus Palus area. Journal of Geophysical Research: Planets, Vol. 117, pp. 1-11, 2012.

[4] Di Pietro, I., Ori, G.G., Pondrelli, M. and Salese, F.: Geological map of Aeolis fluvial sedimentary basin, Mars, HRSC Team Meeting, 4-5 April 2017, Münster, Germany, 2017.

[5] Picardi, G., Plaut, J.J., Biccari, D., Bombaci, O., Calabrese, D., Cartacci, M., Cicchetti, A., Clifford, S.M., Edenhofer, P., Farrell, W.M. and Federico, C.: Radar soundings of the subsurface of Mars. science, Vol. 310, pp.1925-1928, 2005. doi: 10.1126/science.1122165

[6] Seu, R., Biccari, D., Orosei, R., Lorenzoni, L.V., Phillips, R.J., Marinangeli, L., Picardi, G., Masdea, A. & Zampolini, E.: SHARAD: The MRO 2005 shallow radar. Planetary and Space Science, Vol. 52, pp.157–166, 2004. doi: 10.1016/j.pss.2003.08.024.

[7] Xiong, X. and Muller, J.-P.: Automated Reconstruction of Subsurfaces in Promethei Lingula over the Martian South Pole by using SHARAD Data, Planetary and Space Science, 2018. (Under review)

EPSC Abstracts
Vol. 12, EPSC2018-425, 2018
European Planetary Science Congress 2018

Volcanic system of Isidis Planitia

Natalia Zalewska (1,2), Jan Kotlarz (1)
(1) The Institute of Aviation, Warsaw, Poland (2) Space Research Center PAS, Poland (natalia.zalewska@ilot.edu.pl).

1. Introduction

In the 1970s, data sent by the Viking probes showed fields of cones of unknown origin on images from the northern areas of Mars. Ideas for the genesis of these forms were many, from post-glacial forms through cryovolcanic so-called pingo to forms generated by volcanic processes. Volcanism on Mars was certainly there because in the area of Tharsis we have the largest volcanoes in our Solar System. The age of volcanism is estimated for the Noachian/Hesperian period. Little is mentioned about later or quite recent volcanism on the planet [1].

2. Origin of cones on Isidis

Fairly known HiRISE camera images, for example PSP_009177_1985; PSP_006936_1945 [2] caused much trouble for scientists because in general the interpretation of these cones was not clear. Such cones are found especially in the Isidis, Acidalia and Amazonis regions. Cones on Isidis attract special attention of scientists because it is not known why they are arranged in a kind of linear structure with a characteristic arched shape (Figure 1). Such system of cone cover an area of about half of Isidis. They are distinguished from the cones in other regions of Mars by the characteristic furrow through the center. Comparing them with their analogue in Myvatn in Iceland [3] gives rise to such problem that the Icelandic cones are arranged in a chaotic manner and the caldera are quite wide and most importantly Icelandic cones from Myvatn do not have that characteristic furrow through the center. The exception are the cones on Acidalia in the image THEMIS V55617012, which are arranged parallel to the lava tongue and are probably rootless cones. Lava had to flow on the area covered with ice or saturated with water. Cones on Acidalia are much smaller (50 m at the base) than those on Isidis (500 m at the base). It is worth to mention another similar place in Iceland namely the cones from recent eruption in Laki. They have that characteristic furrow and are formed on the line of the magma plume. In the work of Gudmundsson, et al. (2007) [4], depth of the magma chamber's seating and the tension system causing cracks in the characteristic circular structures are calculated. The magma from volcanic chamber penetrates these cracks. The magma from the volcanic chamber penetrates these cracks. We do not see such large chains conical structures on Earth as on Isidis. . There are only volcanic systems with the main central volcano or without the main volcano, but on a comparative scale to Isidis, these are very small cone fields. For example, the Pinacate system created from subduction of the Pacific Plate occupying an area of 30 x 60 km, or in similar scale Etna with its cone system, and Mauna Kea with a system of cones in Hawaii [5]. Tensions that are involved in the formation of arc like volcanic forms can be compared to the passing of a bullet through the glass, where a series of cracks is arranged in a circular and radial form. Tensions of magma penetrating the crust and piercing it can generate a series of circular structures around the volcano. Therefore, the area of the Syrtis Major volcano may be the main volcano, which generated a series of circular cracks around itself, which were filled with magma creating a volcanic system with chains cones on Isidis (Figure 2), [2]. Magma chamber under Syrtis preferred load model is approximately 300 × 600 km in size. Only Bushveld volcanic complex on Earth from 2 billion years ago is of similar size [6]. The Pavonis Mons volcano is an example around which there are such circular cracks and volcanic structures. The works are at the stage of modeling the Isidis volcanic system.

Figure 1: Fields of cones on Isidis with a characteristic furrow through the center, forming arched structures. (Google Mars, width of the image 40 km)

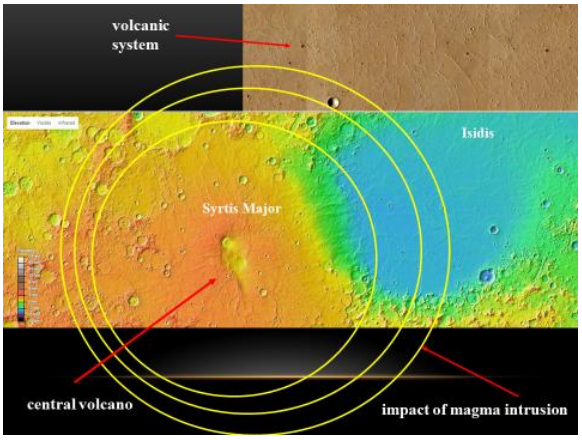

Figure 2. The impact of the magma chamber at Syrtis Major on the surrounding area around the volcano. (Altimeter map is from Google Mars, prepared from MOLA)

References

[1] Kerr R.: Ice or Lava Sea on Mars? A Transatlantic Debate Erupts, Science, Vol. 307, pp. 1390-1391, 2005

[2] Ghent R., Anderson S., Pithawala T.: The formation of small cones in Isidis Planitia, Mars through mobilization of pyroclastic surge deposits, Icarus, Vol. 217, pp. 169-183, 2012

[3] Noguchi R., Höskuldsson A., Kurita K.: Detailed topographical, distributional, and material analyses of rootless cones in Myvatn, Iceland, Journal of Volcanology and Geothermal Research, Vol. 318, pp. 89-102, 2016

[4] Gudmundsson A., Ruth A.: Mechanical interaction between active volcanoes in Iceland.: Geophysical Research Letters, Vol. 34, pp. L10310, 1-5, 2007

[5] Zalewska N.: Global Martian volcanism as a new interpretation of geological past of terrestrial bodies and moons in the Solar System, EPSC Abstracts, Vol. 11, EPSC2017-372, 2017

[6] Kiefer W.: Gravity evidence for an extinct magma chamber beneath Syrtis Major, Mars: a look at the magmatic plumbing system, Earth and Planetary Science Letters, Vol. 222, pp. 349– 361, 2004

EPSC Abstracts
Vol. 12, EPSC2018-429, 2018
European Planetary Science Congress 2018

Depth, volume and density of Mars' seasonal polar caps

David E. Smith and Maria T. Zuber
Department of Earth, Atmospheric and Planetary Sciences, Massachusetts Institute of Technology, Cambridge, MA 02139-4307, USA. (smithde@mit.edu; zuber@mit.edu)

Abstract

We have revisited the laser altimeter data obtained by the Mars Orbiter Laser Altimter (MOLA) [1,2] on the Mars Global Surveyor spacecraft between March 1999 and June 2001 to re-estimate [3] the depth of the accumulated CO_2, its variation with latitude and solar longitude, Ls, estimate its volume and infer the density of the deposited CO_2.

1. Introduction

The atmosphere of Mars is composed primarily of carbon dioxide, CO_2. During the winter seasons some of the CO_2 condenses onto the polar regions of the planet; in the summer season the precipitation sublimes back into the atmosphere. As winter approaches in the opposite hemisphere a very similar process of condensation followed by sublimation occurs creating a seasonal cycle in which 30% of the CO_2 atmosphere moves from one pole to the other with significant changes in atmospheric pressure. This process of exchanging atmospheric CO_2 with the polar caps has been well represented in Mars climate models and the seasonal change in the albedo of the surface has been observed photometrically for many decades.

2. Altimetry Data

The dataset was composed of MOLA altimeter residuals with respect to the best-fit global shape of Mars [4]. The total dataset was ~150 million measurements of elevation residuals referenced to the latitudes 50N & 50S. These elevation residuals are shown in Figure 1.

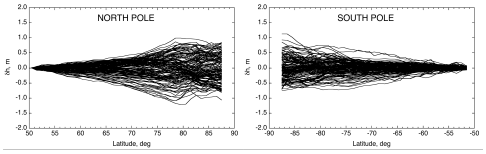

Figure 1: Elevation residuals referenced to 50N & S.

The figure shows ~160 profiles in each hemisphere of the mean residual in each 1 degree latitude band.

3. Depth of Precipitation

The residuals increase with latitude towards the pole with a full range of ~2 meters. Figure 2 shows the maximum depth with latitude independent of when the maximum depth occurs. The residuals were reference to latitude 50 because it is approximately the lowest latitude of seasonal deposition.

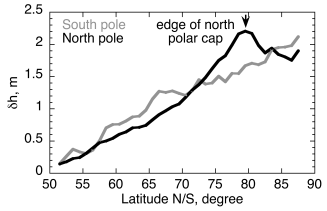

Figure 2: Maximum accumulation of CO_2 vs latitude. The average increase in depth is ~5 cm/degree. The maximum depth in the northern hemisphere occurs at the edge of the permanent cap. In the southern hemisphere the precipitation appears to increase almost linearly with latitude and may reflect the irregularity of the southern highlands and the lack of an identfiable polar cap boundary.

Sublimation begins as the planet warms in the Spring and Summer starting at latitudes nearest the equator and moving towards the pole. A northern hemisphere example is shown in Figure 3.

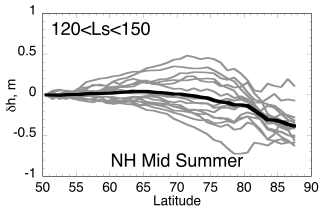

Figure 3: Example of northern mid-summer sublimation for 120<Ls<150. The larger positive values are for Ls<~135 and the larger negative values are for Ls> ~135. The black line is the average for the period.

4. Volume of Precipitation

We have used the average depth of the precipitation and the surface area of each 1-degree of latitude to estimate the volume of deposited material as a function of Ls. Figure 4 is an example of the southern hemisphere volume for late Spring.

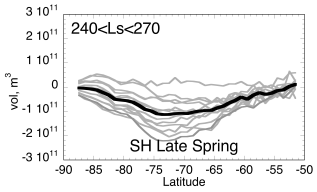

Figure 4: Change in volume during sublimation during the late Spring, 240<Ls<270. The black line is the average for the period. The curves above the avaerage are for Ls<~255; those below the average are for Ls>~255.

The data suggest sublimation in the north does not appear to be complete until the end of summer, particularly at high latitudes. In the south, sublimation is complete by the end of spring suggesting that the phasing of the seasons is not symmetric, probably as a result of the eccentricity of Mars' orbit and consistent with the longer winter and shorter summer in the southern hemisphere.

Figure 5 shows the total volume of precipitated material throughout the Mars year.

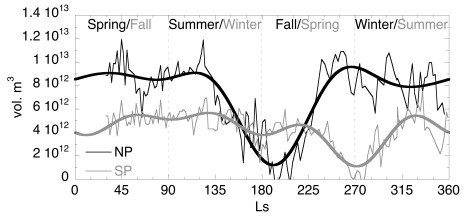

Figure 5: The total volume of precipitation on the surface during a single Mars year for latitudes ±50 and the N&S poles.

The volume in the north is remarkably constant except for the period mid summer through early Fall when sublimation seems to be greatest. In the south the minimum volume occurs around vernal equinox and overall the southern hemisphere has about half the volume of the northern hemisphere even though the winter season is actually longer in the south suggesting a more concentrated deposition, eg. ice or frost rather than snow.

5. Density Implications

Using estimates of the masses of the seasonal caps from gravity [5] and from Mars climate models [6] we can derive the average precipitation density. Since the northern hemisphere mass is estimated to be about half of the mass of the southern hemisphere and considering the volume of the north is about twice that of the south we obtain a significantly higher maximum density in the south of ~1200 kg/m^3 compared ~400 kg/m^3 in the north. This difference, if true, must indicate a different form of the precipitation in the south from the north. The most likely cause is significant block CO_2 ice in the south compared to snow like deposition in the north.

The density is very sensitive to errors in the volume of the precipitation and considering the probability of orbital errors we can only be confident that the densities of the seasonal precipitation are very different. In addition, we must remember that we only have altimeter data for 1 Mars year and it my not be typical.

References

[1] Zuber, M.T., Smith, D.E., Soloman, S.C., Muhleman, D., Head, J., Garvin, J., Abshire, J., Bufton, J: The Mars Observer Laser Altimeter Investigation: *Geophys. Res., vol. 97, no. E5,* 7781-7798, May 1992.

[2] Smith, D.E., et al.: Mars Orbiter Laser Altimeter (MOLA): Experiment Summary after the First Year of Global Mapping of Mars, *J. Geophys. Res.,* 106, 23,689-23,722, 2001.

[3] Smith, D.E., Zuber, M.T. and Neumann, G.A: Seasonal variation of snow depth on Mars: *Science, 294,* 2141-2146, 2001.

[4] Neumann, G.A., Rowlands, D.D., Lemoine, F.G., Smith, D.E. and Zuber, M.T: Crossover analysis of MOLA altimetric data: *J. Geophys. Res., 106,* 23,753-23,768, 2001.

[5] Genova, A., et al: Seasonal and Static Gravity Field of Mars: *Icarus,* https://doi.org/10.1016/j.icarus.2016.02.050

[6} Haberle, R.M., Murphy, J.R., and Schaeffer,J: Orbital Change Experiments with a Mars General Circulation Model: *Icarus*, 161, doi:10.1016/S00019-1035(02)00017-9.

EPSC Abstracts
Vol. 12, EPSC2018-448, 2018
European Planetary Science Congress 2018

Recent rockfalls on Mars

P-A Tesson (1,2), S.J. Conway (1), N. Mangold (1), S. Lewis (3), J. Ciążela (2)
(1) Laboratoire de Planétologie et Géodynamique UMR 6112, CNRS, Nantes, France. (2) Space Research Centre, Polish Academy of Science, Wrocław, Poland. (3) School of Physical Sciences, The Open University, Walton Hall, Milton Keynes MK7 6AA, UK.

Abstract

We study rocks falling from exposed outcrops of bedrock in martian impact craters. Those rockfalls have left trails on the slope over which they have bounced and/or rolled. Craters at ~20°N/S have notably higher frequencies on their equator-facing slopes compared to other slope-orientations. Our interpretation is that thermal stress is playing a more important role than ice-presence in rock breakdown on modern Mars.

1. Introduction

Individual rock falls are one of the currently active surface processes on Mars. Similarly to Earth, clasts detach from upslope outcrops roll/bounce downslope leaving a track on the substratum (Fig. 1B). The presence of these trails shows that these rocks have fallen relatively recently, because aeolian processes are known to infill topographic lows over time (estimations from rover-track erasure rates date these trails at <100 kyr). On Earth, slope instability is usually triggered by phase changes of H_2O [1], but it has also been suggested that solar-induced thermal stress could play a key-role in rock breakdown and triggering of rockfall events [2]. Although liquid water is not stable at the surface of Mars today, water ice can be found as a sub-surface layer from mid- to high-latitudes [3]. Water ice and CO_2 seasonal frost also exist in latitudes down to 30° on shadowed pole-facing slopes [4] and possibly even lower latitudes [5]. Thermal stress linked to insolation is the mechanism proposed to explain fracture orientation pattern in martian boulders observed by MER [6] and other studies suggest that it could cause rock breakdown on airless bodies [7]. Therefore, both phase changes of volatiles and solar-induced thermal stress are plausible mechanisms to cause rock breakdown and trigger rockfalls on modern Mars. The aim of this study is to investigate the mechanism involved in rock breakdown in impact crater walls through the cataloguing of rockfalls in these craters.

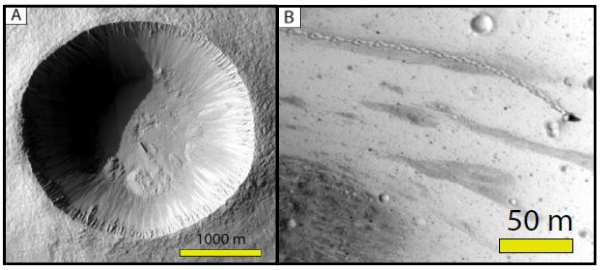

Fig. 1: A: Zumba crater, a morphologically fresh impact crater used in this study. HiRISE image PSP_002118_1510. **B**: Rockfall example displaying a well-preserved trail and 10 m long clast. HiRISE image ESP_037190_1765. Credits NASA/JPL/University of Arizona.

2. Methods

Using HiRISE images at 25-50 cm/pixel, we mapped the tracks left by rocks falling or bouncing from exposed outcrops in 45 impact craters in the equatorial to mid-latitude regions of Mars. Impact craters are widely distributed over the martian surface; thus, one can use them as sample points to test the different factors that may control rockfall. Conveniently, they are circular and therefore allow an assessment of the influence of slope-orientation with respect to the sun. Here, we focus on relatively small (<10 km) and fresh impact craters (Fig. 1A) to reduce the influence of slope-inheritance from other long-term processes. We also calculated surface temperatures of slopes with an angle of 35° facing 4 directions N-S-E-W, in 3 different latitudes using a 1D version of the LMD Mars climate model physics [8] (Fig. 3).

3. Summary and Conclusion

Mid-latitude craters have more numerous rockfalls on equator-facing slopes compared to pole-facing slopes and other orientations. At equatorial latitudes there are more rockfalls on N-S oriented slopes compared to E-W ones (Fig. 2).

In order to verify whether the observed trends are simply a function of asymmetries in slope steepness, we compared our rockfall distribution to slope angle for a sub-sample of craters where we could generate DTM from CTX stereo-pairs. Our results indicate there is no systematic variation in slope angle with orientation that could explain the trends in Fig. 2.

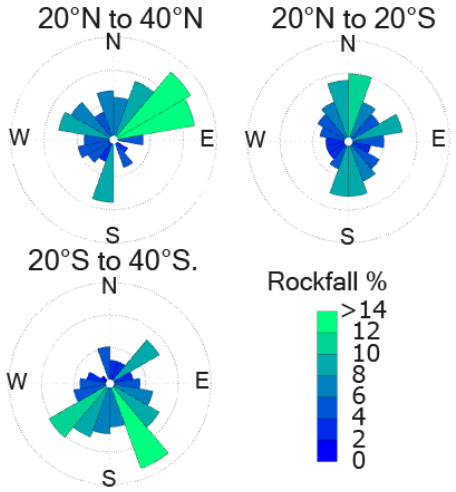

Fig. 2: Standardized distribution of rockfall orientation in fresh impact craters for different latitude ranges (each bin is the mean percentage of rockfalls for a given orientation).

Rockfall events triggered by phase changes should occur where water ice is expected to condense and/or be preserved from previous ice ages (i.e. on pole-facing slopes in the mid to high-latitudes and nowhere at the equator). Therefore, phase changes of H_2O or CO_2 do not seem to play a role in present-day rockfall activity on Mars. Instead, our results show it is likely related to insolation (Fig. 2). Results from the GCM show that at mid-latitude, equator-facing slopes have a higher diurnal range than E-W slopes and pole-facing slopes (Fig. 3), which implies a higher rate of temperature change and potentially higher thermal stress. However, at equatorial latitudes, the model shows that amplitude of temperature is more balanced between different orientations, and E-W slopes have slightly higher diurnal range. This means that simple patterns in insolation are not sufficient to explain the observed rockfall activity trends and other factors not covered by this study (e.g. salt weathering, or combinations of several thermal factors) are likely to influence rock breakdown rate. Moreover, thermal stress mechanisms (thermal shock and thermal fatigue) are still poorly understood and it would require more sophisticated models to take into account combinations of factors.

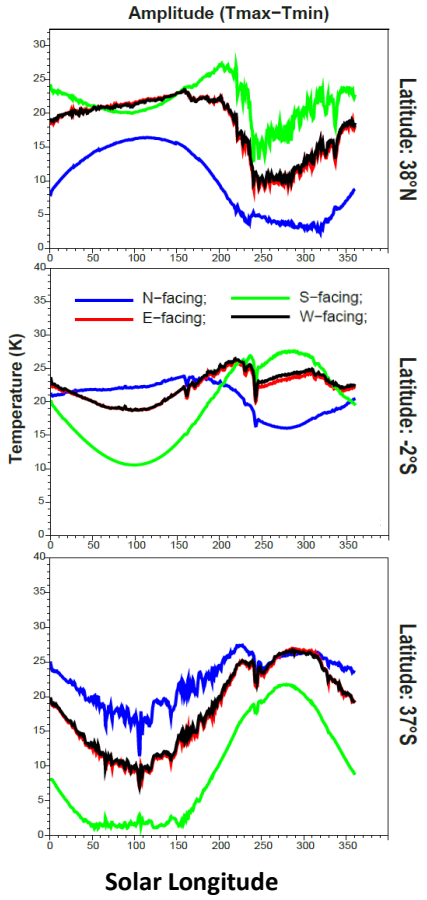

Fig. 3: Surface temperature data calculated using a Global Climate Model [8] for a 35° slope in 4 orientations at different latitudes.

Acknowledgements

This study was funded by CNES (French National Center of Space Studies).

References

[1] Prick, A. (2003) 8th International Conference on Permafrost, Volume 2. [2] Do Amaral Vargas, E. et al. (2013) Rock mechanics and rock engineering 46(1). [3] Feldman, W. C. et al. (2004) JGR, 109(E9). [4] Schorghofer, N. and Edgett, K. S. (2006) Icarus. 180(2), 321–334. [5] Piqueux S. et al. JGR 121(7) 1174-1189. [6] Eppes, M.-C et al. (2015). Nat. Comms. 6, 6712. [7] Molaro, J. L. et al. (2017) Icarus, 294. [8] Forget, F. et al. (1999). JGR 104.

EPSC Abstracts
Vol. 12, EPSC2018-457-1, 2018
European Planetary Science Congress 2018

Active Gullies and Mass Wasting on Equatorial Mars

Alfred S. McEwen (1), Melissa F. Thomas (1), Colin M. Dundas (2)
(1) LPL, University of Arizona, Tucson, Arizona, USA, (2) USGS, Flagstaff, Arizona, USA

Abstract

Mid- to high-latitude gully activity has been directly observed at hundreds of locations on Mars [1]. Here we describe equatorial locations (±25° latitude) with gully-like or other topographic changes in before-and-after images from HiRISE. This activity is concentrated in sulfate-rich sedimentary units, which places constraints on the age and mechanical properties of these deposits. Hydrated sulfates may be the largest equatorial reservoir of H_2O on Mars, and their friability makes them more attractive for in-situ resource utilization (ISRU).

1. Introduction

Mid- to high-latitude gully activity can be explained by the presence of seasonal CO_2 frost and ice, which fluidizes debris flows [1]. The belief persists that gullies do not form in equatorial regions today or in the recent geologic past [2], but there are observations of pristine equatorial features [3, 4] that match the terrestrial definition of gullies in terms of morphology and size. Many of these equatorial gullies are associated with active Recurring Slope Lineae (RSL) [3, 5], but actual topographic changes to the gullies have not been detected except in one possible case [5].

MRO's High Resolution Imaging Science Experiment (HiRISE) [6] has been observing Mars at ~0.3 m/pixel for over 11 years, providing a growing baseline for detection of surface changes. The HiRISE team recently began acquisition of HiKER (HiRISE checK for Exact Repeats) images: full-resolution repeat images within a few degrees of a prior image in illumination and emission angles. We also generated a list of past accidental HiKER image pairs. These image pairs reveal more subtle changes and enable distinguishing where the topography has changed rather than just changing albedo patterns from shifting dust.

2. Equatorial Changes

Previously-reported equatorial topographic changes include slumps on the colluvial fans below active RSL sites in Garni Crater [5] and in Juventae Chasma [7]. These slumps all occurred near the coldest time of year for these locations, L_s 0°-120°, which is opposite to the seasonality of RSL.

We are in the process of searching HiKER pairs over steep equatorial slopes, as well as acquiring new HiKER images. From the effort to date we have found that equatorial changes are most common in sedimentary layers that may be rich is sulfates according to mapping by orbital spectrometers [8], and have concentrated our search in these regions.

The most impressive changes we have found are on bright layered mounds in Ganges Chasma. The steep slopes of these mounds are highly dissected by pristine gullies (Figure 1), and repeat images show multiple changes including movement of boulders down gully channels. Most changes found to date are on south-facing slopes. The active erosion of these mounds suggests that they once filled a much greater volume of Valles Marineris. These mounds are rich in hydrated sulfates, leading to several models for their origin. Perhaps eolian dust and sand were trapped and lithified (weakly) by evaporites formed by evaporation of groundwater discharge [9].

Figure 1: Gullied slopes and colluvial fans on a mound of layered sediments in Ganges Chasm (ESP_032324_1715, 8.4° S, 313.3° E).

A new debris flow with a straight, shallow channel formed on the east-facing slope of a well-preserved 10-km crater at 15.7° S, 203.6° E (Figure 2). This may be better described as a leveed debris flow rather than an erosional gully, but there are many well-developed pristine gullies in this crater, some with distinctive colors from recent activity. Sulfates have been detected near this location [8] but not necessarily in this crater.

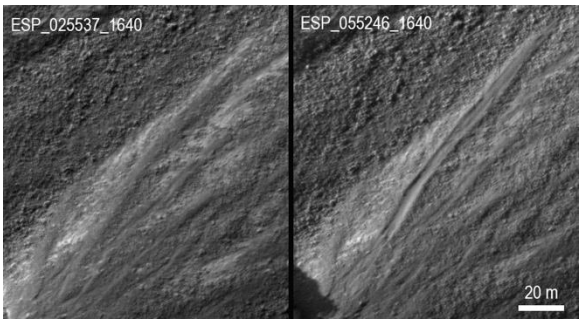

Figure 2: New channel and debris flow that formed on the NE-facing slope of a well-preserved crater at 15.7° S, 203.6° E between 1/7/12 and 6/18/18. Illumination from the left.

Other new topographic changes on steep slopes have been seen in a 9-km impact crater at 23.2° S, 43.2° E; a 3-km impact crater at 11.0° S, 25.9° E; Capri Chasma at 13.2° S, 312.2° E; Aram Chaos at 3.3° N, 339.0° E; Gratteri Crater at 17.8° S, 199.9° E, and Cerberus Fossae at 10.0° N, 157.8° E.

3. Discussion

The origin of mid-latitude gullies appears well-established as CO_2 fluidization [1], but there is no or very little CO_2 deposition in the moderate-to-high thermal inertia regions where we see equatorial gullies, so a different origin is required. Maybe RSL activity carves some of the gullies, but the exact mechanism of RSL activity is unclear. In all cases, we measure or suspect that slopes exceed the stopping angle for cohesionless granular flows, so no fluid is required.

Our observation that hydrated sulfate deposits are especially prone to erosion implies that they are friable and poorly indurated, consistent with the low power required for rock abrasion tool work on such sediments [10] and the near-absence of small impact craters on similar deposits [11]. Typically these sequences are capped by sediments rich in polyhydrated sulfates with up 50% water content [9], a promising unit for ISRU [12], and for which friable deposits can be processed with relatively little energy.

4. References

[1] Dundas C. et al.: The Formation of Gullies on Mars Today. Geol. Soc. London Spec. Pub., 467, http://dx.doi.org/10.1144/SP467.5, 2017.

[2] Harrison, T. N., Osinski, G. R., Tornabene, L. L., Jones: Global documentation of gullies with the Mars Reconnaissance Orbiter Context Camera and implications for their formation. Icarus, 252, 236-254, 2015.

[3] McEwen, A. S., et al.: Recurring slope lineae in equatorial regions of Mars, Nat. Geosci., 7(1), 53–58, doi:10.1038/ngeo2014, 2013.

[4] Auld, K. S., Dixon, J. C.: A classification of Martian gullies from HiRISE imagery. Planet. Space Sci., 131, 88-101, 2016.

[5] Chojnacki M. et al.: Geologic context of recurring slope lineae in Melas and Coprates Chasmata, Mars. J. Geophys. Res. Planets 121, 1204-1231, 2016.

[6] McEwen, A.S., et al.: Mars Reconnaissance Orbiter's High Resolution Imaging Science Experiment (HiRISE). J. Geophys. Res. 112, E05S02, 2007.

[7] Ojha, L. et al.: Seasonal Slumps in Juventae Chasma, Mars, J. Geophys. Res. 122, 2193-2214, 2017.

[8] Ehlmann. B.L., Edwards, C.S.: Mineralogy of the Martian surface. Annu. Rev. Earth Planet. Sci. 42, 291–315, 2014.

[9] Murchie, S. et al.: Evidence for the origin of layered deposits in Candor Chasma, Mars, from mineral composition and hydrologic modeling. J. Geophys. Res. 114, E00D05, 2009.

[10] Thomson, B.J., et al.: Estimating rock compressive strength from Rock Abrasion Tool (RAT) grinds. J. Geophys. Res. 118, 1233-1244, 2013.

[11] Kite, E.S.; Mayer, D.P.: Mars sedimentary rock erosion rates constrained using crater counts, with applications to organic-matter preservation and to the global dust cycle. Icarus 286, 212-222, 2017.

[12] Clarke, J.D.A., Willson, D., Cooper, D.: In-situ resource utilisation through water extraction from hydrated minerals—relevance to Mars missions and an Australian analogue. In: Proceedings of the 6th Australian Mars Exploration Conference, 1–16, 2006.

EPSC Abstracts
Vol. 12, EPSC2018-486-1, 2018
European Planetary Science Congress 2018

Water Content and Mineral Abundances at Gale Crater, Mars as Inferred from OMEGA and CRISM Observations

Y. Liu (1) & F. Stachurski (2); (1) Lunar and Planetary Institute, Houston, TX, USA (liu@lpi.usra.edu), (2) University of Glasgow, Scotland, UK

Abstract

Here we present the water content and mineral abundances at Gale crater as derived from the remote sensing observations. The results can help better understand the aqueous history of the region.

1. Introduction

Gale crater is a 154 km diameter crater on Mars where Curiosity rover started its exploration and investigation since 2012. Previous studies using orbital remote sensing data have revealed the presence of hydrated minerals such as hydrated sulfates and clay which record the aqueous alteration at Gale crater [1]. In-situ analysis of material properties of rocks and soils by Curiosity rover has found numerous evidence for water activities at Gale crater which has raised the possibility of Mars' past habitability [2]. In this work, we use hyperspectral visible/near-infrared (VNIR) data from the Observatoire pour la Minéralogie, l'Eau, les Glaces et l'Activité (OMEGA) instrument onboard Mars Express and the Compact Reconnaissance Imaging Spectrometer for Mars (CRISM) instrument onboard Mars Reconnaissance Orbiter (MRO) to quantitatively analyze the hydration state (i.e., water content) and mineral abundances at Gale Crater.

2. Methodology

We use the Discrete Ordinate Radiative Transfer (DISORT) model to simulate I/F values at the top of the atmosphere and retrieve surface reflectance with spectral corrections for gases and aerosols from OMEGA and CRISM I/F data. Thermal correction is performed on OMEGA data using the OMEGA-derived surface temperature map. The thermal corrected reflectance spectra allow us to evaluate the strength of the 3 μm absorption feature and thus derive the water content. The methodology has been well established in the previous work [3]. For CRISM data, we retrieve surface single scattering albedos (SSAs) using the DISORT model, and then we perform linear unmixing analysis over the SSAs to derive mineral abundances over Gale crater using the method developed in the previous work [4].

3. Results and Conclusions

We will report the water content at Gale crater as derived from OMEGA observations at the meeting. The derived water content from orbital data will allow us to directly compare the results from in situ heating experiments of regolith materials by Curiosity, which in turn helps validate our approach to retrieve water content using orbital datasets. Also we will report the mineral abundances at Gale crater as inferred from CRISM data. The derived mineral abundances will help test and constrain the formation mechanisms of hydrated minerals at Gale crater in a region scale, which will also help route planning to geologically-interesting sites for Curiosity, and for comparison to rover-based results.

References

[1] Milliken, R., J. Grotzinger, and B. Thomson: The paleoclimate of Mars from the stratigraphic record in Gale Crater. Geophysical Research Letters, 37, L04201, doi:10.1029/2009GL041870, 2010

[2] Grotzinger, J. P.: Deposition, Exhumation, and Paleoclimate of an Ancient Lake Deposit, Gale Crater, Mars.Science, 350, n. 6257, 2015

[3] Liu, Y., R. E. Arvidson, M. J. Wolff, M. T. Mellon, J. G. Catalano, A. Wang, and J. L. Bishop: Lambert albedo retrieval and analyses over Aram Chaos from OMEGA hyperspectral imaging data, J. Geophys. Res., 117, E00J11, doi:10.1029/2012JE004056, 2012

[4] Liu, Y., T. D. Glotch, N. A. Scudder, M. L. Kraner, T. Condus, R. E. Arvidson, E. A. Guinness, M. J. Wolff, and M. D. Smith: End-member identification and spectral mixture analysis of CRISM hyperspectral data: A case study on southwest Melas Chasma, Mars, J. Geophys. Res. Planets, 121, 2004–2036, 2016.

EPSC Abstracts
Vol. 12, EPSC2018-493, 2018
European Planetary Science Congress 2018

A numerical model of the SEIS leveling system transfer matrix and resonances: application to SEIS rotational seismology and dynamic ground interaction.

Lucile Fayon (1), Brigitte Knapmeyer-Endrun (2), Philippe Lognonné (1), Marco Bierwirth (2), Aron Kramer (2), Pierre Delage (3), Foivos Karakostas (1), Sharon Kedar (4), Naomi Murdoch (5), Raphael Garcia (5), Nicolas Verdier (6), Sylvain Tillier (1), William T. Pike (7), Ken Hurst (4), Cédric Schmelzbach (8) and William B. Banerdt (4)
(1) Institut de Physique du Globe de Paris-Sorbonne Paris Cité, Université Paris Diderot, Paris, France (2) Department of Planets and Comets, Max Planck Institute for Solar System Research, Göttingen, Germany (3) Ecole des Ponts ParisTech, Laboratoire Navier (CERMES), Paris, France (4) Jet Propulsion Laboratory (JPL), California Institut of Technology, Pasadena, USA (5) Institut Supérieur de l'Aéronautique et de l'Espace (ISAE-SUPAERO), Université de Toulouse, Toulouse, France (6) Centre National d'Etudes Spatiales (CNES), Toulouse, France (7) Imperial College, London, United Kingdom (8) ETH, Zurich, Switzerland. (fayon@ipgp.fr)

1. Context

The seismic sensors of the SEIS (Seismic Experiment for Interior Structure) instrument of the NASA InSight mission (Banerdt et al. 2013) are the VBBs (Very Broad Band) and SPs (Short Period). They are mounted on a mechanical levelling system (LVL) for which the purpose is twofold: provide the mechanical coupling of the instrument to the ground and ensure a level placement of the sensors on the Martian ground under yet unknown local conditions. This is possible thanks to its legs which are motorized in order to adjust their lengths. We developed a simplified analytical model of the LVL structure in order to reproduce its mechanical behaviour by predicting its resonances and transfer function. This model, based on a method to detect and compensate for inconsistent coupling conditions during seismic acquisition (Bagaini and Barajas-Olalde 2007), allows to estimate the LVL effect on the data recorded on Mars by the VBBs and SPs. Indeed, if some structure resonances are in the instrument sensitivity range of frequencies this could affect the seismic signal measurement. Moreover, the different positions of the VBBs and SPs regarding the structure's center of mass could induce off-axis effects at short period which means that a different signal will be measured between both types of sensors.

2. Numerical model

To do that, as it is shown on Fig. 1, the LVL tripod is considered as one platform and three feet, which are linked by springs in the 3 directions of space (with two horizontal k_h^p and one vertical k_v^p components).

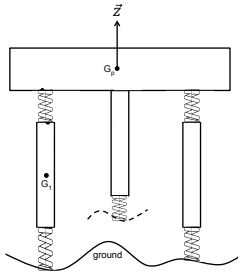

Figure 1: Schematic LVL face view in the leg 2 direction.

The links between the LVL feet and the ground are modelled in the same way (k_h^g and k_v^g parameters).

The model is implemented numerically which allows to determine the mass and rigidity matrices and resolve the eigenvalues problem to determine the LVL response [R] :

$$[R] = [P]^{-1}([K] - [M] \cdot [\Omega^2])^{-1} \cdot [P][D] \qquad (1)$$

where $[P]$ is the transfer matrix toward the eigenvector base, $[\Omega]$ is the eigenpulsation matrix, and [D] represents the three vectors of ground displacement applied to the three feet in contact with the ground.

The model validation is guaranteed thanks to the observation of two horizontal resonances, between 35 and 50 Hz. These resonances are in good agreement with the laboratory measurements realized on the LVL flight model at the MPS in Gottingen, Germany. An-

other proof of the model fidelity to reality is the same evolution of these two resonances than with experiments according to the mass and the leg's lengths.

3. Applications

Some numerical model's parameters are adjustable but after some simulations we noticed that varying k_h^g (horizontal ground stiffness) and C_h^g (ground torque) parameters can strongly change both horizontal resonance frequencies which are in the bandwidth of SEIS measurements. This means that the LVL structure resonances depend on the mechanical coupling between it and the ground. For this reason, an inversion study is performed and compared with some experimental measurements of the LVL feet's penetration in a martian regolith analog (Delage et al. 2017) in order to see if this model could allow to estimate the ground properties at the InSight landing site.

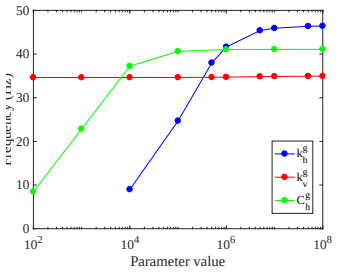

Figure 2: Sensitivity of both horizontal LVL resonances as a function of the elastic ground properties.

Another model application consists in modeling the 6 sensors on the LVL at their real positions, also considering their sensitivity axes. This study allows to compute the performances of the global 6 axes SEIS instrument in translation and rotation. Indeed, the rotation can be an important information to recover the phase velocity of the surface seismic waves (Bernauer et al. 2009). This can be realized on Mars with an active seismic experiment thanks to the other main instrument of the InSight mission: HP^3. Some simulations providing the acceleration on each LVL foot induced by HP^3 hammering (Kedar et al. 2017) are used to show the SEIS capability to estimate the phase velocity of the surface waves produced by HP^3 thanks to the combination of the 6 sensors measurements.

4. Summary

We determined the SEIS LVL's transfer function which is the last part of the seismic transfer of the signal between the Martian surface and the 6 axes accelerometer made by the 3 VBBs and 3 SPs. We have also shown that in the seismic bandwidth of the instrument, the major impact of the LVL on the seismic signal will be associated to both horizontal oscillation modes of the almost rigid LVL placed on the low rigidity ground. These resonances are highly dependent on ground properties and this can help to perform an inversion study. We finally demonstrated that the performances of the 6 axes seismometer are good enough for determining the wavefield gradient of the high-amplitude surface waves generated by the HP^3 penetration. This will allow the measurement of the phase velocity of the associated Rayleigh waves.

Acknowledgements

This is IPGP contribution and InSight contribution. We acknowledge the financial support of ANR-11-IDEX-0005-02, the additional support of ANR-SIMARS and the French Space Agency CNES one for the overall SEIS developments.

References

[1] Banerdt, W. B. et al.: InSight: A discovery mission to explore the interior of Mars, Proc. 44th Lunar Planet. Sci. Conf., Houston, p. 1915, 2013.

[2] Bagaini, C., Barajas-Olalde, C.: Assessment and compensation of inconsistent coupling conditions in point-receiver land seismic data, Geophysical Prospecting, Vol. 55, pp. 39-48, 2007.

[3] Delage, P. et al.: An investigation of the Mechanical Properties of Some Martian Regolith Simulants with Respect to the Surface Properties at the InSight Landing Site, Space Sci. Rev., Vol. 211, pp. 191-213, 2017.

[4] Bernauer, M., Fichtner, A., Igel, H.: Inferring earth structure from combined measurements of rotational and translational ground motions, Geophysics, Vol. 74, pp. 41-47, 2009.

[5] Kedar, S. et al.: Analysis of regolith properties using seismic signals generated by InSight's HP3 penetrator, Space Sci. Rev., Vol. 211, pp. 315-337, 2017.

EPSC Abstracts
Vol. 12, EPSC2018-505, 2018
European Planetary Science Congress 2018

Super-resolution restored HiRISE images for simulating "rover's eye" views in 3D

Divya M. Persaud, Yu Tao and Jan-Peter Muller
Imaging Group, Mullard Space Science Laboratory, University College London, Department of Space & Climate Physics, Holmbury St. Mary, Dorking, Surrey RH5 6NT, UK

Abstract

Super-resolution restored (SRR) HiRISE images over the Mars Exploration Rover traverses have been combined with 25-cm digital terrain models (DTMs) in a 3D visualisation platform and are here compared to rover scenes. The SRR products are shown to better resolve rocks and geomorphology and approach the quality of MER Navcam images than standard resolution HiRISE images.

1. Introduction

Rover landing site selection for future rover missions (e.g. Mars 2020 and ExoMars 2020) requires high-resolution imaging to identify potential hazards as well as regions of scientific interest. A method of super-resolution restoration (SRR) of repeat-pass HiRISE images has previously been developed and provides additional refinement of orbital data [1]. SRR can bridge localised coverage from rovers and multi-resolution orbital coverage, and contextualise geology within a regional and global context.

25-cm HiRISE orthorectified images (ORI) and 5-12.5-cm HiRISE SRR products of the Mars Exploration Rover (MER) traverses have been combined with 25-cm shape-from-shading DTMs and visualised in the NASA DERT platform [2,3]. The SRR and standard resolution ORI images have been compared to evaluate the refinement achieved by super-resolution restoration. "Rover's-eye" scenes have been simulated in this platform and compared with Navcam mosaics from MER-A and MER-B to evaluate the utility of SRR HiRISE images for science operations and mission planning.

2. Methods

"Landscapes" were generated using LayerFactory, a GDAL function in DERT, to drape the SRR images and ORI on the DTMs. The DERT "camera" tool was placed at different sites along the rover traverses and adjusted for the height of the Navcam (1.4 m) to simulate a "rover's eye" view of the terrain. Multiple scenes were captured in each of the SRR and ORI scenes to cover the range of morphologies, e.g. outcrops, rocks, and hills. Midnight Planets (www.midnightplanets.com) and the Mars Analyst's Notebook (https://an.rsl.wustl.edu/) were used to select along-traverse sites and visualise the rover data, and results were compared with Navcam panoramas in Midnight Planets [4].

3. Results

3.1 MER-A at Home Plate

A 5-cm HiRISE SRR orthorectified image over Home Plate was employed. Views were captured at two sols (Table 1). Figure 1 compares the 3D models in DERT. Figure 2 demonstrates the higher detail achieved in the SRR, especially with rocks in the foreground, relative to the MER-A Navcam mosaic.

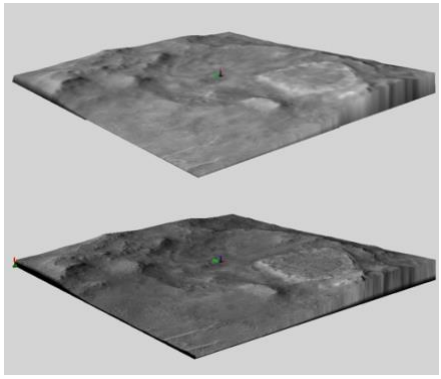

Figure 1: 3D perspective images in DERT: 25cm ORI (top), 5cm SRR (bottom) over Home Plate

Table 1: MER-A sites at Home Plate

Sol	Number of Views
764	6
1352	2

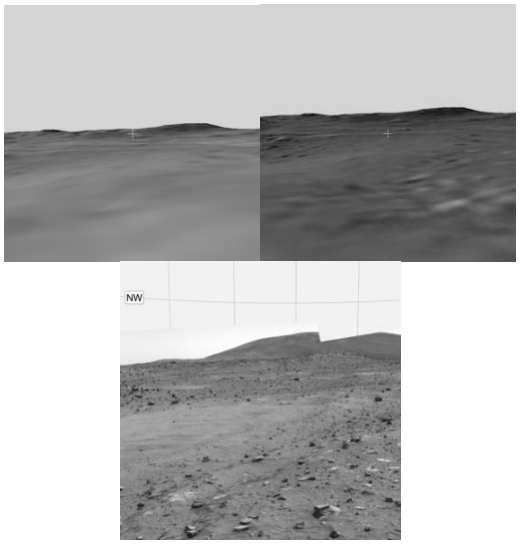

Figure 2: MER-A "rover's eye" scenes from sol 764: 25-cm ORI (left), 5-cm SRR (right), and Navcam (bottom). DERT scenes represent the fore- and middle-ground of the Navcam scene only.

3.2 MER-B at Victoria Crater

A 12.5-cm HiRISE SRR orthorectified mosaic over Victoria Crater was next employed. Views were captured at 4 sols (Table 2). Figure 3 compares the two 3D models in DERT. Despite a lower SRR resolution, the detail enhancement is clearer than for MER-B, as seen in the rocks in the foreground, ripples on the rim floor, and the outcrops of the rim (Figure 4).

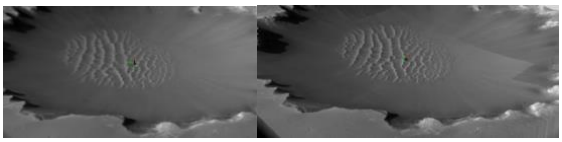

Figure 3: Close-up of the 3D models in DERT: ORI (left), SRR (right)

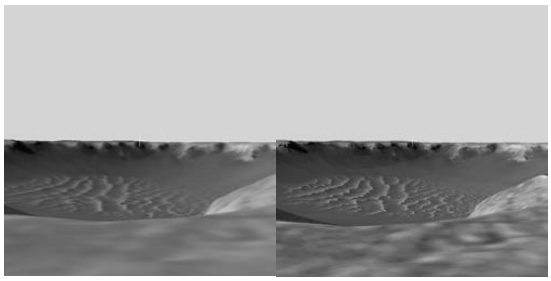

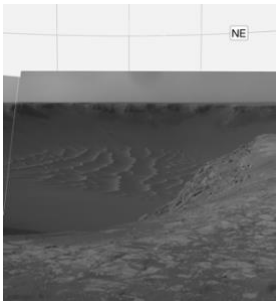

Figure 4: MER-B "rover's eye" scenes from sol 176: 25-cm ORI (left), 12.5-cm SRR (right), and Navcam (bottom).

Table 2: MER-B sites at Victoria Crater

Sol	Number of Views
1039	1
1155	1
1484	3
1676	2

Summary and Conclusions

SRR of repeat-pass HiRISE images provides high-resolution information that displays rocks that are not visible in standard resolution HiRISE images, and thus provides information that may be useful for rover landing site selection when visualised in 3D.

The discrepancies between "camera" location to emulate Navcam scenes and the rover traverse data from the PDS—including on Home Plate, where the rover traverse is visible in the SRR—suggest that rover localisation requires refinement. These results implicate a need to perform ground-to-orbit data fusion for better contextualisation of high-resolution rover data, and 3D platforms to visualise these fused data products, in the interest of scientific analysis and mission planning.

References

[1] Tao, Y., Muller, J.-P., Planet. Space sci., 121, 2016.

[2]. Paar, G., et al., Fusion and Visualisation of HiRISE Super-Resolution, AGU Fall Meet., 2014.

[3] Keely, L. et al., DERT, Planet. Data Workshop, 2017.

[4] Arvidson, R.E., et al., LPSC XLI, 2010.

EPSC Abstracts
Vol. 12, EPSC2018-547, 2018
European Planetary Science Congress 2018

Analysis of Clay Deposits in and around Ladon Basin

Catherine Weitz (1), Janice Bishop (2) and John Grant (3)
(1) Planetary Science Institute, 1700 E Fort Lowell, Tucson, AZ 85719, USA (weitz@psi.edu), (2) SETI Institute, Carl Sagan Center, 189 Bernardo Ave., Mountain View, CA 94043, USA, (3) Center for Earth and Planetary Science, Smithsonian Institution, Washington, DC 20013.

Abstract

We have identified, mapped, and analyzed sedimentary deposits in and around Ladon basin. The study region has sediments and clays that likely formed from multiple aqueous processes, including fluvial, lacustrine, hydrothermal, and in situ alteration. A search through all HiRISE and CTX images for light-toned, possibly layered, deposits in our study region shows numerous locations where we have identified them. CRISM analysis of the light-toned deposits indicates the presence of Fe/Mg-phyllosilicates. Smectite appears to be dominant for deposits having bands near 1.9 and 2.3 μm; however, the spectral character is more consistent with nontronite (2.29 μm) in some regions and saponite (2.31 μm) in other regions. Some deposits have the 2.3 μm absorption but no 1.9 μm hydration band. We divide the light-toned clay deposits into three categories: (1) Uplands around Ladon basin; (2) Ladon Valles; and (3) Ladon basin.

1. Introduction

Light-toned layered outcrops in Holden and Eberswalde craters, near the mouth of Ladon Valles, Ladon basin, and in several of the small upland basins west of Ladon are all characterized by broadly similar morphology [1-8], suggesting that their sedimentary depositional settings were perhaps similar. The deposits are mostly confined within topographic basins and do not drape exterior surfaces, thereby favoring deposition by low-energy alluvial or lacustrine rather than airfall or volcanic (flows or ash) processes. Despite similarities in appearance and occurrence, it is uncertain whether the light-toned layered deposits in Holden crater, Eberswalde crater, Ladon basin, and other depressions are linked in time or process. Some of the phyllosilicate-bearing sediments may be sourced from weathered upland rocks later transported into the basins whereas others may be the result of alteration after the deposits were emplaced [4]. Still other phyllosilicates could relate to laterally extensive phyllosilicate-bearing terrains identified to the west in Margaritifer Terra [9], Xanthe Terra and in the walls and plains surrounding Valles Marineris [10], and northwest Noachis Terra to the south [11]. Nevertheless, while the origin of clays in the deposits is currently ambiguous, it almost certainly reflects past environments characterized by prolonged chemical weathering. Understanding the source-to-sink sedimentary pathways on Mars is key to determining the origin of alteration minerals as they reflect the ancient environmental conditions.

2. Results

2.1 Uplands around Ladon basin

The light-toned layered sediments we have identified along the western uplands of Ladon basin are associated with valley networks that eroded Noachian and Early Hesperian geologic units and deposited these sediments within small basins, likely similar to the valley networks that deposited the delta in the larger Eberswalde basin. One deposit includes an inverted channel (Fig. 1) that lies in a shallow east-west valley that may have been blocked by topography associated with two craters. Spectra from the deposit are consistent with nontronite-type clays as well as additional clay signatures that appear to be saponite, although the phyllosilicate signatures are weak in these deposits. Valleys sourcing many of these deposits head along an ancient ridge to the west forming one of the eroded rings of the ancient Holden impact basin [12,13] that likely exposes rocks weathered during an early wetter period of the Noachian [14]. Drainage from the ridge into the valleys and deposition of the layered sediments likely continued until an outlet was established to the east, thereby enabling incision of the deposits and drainage onto the lower-lying floor of Ladon basin. Such a “source-to-sink” setting on Mars where clay-bearing sediments could be traced to specific source outcrops is rare and provides critical information about understanding the origin and environmental conditions that produced alteration minerals.

2.2 Ladon Valles

The utility of combined CRISM and HiRISE analyses is shown using an example of the deposits located at the mouth of Ladon Valles (Fig. 2). CRISM results include spectral features consistent with multiple types of OH-bearing materials, like Fe/Mg-rich clays, whereas HiRISE images indicate numerous beds with variable lithologies, including color and brightness variations (Fig. 2). Strike and dips for bedding planes on a HiRISE-derived DTM are shallow, between 1-4°, and their fine-scale layering is traceable across tens of kms, consistent with a lacustrine setting or perhaps distal alluvial.

2.3 Ladon Basin

Clays within Ladon basin are associated both with light-toned layered deposits and also medium-toned fractured materials that exhibit no layering. Alteration through burial/diagenesis, pedogenesis, or hydrothermal activity can take place across multiple elevations or conform to topography, and may have produced layering as chemical conditions changed over time. If hydrothermal alteration of a precursor material occurred, then the spectral properties of the phyllosilicates could vary as a function of distance from the heat source. Spectra from several of the clays within Ladon basin exhibit a 2.3 µm absorption but no hydration band at 1.9 µm, which could reflect dehydration from high temperatures that drove out the water in the clays [15].

3. Figures

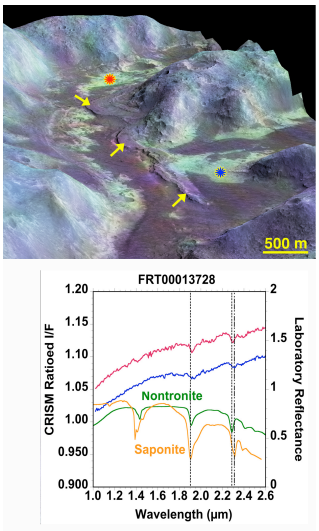

Figure 1. HiRISE DTM perspective view (5X vertical exaggeration) merged with CRISM spectral parameters in color. Red and blue asterisks show the locations where CRISM spectra were extracted and are plotted below. Yellow arrows identify a 15-m high inverted channel.

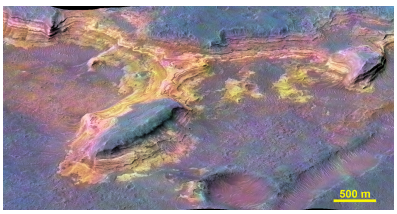

Figure 2. HiRISE DTM (5X vertical exaggeration) showing light-toned layered deposits near the mouth of Ladon Valles. Overlain on the HiRISE DTM is color derived from CRISM FRT00008076 (red is olivine index, green is 1.9 µm band depth, and blue is sulfate index).

4. Summary and Conclusions

The layered clay-bearing deposits in several upland basins identified in our preliminary investigation all occur between 0.5-2 km above similar-appearing deposits on the floor of Ladon basin and near the mouth of Ladon Valles [8]. These results are consistent with local trapping of water and sediment in topographic depressions on the upland flank of Ladon basin. The study of Ladon basin may constrain the number of layers/units on the basin floor (as exposed to in the walls of craters and fractures) and explore reasons why there is no obvious constructional delta or fan near the mouth of Ladon Valles. Our results are providing critical new constraints on the role and timing of aqueous activity in this region.

References

[1] Pondrelli, M., et al. (2005), *J. Geophys. Res*., *110*, 2004JE002335; [2] Pondrelli, M. A. et al. (2008), *Icarus*, *197*, 429-451, doi:10.1016/j.icarus.2008.05.018. [3] Grant, J. A. et al. (2008), *Geology*, *36*, 195-198, doi: 10.1130/G24340A. [4] Milliken, R. E., and D. L. Bish (2010), *Philosophical Magazine*, 1478-6443, DOI: 10.1080/14786430903575132. [5] Rice, M. S., et al. (2011), *Geophys. Res. Letts*., *38*, doi:10.1029/2011GL048149. [6] Rice, M.S., et al. (2013) *MARS 8*, 15-57, doi:10.1555/mars.2013.0002. [7] Weitz, C. M., and J. L. Bishop (2012), *Lunar Planet. Sci. Conf., XXXXIII*, Abstract 1243. [8] Weitz, C.M., et al. (2013) *Lunar Planet. Sci. Conf. 44th*, Abstract 2081. [9] Buczkowski, D. L. et al. (2013), *44th LPSC,* The Woodlands, TX, Abstract 2331. [10] LeDeit, L., et al. (2012), *Journal of Geophysical Research*, *117*(E00J05). [11] Buczkowski, D. L., et al.. (2010), *Geol. Soc. of America Abstracts with Programs*, *42*(5), 645. [12] Schultz, P. H., et al. (1982), *J. Geophys. Res.,* 87, 9803-9820. [13] Grant, J. A. (1987), in *Advances in planetary geology*, NASA Technical Memorandum 89871, p. 1-268. [14] Bibring, J.-P., et al. (2006), *Science 312*, 400-404, DOI: 10.1126/science.1122659. [15] Morris, R.V., et al. (2010) *LPSC 41*, Abstract 2156.

EPSC Abstracts
Vol. 12, EPSC2018-557-3, 2018
European Planetary Science Congress 2018

Modeling the internal architecture of Mars Polar Layered Deposits by HCA method

Paola Cianfarra, Costanza Rossi and Francesco Salvini
(GeoQuTe Lab, Roma Tre University, Rome, Italy, (paola.cianfarra@uniroma3.it)

Abstract

The polar layered deposits (PLD) of the Martian ice caps reveal an architecture analogue to the internal layering of the East Antarctic Ice Sheet (EAIS). The Hybrid Cellular Automata (HCA) modeling of the internal layering of the EAIS allowed to highlight the interaction between the active bedrock tectonics and the ice sheet dynamics. The HCA numerical approach allowed to kinematically simulate the internal architecture of the layered deposits from both the north and the south Martian ice caps and revealed the role played by tectonic movements on the present-day Martian ice cap stratigraphy.

1. Introduction

The polar layered deposits (PLD) of Mars constitute the water ice stratigraphy of polar spiral troughs up to several miles thick [1,2]. The PLD cross section profiles, based on data from the Shallow Subsurface Radar (SHARAD) instrument on NASA's Mars Reconnaissance Orbiter, showed discontinuities within these layers [3,4]. The PLD have been recognized as stratigraphic evidence for migration caused by wind transport and erosion [1]. Nevertheless, their internal stratigraphic architecture strongly resembles the layered geometries evidenced by radargram from radio echo-soundings of the East Antarctic Ice Sheet (EAIS). The important role played by tectonics in the present-day EAIS stratigraphy was proposed by [5,6]. In this way the mechanisms responsible for layered deposits of Mars are still an open issue [7] and this work represents a contribution to the debate.

2. Methodology

Layered ice is simulated by a mesh of cells piled up. Three major types of link exist among adjacent cells: 1. intralayer relations link cells belonging to the same layer and consist of rigid relationships derived from average volume and surface preservation conditions, physical boundary conditions, and rock rheology. 2. Inter-layer relations regulate the relationships among adjacent layers. These relations take into account the weaker rheologies of interlayer material, physical boundary conditions, and volume preservation conditions, while partial freedom is given to surface variations. 3. Discontinuity relations correspond to the presence of ruptures such as faults. No kinematic links exists across them, but physical boundary conditions and slip-induced stresses [8]. The combination of the FEM and CA approaches allows to replicate the natural material anisotropies, such as rocks and ice sheet internal layering, and to simulate complex tectonic evolutionary paths [9,10]. The Hybrid Cellular Automata (HCA) modeling of the internal layering of the EAIS allowed to highlight the interaction between the active bedrock tectonics and the ice sheet dynamics (including ice flow, erosion, and sedimentation) and showed the important role played by the recent-to-active tectonics on the present-day ice sheet stratigraphy.

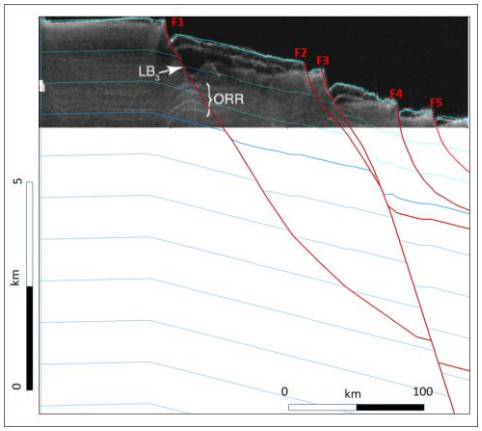

Figure 1: HCA numerical model of the ice layered deposits from Mars south polar region. Subset of the SHARAD radargram 5968-01 (from [2])

3. Summary and Conclusions

The HCA numerical approach allowed to kinematically simulate the internal architecture of the layered deposits from both the north and the south Martian ice caps. In particular the observed stratigraphy (geometries and thickness of the ice layers) was replicated as resulting from the relative, normal movement among blocks separated by shear discontinuities with listric shape (normal faults). In some places the fit between the internal layering revealed from the radar data and the geometries from the numerical model was achieved with minor fault inversions.

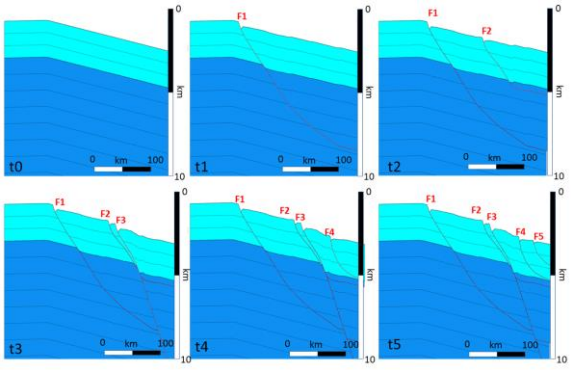

Figure 2: Evolution of the layered deposits from Mars south polar region as derived by HCA modeling. Computed fault displacements are: F1: 4000m; F2: 2000m; F3: 5000m; F4: 1000m and F5: 1000m

Acknowledgements

This research is funded by the GeoQuTe Lab of Roma Tre University.

References

[1] Smith, I. B., and Holt, J. W. Spiral trough diversity on the north pole of Mars, as seen by Shallow Radar (SHARAD). Journal of Geophysical Research: Planets, 120(3), 362-387, 2015. https://doi.org/10.1002/2014JE004720

[2] Phillips, R. J., Davis, B. J., Tanaka, K. L., Byrne, S., Mellon, M. T., Putzig, N. E., *et al*. Massive CO2 ice deposits sequestered in the south polar layered deposits of Mars, Science, 332(6031), 838-841, 2011. doi:10.1126/science.1203091

[3] Foss, F. J., Putzig, N. E., Campbell, B. A., and Phillips, R. J. 3D imaging of Mars' polar ice caps using orbital radar data. The Leading Edge, 36(1), 43-57. 2017. https://doi.org/10.1190/tle36010043.1.

[4] Putzig, N. E., Smith, I. B., Perry, M. R., Foss II, F. J., Campbell, B. A., Phillips, R. J., and Seu, R. Three-dimensional radar imaging of structures and craters in the Martian polar caps, Icarus, 308, 138-147,2017. https://doi.org/10.1016/j.icarus.2017.09.023

[5] Cianfarra P. and Salvini F. Modelling ice flow kinematics and deformation by HCA numerical method (poster presentation), Seventh International Symposium on Antarctic Glaciology (ISAG 7), Milano, Italy, 25-29, 2003.

[6] Cianfarra P. The tectonic origin of the Antarctic Subglacial lakes in the Vostok-Dome C region, East Antarctic craton. PhD Thesis, Roma Tre University, Rome, Italy, 2006.

[7] Guallini, L., Rossi, A. P., Forget, F., Marinangeli, L., Lauro, S. E., Pettinelli, E., Seu, R., Thomas, N. Regional stratigraphy of the south polar layered deposits (Promethei Lingula, Mars): "Discontinuity-bounded" units in images and radargrams, Icarus, 2017. http://dx.doi.org/10.1016/j.icarus.2017.08.030

[8] Salvini F. and Storti F. Active-hinge-folding-related Deformation and its Role in Hydrocarbon Exploration and Development—Insights from HCA Modeling. AAPG Mem. 82, p. 453-472, 2004.

[9] Cianfarra P. and Salvini F. Origin of the Adventure Subglacial Trench linked to Cenozoic extension in the East Antarctic Craton. Tectonophysics, 670, 30-37. 2016. http://dx.doi.org/10.1016/j.tecto.2015.12.011

[10] Cianfarra P. and Maggi M. Cenozoic extension along the reactivated Aurora Fault System in the East Antarctic Craton, Tectonophysics, 703, 135-143, 2017. doi: 10.1016/j.tecto.2017.02.019

EPSC Abstracts
Vol. 12, EPSC2018-574, 2018
European Planetary Science Congress 2018

Preliminary wavelengths selection for multispectral detection mode of Mars Mineral Spectrometer of China's First Mars Exploration

D. Liu (1, 2), X. Ren (1, 2), H. Zhang (1, 2), Q. Fu (1,2), Z. Zhang (1,2), Z. He (3), B. Liu (1,2), R. Xu (3), and Y. Chen (1,2)
(1) National Astronomical Observatories, Chinese Academy of Sciences, Beijing, China, (2) Key Laboratory of Lunar and Deep Space Exploration, Chinese Academy of Sciences, Beijing, China. (liudw@nao.cas.cn) (3) Key Laboratory of Space Active Opto-Electronics Technology, Shanghai Institute of Technical Physics, Chinese Academy of Sciences.

Abstract

Six sets of band combinations were specifically determined for multispectral observation mode of Mars Mineral Spectrometer (MMS) on the obiter of China's first Mars exploration mission. The first five sets of band combinations are suited for the detection of phyllosilicate, sulfate, carbonate, hydrated salt, and Fe oxide and primary silicate respectively with high accuracy. The last set of band combination is suited for the detection of all mineral groups yet with a slightly lower accuracy.

1. Introduction

The Mars Mineral Spectrometer(MMS) is one payload onboard the orbiter of China's first Mars exploration mission. The scientific objectives of MMS are to investigate the mineralogy and to constrain the resource areas on Mars surface. Considering the engineering restriction of reducing amount of data sent back to the Earth, MMS should enable the acquisition of multispectral data of Mars surface in addition to retrieving hyperspectral data. To meet this requirement and avoid misidentification of minerals on Mars surface, wavelength positions of multispectral observation mode of MMS should be designed. In this study, six sets of band combinations with each set composed of 72 bands were designed for multispectral observation mode of MMS. The first five sets can be used to detect phyllosilicate, sulfate, carbonate, hydrated salt, and Fe oxide and primary silicate respectively with high accuracy. The last set (versatile band set) can be used to detect all mineral groups yet with a slight lower accuracy. Different set of band combination will be selected from this six sets for detecting different targets during the mission.

2. Dataset

Selecting each set of band combination utilized the reflectance spectra of the corresponding mineral group [1]. Table 1 shows the minerals selected for each group in this study. Spectra of all these minerals were downloaded from RELAB, which are also used by CRISM spectra laboratory for mineral identification [2].

3. Method

All the spectra were first resampled to the wavelength range between 450nm and 3400nm with 1nm interval. The average spectrum was then taken if a mineral has several measured spectra (e.g. varying particle size). For the selection of the first five sets, the main absorptions and absorption shoulders of each mineral within each group were manually determined in the first round. Then, spectra of the minerals within the same group were plotted together and their band positions determined from the first-round were further manually optimized to 72 bands (engineering restriction) in the second-round selection. Different from bands selection procedure for the first five sets, the last set of band combination was determined by considering the following aspects: (1) The bands selected should be close to that of CRISM multispectral nadir-looking mode, which helps to compare the data acquired by MMS with that of CRISM; (2) The bands selected should involve eight bands of Multispectral Camera on the rover of China's First Mars Exploration. The selected six sets of band combinations were assessed based on the following criteria: (1) Capturing the spectral features of corresponding mineral group; (2)A low root mean squared error (RMSE) between the multispectral data and original hyperspectral data.

No.	Phyllosilicate	Sulfate	Carbonate	Hydrated Salt	Fe Oxide and Primary Silicate
1	Nontronite	gypsum	Siderite	Magnesium perchlorate	Goethite
2	montmorillonite	Jarosite	Calcite	Calcium perchlorate	Hematite
3	illite	Copiapite	Dolomite	Sodium perchlorate	Magnetite
4	Kaolinite	Alunite	Magnesite	K-perchlorate	Ferrihydrite
5	saponite	Magnesium		Fe^{2+}-perchlorate	Forsterite
6	chlorite	Kieserite		Fe^{3+}-perchlorate	Fayalite
7	serpentine			Al-perchlorate	Plagioclase
8					Orthopyroxene
9					Clinopyroxene

Table 1: Minerals selected for each mineral group

4. Results and Discussion

Fig.1 shows the performance of the first five sets of band combinations in detecting the corresponding mineral groups (one example mineral for each group). It can be seen that the first five sets (triangles) can adequately capture the spectral features (solid lines) of phyllosilicate, sulfate, carbonate, hydrated salt, and Fe oxide and primary silicate respectively. The versatile band set designed for detection of all mineral groups also shows a good performance in characterizing the spectral features of all mineral groups (Fig.2). Shown in Fig.3 is RMSE between hyperspectral data and multispectral data linearly interpolated to the same bands as the hyperspectral data for each mineral. The low RMSE also indicates the efficiency of the first five band sets in detecting corresponding mineral groups. The versatile band set can detect all mineral groups although with a slightly lower accuracy.

5. Conclusions

Six sets of band combinations were designed for multispectral detection mode of MMS in this study. Results suggest that the first five set performs well in detecting phyllosilicate, sulfate, carbonate, hydrated salt, and Fe oxide and primary silicate respectively. The versatile band set is also capable of capturing the spectral features of all mineral groups.

Acknowledgements: This work was supported by Key Laboratory of Space Active Opto-Electronics Technology, Shanghai Institute of Technical Physics, Chinese Academy of Sciences and by National Natural Science Foundation of China (41601374).

References

[1] Cousins, C. R., et al.: Selecting the geology filter wavelengths for the ExoMars Panoramic Camera instrument, Planet Space Sci., 70, 80-100, 2012.

[2] Viviano-Beck, C. E., et al.: Revised CRISM spectral parameters and summary products based on the currently detected mineral diversity on Mars, JGR, 119, 6, 1403-1431, 2014.

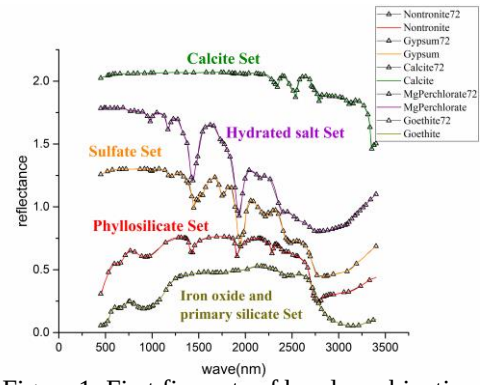

Figure 1: First five sets of band combinations

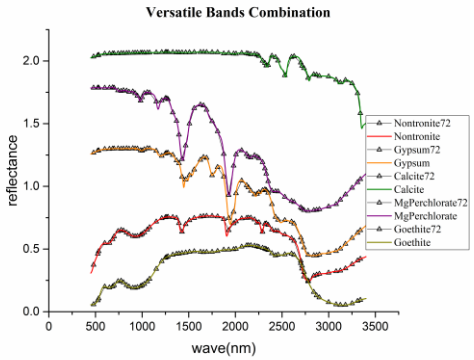

Figure 2: Versatile band set

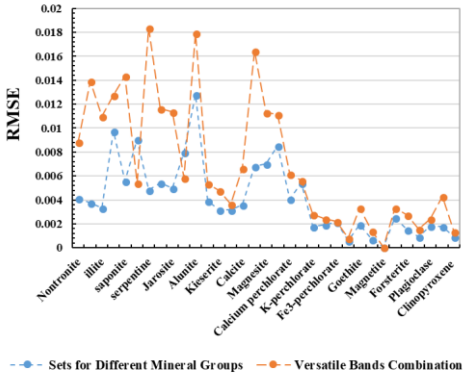

Figure 3: RMSE between hyperspectral data and multispectral data for each mineral

EPSC Abstracts
Vol. 12, EPSC2018-682-2, 2018
European Planetary Science Congress 2018

An Investigation of Hydrated Minerals in Jezero Crater

Vidhya Ganesh Rangarajan*, Rishikesh Bharti and S. Dutta

Department of Civil Engineering, Indian Institute of Technology Guwahati, Assam, India (*vidhyaganeshr@iitg.ac.in)

Abstract

Jezero, an impact crater located in NE Syrtis is home to a large diversity of alteration minerals and fluvial features. The current study aims to map the abundance of rock-bearing mafic minerals in the region and analyze them with the estimated surface thermal inertia and thereby generate a hydrated mineral potential map. It is seen that the crater is made up of a central LCP unit characterized by higher thermal inertia values when compared to its surroundings which are dominant in Fe-rich phyllosilicates. It is evident from the result that the presence of large amounts of LCP deposits are possibly due to erosion from fluvial activities. The LCP spatial distribution indicates that mineral emplacement might have occurred over the volcanic floor due to flow from the western delta.

1. Introduction

Jezero possesses two inflow channels from its north and west, well represented by the fan deposits formed near the entry points and has a single outflow channel located towards its east draining into Isidis. It is considered as a middle to early Noachian (~3.95-3.97 Ga) paleolake system thought to be shaped by the Isidis basin formation [4]. Such formations provide a favourable geological setting to investigate relationships between alteration mineralogy, associated lithology and fluvial geomorphology. Several researchers have been working to identify hydrated mineral signatures in and around Syrtis Major [1,7]. The present study aims to understand the mineralogical distribution in Jezero crater, associated lithological context and thereby generate a hydrated mineral potential map.

2. Methodology

Mineral Potential Mapping: CRISM TRDR radiance data were preprocessed using volcano scan technique (new McGuire wavelengths) [5] for photometric and atmospheric correction. From the list of spectral summary products generated [8], MAF browse product, obtained using the band combinations OLINDEX3, LCPINDEX2 and HCPINDEX2 set to R, G and B respectively was selected for analyzing qualitative mineralogical abundances of major rock forming mafic minerals.

Thermal inertia (TI) mapping: THEMIS IR RDR datasets were used for brightness temperature estimation. Since the effects of albedo and sun-heated slopes get dissipated through the night and thermal contrast due to particle sizes will be at a maximum, night-time THEMIS datasets were used [3]. TI estimation is done using the Mellon thermal model which uses a 7D lookup table containing values of albedo, thermal inertia, surface pressure, dust opacity, latitude, longitude and time of the day [6]. MOLA elevation and TES albedo layers were also served as additional inputs into the model.

3. Results and Discussions

Fig 1(a) shows the mafic mineral abundance map for Jezero crater. The red regions correspond to regions rich in olivine and other Fe-phyllosilicates. The image derived endmembers from this region show a very good spectral match at 1.4, 1.9 and 2.35µm absorption positions with CRISM library spectra of common Fe-Mg smectites like nontronite and saponite giving SFF spectral matching scores of 0.86 and 0.87 respectively (Fig 1(b)). The result corroborates well with the previous observations of Fe-Mg smectites near the western delta region of the crater [2]. The green and cyan regions indicate regions rich in low Ca-pyroxenes (LCP) supported by the spectral matching (1.5-2.4µm) of image derived endmembers with the library spectra of LCP minerals - enstatite and bronzite with SFF spectral matching scores of 0.847 and 0.852 respectively (Fig 1(b)). It is seen here that the central portion and the rim of the crater are dominated with LCP minerals as opposed to Fe-rich phyllosilicate abundance in other regions.

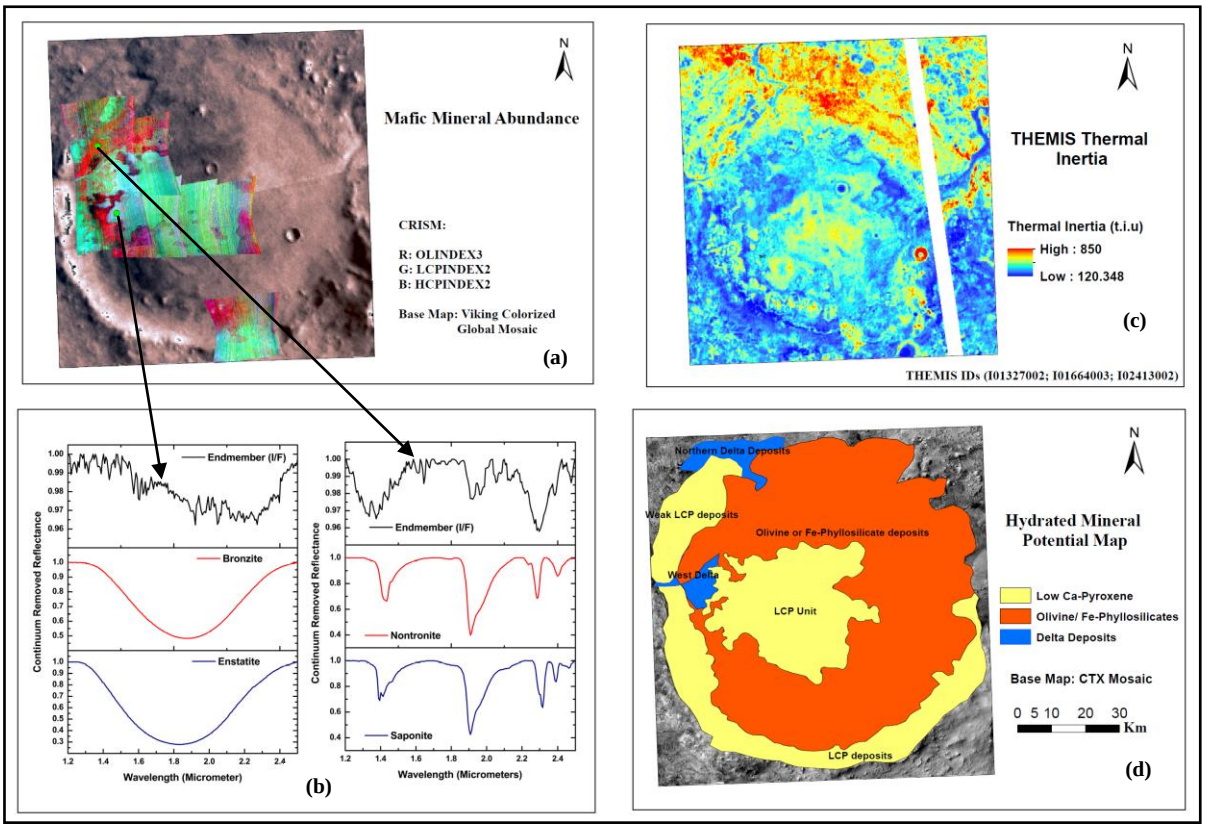

Fig 1 (a) Mafic mineral abundance of Jezero crater (b) Comparison of image derived endmember spectra with CRISM library spectra for mafic mineral abundances (c) THEMIS derived thermal inertia (d) Hydrated mineral potential map of Jezero crater

The fact that hydration in LCP units tends to significantly increase thermal conductivity and hence increase thermal response time is well supported by larger TI values in the central LCP unit when compared to other regions in the crater. Surface thermal inertia observations are found to corroborate very well spatially with observed mineralogical abundances (Fig 1(c)). Fig 1(d) shows the hydrated mineral potential in the region.

4. Conclusions

The large abundances of Fe-phyllosilicates and LCP units as observed in this study support the fact that flowing water has played a key role in shaping the geology and geomorphology of the crater. The presence of large amount of LCP deposits may also indicate that the crater was under constant erosion due to fluvial activities and their spatial distribution also points towards possible emplacement of the minerals over the crater volcanic floor during flow entry through the western fan. The fact that such a hydrologically rich site exists in a basaltic volcanic construct like Syrtis Major is quite intriguing, thereby making this place an interesting one to study on the Martian surface.

Acknowledgements

Financial support from Indian Space Research Organization (ISRO), Department of Space, Government of India under MOM-AO project (CESPNISRO01140xRIB002) is acknowledged.

References

[1] Ehlmann et al., 2008. Nature Geoscience 1, 355–358 [2] Ehlmann et al., 2009. JGR 114 [3] Fergason et al., 2006. JGR 111, 01-21. [4] Goudge et al., 2015. JGR 120, 775–808 [5] McGuire et al., 2009. Planetary and Space Science 57, 809–815 [6] Mellon, M., 2000. Icarus 148, 437–455 [7] Rangarajan et al., 2018. IGARSS 2018, Spain [8] Viviano-Beck et al., 2014. JGR 119, 1403–1431.

EPSC Abstracts
Vol. 12, EPSC2018-703, 2018
European Planetary Science Congress 2018

Hydrological History of a Complex Lake and Valley System in Western Arabia Terra, Mars

Zachary Dickeson (1,2), Peter Grindrod (1), Matt Balme (3), and Joel Davis (1)
(1) Natural History Museum, London, UK, (2) Birkbeck College, University of London, London, UK, (3) Open University, Milton Keynes, UK (z.dickeson@nhm.ac.uk)

Abstract

We present a detailed geomorphological study of an area in western Arabia Terra that shows evidence for fluvial processes. Sedimentary fan deposits and palaeolake extents inferred from outlet channel elevations serve to reconstruct the hydrological setting at the time of formation, and reveal two valley and lake systems with no surface connection. The close proximity of the two systems, their shared surface elevation, and the limited potential watershed of the smaller system suggests groundwater connectivity and filling. Palaeolake and channel topographies inconsistent with inferred flow directions also suggest significant subsidence and collapse that could be linked to groundwater drawdown or base level change.

1. Background

Arabia Terra hosts diverse landforms indicative of hydrological processes including: fluvial channels [1], deltas [2], palaeolakes [3], ocean shorelines [4], and groundwater upwelling [5]. However, there is little consensus on the timing, duration or interaction of hydrological processes, and detailed study is often limited by the resolution of topographic data. This study focuses on a small area in western Arabia Terra of middle Noachian age [6] situated near the crustal dichotomy that hosts discontinuous channels and sedimentary fans. The goal of this study is to reconstruct the past hydrological system in this region.

2. Data and Methods

This study utilised CTX, HiRISE and THEMIS images to map geomorphological features. Topographic data was obtained by producing a 20 m/pixel DTM mosaic from CTX stereo imagery with SOCET SET, and supplemented by 200 m/pixel HRSC MOLA Blended DEM data.

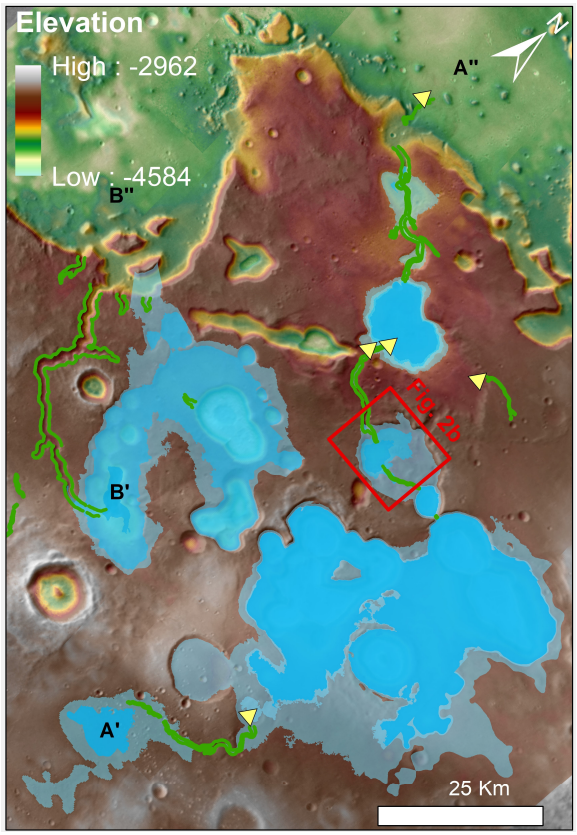

Figure 1 – Topographic map of study area, with channels (green outlines), sedimentary fans (yellow triangles), and palaeolakes inferred from outlet channel start (dark blue), channel spillover (blue), and bank spillover (pale blue). The beginnings and ends of two valley systems are marked as A'/B' to A''/B'' respectively. (CTX DTM and HRSC MOLA Blended DEM over THEMIS IR Day mosaic, top left corner of map at 16°W 31°N)

3. Observations

A combined ~166 km of channels were mapped in the study area with the longest section being ~43 km long (Fig.1). Seven distinct basins were identified and palaeolake extents in each were inferred from

three different outlet channel elevations (Fig.2). The total maximum surface area of all inferred palaeolakes is 2187 km^2, with the largest individual body being 1045 km^2. Two sedimentary fans empty into closed basins at elevations similar to outlet channels in the same basins. Three other sedimentary fans occur at locations and elevations open to the northern lowlands, at -3430 m, -3560 m and -3860 m.

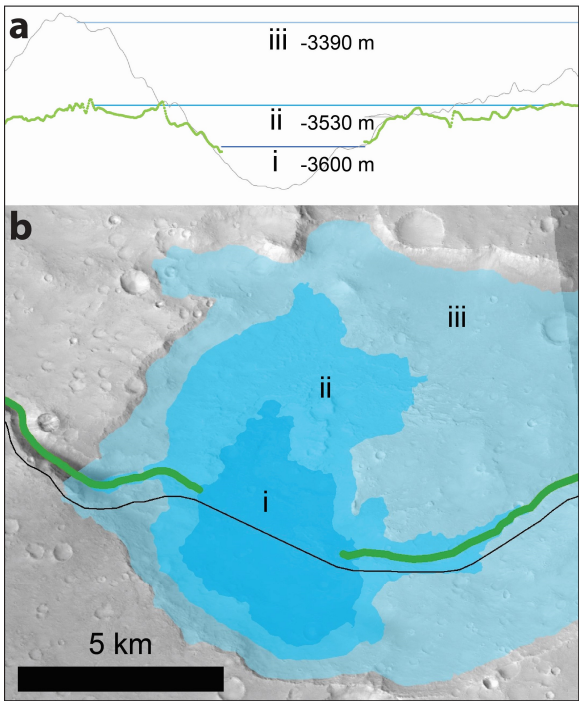

Figure 2 – Detail of inferred palaeolake (a) levels and (b) extents derived from outlet elevations at (i) start of outlet channel (dark blue), (ii) spillover at channel base (blue), and (iii) spillover at channel bank (pale blue) with topography (black line) and channel base (green line). Inferred direction of flow is right to left. (CTX image D16_033549_2114_XI_31N014W)

4. Discussion

Bank spillover elevations are interpreted as representing earlier palaeolake extents, while channel base and outlet start elevations represent progressively later post-incision extents. The locations and elevations of inferred palaeolakes link the majority of discontinuous channel segments into connected valley and palaeolake systems (Fig. 1). Two separate valley systems are identified that do not appear to be connected at surface level, and drain into the northern lowlands through different channels. The surfaces of the largest palaeolakes in both systems share an elevation (-3390 m), and based on current topography are only separated laterally by ~1.5 km. These correlations along with the observation that the smaller system has a limited watershed may suggest groundwater connectivity between the bodies. One palaeolake in valley system B (Fig. 1) inferred by bank spillover did not describe a closed basin on current topography, and so its extent was artificially truncated to be isolated from the northern lowlands. This inconsistent open basin can be described as a result of raising the bank or by lowering or removal of a bounding basin edge. The narrow areas in which the basin opens to the lowlands are steep-sided asymmetrical depressions, and may be the result of collapse at a time after the palaeolake existed. In basins where inlet and outlet channel were not connected, the elevations at the start of the outlet and the end of the inlet were a good match (Fig.2,i), supporting the existence of a standing water body. However, all outflow channels beginning in palaeolake basins are lower (up to 270 m) than the channel base spillover elevation (Fig.2,i&ii). These upslope channels in the downstream direction suggest topographic changes to the channel that may be the result of groundwater subsidence towards the basin centre.

Acknowledgements

Funding provided by the UK Science and Technology Facilities Council.

References

[1] Molina, A., et al.: Coogoon Valles, western Arabia Terra: Hydrological evolution of a complex Martian channel system, Icarus, Volume 293, 27-44, 2017.
[2] Di Achille, G. et al.: Ancient ocean on Mars supported by global distribution of deltas and valleys, Nature: Geoscience, Vol. 3, 459–463, 2010.
[3] Wilson, S., et al.: A cold-wet middle-latitude environment on Mars during the Hesperian-Amazonian transition: Evidence from northern Arabia valleys and paleolakes, J. Geophys. Res. Planets, 121, 1667–1694, 2016.
[4] Rodriguez, J., et al.: Tsunami waves extensively resurfaced the shorelines of an early Martian ocean, Sci. Rep., 6, 25106, 2016.
[5] Andrews-Hanna, J.: Early Mars hydrology: Meridiani playa deposits and the sedimentary record of Arabia Terra, J. Geophys. Res., 115, 2010.
[6] Tanaka, K., et al.: Geologic map of Mars - Scientific Investigations Map 3292, U.S. Geological Survey, 2014.

EPSC Abstracts
Vol. 12, EPSC2018-759-2, 2018
European Planetary Science Congress 2018

Preliminary Scientific Exploration Programs for Mars Surface Composition Detection Package of China's First Mars Exploration

X. Ren (1, 2), T.N. Cai(1,2), D.W. Liu (1, 2), J.J. Liu(1,2), H.B. Zhang (1, 2), Q. Fu (1,2), Z.B. Zhang (1,2), W.M. Xu (3)
(1) National Astronomical Observatories, Chinese Academy of Sciences, Beijing, China (renx@nao.cas.cn), (2) Key Laboratory of Lunar and Deep Space Exploration, Chinese Academy of Sciences, Beijing, China. (3) Shanghai Institute of Technical Physics, Chinese Academy of Sciences, Shanghai, China.

Abstract

LIBS technique has been widely used in recent deep space explore missions to identify planetary material because of its advantage in requiring no sample pre-treatment, non-contact measurement and simultaneously rapid multi-element analysis. It will be adopted by Mars surface composition detection Package(MarsCoDe) on-board the rover of China's first Mars exploration mission(HX-1) in 2020. This article introduces the scientific exploration programs of MarsCoDe.

1. Background

LIBS technique was first used by ChemCam on-board Curiosity launched on 2011 to detect Mars surface element composition[1,2]. ESA ExoMars equipped a Raman spectrometer to identify surface elements of Mars on March 2016. Although the mission failed, it will continue to perform the second exploration in 2020. LIBS technique will also be adopted by Mars surface composition detection Package on-board the rover of China's first Mars exploration mission in 2020. The rover of Mars 2020 mission will be equipped with a SuperCam which combines the LIBS and Rama techques to detect the surface element of Mars[3,4,5]. So, in 2020, ESA ExoMars 2020, China First Mars Mission and NASA Mars 2020 will be launched together. LIBS technique will be used in all these missions. LIBS data will be used for 1)Information on elemental composition of Mars surface helps get insight into geological evolution history of Mars and 2)Quantitative determination of element (e.g. C,H,P,O,S) provides evidence for life on the Mars surface.

2. MarsCoDe

China first Mars exploration mission (HX-1) plans to launch to Mars in 2020, with an orbiter and a landing rover . The mission will collect a tremendous amount of data with its various onboard payloads for the global exploration by orbiter, and high precision detection in regional area by rover

The Mars Surface Composition Detection Package (MarsCoDe) is one payload onboard the rover of China's first Mars exploration mission. The scientific objectives of MarsCoDe is to perform Laser-induced spectrum observation of Mars surface materials in a distance between 1m and 7m, and obtain the emission lines of plasma between 240nm and 850 nm at high spectral resolution. It also can obtain high resolution reflectance spectra between 850nm and 2400nm. At lease ten elements of Mars surface materials will be expected to analysis. Its primary scientific goal is: 1)Determination of element composition of Mars surface materials; 2)Identification and classification of Mars surface mineral and rock.

MarsCoDe includes six modules: 1)The laser can ablate the target and generate a plasma and also measure the distance between the target and instrument. The distance will be used for data processing. 2)It has two spectra detection modules(one is LIBS spectra detection module(240nm~850 nm), another is SWIR spectra detection module(850nm~2400nm)). 3)A micro-imaging camera can obtain high spatial resolution image for targets. At a distance of 3m, its spatial resolution is about 0.3mm/pixel. 4)A two-dimensional pointing mirror can be pitching and yawing movement. So the laser beam can accurately point to the target. 5)Calibration target will be used for onboard calibration. The calibration target have 12 cylindrical disks, used for LISB spectra calibration and SWIR spectra calibration.

3. Scientific Exploration Programs

Topography camera, multi-spectral camera and micro-imaging camera are three cameras on HX-1 rover. Their spatial resolution are similar at distance between 1m to 7m. According to reduce downloading data, we plan to only use topography camera images for MarsCoDe target selecting. Topography camera have two cameras, we can get stereo image for mars surface and calculate three-dimensional coordinates and distance for selected target. So the laser beam can accurately point to the target.

Three Scientific Exploration Model are designed for MarsCoDe working on mars. 1)Single-point detection, including: One time laser ablating, 50 times LIBS plasma spectra collecting(first five spectra are abandoned, latter 45 spectra are averaged); One time SWIR reflectance spectra collecting; One microscopic Image taking after spectra detection. 2) Depth profile detection, including: 200 times laser ablating at the same location, Cumulative breakdown is expected to be 10um to 500um; For each time, LIBS plasma and SWIR reflectance spectra are same as single-point detection; Two microscopic images taking after first time and last time respectively. 3)Scanning detection: in order to study horizontal variation of element composition and layered structure of martian rocks. Including two ways scanning：1) 5 to 20 points of line scanning; 2) 2 × 2 or 3 × 3 matrix.

Before HX-1 rover is separated from the landing platform, topography camera will be used to obtain stereo images around the landing site, and a mosaic image and terrain data results will be generated. And a preliminary scientific exploration path and detection point distribution will be planned out. The rover mission cycle is about 90 martian days. Every 3 Martian days are a cycle of Scientific exploration.During each exploration cycle, when the rover arrives at one scientific point. Firstly, topography camera will be used to obtain stereo images in the front of the rover. A background topography data will be generated from these images. Several scientific exploration target will be selected by scientists. Then, LIBS plasma spectra , SWIR reflectance spectra and microscopic Image will be obtain for each target. In order to obtain the background rock type around the detection targets, multispectral images(including eight visible-near infrared spectra) may be obtained by multispectral camera.

4. Summary

LIBS technique has been widely used in recent deep space explore missions. In 2020, ESA ExoMars 2020, China First Mars Mission and NASA Mars 2020 will be launched together. LIBS technique will be used in all these missions. And it will be used to determine elemental composition and provide evidence for life on the Mars surface. MarsCoDe is one payload onboard the rover of China's first Mars exploration mission(HX-1). It has two spectra detection modules, one for LIBS spectra detection (240nm~850 nm), another for SWIR spectra detection (850nm~2400nm). Three Scientific Exploration Model of MarsCoDe will be used during the rover mission cycle. Its exploration data will be used for 1)Determination of element composition of Mars surface materials; 2)Identification and classification of Mars surface mineral and rock.

Acknowledgements: We wish to thank all related members from the Ground Research and Application System(GRAS) and Shanghai Institute of Technical Physics, Chinese Academy of Sciences of the HX-1 program, whose joint efforts have made MarsCoDe Scientific Exploration Programs for this article possible.

References

[1] Wiens, R. C., et al.: The ChemCam Instrument Suite on the Mars Science Laboratory (MSL) Rover: Body Unit and Combined System Tests. SSR, 170(1-4), 167-227, 2012.

[2] Maurice, S, et al.: ChemCam activities and discoveries during the nominal mission of the Mars Science Laboratory in Gale crater, Mars. JAAS, 31(4), 863-889, 2016.

[3] Gasnault, O., et al.: SuperCam remote micro-imager on Mars 2020. LPSC, 1832, 2990, 2015.

[4] Clegg, S.M., et al.: Remote geochemical and mineralogical analysis with SuperCam for the Mars 2020 Rover. LPSC, p.2781, 2015.

[5]Maurice1, S, et al.: The SuperCam Instrument for the Mars2020 Rover. EPSC, 10, 185, 2015.

EPSC Abstracts
Vol. 12, EPSC2018-781, 2018
European Planetary Science Congress 2018

Hydrothermal alteration in association with large impact basins on Mars

Christina E. Viviano (1) and Michael S. Phillips (2)
(1) Johns Hopkins University Applied Physics Laboratory, Laurel, MD (christina.viviano@jhuapl.edu)
(2) The University of Tennessee, Knoxville, TN

Abstract

Detailed mapping of CRISM targeted and mapping data across the region between Isidis and Hellas Basins reveal diverse metamorphic and hydrothermal alteration products that may be the result of processes related to basin impact formation.

1. Introduction

The area west of Isidis Basin (Nili Fossae) exposes a region diverse in alteration mineralogy composition, including phyllosilicates and other silicates indicative of metamorphic alteration across the region. The underlying low-Ca pyroxene bearing basement unit in the Nili Fossae region has experienced varied metamorphism, resulting in metamorphic grades from diagenesis to prehnite-pumpellyite facies (and perhaps greenschist facies) [1-3]. An overlying olivine-bearing unit in the easternmost portions of Nili Fossae (along the western Isidis rim) reveals differing alteration products including serpentine, magnesium carbonate [4], and a spectrally unique Mg-bearing phyllosilicate, possibly consistent with talc [2,5]. One interpretation of the association of these products is that they are evidence for hydrothermal alteration of the olivine-rich protolith, from the formation of talc and carbonate through the carbonation of serpentine [2,5].

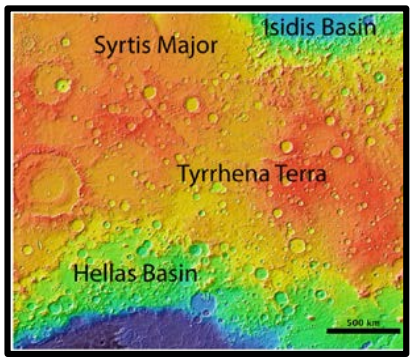

Figure 1. MOLA elevation map of study region.

2. Methods

Here we analyze CRISM targeted and mapping data for the presence of metamorphic- and hydrothermally-related alteration phases in the greater Tyrrhena Terra region between Isidis and Hellas Basins (Fig. 1), where past studies indicate similar assemblages may be present [6,7]. Several hundred new prototype MTRDR calibrated images [8] (through 06/2008) and updated spectral parameters [9] were analyzed within this region to allow for more complete mapping of phases. Multispectral mapping data across this region are also used to map and examine the distribution of alteration (metamorphic vs. hydrothermal) and determine potential associations with Isidis and Hellas basins.

3. Results

Initial mapping efforts of the primary lithology reveals significant plagioclase abundance in the northern Hellas Rim [10], even more extensive than initially identified by [11]. Low-Ca pyroxene (LCP) dominates the Noachian-aged crustal materials between Hellas and Isidis, whereas high-Ca pyroxene (HCP) appears more often associated with younger volcanic provinces (e.g., Syrtis Major) and sands that may not be locally derived. Alteration phases, including Mg-smectite, chlorite/prehnite, hydrated silica, kaolinite, illite/muscovite, analcime and other zeolites, Mg-carbonate, and possible talc, appear throughout the region. At a minimum, low temperature diagenetic to zeolite-facies metamorphic grade, indicated by the presence of illite and chlorite (the transformation of trioctahedral smectites to chlorites and dioctahedral smectites to illites during diagenesis) and zeolite (including analcime), is prevalent throughout Tyrrhena Terra. Prehnite, which forms at 200-400°C, provides clear evidence for higher temperature alteration (prehnite-pumpellyite facies [e.g., 1]) and appears only in the region

between two basins in mapping thus far. Carbonate, possible talc, and kaolinite appear to be associated with the southern rim of Isidis Basin (and western rim near Nili Fossae [2]) and the northern rim of Hellas Basin (Fig. 2). There is also a region surrounding Oenotria Scopuli, a basin-ring structure [12] circumferential to Isidis (black dashed line, Fig. 2), where carbonate is identified [7]. Kaolinite and possible talc are also observed near this scarp.

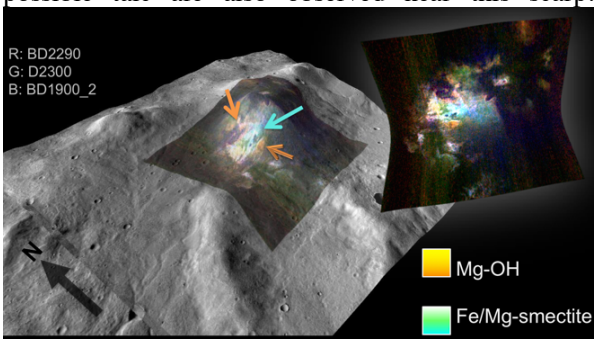

Figure 2. CRISM image FRT00008144 summary parameter RGB composite [2] used to discriminate Fe- vs. Mg-bearing phyllosilicates overlain on CTX imagery. Data are draped on HRSC topography data with vertical exaggeration.

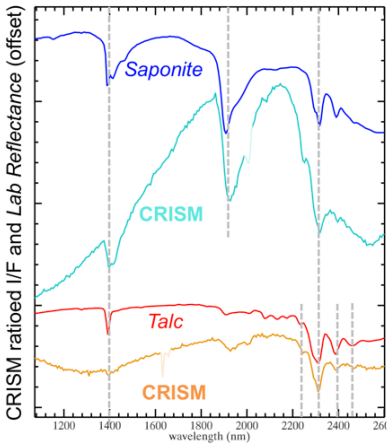

Figure 3. Extracted CRISM spectra (from arrows in Fig. 2) as compared to laboratory spectra of Mg-bearing phyllosilicate species.

Particularly along the northern rim of Hellas, we observe an Mg-OH spectral component. The CRISM spectra have distinctly little to no spectral features due to bound water (lack of deep 1.4- and 1.9-μm bands; Fig. 3, bottom). The material displays strong 2.31- and 2.39-μm bands and shallow, but present ~2.25-μm band and narrow 1.39-μm band. The ~1.4-μm band depth is commonly weak in Fe/Mg-phyllosilicates on Mars and may be due to effects of mixing with other opaque Fe-bearing oxides [e.g., 1]. More hydrated Mg-phyllosilicate phases consistent with Mg-smectite (Fig. 3, top) is present throughout the region, though chlorite dominates in the region between the two basins.

4. Discussion and Conclusions

Although the talc-related spectral component appears related to plagioclase-bearing knobs, it is more likely derived from an Mg-rich pyroxene/olivine lithology that co-occurs with these features [10]. The apparent association of plagioclase-rich material, potentially emplaced as anorthositic plutons [11], and talc (+/- carbonate) may suggest a metasomatic origin for the talc via contact metamorphism of an Mg-rich ultramafic unit during intrusion of the anorthositic pluton. Variability in metamorphic grade will be tested for any spatial trends associated with proximity to the basins, and may be revealed with the completion of the mapping effort.

Acknowledgements

This work was completed with the support of NASA MDAP grant number NNX14AM16G.

References

[1] Ehlmann et al. (2009), JGR, 114.

[2] Viviano et al. (2013) JGR, 118, 1858-1872.

[3] Carter et al. (2013) Planet. Space Sci., 76, 53-67.

[4] Ehlmann et al. (2008) Science, 322, 1828-1831.

[5] Brown et al. (2010) EPSL, 297, 174-182.

[6] Fraeman et al. (2009) LPSC, #2320.

[7] Bultel et al. (2015) Icarus, 260, 141-160.

[8] Seelos et al. (2012) Planet. Data Workshop, USGS, VA.

[9] Viviano-Beck et al. (2014) JGR, 119, 1403-1431.

[10] Phillips et al. (2018) 1st Gy: Differentiation, #4026.

[11] Carter & Poulet (2013) Nat. Geo., 6, 1008-1012.

[12] Tanaka et al. (2013) USGS, 3292.

EPSC Abstracts
Vol. 12, EPSC2018-804, 2018
European Planetary Science Congress 2018

Constraining the geometry and volume of Tharsis dome, Mars using impact craters central peaks

Clément Brustel (1,2), Cathy Quantin (2), Jessica Flahaut (3), Chloe Michaut (2), Gareth. R. Davies (1),
(1) Vrije Universiteit, Faculty of Science, Geology and Geochemistry, The Netherlands, (brustel.clement@gmail.com); (2) Université de Lyon, UCBL, ENSL, CNRS, LGL-TPE, Villeurbanne, France; (3) CRPG, CNRS/UMR7358, Univ. Lorraine, Vandoeuvre–lès-Nancy, 54500, France

1. Introduction

The Tharsis dome is about 5000 km across and represents the largest volcanic province in the solar system. The dome is composed of successive volcanic eruptions spanning the Noachian to Amazonian periods but is thought to have mostly formed at the end of the Noachian epoch [1]. Previous authors [2] determined that the Tharsis dome would have modified the global shape and gravity field of the planet during its formation, producing a major load on the lithosphere and influencing the climate by releasing a large amount of water and carbon dioxide. Using topography and gravimetry models, the volume of the Tharsis dome volume to be $3x10^8$ km^3. However, little is known about the dome 3D geometry. Is the dome symmetrical?, How are its boundaries? Based on an small elastic thickness, of 10 to 40 km [3], estimated for the Noachian period, [4] argued for a late growth (until the Hesperian) of Tharsis. The study of the 3D Tharsis geometry may inform on the elastic properties of the lithosphere such as its elastic thickness, and then on the heat flux of the planet of the time of Tharis formation [5].

A promising study by [6] showed that impact craters located around Valles Marineris, to the east of Tharsis dome, exhibit two different lithologies in their central peaks: Dark, volcanic material to the west, towards the dome center, and light-toned, massive fractured rocks to the east, around the dome possible margin. A simple relation (equation 1) allows us to determine the initial depth of the excavated material in central peaks. [6] have shown that the boundary between the western volcanic material and the eastern light-toned bedrock is sharp and could be followed at depth. This light-toned bedrock is observed in Valles Marineris below the volcanic layers and is interpreted as a mafic lower crust [7].

This study follows the work of [6] in order to study the dome margins, its structure at depth, and to determine its volume.

2. Material and Methods

An initial Tharsis outline was drawn along the Tharsis rise. A buffer zone of 1000 km has been added outwards to define our study area. Imagery and altimetry data from the HiRISE (High Resolution Imaging Science Experiment) [8], and the MOLA (Mars Orbiter Laser Altimeter) [9] instruments were used in this study. All complex craters of at least 30 km of diameter, and with HiRISE coverage, were investigated. Craters were sorted in two categories based on their central peaks lithologies: dark volcanic layers or light-toned massive rocks.

The pre-impact elevation of central peaks materials was found by subtracting the maximum stratigraphic uplift to the central peak elevation. Central peaks of impact craters provide a way to investigate planetary crusts interior as they rise material from depth.

On Earth, [10] established a relation between a crater rim diameter and the amount of uplift undergone by the deepest layers exposed in the centre of the peak. This value represents the maximum possible origin depth of the material which compose the central peak. The Stratigraphic Uplift (SU) is given by the relation:

$$SU(km) = 0.086*D^{1.03} \quad (1)$$

With D the rim crater diameter in km.

As no comparable relationship exists for Mars, we used the maximum stratigraphic uplift to assess the maximum pre-impact elevation of the central peak material. Elevations of central peaks were measured using MOLA topographic data, and pre-impact elevations were calculated by subtracting the SU from the peak elevation.

The dome's geometry was mapped using lithologies of the central peaks of impact craters. Using depth estimates from cratering equation, we assessed the

minimum volume of volcanic material thickness accumulated over time.

In order to perform the volume calculations, all craters exhibiting volcanic layers were projected on an equal area map. A regular grid was used to select each lower points in each grid of equal areas. A surface was drawn using these lower points and this surface was subtracted from the Mola topography.

3. Results

We identify two distinct lithologies exposed in central peaks of impact craters: volcanic layers and massive bright rocks. Some time, both lithologies are exposed in the same central peak. 48 craters expose layers interpreted to be of volcanic origin (ashes or lavas), 11 from [11], 17 from [6] and 20 from this study. 56 craters expose massive, fractured light-toned rocks in the study area. 1 from [12], 12 from [6], which were previously found to be enriched in LCP and 43 craters from this study. Volcanic layers are observed towards the dome center, light-toned rocks all around its periphery, which is consistent with the preliminary observations of [6].

These observations support the hypothesis of [7] and [6] that the light-toned rocks constitute the regional bedrock and possibly represents Mars primitive crust, covered by Noachian to Amazonian volcanic products at the location of Tharsis dome. [6] estimated a thickness of volcanic products of at least 18 km at the location of Oudemans crater confirmed by the absence of bedrock outcrops in the 10 km deep western VM walls [7]. Based on this vertical and horizontal distribution, radial cross-sections were performed at several locations (see example in figure 1). Each cross-section shows a clear transition from massive light-toned rocks to volcanic layers from the outside of the dome toward its center. The boundary between lithologies is sharp and can be followed along the South-East part of the dome where large impact crater central peaks are well-exposed. Craters with both lithologies are located near this boundary.

Volume calculation

A surface was drawn using all the lower points of volcanic material in each box of an equal-area 10 by 10 grid. The sizes of the boxes were define in order to obtain the maximum possible volume. By subtracting this surface to the topography, we estimated a volume of 1.8×10^8 km^3, which is in the same order as found by [2] (3×10^8 km^3). This volume corresponds to a minimum volume as no craters on the dome itself excavated the underlying massive light-toned crust, providing no upper limit for our volume calculations.

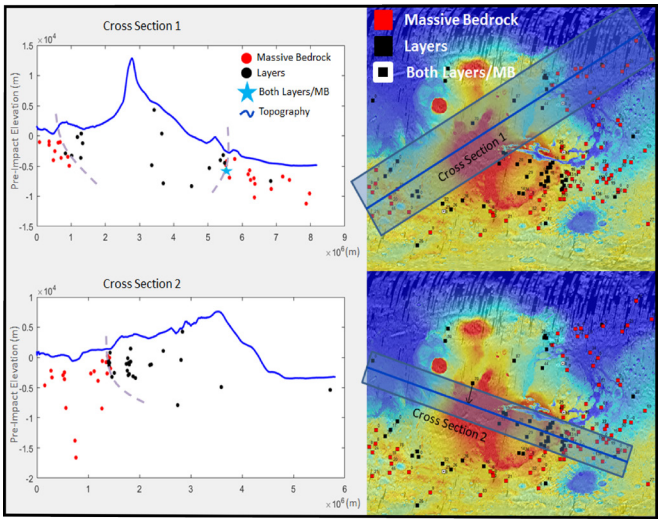

Figure 1: Geologic section of Tharsis dome using stratigraphic uplift of impact craters. Red dots are massive rocks, black dots are volcanic materials. Cf text for more details.

4. Conclusion and Discussion

Geologic sections from this study, based on craters pre-impact elevations, show a sharp boundary between massive rocks and Tharsis volcanic materials along more than half of the dome. This observational bias is explained by the low crater density on younger terrains as the late Hesperian lowlands or Amazonian volcanic units of the dome where few craters with well-exposed central peaks were found. As no craters excavating the underlying massive crust were found on the dome, the volume of 1.8×10^8 km^3 calculated is then a minimum possible volume but is still compatible with previous studies. The edge dip angle still have to be precisely measured and will be used to estimate the resulting lithospheric flexure and a heat flux of the planet at the time the dome was emplaced. These results will be presented at the conference time.

References

[1] R.C. Anderson *et al.*, *Journal of Geophysical Research*, 2001, **106**, 20563.
[2] R.J. Phillips *et al.*, *Science*, 2008, **291**, 2587.
[3] M. Grott *et al.*, *Space Science Reviews*, 2013, **174**, 49.
[4] S. Bouley *et al.*, *Nature*, 2016, **531**, 344.
[5] F. Nimmo, R.T. Pappalardo, B. Giese, *Geophysical Research Letters*, 2002, **29**, 1158.
[6] C. Quantin *et al.*, *Icarus*, 2012, **221**, 436.
[7] J. Flahaut *et al.*, *Icarus*, 2012, **221**, 420.
[8] A.S. McEwen *et al.*, *Journal of Geophysical Research E: Planets*, 2007, **112**, 1.
[9] D.E. Smith *et al.*, *Journal of Geophysical Research: Planets*, 2001, **106**, 23689.
[10] R.A.F. Grieve, M. Pilkington, *AGSO Journal of Australian Geology and Geophysics*, 1996, **16**, 399.
[11] C.M. Caudill *et al.*, *Icarus*, 2012, **221**, 710.
[12] C. Pan, A.D. Rogers, J.R. Michalski, *Journal of Geophysical Research: Planets*, 2015, **120**, 662.

EPSC Abstracts
Vol. 12, EPSC2018-805, 2018
European Planetary Science Congress 2018

Experimental, spectral and colour analysis of H_2O and CO_2 ices and dust samples. Application to Martian icy surfaces.

Z. Yoldi (1), A. Pommerol (1) and N. Thomas (1).
(1) Physikalisches Inst., University of Bern, Sidlerstrasse 5, CH-3012 Bern, Switzerland (zurine.yoldi@space.unibe.ch)

1. Introduction

At the Laboratory for Outflow Studies of Sublimating icy materials (LOSSy, Bern) [1], we have studied the VIS-NIR reflectance of a variety of H_2O/CO_2 ices and Martian regolith analogues associations. Last year, we presented our preliminary results at EPSC [2]; this time, we propose to present the complete results of both H_2O and CO_2 samples, and how to use them to fully exploit data acquired from the surface of Mars.

We will also present the first applications of our work by analysing some images acquired with CaSSIS, the colour camera on board TGO [3]. CaSSIS, whose characteristics make it ideal to monitor volatiles such H_2O and CO_2, has already started sending images from the Martian surface [4,5].

2. Samples and methods

2.1 End-members

We have used, as Martian simulants, the Martian soil analogue JSCM-1 [6] and a more pristine dark basalt [7]. As ice simulants, we have used the grained, water SPIPA ices [8] and CO_2 ices in the range of the hundred micrometres.

2.2 Associations

- *Intimate mixtures*: salt-and-pepper like mixtures of dust-H_2O ice, dust-CO *Intimate mixtures*: salt-and-pepper like mixtures of dust-H_2O ice, dust-CO_2 ice and CO_2-H_2O ices.
- *Frost on dust*: condensed atmospheric water onto both JSCM-1 and dark basalt.
- *Frost on intimate mixtures*: condensed atmospheric water onto dark basalt and water ice intimate mixtures (serendipitous samples)
- *Frost on CO_2 slab*: water frost condensed onto a slab of CO_2.
- *Frozen soils*: matrix of water ice surrounding JSCM-1.

2.3 Spectral and colour analysis

We have measured the reflectance spectra (0.4-2.4 μm) of the samples within our simulation chamber, SCITEAS [1]. Second, we have conducted an analysis of the absorption bands and spectral slopes of the spectra. Finally, we have used the ground-calibration data from CaSSIS [9] to convolve our reflectance measurements with the spectral response of CaSSIS.

3. Results

Frost deposition: we observe three stages of spectral changes. In the first one, the substrate is almost homogeneously covered by fine particles; photons have a large probability of encountering ice. The great surface-to-volume ratio of tiny particles makes the reflectance increase. As frost grows thicker, the probabilities for photons to encounter ice barely increase, whereas the path length inside ice gets longer. Hence, we observe a deepening of the absorption bands rather than an increase of reflectance. In a third step, the highly-scattering frost layer masks the substrate beneath.

Intimate mixtures: the probability for a photon to encounter ice at the surface is smaller than in the case of frost. Once the photon finds a grain of ice, its chances of being scattered increase for greater surface-to-volume ratio of the ice grain. In this way, bigger particles are more likely to absorb or transmit the photon deeper into the soil. The reflectance of intimate mixtures with coarse ice grains is generally lower than the one of mixtures with fine ice grains.

At wavelengths that correspond to water absorptions, the situation can twist since coarse enough ices become the absorptive material of the mixture. At these locations, the great absorptivity of water becomes predominant in the reflectance spectrum.

Frozen soils: here, water is almost a continuum medium, which results in a low surface-to-volume ratio; samples are highly absorptive and the bands saturate. When cracks appear inside the slabs, the surface-to-volume ratio increases, raising the reflectance. The BLU colour of water, nevertheless, is still distinguishable.

CO_2: When dust is mixed with CO_2 instead of H_2O ice, reflectance behaves in a similar way since CO_2 is the non-absorptive component of the mixture and dust the absorptive one. In mixtures of CO_2 and H_2O ices, water ice becomes the absorptive component. Thus, water ice behaves in an H_2O-CO_2 mixture as JSCM-1 behaves in an H_2O-JSCM-1 one; its spectrum predominates the reflectance spectrum of the mixture. H_2O and CO_2 are almost indistinguishable from their colour in the visible.

4. Application to Mars

Figure 1 shows the comparison of the PAN/RED and BLU/RED ratios with the RED band of the laboratory samples. For simplicity, we have grouped the samples by their association mode and presented the trends they draw as the presence of ice increases (direction of the arrows).

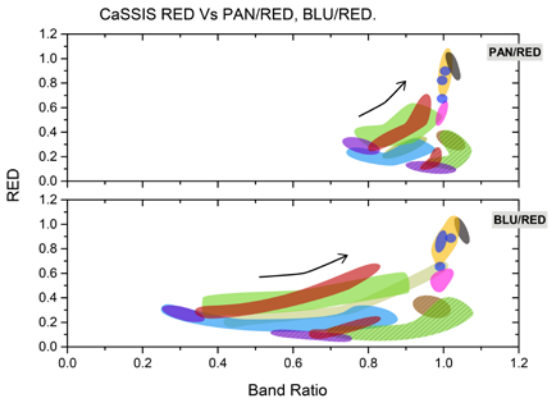

Figure 1 CaSSIS RED band vs PAN/RED and BLU/RED band ratios.

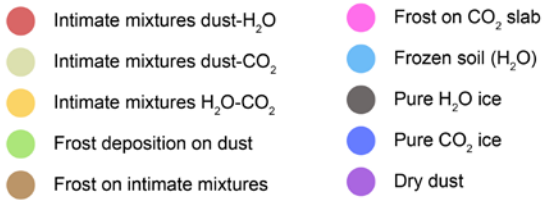

Figure 2 Colour legend for Fig. 1

Depending on their association mode and their ice percentage, samples mark different trends (notably in the BLU/RED plot). The filters of CaSSIS and those of HiRISE are comparable [3]; we will therefore compare the colours of the laboratory samples with the ones of Martian surfaces acquire with HiRISE.

At this conference, we will be able to show the first analysis of CaSSIS images. Of special interest for us will be the study of the colour evolution of the surface in a daytime scale and the changing colours of the retreating, southern, seasonal polar cap.

Acknowledgements

This work has been carried out within the framework of the NCCR PlanetS supported by the Swiss National Science Foundation.

References

[1] Pommerol et al., (2015a). PSS., Vol 109-110
[2] Yoldi et al., (2017) EPSC 2017-249.
[3] Thomas, N. et al. (2017) Space Sci. Rev., 212, 1897
[4] Thomas et al., this conference.
[5] Pommerol et al., this conference.
[6] Allen, et al., (1998) Space, 469–476.
[7] Pommerol et al., (2013) JGR, 118. 2045-2072.
[8] Yoldi, et al., (2015) GRL, 42, 6205–6212.
[9] Roloff et al. (2017) Space Sci. Rev., 212, 1871.

EPSC Abstracts
Vol. 12, EPSC2018-815-1, 2018
European Planetary Science Congress 2018

Tectonics structures in Noctis Labyrinthus area based on HRSC and CTX photogeological mapping

Mayssa El Yazidi (**2**), Riccardo Pozzobon (**1,2**),Stefano Debei (**2**) and Matteo Massironi (**1,2**).

1 Dipartimento di Geoscienze, Universita degli Studi di Padova, via Gradenigo 6, 35131 Padova, Italy.
matteo.massironi@unipd.it , riccardo.pozzobon@unipd.it.
2 Centro di Ateneo di Studi e Attività Spaziali "Giuseppe Colombo" – CISAS, Via Venezia 15, 35131Padova, Italy.
stefano.debei@unipd.it , mayssa.elyazidi@unipd.it .

1. Abstract

Noctis Labyrinthus is made up by inter-connected canyons with complex branched networks of extensional faults and grabens whose origin and evolution is still debated [2,4,5,6,7,8,9]. It is located in the Northern hemisphere at the western part of Valles Marineris, and is bordered by Noctis Fossae to NE and by Syria Planum and Syria Colles to the S-SE (defined on the surface by the coordinates 6.36° S, 258.81 °E).

Our work was carried out on HRSC and CTX images and was focussed at mapping at different scales faults, scarps and grabens and identifying their cross-cutting relationship in order to assess the strain field responsible for their formation.

2. Data and Methods

As a basemap to delimit all the lineaments, we have used two orthoimages and DEM pertaining h3210_0000 and h3221_0000 datasets acquired from HRSC camera onboard Mars Express Spacecraft with 12 to 13m/Pixel of spatial resolution and a images mosaic from CTX camera of Mars Reconnaissance Orbiter with 5.2m/Pixel of spatial resolution [1,9]. We focused our work to draw at different scales faults, scarps and grabens and we have checked their orientation using rose diagrams.

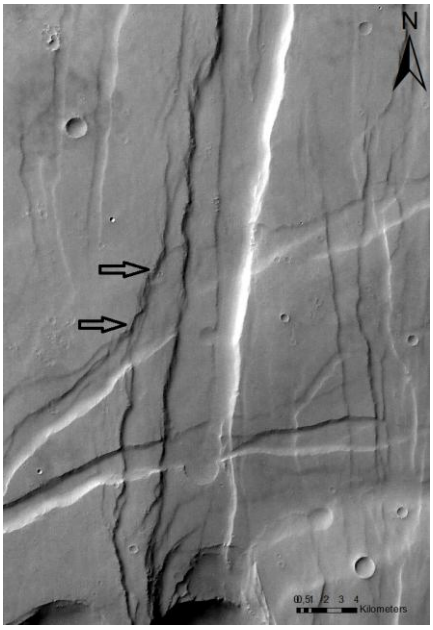

Figure.1. Interference patterns at fault intersection (4°13'43.85"S – 104°50'57.48"W), HRSC H3221_0000_ND2, orthoimage (sinusoidal projection).

3. Results and Conclusions

The resulting rose diagrams show at all scales two main trends of faults in the studied area: ENE-WSW and N-S (Fig.2). These systems do not show a preferential cross-cutting relationship of one direction over the others. This seems to support a coeval development of the two systems potentially generated in response of a bidirectional or a radial extension. The overlapping zones represented by interference patterns are interested by slump structures, steeper slopes, wrinkle ridges and concentric ring fractures (Fig.1).

Particularly relevant are also the pits which can be find within the tip and at the margin of the Noctis Labyrinthus grabens [3]. They seem due more to graben propagation than impact cratering phenomena and thus might give hints on the rheological subsurface layering which underwent the extensional deformation. We propose that the oblate strain field drove an extensional tectonism responsible of the evolution of pits chain and faults into grabens.

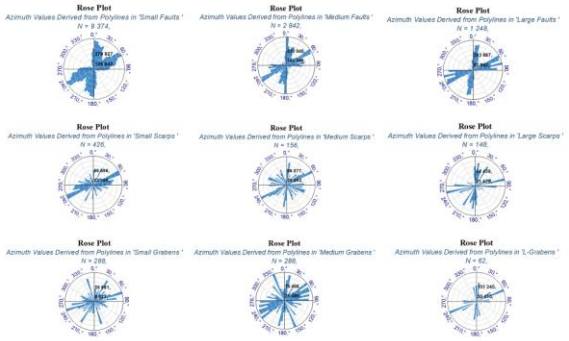

Figure.2. Rose diagrams of the faults, scarps and grabens relative to the tectonic tectonic context of the selected area (6.36° S, 258.81 °E).

Acknowledgements

The authors appreciate the efforts of the CTX and HRSC experiment and instrument teams of the Mars Reconnaissance Orbiter and Mars Express to produce and make available their data sets. We also acknowledge the comments and suggestions made by two reviewers for this work.

Keywords : Noctis Labyrinthus, faults, grabens, rose diagrams, cross-cutting relationship, tectonic extension,pits, scarps, strike Slip, Interference patterns, mapping.

References

[1] Rodriguez et al. (2015) Planetary and Spac.Sci, 124,1-14.
[2] Spagnuolo et al. (2014) Earth Planet.Sci.Lett.,401, 83-94.
[3] Bridges et al. (2009), Icarus, 205, 165-182.
[4] Yin (2012), Geological Society of America, Vol.4, 286-330, doi: 10.1130/L192.0.
[5] Montgomery at al. (2009), Geological Society of America Bulletin, 121, 117-133, doi: 10.1130/B26307.1.
[6] Massironi et al. (2017), EPSC, Vol.11, 618-1.
[7] Mudric et al. (2017), 48th LPSC Abstract, 1464.
[8] Weitz et al. (2016), APGMM, 7029.
[9] Baioni et al. (2017), Acta Carsoligica 2017, 46/1, 73–82.
[10] Massironi et al. (2012), 43rd LPSC Abstract, 1924.

EPSC Abstracts
Vol. 12, EPSC2018-848, 2018
European Planetary Science Congress 2018

Morphological and spectroscopic analysis of light-toned materials in southeastern Gorgonum Chaos, Mars

David Haack (1), Solmaz Adeli (1), Ernst Hauber (1), Katrin Stephan (1), Ralf Jaumann (1,2)
(1) Institute of Planetary Research, Deutsche Zentrum für Luft- und Raumfahrt, Rutherfordstrasse 2, 12489 Berlin, Germany, (David.Haack@dlr.de)
(2) Planetary Sciences and Remote Sensing Group, Institute of Geological Sciences, Freie Universität Berlin, Malteserstr. 74-100, 12249 Berlin, Germany

1. Introduction

Gorgonum Chaos is an eastern sub-basin of the hypothesized Eridania paleolake system [1] in the southern highlands of Mars. The basin morphology is characterized by a bowl-shaped floor and numerous fluvial valleys and erosional features at its rim [2]. Its floor consists of light-toned material which forms hundreds of meters-thick deposits and is observable at numerous outcrops throughout the basin [3,4]. This light-toned material contains hydrated minerals such as phyllosilicates and indicates a genesis in which abundant liquid water was involved [e.g. 3,4]. Therefore, the analysis of these materials and their geomorphological history is crucial to understand the evolution of Gorgonum Chaos and the role of liquid surface water in its current morphology. Here, we present a reconstruction of the past geological events and aqueous activities in the study area.

2. Data

To study the morphological context between units and relief, CTX, HiRISE, HRSC images and HiRISE based DEMs were used. The spectroscopic analysis was realized with THEMIS and CRISM data.

3. Results

3.1 Geomorphological investigation

At the southeastern rim of Gorgonum Chaos a heavily degraded crater with 22 km diameter forms an approximately horizontal plain (Figure 1). A prominent gap appears in the northern crater wall and forms a curved, 60 m deep path towards the north.

Adjacent to the west of the degraded crater a depression extends over ~380 km^2, which displays numerous km-scaled inverted fluvial valleys and impact craters with diameters up to 1.5 km. Both inverted features are up to 150 m high. The valleys trend to originate near the northern gap in the crater wall. The inverted valleys and craters are completely embedded in highly polygonised bedrock of light-toned units, which were heavily degraded by aeolian erosion. The unit formed of light-toned material is covered with different darker units of varying texture, morphology, and thickness.

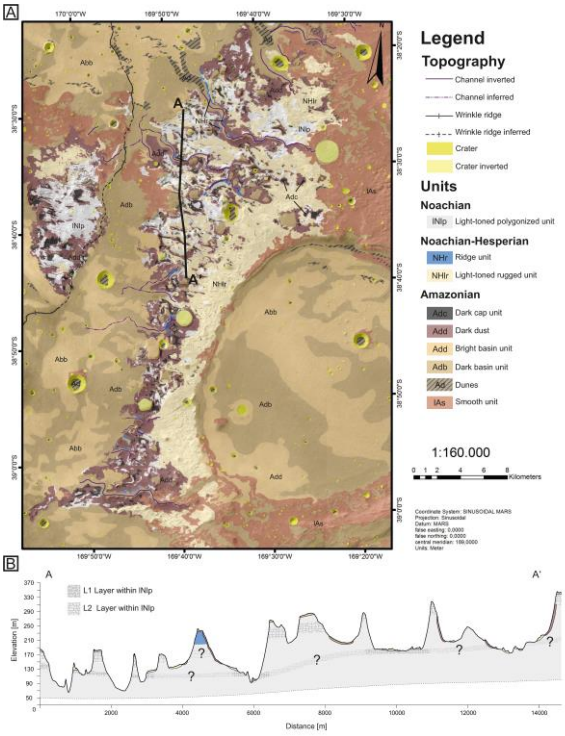

Figure 1: (A) Geological map of the study area. (B) Interpretative cross section of profile line AA' based on a HiRISE DTM. The topography is exaggerated by factor 10.

3.2 Spectroscopic analysis

CRISM spectra from the light-toned material revealed the presence of Al-phyllosilicate similar to kaolinite and a sulfate similar to jarosite (Figure 2) This material was deposited in the Late Noachian – Early Hesperian. These minerals were most likely deposited under humid conditions and form the upper layer of lacustrine sediments that is at least 150 m thick.

Chlorides were detected locally at upper layers of inverted features and do not occur over extended areas. They were deposited most likely in the Late Noachian – Early Hesperian after the formation of light-toned materials when sediments transported with brines refilled fluvial valleys and small craters.

Olivine and pyroxene are ubiquitous in the 3-m thick mantling units of Amazonian age. They may represent airfall material of ultramafic volcanic ashes.

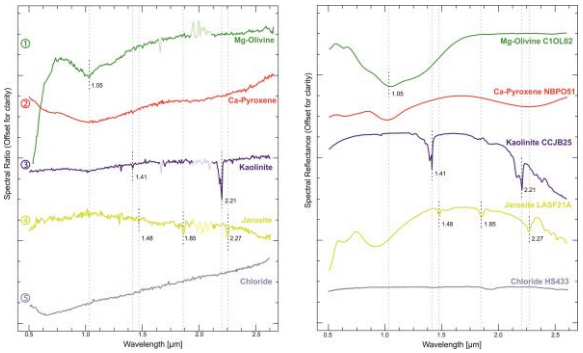

Figure 2: (Left) Measured and ratioed CRISM spectra. (Right) Laboratory spectra of analog materials to compare with measured spectra.

4. Summary and Conclusions

In the Late Noachian a hundreds of meter thick light-toned unit, enriched in hydrated minerals, was deposited on the floor of the hypothesized Eridania paleolake. Approximately during the Noachian-Hesperian transition the paleolake desiccated [1] and fluvial systems and impacts started to modify the surface. Deposits have accumulated later in these fluvial valleys or craters when liquid surface water was present after the desiccation of Eridania. These deposits contain considerable amounts of chlorides that may have cemented the sediments and increased their competence.

During a period of aeolian erosion and deposition throughout Hesperian the formation of hydrated minerals was reduced to marginal amounts. The depressions with inverted structures as sinuous ridges and circular mesas were formed and partially refilled with new sediments. They are of low competence and reminiscent of loess-like sediments [5]. The ultramafic and morphological characteristics of these younger deposits are consistent with arid conditions.

In the Amazonian all features were covered with a thin layer of ultramafic air fall material of probably volcanic origin. The olivine in this latest unit is stable only under anhydrous conditions over long periods of time. This indicates the complete absence of water during and after their deposition.

The stratigraphic sequence of all units and their mineralogical composition indicates an environmental transition in this region from wet conditions during the Late Noachian over rather dry environments during Hesperian to ultra-arid conditions in the Amazonian and today.

References

[1] Irwin, R. P., Maxwell, T. A., Howard, A. D., Craddock, R. A., and Leverington, D. W.: A large paleolake basin at the head of Ma'adim Vallis, Mars, Science, Vol. 296, pp. 2209–2212, 2002.

[2] Howard, A.D., Moore, J.M.: Late Hesperian to early Amazonian midlatitude martian valleys: Evidence from Newton and Gorgonum basins. J. Geophys. Res. 116 (E5), E05003, 2011. doi: 10.1029/2010JE003782.

[3] Wendt, L., Bishop, J. L., and Neukum, G.: Knob fields in the Terra Cimmeria/Terra Sirenum region of Mars: Stratigraphy, mineralogy and morphology, Icarus, Vol. 225, pp. 200–215. doi:10.1016/j.icarus.2013.03.020.

[4] Adeli, S., Hauber, E., Le Deit, L., and Jaumann, R.: Geologic evolution of the eastern Eridania basin: Implications for aqueous processes in the southern highlands of Mars, J. Geophys. Res. Planets, Vol. 120, pp. 1774–1799, 2015. doi:10.1002/ 2015JE004898.

[5] Grant, J.A., Wilson, S.A., Noe Dobrea, E., Fergason, R.L., Griffes, J.L., Moore, J.M., Howard, A.D.: HiRISE views enigmatic deposits in the Sirenum Fossae region of Mars. Icarus, Vol. 205 (1), pp. 53–63, 2010.

EPSC Abstracts
Vol. 12, EPSC2018-860-2, 2018
European Planetary Science Congress 2018

Comparative studies of Gravitational Influence of Phobos and Deimos on Mars

Adhithiyan Neduncheran(1), Dr.Ugur Guven, Rohan Chandra, LV Gireesh, Amritansh Mehrotra
(1)University of Petroleum & Energy Studies, India(adhithiyan.n@gmail.com)

Moon is Earth's only natural satellite. It is known that it orbits the earth every 27 days. The gravitational forces exerted by moon influences Earth in the formation of oceanic tides and the movement of the tectonic plates. It is also known that it influences in the growth of plants. It is right to say that the movement of moon around the Earth influences the life on earth. We have sufficient knowledge that this satellite of ours influences our planet in many ways. Similarly the gravitational effects of Mars' moons has an impact on the Mars's planetary conditions. Mars has two moons orbiting at different orbital parameters. The cumulative effect of both of them on the planet is different and bit more complex than Earth. Human exploration of Mars is mainly because of its similar nature to Earth. Studying the influence of Mars's moons influence on the planet will increase the scientific knowledge of the planetary community. This paper aims to present all the causes and effects of the gravitational influences on Mars caused by it's two Moons namely Phobos and Deimos. Also, if there is any relation between the shape and size of the moon on the planets. This will provide us with a perspective of the formation of the planet and the conditions of the atmosphere and climate models. It shall also answer how the moons influences the planetary motion and the geographical/biological phenomena taking place in the planet.

EPSC Abstracts
Vol. 12, EPSC2018-873, 2018
European Planetary Science Congress 2018

Morphometric Study of Longitudinal Striations on Long Run-out Mass Movements and Ejecta Blankets on Mars: Assessment of a common formation mechanism

Alexa Pietrek, Stefan Hergarten and Thomas Kenkmann
Faculty of Earth and Environmental Sciences – Geology, Albert-Ludwigs-University Freiburg, Germany
(alexa.pietrek@geologie.uni-freiburg.de)

1. Introduction

Distinct longitudinal grooves and ridges ("striations") are an enigmatic and unexplained feature of long run-out landslides on Earth [1, 2] and Mars [3, 4, 5, 6]. They form in different materials and in a wide variety of geological settings, for example in rock avalanches [1, 3, 7], landslides deposited on a glacial substrate [1] and volcanic debris flows [2]. Similar features can also be observed on the ejecta blankets of Martian SLE (single-layered ejecta) craters and DLE (double-layered ejecta) craters [8, 9, 10,11]. Several formation mechanisms have been proposed [5, 6, 7, 8, 9, 10, 11], but it remains a central question whether the striations on different types of deposits form by a common mechanism. We conducted a morphometric analysis on topographic profiles of well-preserved Martian landslides and ejecta blankets of DLE and SLE craters to evaluate the possibility of a common formation process.

2. Methods

Topographic tracks were extracted from DEMs generated from high-resolution CTX (5 m/px) and HiRISE (0.5 m/px) stereo data. Decomposition of the signal with a Fourier analysis shows a power law dependency of power spectral density $S(k)$ on wavenumber k for all profiles, as it can be expected for the self-affine properties of topography in general [12]. The data was fitted using a Maximum Likelihood method in the form

$$S(k) = \alpha k^{-\beta} + \gamma \qquad (1)$$

where γ is noise, α is a scaling factor and β the power law exponent. The power law dependence inherently means that the topography of longitudinal striations is scale-invariant and self-affine, e.g. there is no "characteristic width" that can be used to quantify those structures. Instead, the power law exponent β and scaling factor α can be interpreted as surface roughness, since a higher slope of the power law means greater importance of longer wavelengths and a higher scaling factor means a greater absolute height of asperities.

Table 1: List of Datasets used for evaluation.

Deposit	Type	Location	DEM res. $[m/px]$
Capri1	Landslide	8.6°S 44.5°W	5.1
Capri2	Landslide	7.6°S 44.2°W	5.1
Coprates	Landslide	11.8°S 67.8°W	5.1
OphirW	Landslide	11.1°S 68.3°W	5.1
OphirE	Landslide	11.1°S 67.9°W	5.1
Melas	Landslide	8.9°S 71.8°W	6.1
Blunck	Landslide	27.5°S 37.0°W	4.7
Steinheim	DLE crater	54.5°N 169.3°W	4.8
Bacolor	DLE crater	33.0°N 118.5°E	5.5
SL5	SLE crater	34.2°N 109.5°E	0.65
SL7	SLE crater	23.6°N 122.3°E	0.6

3. Results and discussion

We compared the power law exponents and scaling factors of topographic tracks perpendicular to striations ("across") and parallel to flow direction in longitudinal direction ("along"). Additionally we used the values of profiles from the surrounding terrain as reference values, e.g. we assume that those profiles are representative for substrate properties. A preliminary summary of results revealed the following relationships: A) The overall range of values for the power law exponent for all deposits is between β = 1.5 and β = 3.5, but covers a specific, smaller range of values for each deposit (Fig. 1). The power law exponents are in the same range regardless of orientation. Furthermore

the topography of the terrain surrounding each individual deposit has similar statistical properties as the tracks across deposits. This implies that the roughness of striations is possibly inherited from the substrate. B) For landslides, the scaling factors are lower in longitudinal direction than in perpendicular profiles, e.g. the relief is more subdued along striations. This implies horizontal stretching of the topography in flow direction. More interestingly, for ejecta deposits, the scaling factors in longitudinal direction are higher than in perpendicular direction. It can be concluded that the Fourier analysis is a suitable method for the quantification and comparison of striations. The results show some common relationships, but also reveal important differences regarding the scaling of ridges. Furthermore the results suggest that the formation process might be influenced by substrate properties. This is indicative for formation by a flow process.

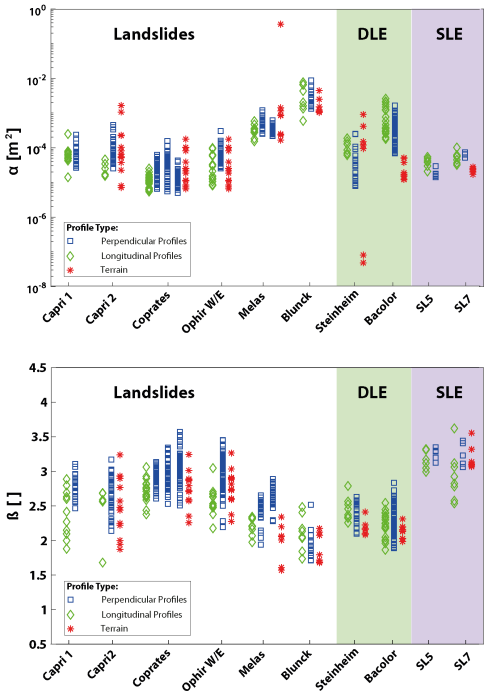

Figure 1: Results for the power law parameters. The different types of topographic profiles are grouped for each dataset (see bottom axis). Top: Results for the scaling factor α, that is a measure for the amplitude of ridges. Bottom: Results for the spectral exponent β, that can be interpreted as surface roughness.

Acknowledgements

This work was funded by a stipend of the LGFG of the Albert-Ludwigs Universität Freiburg.

References

[1] McSaveney, M.J.: Sherman Glacier rock avalanche, Alaska, U.S.A., In Rockslides and Avalanches, pp. 197-258, 1978.

[2] Naranjo, J.A., and Francis, P.: High velocity debris avalanche at Lastarria Volcano in the North Chilean Andes, Bulletin of Volcanology, Vol. 49, pp. 509-514, 1987.

[3] McEwen, A.: Mobility of large rock avalanches: Evidence from Valles Marineris, Mars, Geology, Vol. 17, pp. 1111-1114, 1989.

[4] Quantin, C., Allemand P., and Delacourt C.: Morphology and geometry of Valles Marineris landslides, Planetary and Space Science, Vol. 52, pp. 1011-1022, 2004.

[5] De Blasio, F.V.: Landslides in Valles Marineris (Mars): A possible role of basal lubrication by sub-surface ice, Planetary and Space Science, Vol. 59, pp. 1384-1392, 2011.

[6] Watkins, J.A.: Long-runout landslides and the long-lasting effects of early water activity on Mars, Geology, Vol. 43, pp. 107-110, 2015.

[7] Dufresne, A., and Davies, T.R.: Longitudinal ridges in mass movement deposits, Geomorphology, Vol. 105, pp. 171–181, 2009.

[8] Boyce, J.M., and Mouginis-Mark, P.J.: Martian craters viewed by the Thermal Emission Imaging System instrument: Double-layered ejecta craters, Journal of Geophysical Research, Vol. 111: E10, 2006.

[9] Weiss, D.K., and Head, J.W.: Ejecta mobility of layered ejecta craters on Mars: Assessing the influence of snow and ice deposits, Icarus, Vol. 233, pp. 131-146, 2014.

[10] Wulf, G., and Kenkmann, T.: High-resolution studies of double-layered ejecta craters: Morphology, inherent structure, and a phenomenological formation model, Meteoritics and Planetary Science, Vol.50, pp.173-203, 2015.

[11] Barnouin-Jha, O.S., Baloga, S., Glaze, L.: Comparing landslides to fluidized crater ejecta on Mars, Journal of Geophysical Research E: Planets, Vol. 110, pp. 1-22, 2005.

[12] Malamud, B.D., and Turotte, D.L.: Journal of Geophysical Research, Vol. 106, pp. 17,497-17,504, 2001.

EPSC Abstracts
Vol. 12, EPSC2018-882-1, 2018
European Planetary Science Congress 2018

Locating new areas favourable for Recurring Slope Lineae formation in the northern hemisphere on Mars using GIS and the Mars Climate Database

Andreas Eriksson (1), Andreas Johnsson (1)
(1) Department of Earth Sciences, University of Gothenburg, Gothenburg, Sweden (guserianbr@student.gu.se).

1. Introduction

Recurring Slope Lineae (RSL) are low-albedo markings found on slopes with a steepness of 25°-45°. Their width is between 0.5-5 m but they can become hundreds of meters long. They grow incrementally during warm seasons; fade during cold seasons and appear again the following martian year [1-2]. They occur mainly in the equatorial and southern mid-latitudes and appear less abundant in the northern hemisphere. After the first confirmed observations of RSL, research about them accelerated quickly. This is primarily due to their possible association with liquid water flows at the modern-day martian surface. The main scope of this study is to find new RSL candidate sites in the less investigated northern hemisphere with the use an ArcGIS model and Mars Global Climate data base simulations. Furthermore, we explore whether potential candidate sites are likely wet- or dry flows, or a combination of both.

2. Data and Methods

In order to work with the available data sets several types of software's were used. The Mars Climate Database (MCD) was used in order to get temperature data for an analytic model in the first part of the study (Fig. 1). MCD provided "average max mean daily temperature" for the model at specific parameters found in literature. It was possible to retrieve information from MCD for parameters used in the third phase of the project (assessing wet- or dry flows) [3-4]. The near surface parameter was set to 2 meter above the surface. Most of the HiRISE images used in the study are taken in the afternoon by the instrument, which leads to a local time of Martian hour 15. The solar longitude was set to be during the summer season (110 Ls) in order to meet the utmost conditions for RSL. Data set coordinates were all set to match the extent of the study area [3-4].

Data processing for the first phase and image analysis were done in the Geographical Information System (GIS) ArcMap. All data coordinates from MCD used the "Inverse Distance Weighted" (IDW) Interpolation spatial analyst tool to display data on the GIS maps. The interpolation tool interpret values closer to each other to be similar than those further away. To obtain a value in an area where there is none, the tool uses measured values in close proximity to the unmeasured area to get a good prediction of a potential value. Values closer to an unmeasured site have a higher impact on the result than values further away. Distances to values are very important in this interpolation tool [5-6].

3. Results

By using an ArcMap GIS model, data from the High Resolution Imaging Science Experiment (HiRISE) instrument and parameters based on previous literature, 408 optimal sites for RSL were found with 29 of those being classified as new potential candidate RSL sites (Fig. 2).

4. Summary and conclusions

Analyses of candidate sites with modelled surface temperature, grain-size approximations, modelled water vapor and parameters derived from previous studies suggests that a combination of wet flows and dry flows may be responsible for the creation of RSL.

The reason for the scarcity in the northern region is due to less favorable RSL forming areas (less available slopes), poorer HiRISE coverage of existing topography and less favorable temperatures.

In our model we have identified 29 sites that fulfill the RSL criteria thus warranting more HiRISE images to be able to confirm the presence of RSL.

References

[1] McEwen, et al. (2011). Seasonal Flows on Warm Martian Slopes. *Science, 333*(6043), 740.[2] Ojha, et al. (2014). HiRISE observations of Recurring Slope Lineae (RSL) during southern summer on Mars. *Icarus, 231*, 365-376. [3] Forget et al. (1999). Improved general circulation models of the Martian atmosphere from the surface to above 80 km. *Journal of Geophysical Research: Planets, 104*(E10), 24155-24175.

[4] Millour et al. (2015). *The Mars Climate Database (MCD version 5.2)* (Vol. 10). ESPC. [5] Philip and Watson (1982). A precise method for determining contoured surfaces. *The APPEA Journal, 22*(1), 205-212. [6] Watson and Philip (1985). A refinement of inverse distance weighted interpolation *geo-processing, 2*(4), 315-327.

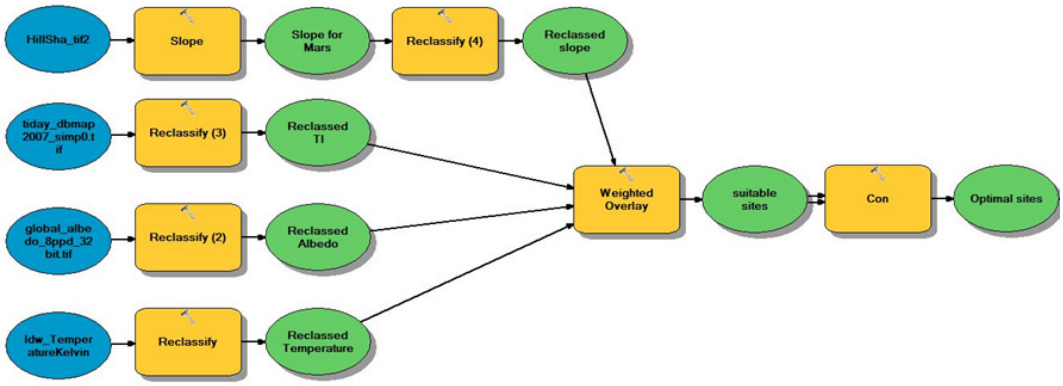

Figure 1: Flow chart for the model in the GIS software ArcMap. From top to bottom in the blue ellipses are the slope data, Thermal inertia, Albedo and Temperature data. All were reclassified and run in a weighted overlay. A condition value was set in order to find the most optimal sites from the suitable sites.

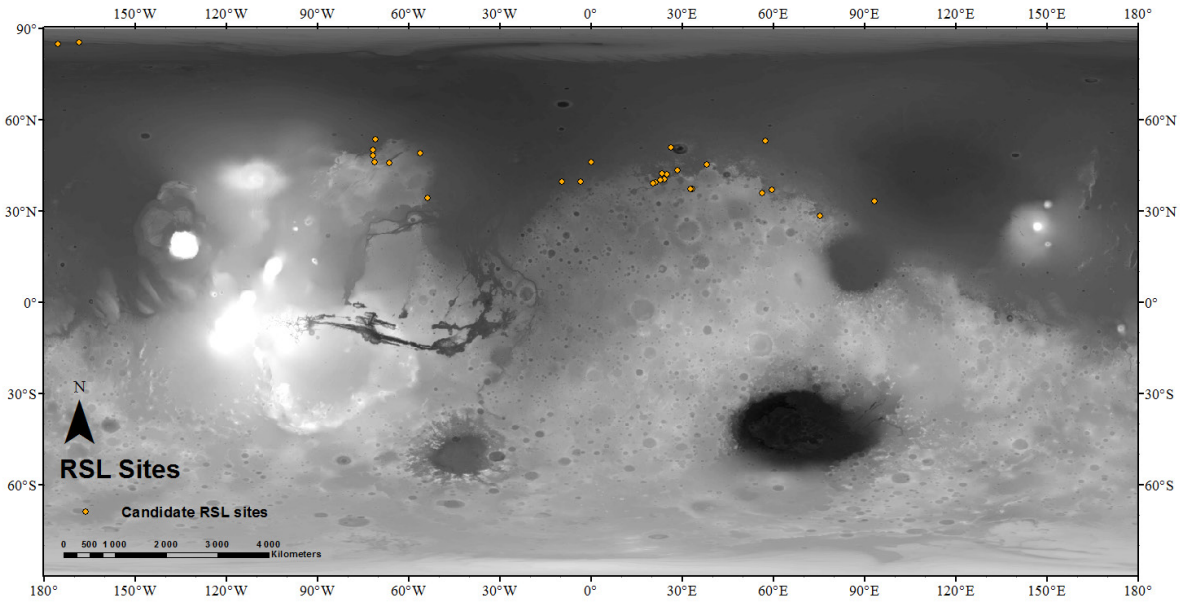

Figure 2: The location of all 29 new potential candidate RSL sites distributed on the northern hemisphere (yellow dots).

EPSC Abstracts
Vol. 12, EPSC2018-929, 2018
European Planetary Science Congress 2018

Investigation of regional settings for formation of Araneiform Terrain, Mars

J. Hao (1), G.G. Michael (1), S. Adeli (2), R. Jaumann (1,2)
(1) Planetary Sciences and Remote Sensing, Institute of Geological Sciences, Freie Universität Berlin, Malteserstrasse 74, 12249 Berlin, Germany (**J.Hao@fu-berlin.de**)
(2) Institute of Planetary Research, German Aerospace Centre (DLR), Rutherfordstrasse 2, 12489 Berlin, Germany

1. Introduction

Seasonal variations of solar insolation cause sublimation/condensation cycle of CO_2 ice annually. This seasonal behaviour creates an impermeable and translucent CO_2 ice which lay partly in the south polar area every winter [1]. In the spring, sunlight penetrates the ice layer directly heating the substrate which causes basal sublimation. The sublimating gas is trapped inside the substrate [2] or between the substrate and the ice layer [1, 3-4]. With pressure building up, the overlying translucent ice layer finally ruptures, entraining dust and sand from the inside of substrate into the atmosphere causing sculpture into the ground [1-4]. This is proposed to be essential formation mechanism for araneiform terrain (dubbed "spider") which is characterised by radial-organized or dendritic troughs (Fig.1) exclusively observed in south polar area.

Spiders had long been reported as distributed only in the south polar layer deposits (SPLD) [3]. This has been interpreted that SPLD not only has seasonal translucent CO_2 ice slab, but also hosts unconsolidated upper surface with high erodibility [3]. However, recent research [5] reported the observation of spiders outside the SPLD [5]. This raises some new questions as follow:

What are similarities and differences of regional settings between SPLD and these new spider host locations (e.g., substrate properties)? Do the spatial settings of spiders have regional characteristics? How and to what extent are they indicative of regional or local substrate properties?

Thus, in order to answer these questions, it is necessary for us to conduct an investigation of regional settings for spiders. Hence, we chose areas from all known spider hosting regions with HiRISE observations to measure their spatial randomness and investigate their regional settings and analyse their correlations. Our work can improve the understanding of spider formation mechanism and provide insight into the polar surface processes.

2. Background

Our research [2] suggests that the sublimating gas is trapped inside the substrate and consequent gas jetting activities originate from the inside of the substrate. Thus, the substrate properties (i.e., porosity and degree of cohesion) are crucial parameters for spider formation. On account of mutual influence of neighbouring spider extremities to pressure accumulation and gas-jetting efficiencies, we can expect that in the vicinity of one spider, initiations of new spiders are inhibited, indicating the existence of an inhibited zone [2]. The spatial randomness analysis results of one sample spider population indicate that spider spatial distribution is non-random, which is consistent with the above suggestion for spider formation mechanism [2]. This analysis yields a value (the mean 2nd-closest neighbour distance, hereafter "M2CND") not only corresponding to average spacings but also indicating the minimal size of inhibited zones in one spider population [2][6]. One could expect that this value is indicative of regional substrate properties and varies from region to region. These are our suggestions for scenarios of araneiform (spider) formation and its distribution characteristics (for more details see [2]).

3. Results and discussions

The spatial randomness analysis can measure average spacing for one spider population (Details see [2][6]). Here we chose eight regions from all of the reported area where spider have been observed. Since HiRISE's high spatial resolution [7] can substantially improve the accuracy to map spider spatial distribution and identify its morphologies, only regions which have available HiRISE images were chosen.

We conducted spatial randomness analysis for each region (Fig.2), and results show that spider

distributions in these regions are non-random. We classified these M2CND values into three types (Table 1) according to their orders of magnitude. These values show a link with the latitudes of the host regions (Fig.1). In the poles, increase in the latitude will receive a considerably increased amount of solar energy. For example, the latitude of around 86° (region A, B, C and D) receives around 2.5 times more solar energy than that of around 81° (region In1, In2 and F). Thus, we suggest significant differences of average spacings among 3 Types can be partly attributed to Latitude differences.

Generally, regions of the larger spacings have higher elevations (Fig.1) except region E. This is likely because the major host of spiders, SPLD, is located on the southern plateau (Fig.1). Another possibility is that elevation distributions also essentially coincide with geological units.

Table 1. The three types of spider distribution regions

Type	Region	M2CND (m)
Type1	A	195
	B	197
	C	220
	D	273
Type2	E	417
Type3	F	76
	In1	55
	In2	62

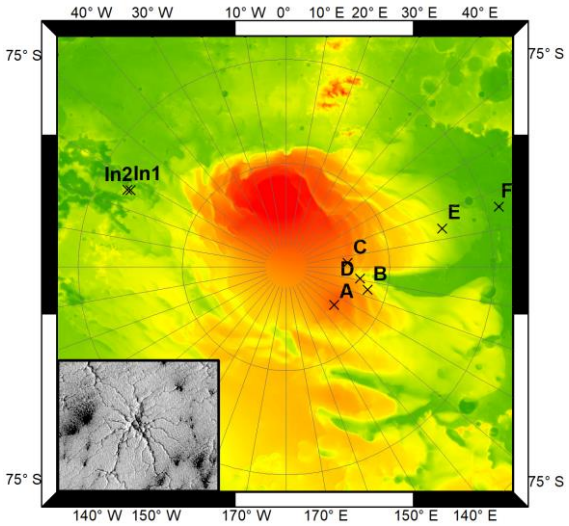

Figure 1. Eight regions which host spiders chosen in this work. They are indicated by black cross shapes. The color ramping map is MOLA DEM with 100m/pix (provided by Sebastian Walter). The inset image HiRISE PSP_003928_0815 shows an example of spider morphologies. The intervals in latitude and longitude are 5º and 10º respectively.

4. Conclusions and future work

The preliminary results we present here indicate spatial formation of spiders is influenced by the regional settings. Non-random spatial distributions in different regions lend more support to our suggestion for spider formation mentioned above [2]. With acquisition of more accurate data in the future, we expect to take other regional parameters (e.g., porosity, degree of cohesion, albedo, thermal inertial, soil water ice content, particle size, local topography) into consideration to perform more comprehensive investigations on influences of regional parameters on spatial settings of spiders.

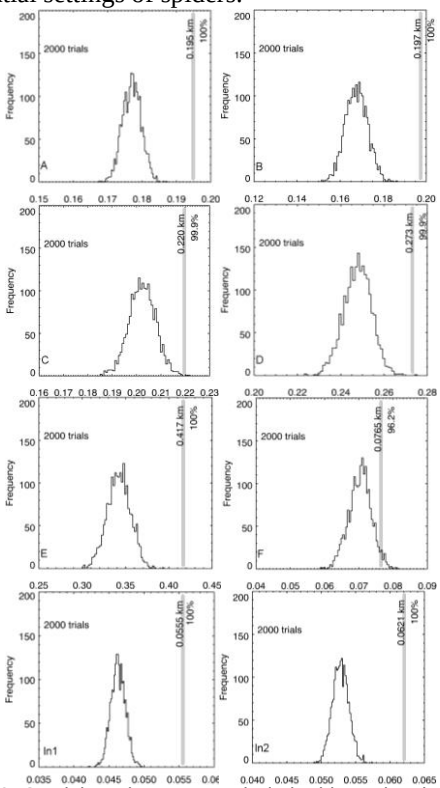

Figure 2. Spatial randomness analysis in this work. Histograms showing M2CNDs for 2000 random configurations relative to the M2CND values (grey bar) of observed spider populations [2][6]. If the measured M2CND is larger than the majority of random configurations, it shows that the spatial distribution is 'more separated than random' or non-random. All of these eight regions exhibit non-random spatial distributions of spiders.

References

[1] Kieffer et al. (2007) Nature 442, 793-796. [2] Hao et al., Icarus, under revision. [3] Piqueux et al. (2003) JGR, 108 (E8), 5084. [4] Hansen et al. (2010) Icarus 205(1), 283-295. [5] Schwamb et al. (2017) Icarus, 308, 148-187. [7] McEwen et al. (2007a) JGR, 112, E05S02. [6] Michael et al. (2012) Icarus 218, 169–177.

EPSC Abstracts
Vol. 12, EPSC2018-1005, 2018
European Planetary Science Congress 2018

Possible slow "wet" mass wasting on Mars

A. Johnsson (1), S.J. Conway, (2), Reiss (3), E. Hauber (4), H. Hiesinger (3). (1) Department of Earth Sciences, University of Gothenburg, Gothenburg, Sweden (andreasj@gvc.gu.se /Fax: +46-31-786 19 86). (2) Laboratoire de Planétologie et Géodynamique, Nantes, France. (3) Institut für Planetologie, Westfälische Wilhelms Universität, Münster, Germany. (4) Institut für Planetenforschung, Deutsches Zentrum für Luft- und Raumfahrt (DLR), Berlin, Germany.

1. Introduction

Small-scale lobes (SSL's) on Mars are landforms that show striking morphologic resemblance to solifluction lobes on Earth [1-3,5]. On Earth solifluction is the net downslope movement of soil driven by phase changes of near-surface water due to repeated freeze-thaw activity [4]. SSL's on Mars consist of an arcuate front (riser) tens to hundreds of meters wide [1] (Fig. 1). Risers are typically decimeters to a few meters (<5m) in height [1]. SLL's often display "overlapping" of individual lobes when they occur as groups.

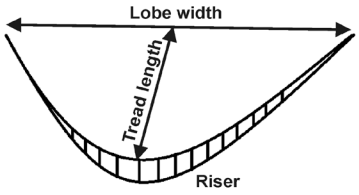

Figure 1. Sketch showing the lobe components. Lobe front points downhill.

Previously SLL's have only been studied in detail in the northern hemisphere on Mars [1,2,5,6] where they have been found to be latitude-dependent landforms [1,2]. In contrast, only a couple of observations have been made in the southern hemisphere [7,8]. Several authors argue for a freeze-thaw hypothesis for SSL formation on Mars [1,2,5-8], although this notion has recently been challenged [9]. If the interpretation of a freeze-thaw origin is correct, the implication is significant since it would require transient H_2O liquids in relatively recent history. Thus a better understanding of SLL's will allow identifying environments that are of value for astrobiological inquiries. Moreover, it may represent a previously underinvestigated process of recent hillslope degradation.

This study aims to determine the distribution of SSL's in the southern hemisphere and to investigate their relationship to other possible periglacial landforms such as patterned ground, polygonal terrain and gullies. Collectively, these landforms may be linked to phase changes of water at the surface or in the shallow subsurface.

2. Data and Methods

We used images obtained by the High Resolution Imaging Science Experiment (HiRISE) that has a spatial resolution of ~25–50 cm/pixel. We catalogued and investigated all available HiRISE images that were acquired between 2007 and 2013 in the latitude band 40°S and 80°S on Mars. A total of 2200 HiRISE images have been studied in detail. For comparison to terrestrial solifluction lobes we used the airborne High Resolution Stereo Camera (HRSC-AX). The benefits of using HRSC-AX are its ability to render detailed DTM's and a similar pixel size (20 cm/pixel) as HiRISE.

3. Observations

SLL's are observed on impact crater walls. SLL's observed in HiRISE (n: 30) show a close spatial association with gullies (77%) and polygonal terrain (47% [Fig. 2]). Moreover some lobes are superposed by striped patterns (Fig. 3). Stripes were also observed separately from SLL but within the same crater environment. On Earth stone stripes and sorted stone stripes are landforms that develop in the active layer, a layer that undergoes seasonal and/or diurnal freezing and thawing. SLL's are often, but not always, associated with slopes covered by latitude-dependent mantle (LDM) [10]. Several SLL locations show evidence of dissected mantle (26%). Moraine-like landforms were observed at ten locations (25%).

4. Summary and conclusions

A type of landform called small-scale lobes has been examined within latitude band 40°S-80°S to understand their origin. Combined with previous studies of the northern hemisphere we have shown that these small-scale lobes are located in two latitude bands in each hemisphere respectively. As such they represent a landform with latitude dependency such as polygonal terrain and gullies. Small-scale lobes occur on topography associated with relatively well-preserved craters in areas underlain by ground ice. Based on their morphology, physical setting, and comparison to Earth analogues and relation to other landforms with ground ice affinity we found that the process likely to cause the landforms are by freeze-thaw action (solifluction) within an active layer. Although we cannot rule out a formation by other processes based on image interpretation alone, there are currently no known terrestrial processes that result in the same morphological characteristics other than solifluction.

SSL's are not as common in the southern hemisphere as in the northern hemisphere even though there is a larger abundance of available hillslopes. This may be due to different surface properties that inhibit solifluction. Further work is needed to fully explain the hemispherical asymmetrical distribution of these lobes.

[11] investigates a recently emerged new potential analog landform in the Atacama Desert. Please see abstract EPSC2018-339 (this conference) for further details.

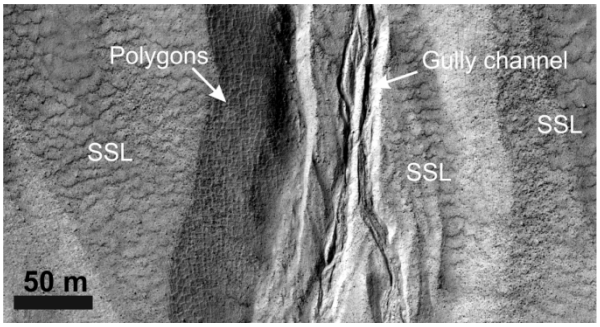

Figure 2. SLL, polygons and gullies in Ruhea crater (43.26°S/173.08°E). Fresh appearing gully channels with polygonal patterns on the gully walls. SLL dominate the scene covering the adjacent walls with overlapping lobes. The stratigraphy suggests close temporal relationship.

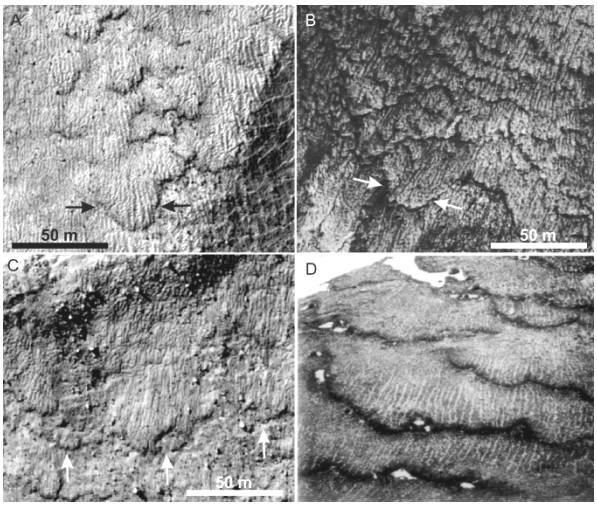

Figure 3. Examples of martian SSL and solifluction lobes on Earth. A) SSL in Ruhea crater, Mars. Overlapping lobes superposed by striped pattern. Note the polygonal terrain in lower right corner. B) Solifluction lobes superposed by stone stripes in Adventdalen, Svalbard. C) SSL in unnamed crater, Mars (45.42°S/25.74°E). Stripes are seen on the lobes. D) Solifluction lobes in New Zealand superposed by sorted stone stripes. Lobe front ~25 cm high.

Acknowledgements

This project has been supported by the Swedish national Space Board.

References

[1] Johnsson et al. (2012) Icarus 21, 489–505. [2] Gallagher et al. (2011) Icarus 211, 458–471. [3] Johnsson et al. 2018. In: Dynamic Mars, Elsevier, ISBN: 9780128130186. [4] Matsuoka (2001) Earth-Sci. Rev. 55, 107–134. [5] Gallagher and Balme (2011) GSL 356, 87–111. [6] Nyström and Johnsson (2014) EPSC, #EPSC2014-480. [7] Mangold (2005) Icarus 174, 336-359. [8] Soare et al. (2016). Icarus 264, 184-197. [9] Dundas and Mellon (2018) LPSC #2018. [10] Kreslavsky et al. (2008). PSS 56. [11] Gastineau et al. (2018). EPSC, #EPSC2018-339.

EPSC Abstracts
Vol. 12, EPSC2018-1009-1, 2018
European Planetary Science Congress 2018

Geodynamic Evolution of Wrinkle Ridges and Rate of Crustal Shortening on Lunae Planum, Mars

O. Karagöz (1), M. E. Aksoy (2), G. Erkeling (3).

(1) Institute of Earth and Environmental Sciences - Geology, Albert-Ludwigs-University Freiburg, Albertstrasse 23B, 79104 Freiburg, Germany (oguzcan.karagoz@mars.uni-freiburg.de),
(2) Mugla Sıtkı Kocman University, Geological Engineering, Turkey,
(3) Institut für Planetologie, WestfälischeWilhelms Universität Münster, Germany.

Abstract

Preliminary results of the crustal shortening analyses and geochronological stratigraphy of the Lunae Planum are presented. They indicate a wrinkle ridges refer an age distribution from ~3.7 Ga to ~3.0 Ga, with surfaces getting younger towards the East. Our observations are in accordance with earlier observations of greater shortening amounts towards the West (in older ridges) and the age distribution of wrinkle ridges suggests a 700 Ma time interval for the proposed ~1110 m horizontal shortening at a deformation rate of $1.59E^{+02}$ cm/Ma for compressional deformation on the Lunae Planum.

1. Introduction

The Lunae Planum is a unique plain extending up to Acidalia Planitia, which contains the basalt lava flows formed by the Tharsis volcanism. The topography of this area descends from west to east, from 800 m to -750 m.

Wrinkle ridges are probably one of the most common, but least understood, types of planetary structures on terrestrial planets. These structures indicate the surface deformation of the Martian crust formed by folding and thrust faulting [1]. Despite the interpretation of the morphology, deformations and geodynamic importance of many wrinkled ridges, different conceptual, kinematic and mechanical models applied in previous studies [2]. However, the age relation and formation processes of these structures in the Lunae Planum region are still not clear.

The purpose of this study is to understand main mechanism of the wrinkle ridges, chronological order of geomorphological structures and determine the timing and duration of the crustal shortening of Lunae Planum.

2. Methods

The Lunae Planum (15°N 67.5°W) covers a basin of 900 square kilometers, lies north of the Valles Marineris, a well-known rifting system on Mars. The unique coverage of high-resolution image data, especially HRSC (12.5 m / pixel), CTX (6 m / pixel) and HiRISE (0.3 m / pixel), allows the detailed mapping and analysis of wrinkle ridge structures. The high-resolution digital elevation model was processed by using ISIS3 (The Integrated System for Imagers and Spectrometers) and AMES Pipeline to get the exhaustive profiles along to wrinkle ridges for further mapping in ArcGIS. The crater size-frequency distribution (CSFD) and buffer crater counting (BCC) method were preferred to the obtained absolute age of the wrinkle ridges and geomorphological structures on the Lunae Planum.

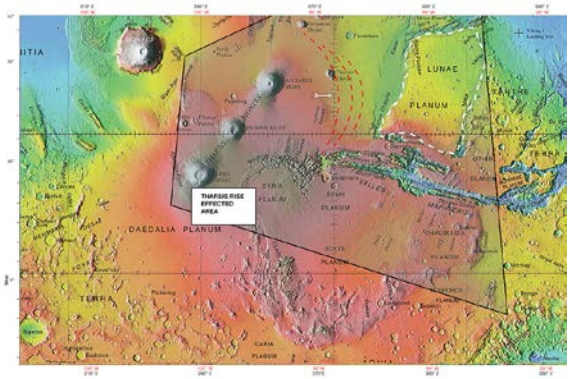

Figure 1: Geographic map of the Tharsis Rise with research area Lunae Planum basin.

3. Results and Discussion

The formation of wrinkles ridges is widely discussed and different tectonic mechanisms are suggested to explain their origin. Our analysis is based on determining the amount of total shortening and calculating an absolute age for wrinkle ridges by

using crater-size frequency distribution and buffer crater counting methods. Age determination analysis were indicated that the BCC method according to the asymmetric structures of wrinkle ridges represented absolute age with higher accuracy. Thus, wrinkle ridges cumulated in three groups according to age and geodynamic periods, these structures were classified and dated using the buffer crater counting (BCC) method [3].

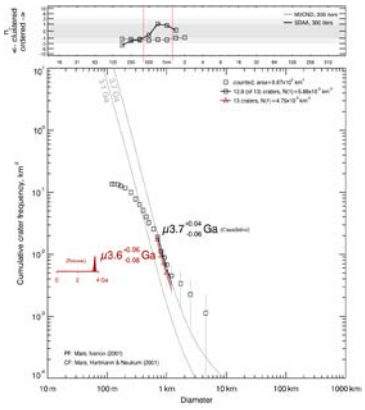

Figure 2: The highest absolute age of wrinkle ridges derived from buffer crater counting method.

BCC measurements of wrinkle ridges refer an age distribution from ~3.7 Ga to ~3.0 Ga, with surfaces getting younger towards the East (Fig 2). Respectively, wrinkle ridges formed between ~3.6 Ga to ~3.3 Ga years in the west, ~3.3 Ga to ~3.2 Ga in the middle and ~3.2 Ga to ~3.0 Ga in the east group. More than 50 wrinkle ridges were examined in detail for obtaining the elevation offset, width and total relief (Fig 4). [5].

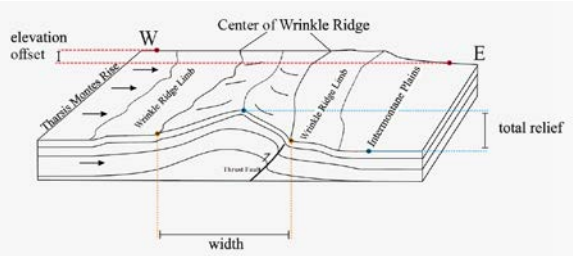

Figure 2: Schematic reconstruction of the wrinkle ridge parameters for calculating shortening by faulting and folding.

The width corresponds to the distance of the two lowest points across the wrinkle ridge, where the slope angles reach minimum; the limit between wrinkle ridge limb and intermontane plain (Fig. 3). The total relief is measured by taking the difference between the elevation of the lowest flat and the highest point of the ridge. The elevation difference between the two plains across the ridge corresponds to the elevation offset value (Fig. 3). The age distribution of wrinkle ridges suggests a 600 Ma time interval for the proposed ~1110 m horizontal shortening at a deformation rate of $1.59E^{+02}$ cm/Ma for compressional deformation on the Lunae Planum.

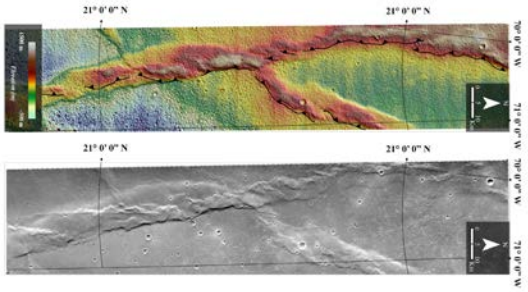

Figure 4: Schematic reconstruction of the wrinkle ridge parameters for calculating shortening by faulting and folding.

Acknowledgements

Special thanks to Ralf Jaumann, Katrin Stephan and Solmaz Adelli for helpful comments to improve this research.

References

[1] Watters, T.R., 2004, Elastic dislocation modeling of wrinkle ridges on Mars, Icarus, 171, 284-294.[2] Golombek, M. P., Anderson, F. S., & Zuber, M. T. (2001). Martian wrinkle ridge topography: Evidence for subsurface faults from MOLA. Journal of Geophysical Research: Planets, 106(E10), 23811-23821. [3] Kneissl, T., & Michael, G. (2013, March). Crater Size-Frequency Measurements on Linear Features Buffered Crater Counting in ArcGIS. In Lunar and Planetary Science Conference (Vol. 44, p. 1079).[4] Plescia, J.B., 1991.Wrinkle ridges in Lunae Planum, Mars: implications for shortening and strain. Geophys.Res. Lett. 18, 913–916.

EPSC Abstracts
Vol. 12, EPSC2018-1019-1, 2018
European Planetary Science Congress 2018

An Investigation of Araneiform Terrain in Angustus Labyrinthus, Mars.

J. Hao (1), G.G. Michael (1), S. Adeli (2), R. Jaumann (1,2).
(1) Planetary Sciences and Remote Sensing, Institute of Geological Sciences, Freie Universität Berlin, Malteserstrasse 74, 12249 Berlin, Germany (**J.Hao@fu-berlin.de**)
(2) Institute of Planetary Research, German Aerospace Centre (DLR), Rutherfordstrasse 2, 12489 Berlin, Germany

1. Introduction

Seasonal condensations and sublimations of CO_2 in the south pole not only drive energy exchange between the pole and atmosphere, but also have created a host of enigmatic phenomena exhibiting intriguing patterns. Araneiform terrain is one striking example (informally called "spider") which is observed exclusively in the southern polar area and characterized by radially organized troughs usually with central depressions [1-3] (Fig.1). Their formation is suggested to involve with gas jetting activities invoked by basal sublimation of translucent CO_2 ice slabs [1-3]. However, its detailed formation mechanism as well as thorough schematic of erosion process is still incompletely understood. The objective of this work is to address these issues.

Angustus Labyrinthus (81ºS, 296ºE, dubbed "Inca City") hosts a considerable number of spiders [2] and has been repeatedly covered by the High Resolution Imaging Science Experiment (HiRISE) with image scale as high as 0.25 m/pix [4]. Thus, it offers a prime site for us to conduct an in-depth study.

2. Results

In this work, we (1) reported two new spider species (elongated half and spiders) based on the detailed geomorphological investigation; (2) proposed a new formation mechanism for spiders, indicating the existence of an inhibited zone around a newly formed spider which is consistent with the non-random distribution characteristics confirmed by the spatial randomness analysis; (3) explained effects of local topography (e.g., ridges) and pre-existing linear depressions in the formation process of half and elongated spiders.

We mapped spatial disruption of spiders in the Inca City region based on HiRISE images (Fig.1a). Two newly-reported spider types (half and elongated spiders) are identified.

Elongated spiders: Located in one region with current available observations and characterized by short sinuous troughs emanating from straight linear depressions (Fig.1c).

Half spiders: Located along ridge boundaries with one-half observable (Fig.1d).

Through spatial randomness analysis (Fig.2, details of this method see [5]) of one spider population (Fig.2a), we can see the spatial distribution of spiders is non-random or more separated than random (Fig.2b).

3. Discussions and conclusions

In this work, we suggest that seasonal CO_2 ice slab layer remains in contact with the substrate during basal sublimation thus the gas is trapped inside the substrate (Fig.3a), in contrast with general understanding that the sublimating gas is trapped between the substrate and the CO_2 ice slab layer [1-3]. Then released gas disperses into the porous substrate, building pressure. The ice layer cracks at certain threshold pressure leading to gas-jetting and consequent erosion (for more detail see Fig.3 and 4). Therefore, substrate porosity and degree of cohesion are crucial parameters for spider formation.

When the extremities approach those of a neighboring spider, pressure accumulation becomes shared, weakening the carving force, and thus causing the spider growth to slow down. We expect that in the vicinity of one spider, the dispersed pressure should inhibit the initiation of a new spider. In other words, an inhibited zone exists in which another spider is less likely to occur.

The spatial randomness analysis in our sample population (Fig.2a) confirmed that spatial distribution of spiders is non-random and yields a value which is 55 m. We suggest it indicates the minimal size of the inhibited zone in this spider population. We expect this value is closely associated

with the substrate porosity and varies from region to region.

The linear depressions in the elongated spider distribution region are likely pre-existing features produced by different geological processes and offer a ready-made path for gas migration towards a vent. Some linear depressions with sparse troughs could express an early stage of elongated spider formation (Fig.1c). For half spiders, more consolidated material with lower porosity on the slope area than the flat region results in a faster pressure-rising which leads to gas flows towards the neighboring flat region. This may enhance the initiation of jetting near the boundary. The sun-facing slopes may reinforce this trend for receiving more solar insolation. In addition, the more consolidated material of slope area also likely prevents the growth of spider "legs" up the slopes.

Our case study in the Inca City region provides new understanding in the formation process of basal sublimation-driven features and thus offers new insights into polar surface processes.

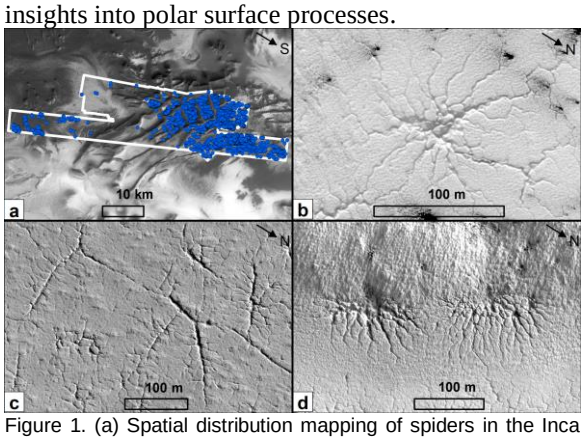

Figure 1. (a) Spatial distribution mapping of spiders in the Inca City region. White polygon indicates the HiRISE coverage; blue points indicate the locations of spiders. (b) An example of spiders. (c) Elongated spiders. (d) Half spiders.

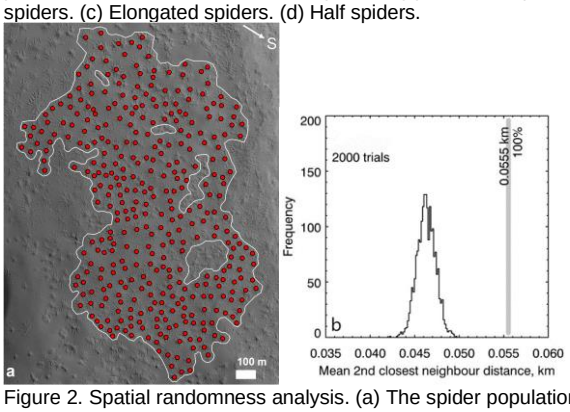

Figure 2. Spatial randomness analysis. (a) The spider population chosen for this analysis. The white polygon delineates the extent of mapped area. Red points show positions of spider centers. (b) Histogram showing the mean 2nd-closest neighbor distances (M2CNDs) for 2000 random configurations relative to the M2CND value (grey bar) of observed spider population (details see [5]).

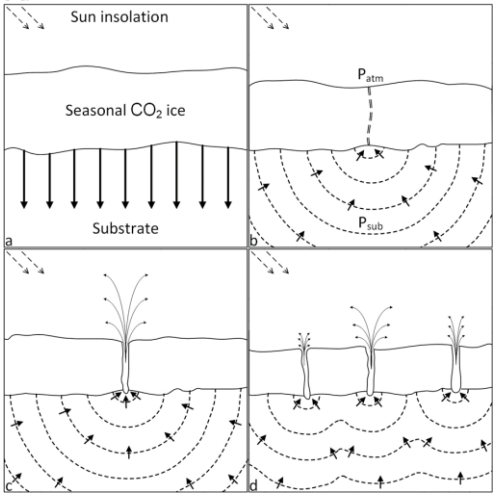

Figure 3. (a, b) In the spring, with sunlight penetrates to the substrate, basal sublimation occurs. The sublimating gas disperses into the porous substrate and migrates towards the rupture along the pressure gradient. (c) The pressure gradient leads to gas eruption at certain value, which results in rapid escape of gas entraining sand and dust, forming cavities or holes. (d) Beyond a certain range, the rate of lateral flow becomes lower than the local rate of accumulation from basal sublimation. A new rupture occurs. Below this range, the lateral flows act to inhibit accumulation of sufficient pressure to cause a rupture.

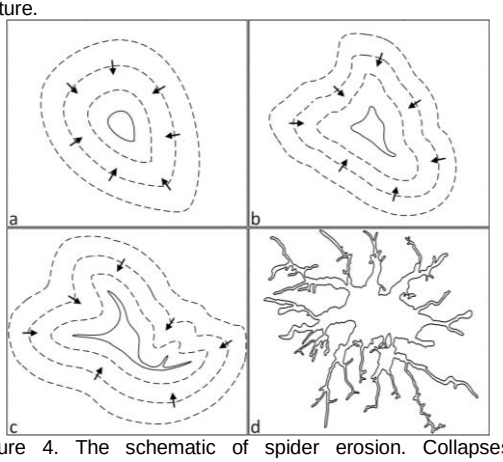

Figure 4. The schematic of spider erosion. Collapses at substrate-atmosphere boundary may initiate irregular prominence in pit. Pressure gradient diverts gas flow preferentially towards any prominences of a pit, enhancing irregularity, and leading to growth of troughs. (d) shows a mapping of a real spider in our study area.

References

[1] Kieffer et al. (2007) Nature 442, 793-796. [2] Piqueux et al. (2003) JGR, 108 (E8), 5084. [3] Hansen et al. (2010) Icarus 205(1), 283-295. [4] McEwen et al. (2007a) JGR, 112, E05S02. [5] Michael et al. (2012) Icarus 218, 169–177.

EPSC Abstracts
Vol. 12, EPSC2018-1025, 2018
European Planetary Science Congress 2018

Hyperspectral characterisation of the Martian south polar residual cap using CRISM

Jacqueline D. Campbell, Panagiotis Sidiropoulos and J-P. Muller.

Imaging Group, Mullard Space Science Laboratory, University College London, Holmbury St Mary, Surrey, RH5 6NT, UK, Jacqueline.campbell.16@ucl.ac.uk

Abstract

We present our research on hyperspectral characterization of the Martian South Polar Residual Cap (SPRC), with a focus on the search for organic signatures within the dust content of the ice. The SPRC exhibits unique CO_2 ice sublimation features known colloquially as 'Swiss Cheese Terrain' (SCT). These flat floored, circular depressions are highly dynamic, and may expose dust particles previously trapped within the ice in the depression walls and partially on the floors. Here we identify suitable regions for potential dust exposure on the SPRC, and utilise data from the Compact Reconnaissance Imaging Spectrometer for Mars (CRISM) on board NASA's Mars Reconnaissance Orbiter (MRO) satellite to examine infrared spectra of dark regions to establish their mineral composition, to eliminate the effects of ices on sub-pixel dusty features, and to assess whether there might be signatures indicative of Polycyclic Aromatic Hydrocarbons (PAHs). Spectral mapping has identified compositional differences between depression rims and the majority of the SPRC and CRISM spectra have been corrected to minimise the influence of CO_2 and H_2O ice. Laboratory experiments have generated new spectra for PAHs relevant to Mars, and their detectability limits within the SPRC. Whilst no conclusive evidence for PAHs has been found, depression rims are shown to have a higher water content than regions of featureless ice, and there are indications of magnesium carbonate within the dark, dusty regions.

1. Introduction

While Mars was initially not thought to have been a planet with a dynamic surface, repeat observations starting with the Mariner missions of the 1960s [1] have indicated otherwise. In particular, the polar caps exhibit significant change over time. On board MRO is an imaging spectrometer, CRISM [2] attaining spatial resolutions of ~20m and spectral resolutions of 6nm, which can analyse compositional properties of the Martian surface. Mars' south polar cap consists of a permanent 400km diameter layer of solid CO_2, 8m thick, overlaying water ice [3].

Swiss Cheese Terrain (SCT) is an unique surface feature found only in the SPRC. Its characteristic appearance (shown in Figure 1) is thought to be caused by seasonal differences in the sublimation rates of water and CO_2 ice [4]; scarp retreat through sublimation may expose dust particles previously trapped in the SPRC which can then be analysed using CRISM.

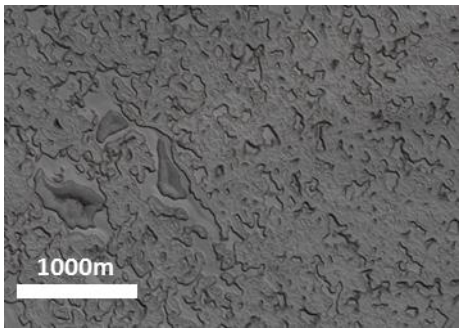

Figure 1: SCT sublimation features (CTX: B08_012572_0943_XI)

1.1 Polycyclic Aromatic Hydrocarbons

PAHs are a group of chemical compounds consisting of benzene rings of hydrogen and carbon [5] and are considered to be important in theories of abiogenesis; the search for organic molecules on Mars is important in ascertaining Mars' past conditions, and current habitability [6].

PAHs are abundant throughout the universe, and have been found to coalesce in space within dust clouds, [7] and have been detected on two of Saturn's icy moons, Iapetus and Phoebe and comet 67P [8][9]. The delivery of complex organic compounds to established, habitable planets via bolide impact is a very important concept in astrobiology. The ability to identify PAHs

could prove a critical tool in the search for putative locations for extra-terrestrial organisms.

To date, the hypothesised connection of Martian Swiss Cheese Terrain and the presence of PAHs has not been systematically examined.

2. Methods

Initially, only Full Targeted Resolution (FRT) CRISM products have been considered for study to try to maximise spatial resolution (~20m/pixel) of small-scale SCT features. The CRISM Analysis Tool (CAT) plugin for ENVI software was used to process the CRISM scenes with corrections for photometry, atmosphere, image artefacts, 'despiking' and 'destriping', and to generate summary products. Forty-four (44) spectral summary products based on multispectral parameters are derived from reflectances for each CRISM observation that can be used as a targeting tool to identify areas of mineralogical interest for further analysis [10]. Region of Interest (ROI) band thresholds were used to identify the strongest 10% of CO_2 and H_2O ice signatures from each scene (Figure 2, left), and then ROIs of a minimum of 25 pixels chosen from the same across-track region of the scene as the dark-rim features to provide local 'pure' ice spectra. These samples were then used to carry out correction to remove the overwhelming effects of ice spectral signals on dust rim spectra. Pelkey's summary products [9] were utilized to create RGB composite images of regions of interest to identify spectral differences around dust rims (figure 2, right). Spectra for specific rim features with strong carbonate overtone responses, corrected for ices, were then analysed and compared to laboratory spectra for Martian mineralogy and PAH signatures.

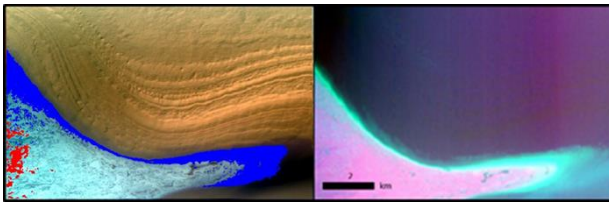

Figure 2: : Left: 'True colour' visualisation of Site 1 from CRISM bands R = 230 G = 75 B = 10. Strongest 10% spectral responses for ices shown in red (CO2) and blue (H2O). Right: False colour visualisation of Site 1 using Pelkey (2007) summary products R = 1435 (CO2 ice) G = 1500 (H2O ice) B = BDCARB (carbonate overtones)

In addition, the Europlanets Transnational Access Award was used in order to carry out a series of laboratory experiments to generate a diagnostic spectrum for PAHs of astrobiological interest in the context of Mars, to constrain the detectability limit of PAHs in CO_2 ice, and to establish PAH spectral features at wavelengths other than the absorption feature at 3.29 μm, where they might be easier to discern within the CO_2 ice spectrum.

3. Conclusions

There are clear spectral differences between dust rims and non-rim regions, with possible indications of carbonate components within SCT dust rims. CO_2 ice signatures are a limiting factor in identifying PAHs as the removal of CO_2 ice spectrum may also destroy subtle features in the 3.3μm region of CRISM spectra. New features for PAHs at lower wavelengths have been established through laboratory experiments, as well as their detectability limit in SPRC conditions using the CRISM instrument's parameters. These will be applied in future to search for PAHs.

Acknowledgements

Part of the research leading to these results has received partial funding from the European Union's Seventh Framework Programme (FP7/2007-2013) under iMars grant agreement n˚ 607379; MSSL STFC Consolidated grant no. ST/K000977/1 and the first author is supported by STFC under PhD studentship no. 526933.

Europlanet 2020 RI has received funding from the European Union's Horizon 2020 research and innovation programme under grant agreement No 654208.

References

[1]NASA(2015) http://science.nasa.gov/missions/marinermissions
[2] Murchie et al. (2007) JGR, doi:10.1029/2006JE002682
[3] Vita-Finzi, C. (2005) Planetary Geology, 146-159.
[4] Tokar et al., (2003) GRL, 30, 1677, 13.
[5] Carey, F.A. Organic Chemistry, 398-423 [7] Vita-Finzi, C. (2005) Planetary Geology, 146-159.
[6] Benner, S.A. et al. (1998) PNAS, 96,6,2425-2430
[7] Allamandola, L.J. (2011) EAS, 46,305-317
[8] Cruikshank. D.P. et al. (2008) Icarus, 193, 334-343
[9] Davidsson, B.J.R et al., (2016). A&A. vol. 592, p. A63
[10]Pelkey, S.M.et al. (2007) JGR, doi:10.1029/2006JE002831

EPSC Abstracts
Vol. 12, EPSC2018-1119, 2018
European Planetary Science Congress 2018

The study of the influence of the composition and structure of Martian surface on detection the spectral features of atmospheric trace gases in IR spectra of Mars

Maria I. Błęcka
Space Research Centre PAS , Bartycka 18a, Warsaw, Poland mib@cbk.waw.pl

Abstract

The presented work is connected with the measurements of the stereoscopic camera CASSiS (The Colour and Stereo Surface Imaging System) a part of payload of *ExoMars Trace Gas Orbiter* (TGO) of the ESA mission in which researchers from SRC – PAS are engaged. The Cassis camera give the opportunity of analysis the structure of the possible sources of trace gases on the surface of Mars. Identification of minor species in the atmosphere are performed from orbiter by spectrometric instruments (e.g. NOMAD, ACS).
There are various types of features on Martian surface that could be associated with trace gases release e.g methane . The good examples are: volcanos in Utopia, Gusev Crater, Arabia Terra and Valles Marineris . In various locations the processes making possible emission of methane were probably created in different ways among others the production from serpentinized rocks.

In general the way of production of trace gases depends on the structure and composition of the soil and on physical state of the atmosphere.

In the paper the common influence of optical spectral features of the surface and atmosphere contains trace gases on radiance spectra were analyzed. The elaborated model provides estimates of the spectral reflectance/emittance and total radiance from Martian surface and atmosphere in the Mid-infrared spectral range. The examples of diverse shapes of the surface with various subtle structures of the soils were selected from the pictures done by HIRISE instrument . These various kinds of surfaces were spectrally described by presumable reflectance or emissivity of minerals and rocs (e.g. the serpentinized rocks) appropriate for selected locations. Spectral reflectance or emissivity of the modelled regions were calculated from *n,k* with Mie and Hapke theories or measured. The physical properties of the atmosphere were characterized by its thermodynamical parameters and absorbing or scattering properties.

The performed analysis of Mid-infrared spectral signatures of the surface and the atmospheric trace gases in various physical conditions on total radiance is shown. The conclusions related visibility of spectral features of trace gases (methane) in radiance spectra are discussed.

References

[1] Formisano, V., Atreya, S., Encrenaz, T., Ignatiev, N.,Giuranna, M. Detection of Methane in the Atmosphere of Mars. Science, Vol. 306, pp. 1758-1761, 2004

[2] Oehler,D.Z. and Etiope G, Methane Seepage on Mars:Where to Look and Why, ASTROBIOLOGY, Vol.17, Number xx, 2017; DOI: 10.1089/ast.2017.1657

[3] Stevens, A. H., Patel M. R., Lewis, S., R., Numerical modelling of the transport of trace gases including methan in the subsurface of Mars, Icarus 250 (2015) 587–594

[4] Sizemore,H,G.,Mellon, M.T. Laboratory characterization of the structural properties controlling dynamical gas transport in Mars-analog soils, Icarus 197 (2008) 606–620

[5] Ehlmann, B.L. , Mustard J.F. and S. L. Murchie Geologic setting of serpentine deposits on Mars GEOPHYSICAL RESEARCH LETTERS, VOL. 37, L06201, doi:10.1029/2010GL042596, 2010

EPSC Abstracts
Vol. 12, EPSC2018-1130, 2018
European Planetary Science Congress 2018

Rootless cones as a consequence of Martian volcanism- numerical kinetic simulation.

Natalia Zalewska (1,2), Jan Kotlarz (1)
(1) The Institute of Aviation, Warsaw, Poland (2) Space Research Center PAS, Poland (natalia.zalewska@ilot.edu.pl).

Cones on Acidalia in the image THEMIS V55617012, (Figure 1,2) which are arranged parallel to the lava tongue and its are probably rootless cones. Lava had to flow on the area covered with ice or saturated with water (Figure 3). These cones on Acidalia are much smaller (50 m at the base) than for exmple on Amazonis (300-500 m at the base). We have created a numerical simulation showing the formation process of such cones. [1]

The simulation of magma-water ice interaction was performed using the EMMA Particle-In-Cell code. Particle-In-Cell (PIC) [2] is a technique commonly used to simulate motion of charged particles, or plasma. In our problem we applied mass density and the pressure of matter. We assumed that the analysis of electric charges of magma, ice, water or the atmosphere is not necessary. In other words we assumed that 100% of particles in our model are neutral particles. Characteristics of the model: dimensions: 2,000 m x 2,000 m x 1,000 m, cell size: 10 m x 10 m x 10 m, time step 10 s. The following molecules were introduced representing the mater: magma, water ice, atmosphere (CO2). We assumed following characteristics of particular molecules in the model: magma density: 2800 kg / m³ (comatite), initial magma temperature: 1700 K, initial magma layer thickness: 50 m, initial horizontal magma velocity: 50 km / h, the possibility of magma particle phase transition: true, initial temperature of water ice particle: 210 K, the possibility of water ice phase transition: true, we assumed that atmosphere particles are simply CO2 particles and the possibility of CO2 particle phase transition is false. We assumed in our PIC model that in each iteration a thermodynamic equilibrium will be achieved in a single cell of the model. In addition, phase transformations of magma and water ice have been implemented in the model and they were applied after each iteration. There are three forces operating on model cell nodes: general gravity of Mars with additional assumption of additional force and velocities compensating for the effect of gravity at reaching the minimum height of changes (position of the component r = 0.000), atmospheric pressure 636 Pa, pressure force dependent on the densities of the matter and general gravity force size and direction.

The Particle-In-Cell method consists of an initial setup, the main loop, and a final clean up / results output. All computation happens in the loop. The loop consists of the following steps:

1. Compute matter density: particle positions are scattered to the grid,
2. Compute gravity potential: performed by solving the equilibrium equations,
3. Compute gravity and pressure fields: from the gradient of potential,
4. Move particles: update velocity and position from Newton's second law.
5. Generate particles: sample sources to add new particles
6. Output: optional, save information on the state of simulation
7. Repeat: loop iterates until maximum number of time steps is achieved or until simulation reaches steady state. (Figure 4)

The outbreaks of pseudo-craters created on Mars 5 to 10 times larger cones than on Earth. 4 to 16 times less gas is required for each explosion to create craters despite their larger size. This is consistent with the view that propably water was less available in the Martian regolith than in Iceland. [3]

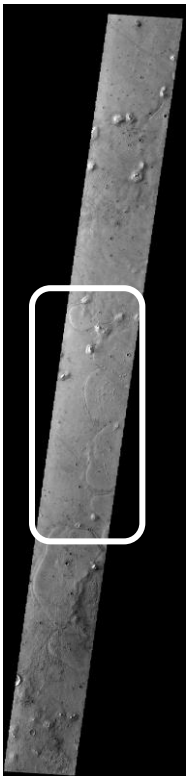

Figure 1: Acidalia Planitia. Rootless cones on lava tongue. THEMIS V55617012. Center Latitude 38.257454°, Center Longitude 319.3534°

Figure 2. Rootless cones on lava tongue. Acidalia Planitia. THEMIS V55617012. White arrows indicate the direction of lava flow. Selected fragment from Figure 1.

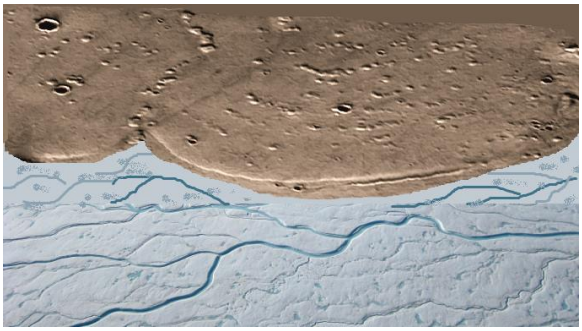

Fig.3 Acidalia Planitia. The process of creating rootless cones. Visualization of lava (V55617012) entering on the ice surface.

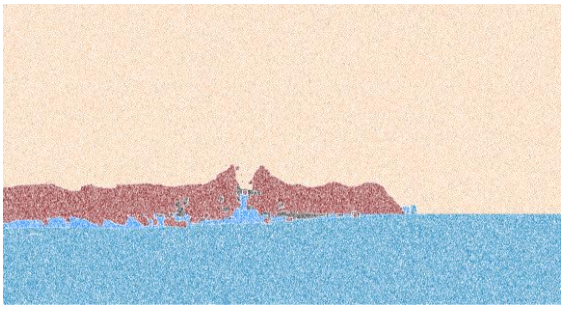

Figure 4. Modeling of the process of creating rootless cones. The simulation was prepared using a Particle-In-Cell code.

References

[1] Zalewska N. Global Martian volcanism as a new interpretation of geological past of terrestrial bodies and moons in the Solar System, EPSC Abstracts, Vol. 11, EPSC2017-372, 2017

[2] Konior, W. Particle-in-Cell electrostatic numerical algorithm. Prace Instytutu Lotnictwa, Vol. 3(248), pp. 24-45, 2017

[3] Ronald Greeley and Sarah A. Fagents Icelandic pseudocraters as analogs to some volcanic cones on Mars, Journal Of Geophysical Research, Vol. 106, pp. 20,527-20,546, 2001

EPSC Abstracts
Vol. 12, EPSC2018-1153-1, 2018
European Planetary Science Congress 2018

Methane transport in the subsurface of Mars

Elodie Gloesener (1,2), Özgür Karatekin (2) and Véronique Dehant (1,2)
(1) Université catholique de Louvain, Louvain-la-Neuve, Belgium, (2) Royal Observatory of Belgium, Brussels, Belgium
(elodie.gloesener@observatory.be)

Abstract

The detection and characterization of trace gases such as methane is among the main objectives of ExoMars Trace Gas Orbiter (TGO). The interpretation of the TGO measurements and the study of methane outgassing scenarios require an understanding of gas transport in the martian subsurface. Here, we model the CH_4 transport through the porous martian regolith using the dusty gas model (DGM) [1] for the binary CH_4-CO_2 mixture. The effects of different parameters on the transport are also investigated.

1. Introduction

The multiple detections of CH_4 in the martian atmosphere have raised numerous questions about its potential sources. It has been suggested that methane on Mars could have a biological origin and be generated by organisms living in the subsurface where conditions are more hospitable [2]. Methane could also be produced through several abiologic processes, including Fischer-Tropsch Type (FTT) reactions where H_2 reacts with CO_2 in the presence of a metal catalyst [3]. The H_2 necessary for the FTT reactions can be produced by several processes and notably by serpentinization [4]. Many of the proposed generation mechanisms for CH_4 would take place hundreds of metres to several kilometres deep in the crust of Mars, while subsurface reservoirs such as clathrate hydrates [5] could release methane from shallower depths. Once produced, CH_4 has to be transported from its source through the martian subsurface.

Gas transport through porous media can be divided in different mechanisms [1]:

- Free molecule or Knudsen flow occurs when the pore radius is less than one tenth of the gas mean free path, and molecule-wall collisions dominate.
- Viscous or advective flow, in which the gas acts as a continuum fluid under the influence of a pressure gradient. In this mode, molecule-molecule collisions dominate.
- Continuum or molecular diffusion refers to the relative motion of the different gas species under the influence of concentration gradients, temperature gradients or external forces. In this regime, the pore radius is larger than 10x the gas mean free path and collisions between gas molecules dominate.
- Surface flow or diffusion in which molecules move along a solid surface in an adsorbed layer.

Methane transport through the porous martian regolith has been modelled using the DGM [1] for the binary CH_4-CO_2 mixture and neglecting thermal transpiration, baro-diffusion and surface diffusion.

2. The model

The dusty gas model is based on the full Chapman Enskog kinetic theory of gases. In this model, the porous medium is considered as one component of the mixture and is treated as a collection of giant spherical molecules (dust particles) kept in space by external force. The total flux of a gas mixture is represented as the sum of the diffusive flux (molecular and Knudsen diffusion) and the viscous flux. The flux equation of a binary gas mixture may be written as:

$$\frac{N_1}{D_{1K}} + \frac{y_2 N_1 - y_1 N_2}{D_{12}} = - c_T \frac{dy_1}{dz} - y_1 \frac{dc_T}{dz}\left(1 + \frac{B_0 P}{\mu D_{1K}}\right) \quad (1)$$

where subscripts 1 and 2 refer to components 1 and 2 of the gas mixture repectively, N is the total molar flux, D_{1K} is the effective Knudsen diffusion coefficient of component 1, y is the mole fraction, D_{12} is

the effective molecular diffusion coefficient of the binary mixture, c_T is the total molar concentration, B_0 is the permeability, P is the pressure and μ is the gas mixture viscosity.

3. Preliminary results

In a first time, methane transport was studied taking into account only the diffusion process and different parameters were varied to investigate their effect on the CH_4 transport. Results showed that the flux is strongly dependent on the pressure gradient. On the other hand, it is less sensitive to temperature changes even if it increases slightly during warmer seasons. Similarly to what was found by [6], diffusion is not an efficient process to generate short-lived methane plume from deep sources. Indeed, when diffusion is the only transport mechanism considered, the methane source has to be located at very shallow depth (on the order of few meters) to observe temporal variations in surface flux. Even though near-surface metastable reservoirs could provide long-term release of atmospheric methane, it is very likely that CH_4 is produced at depth in the martian crust. Methane generated at depth should move preferably via advection following pathways along faults and fractures [3]. Results regarding this last process and their implications will be presented.

Finally, it is important to note that methane outgassing scenarios are strongly dependent on the subsurface environment and new constrains could be provided by current and future missions such as InSight and ExoMars.

Acknowledgements

This work was financially supported by the Belgian Science Policy Office (BELSPO) through the BRAIN-be SCOOP project and the ESA/PRODEX Program. This research was performed as part of the "Excellence of Science" project "Evolution and Tracers of Habitability on Mars and the Earth" (FNRS 30442502).

References

[1] Mason, E. A. and Malinauskas, A. P.: Gas transport in porous media: the dusty-gas model, Elsevier Science Ltd, 1983.

[2] Atreya, S. K., Mahaffy, P. R., and Wong, A.-S.: Methane and related trace species on Mars: Origin, loss, implications for life, and habitability, Planetary and Space Science, Vol. 55(3), pp. 358-369, 2007.

[3] Oehler, D. Z. and Etiope, G.: Methane seepage on Mars: where to look and why, Astrobiology, Vol. 17(12), pp. 1233-1264, 2017.

[4] Oze, C. and Sharma, M.: Have olivine, will gas: Serpentinization and the abiogenic production of methane on Mars, Geophysical Research Letters, Vol. 32(10), 2005.

[5] Chastain, B. K. and Chevrier, V.: Methane clathrate hydrates as a potential source for martian atmospheric methane, Planetary and Space Science, Vol. 55(10), pp. 1246-1256, 2007.

[6] Stevens, A. H., Patel, M. R., and Lewis, S. R.: Modelled isotopic fractionation and transient diffusive release of methane from potential subsurface sources on Mars, Icarus, Vol. 281, pp. 240-247, 2017.

EPSC Abstracts
Vol. 12, EPSC2018-1158, 2018
European Planetary Science Congress 2018

Constraining the soil-moisture interaction at Gale Crater of Mars

Priyabrata Das (1), Amit Basu Sarbadhikari (1), Jayanta Ghosh (1), Subham Sarkar (2)
(1) Physical Research Laboratory, Ahmedabad, India, (2) Space Application Centre (ISRO), Ahmedabad, India
(das.priyabrata@outlook.in)

Abstract

This study explores the effect of surface hydration at the present-day aeolian sediment system of Gale crater, Mars. Careful sedimentological investigations of the soil surface reveal that trapping and binding of sediment grains, aided by hydrous activity, is still an active mechanism at the surface-atmosphere boundary layer of the red planet. Moreover, the estimated relative humidity of the surface suggests that the hydrous activity is predominantly diurnal in nature, rather being seasonal. The hydration-dehydration phenomena at the equatorial driest and warmest region perhaps define the lowest threshold of surface hydration in the present-day large-scale climatic model of Mars.

1. Introduction

The planet has small quantities of water vapor in the atmosphere, ice and frost on the surface of the polar region and shallow subsurface at certain regions other than the poles [1]. However, the present-day low atmospheric pressure (6.0 mbar) and low average global temperature (210K) do not allow the liquid phase of pure water to be stable at the surface. On contrary, perchlorate (ClO_4^-) salts, abundantly present at the surface, can produce a small amount of transiently stable brine by absorbing atmospheric water through deliquescence processes [2]. Shreds of evidences of hydrous activity at the surface of Gale crater has been proposed, based on the calculations of phase equilibration of perchlorates and thermal inertia of the surface materials from *in-situ* rover observations [2, 3]. In this study, we have demonstrated the events of surficial feedback of hydrous activities using high-resolution images and atmospheric data acquired by Mars Science Laboratory (MSL) of Curiosity rover. We have further used Rover Environmental Monitoring Station (REMS) data to evaluate the ground humidity and the climatic variations.

2. Observations

We have carried out observations at several locations in and around the Bagnold dune field and inter-dune areas located in Gale crater between summer and spring in a single Martian year (Fig. 1A).

In this study, we have identified features related to the disintegration of surface, such as horizontal fractures, break-apart laminae, and brecciated sand aggregates at multiple places but uniquely at the slopes of the regional dunes, large ripples, sand patches and wheel-cut section (Fig. 1B, 1C). Such features have been associated with the fresh grain flow activities, identified by their darker tones and distinct flow lobes, demarked by sharp outlines at the slip-face of the large ripples. However, we have not encountered any compressional deformation features, such as crumpled surface, folded lamellae or thrust slices neither at the encrusted surface nor at the grain flow lobes.

Martian impact ripples are perhaps the most dynamic and atmosphere-sensitive surface component on the present-day Mars. Migration of these small-scale bedforms was observed in diurnal intervals (source: https://mars.nasa.gov/resources/sand-moving-under-curiosity-one-day-to-next/). However, we have recognized few patches of non-migratory but eroded centimeter-scale bedform by their characteristic flat crests (Fig. 1D). We have also identified associated surface fracturing and grain flow along with the flat-crested ripple bedforms in few locations. The observation indicates the structural stability of these three dimensional aeolian bedforms.

3. Interpretation and Summary

Occurrences of the strike parallel fractures, fragments of sand aggregates and detached breccias associated with grainflow activities indicate that the underlying material is loosely bound than the top. Hence, a sharp variations of material strength vis-à-vis rheological difference between the underlying granular materials

and the overlying encrusted cap can be inferred here. The natural processes of soil disintegration were most likely explained by lowering of the critical angle possibly due to change in pressure gradient by thermal creep under dry condition and by triggering gas flow following Knudsen pump effect [4]. The lack of evidence of compressional deformation features along with the dominance of sand fragments bearing grainflow indicate that the rheology of the encrusted materials is well within the brittle domain, which suggest that the pore-fluid pressure was well below the saturation limit to promote liquefaction or hydro-plastic deformation. Therefore, we can infer that the soil stabilization in the form of surface encrustation occurred during early stage of salt cementation by sublimation of pore moisture at undersaturated condition, prior to the dry grainflow event. Farther we can also infer that the structural stability of the non-migratory impact ripples perhaps achieved due to similar phenomena. However, subsequent reworking of the surface indicates the dry events.

Moreover, we have calculated ground relative humidity (RH_g) for ~15 days prior to the date of observations, to check the contemporaneous events of soil hydration during summer, winter and spring (Fig. 1E). The enrichment of RH_g recorded during 3.00 to 6.00 hrs for all the three Martian seasons implies that the hydration-dehydration events are strongly controlled by diurnal effects, perhaps more than the seasonal variation.

Even though the present atmospheric conditions do not support liquid water to exist on the Martian surface, our findings indicate that in certain given conditions short term preservation of aeolian strata is still feasible. We have inferred that the early cementation is the most preferred mechanism that endorses the sediment support. Moreover, the estimated relative humidity of the surface suggests that the hydrous activity is predominantly diurnal in nature, rather controlled by seasonal variation. These observed phenomena at the equatorial driest and warmest region perhaps define the lowest threshold limit in the present-day, large-scale climatic model of Mars, and therefore wetting can occur more abundantly and at a greater scale for the rest of the planet.

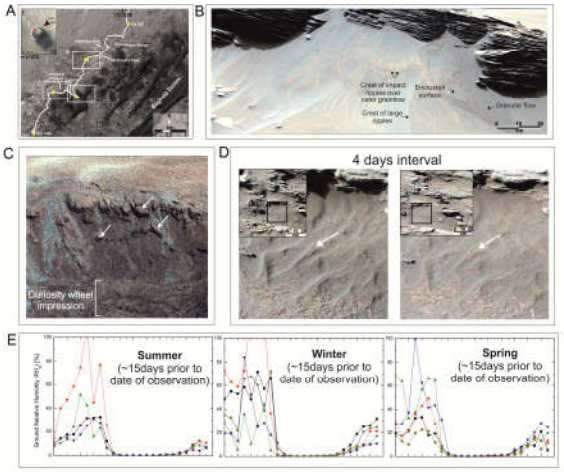

Figure 1: (**A)** Floor of Gale crater is marked with major geological way points along the Curiosity traverse, the studied location is marked in red square on MOM's MCC image. (**B)** Fresh grainflow deposits and overlying encrusted surface (black arrows), observed during summer. **(C)** Aggregates of sand were observed at the top part of Curiosity wheel-cut section during winter. **(D)** Flat-crested ripple structures on the surfaces of the sand patches in captured images of different time intervals. **(E)** Diurnal variation of Ground Relative Humidity for all three corresponding time intervals.

Acknowledgements

This work was funded by Department of Space, Government of India.

References

[1] Dundas, C.M., Bramson, A.M., Ojha, L., Wray, J.J., Mellon, M.T., Byrne, S., McEwen, A.S., Putzig, N.E., Viola, D., Sutton, S., Clark, E., and Holt, J.W: Exposed subsurface ice sheets in the Martian mid-latitudes: Science, vol. 359, pp. 199-201, 2018.

[2] Martín-Torres, F.J., et al.: Transient liquid water and water activity at Gale crater on Mars: Nature Geoscience, vol. 8, pp. 357, 2015.

[3] Martínez, G.M., et al.: 2016, Likely frost events at Gale crater: Analysis from MSL/REMS measurements: Icarus, vol. 280, pp. 93-102., 2016.

[4] Schmidt, F., Andrieu, F., Costard, F., Kocifaj, M., and Meresescu, A.G: 2017, Formation of recurring slope lineae on Mars by rarefied gas-triggered granular flows: Nature Geoscience, vol. 10, pp. 270, 2017.

EPSC Abstracts
Vol. 12, EPSC2018-1171, 2018
European Planetary Science Congress 2018

The Radar and Visible Stratigraphic Records of Mars' North Polar Layered Deposits

P. Becerra (1), D. Nunes (2), I. Smith (3), M.M. Sori (4), Y. Brouet (1), N. Thomas (1)
(1) Physikalisches Institut, Universität Bern, Switzerland (2) Jet Propulsion Laboratory, Pasadena, California, USA (3) Planetary Science Institute, Boulder, CO, USA. (4) University of Arizona, Tucson, AZ, USA.

Abstract

We present an initial correlation of visible imagery and stereo-topography from HiRISE and sub-surface radar from SHARAD of Mars' NPLD. Resulting stratigraphic columns can constrain NPLD formation models to explore a connection to Mars' climate.

1. Introduction

A long-standing problem in Mars Polar Science is the interpretation of the stratigraphic record preserved in Mars' icy North Polar Layered Deposits (NPLD) [1] (Fig. 1a), whose accumulation patterns of ice and dust are associated with recent climatic changes forced by variations in the planet's astronomical parameters [2]. The internal bedding is visible from orbit in exposures within spiraling troughs that dissect the NPLD dome (Fig. 1a,b). Studies have used remote images of these troughs to map the stratigraphy [3-6] and search for a connection between NPLD accumulation and astronomical forcing [7-10]. Sub-surface radar sounding also observes this internal structure. The Shallow Radar (SHARAD) [11] detects changes in dielectric properties with depth. As these vary for layers with different amounts of dust contamination, layering is observed in the radar data as "reflector" surfaces [12].

The optical and radar-based stratigraphies have predominantly been studied in isolation. In terrestrial climate science [13], orbital climate forcing was ultimately confirmed by the correlation of sedimentary, geochemical and paleo-magnetic records, suggesting that integration of datasets is key to understanding the climate record of the NPLD. In general, both radar and optical layers are assumed to result from varying amounts of dust impurities in the ice [14], which was supported by [15], who in attempting the first quantitative correlation between these data found an agreement between large-scale properties of radar reflectors and visible layers. The unique correlation of a particular radar reflector with one exposed bed or packet remains an open problem.

Here, we present our approach to this correlation. We test the hypothesis that highly protruding 'Marker Beds (MBs)' have sufficient dielectric contrast with neighboring beds to create radar reflections. If true, this would associate individual reflectors to exposed beds, allowing for the construction of dust/ice columns based on the combined data. These could then constrain orbitally-forced accumulation models [16,17] that could unlock the temporal climate record of the NPLD.

2. Methods

Becerra et al. [8] mapped the stratigraphy of the NPLD by identifying sequences of MBs in "protrusion profiles" of bed exposures in troughs made from HiRISE [18] Digital Terrain Models (DTMs; [19]), and correlating these from different locations (Fig. 1; [8]). We take advantage of this work, and take the following approach:
(1) *Average SHARAD data near the exposures to obtain representative radargrams.* The variability of the SHARAD subsurface response within small regions of interest (ROIs) next to exposure sites must be taken into account. To assess this, we selected segments of three SHARAD radargrams that fall within a 3 km ROI near N0, and averaged all soundings contained in each segment (Fig. 2). Two have similar responses at the range of interest (blue and green), and one does not (red). This is representative of the variations in radar response observed within the ROI.
(2) *Compare average radargrams directly to the protrusion profiles of* [8] *to search for an MB-reflector correlation*. For this, we subtract the linear attenuation in the data and normalize all quantities to mean = 0 and variance = 1. We then search for the maximum cross-correlation between protrusion profiles and average radargrams.
(3) *Model the radar wave propagation (following* [15]*) through synthetic permittivity (ε) profiles.* These would be constrained by the best-fit correlations from step 2, such that MBs translate into layers of high ε. We test a preliminary version of the model, in which we select specific MBs from the N0 profile and assign them ε = 4, over a water ice background with ε = 3.12. We then compare the model radargrams to the real ones from each location. Fig. 3 shows the dielectric profile (center) modeled

after the protrusion profile (left) of site N0, and the resulting simulated radargram (right).

(4) *Correlate the simulated radargrams to real SHARAD data using spectral analysis and pattern-matching algorithms.* This correlation will result in representative HiRISE/SHARAD-based stratigraphic columns of ε, which can be transformed to fractional dust-content [20,21] that can serve as virtual ice cores and be used to constrain accumulation models.

3. Preliminary Results

Results of the cross-correlation of SHARAD with the protrusion profiles and model radargrams for site N0 are shown in Fig 4. For the direct comparison with protrusion we select only the sections of the radargrams that correspond to the estimated relevant depth range [2–8 ms], while the comparison with the models includes the surface reflection and an "overburden" [0–8 ms]. In the former, the blue and green radargrams show good matches between reflectors and protrusion peaks, and while the red does not, lags of maximum correlation are similar for all three. In the latter, not all three radargrams showed similar maximum-correlation lags: The blue and green matches are close to what would be expected, while the red correlation fails.

4. Conclusions and Future Work

Beds of high protrusion appear to match radar reflectors at site N0, showing that this method is the correct approach to this problem. However, variability within the radar data must be taken into account. We must also study all geometrically favorable locations and test for statistical significance at each one. In addition, we will use the correlations with protrusion to inform the model and then use Dynamic Time Warping [7,22] to tune the model and find the best-fit dielectric profile at each site. The final step of the work will be to transform these profiles into dust/ice ratio columns [20,21] for use as input on accumulation models [17].

5. Figures

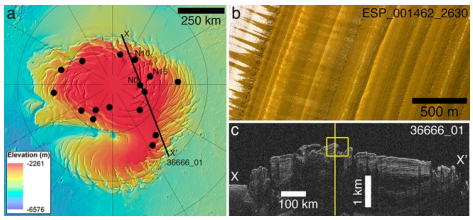

Figure 1. (a) Topographic map of the NPLD. Dots = locations of study sites and HiRISE DTMs [9]. Line is the ground track of the SHARAD radargram in (c). (b) HiRISE image of exposed layers in an NPLD trough. (c) SHARAD radargram (X-X' in 1a). Square marks the location of site N0. The line shows the position of the profiles of Fig. 2.

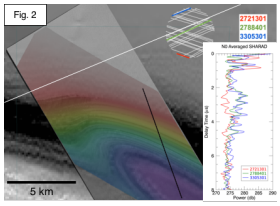

Figure 2. Zoom view of site N0. ROI for radargram averaging in top right. Plot of each average radargram.

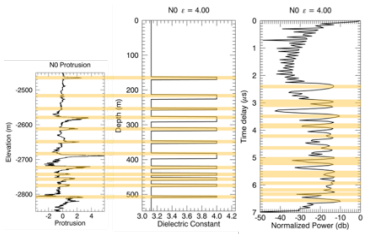

Figure 3. N0 protrusion profile (left) used to build a dielectric profile (center), through which a model radar wave is propagated to obtain a simulated radargram (right).

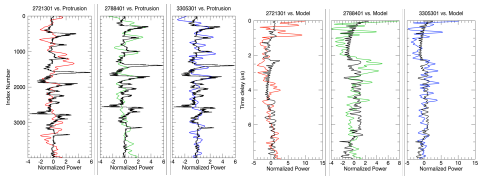

Figure 4. Cross-correlation of N0 average radargrams with N0 protrusion (left) and simulated radargrams (right).

Acknowledgements

This work is funded by Swiss National Science Foundation grant number 200020_178847. We thank the HiRISE and SHARAD Science and Operations team for the acquisition of the data and production of the DTMs.

References

[1] Smith, et al. *Icarus* (2018) [2] Cutts, et al. *Science* (1976) [3] Fishbaugh et al. (2006) [4] Fishbaugh et al. *GRL* (2010) [5] Limaye et al. *JGR* (2012) [6] Becerra et al. *JGR* (2016) [7] Laskar et al. *Nature* (2002) [8] Milkovich and Head, *JGR* (2005) [9] Perron and Huybers, *Geology* (2009) [10] Becerra et al. *GRL* (2017) [11] Seu et al. *JGR* (2007) [12] Putzig et al. *Icarus* (2009) [13] Imbrie, *Icarus* (1982) [14] Nunes & Phillips, *JGR* (2006) [15] Christian, et al. *Icarus* (2013) [16] Levrard et al. JGR (2007) [17] Hvidberg et al. *Icarus* (2012) [18] McEwen et al. JGR (2007) [19] Kirk et al. JGR (2008) [20] Stillman, et al. *J.Phys.Chem.* (2010) [21] Brouet et al. *(in prep.)* [22] Sori et al. Icarus (2014).

EPSC Abstracts
Vol. 12, EPSC2018-1237, 2018
European Planetary Science Congress 2018

Sediment transport by boiling seeping water: exploring effects of grainsize and atmospheric conditions

Susan J. Conway (1), Sabrina Carpy (1) Marion Massé (1), Zoe Perrin (1), Pauline Enguehard (1) and Manish Patel (2)
(1) CNRS, LPG, University of Nantes, France (2) School of Physical Sciences, Open University, Milton Keynes, UK. (susan.conway@univ-nantes.fr)

Abstract

Many active and recently active surface processes on Mars have been controversially linked to the action of liquid water, yet the sediment transport capacity of water under martian environmental conditions is poorly understood. An understanding of the sediment transport capacity allows the amount of water required for any given landform to be back-calculated from its observed size/volume at the martian surface. Here we present a series of experiments where we explore the effects of grainsize, atmospheric pressure, humidity and temperature on the sediment transport capacity of seeping liquid water under martian conditions.

1. Introduction

A variety of active features including gullies [1], recurring slope lineae (RSL)[2], dune flows [3] and slope streaks [4] have been linked to liquid water flowing on the martian surface. However, liquid water is only transiently stable at the martian surface [e.g., 5] and this has led to these activities being linked to other (dry) processes [6–9]. Recent laboratory work has shown that, under martian atmospheric conditions, liquid water boils and in doing so transports more sediment than would otherwise be the case [10–12]. Here we expand the work of Massé et al. [10] and explore the factors that could influence the sediment transport by seeping flows, which under terrestrial atmospheric conditions transport no sediment, but under martian conditions transport sediment via boiling induced saltation.

2. Experimental set-up

As for previous experimental work [10–12] we use the Open University's large Mars Chamber to recreate the atmospheric conditions on Mars. For each experiment a roughened plane measuring 0.5x0.90 m is placed at an angle of 31° and covered with 3.5 mm of sediment. The water is introduced from an external reservoir via a series of solenoid values to produce a dripping flow at ~1.7g/min. We monitored: the temperature of the sediment, the air and the water, the atmospheric pressure and humidity. Time lapse video recordings and opportunistic stills and videos were used to monitor the progress of the experiment and record pertinent aspects of the sediment transport process(es). The water was run for ~40 min and the chamber was maintained at low pressure for 5 min after the water was stopped. In order to quantify the sediment transport we used close-range photogrammetry to produce elevation models before and after the experiments as per [11,12], which were then differenced to obtain a volume. We performed experiments at 6 and 9 mbar. We used three natural sediments with modal grainsizes of 200, 375 and the last with >1000 µm but comprising a mixture of various grain sizes.

3. Preliminary results

Our initial findings reveal that, as expected, the amount of sediment transported depends on grainsize: the smaller the grains the more saltation occurs and the more material is moved by saltation and granular avalanches (Fig. 1). This results in the more obvious ridges at the surface of the finer grained material (Fig.1). Interestingly in a mixed grainsize substrate, the smallest grains still saltate, so ridges are formed, but are less obvious as the larger grains do not move much. A lower atmospheric pressure seems to result in less sediment transport, as noted by Massé et al. [10]. Our results indicate that the saltation process is sensitive to atmospheric humidity as expected for a process driven by phase-change. As the surface conditions of Mars are at or below to the triple point, liquid water either dominantly boils or freezes. We found that when freezing dominates, the saltation process still occurs because the atmospheric humidity is maintained near zero (Fig. 1). Despite the bed being armoured by the ice [13], the sediment

transport is on the same order as non-freezing conditions is still non-negligible.

4. Summary and Conclusions

We have expanded the range of atmospheric conditions and grainsizes under which transport of sediment via boiling induced saltation can occur. We find the process is robust to freezing conditions and can occur over a range of realistic humidity, temperature and pressure conditions. Future work includes scaling these present results to martian gravity and geoemorphic-scales and exploring a wider range of Mars-relevant grainsizes.

Acknowledgements

We acknowledge financial support from Europlanet TA programme transnational facility access and from "Programme National de Planétologie" (PNP).

References

[1] M.C. Malin et al. (2006) *Science*, 314, 1573–1577. [2] A.S. McEwen et al. (2011) *Science*, 333, 740–743. [3] A. Kereszturi et al. (2009) *Icarus*, 201, 492–503. [4] E.S. Brusnikin et al. (2016) *Icarus*, 278, 52–61. [5] M.H. Hecht (2002) *Icarus*, 156, 373–386. [6] F. Schmidt et al. (2017) *Nat. Geosci*, 10, 270-273. [7] C.M. Dundas et al. (2017) *Geol. Soc. Lond. Spec. Publ.*, 467. [8] S. Diniega et al. (2013) *Icarus*, 225, 526–537. [9] C. Pilorget and F. Forget (2016) *Nat. Geosci*, 9, 65–69. [10] M. Massé et al. (2016) *Nat. Geosci.*, 9, 425–428. [11] J. Raack et al. (2017) *Nat. Commun.*, 8, 1151. [12] C. Herny et al. (2018) *Geol. Soc. Lond. Spec. Publ.*, 467. [13] S.J. Conway et al. (2011) *Icarus*, 211, 443–457.

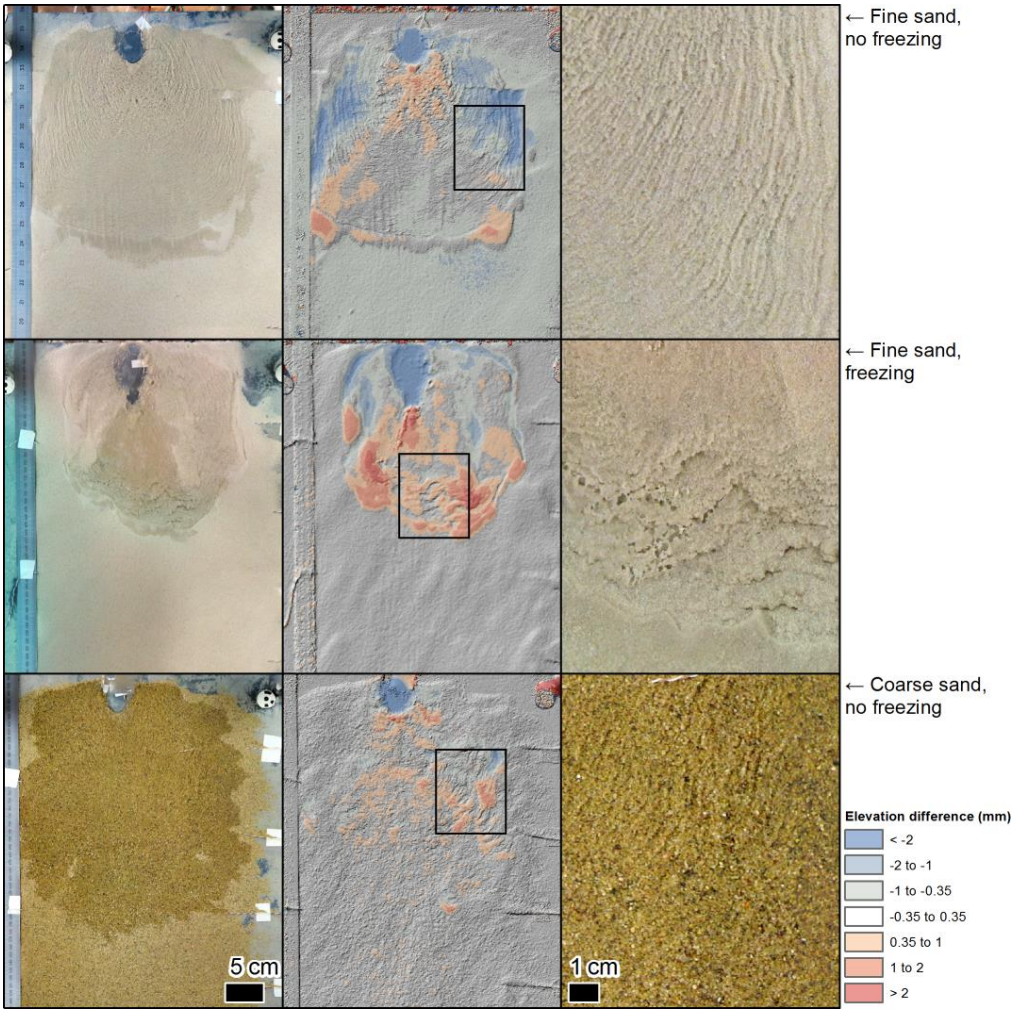

Figure 1: Top-down view of sediment surface after the experiment. Left: colour image, middle: height change superposed on a relief shaded elevation model, and right: detailed view of the ridges created by boiling – position on sediment indicated by box on middle panel.

EPSC Abstracts
Vol. 12, EPSC2018-1239, 2018
European Planetary Science Congress 2018

The subsurface water distribution in Gale crater from DAN instrument onboard NASA Curiosity rover.

M.L. Litvak (1), I.G. Mitrofanov (1), D. Lisov (1), S.Y. Nikiforov (1) , A.B. Sanin (1), M. V. Djachkova (1)
(1) Space Research Institute of the Russian Academy of Sciences (IKI), 117997, 84/32 Profsoyuznaya st., Moscow, Russia, (litvak@mx.iki.rssi.ru)

Abstract

In our study we have used data gathered from Dynamic Albedo of Neutron (DAN) instrument installed onboard NASA Curiosity rover for 6 years of surface observations. The main objective is to study variations of the bound water in subsurface layer along rover traverse (more than 20 km). We have reconstructed continuous profile of subsurface water using DAN passive and active observations and compared it with other Curiosity observations, stratigraphy column, geological patterns and distribution of different minerals.

EPSC Abstracts
Vol. 12, EPSC2018-1273, 2018
European Planetary Science Congress 2018

Erosion rate of the north polar scarps of Mars based on automated detection of block falls in HiRISE images

L. Fanara (1,2), K. Gwinner (1), E. Hauber (1) and J. Oberst (1,2)
(1) Institute of Planetary Research, DLR, Berlin, Germany, (2) Institute of Geodesy and Geoinformation Science, Technical University of Berlin, Berlin, Germany (Lida.Fanara@dlr.de)

Abstract

We automatically detected ice block falls in high resolution satellite images of the north polar region of Mars, with the aim of understanding their role in erosion processes and the morphological evolution of the region. Our change detection method is based on the combination of Binary Large OBjects (BLOB) detection and machine learning and we aim to extend our investigation to all steep scarps of the margin of the north polar ice cap where suitable high resolution data exist.

1. Introduction

Based on radar measurements, ice is currently accumulating at the North Polar Layered Deposits (NPLD) [1], while modelling has shown significant viscous flow of the outmost scarps [2], which are nevertheless very steep. After the CO_2 ice layer sublimates in spring, temperature oscillations lead to fracturing of both the NPLD and the underlying Basal Unit (BU) [3]. This results in block falls that are responsible for the scarp retreat [4].

High Resolution Imaging Science Experiment (HiRISE) was the camera to reveal how dynamic this area is, with frequent avalanches [5] and block falls [6]. It has been imaging the scarps regularly for the past 10 years making change detection possible. Manual investigation for block falls for estimating their volume and the erosion rate costs a lot of time. We have developed a change detection method to amend this.

Wagstaff et al. [7], Di et al. [8] and Xin et al. [9] have presented methods for detecting large-scale changes that commonly occur in regions of Mars with a stable background. Block falls, however, are very small changes occurring in a variable environment and therefore require a process-specific approach with high geometric accuracy.

2. Change Detection

Using Ames Stereo Pipeline (ASP) [10] we produce HiRISE Digital Terrain Models (DTM) at the locations along the outmost scarps of the north polar ice cap for which stereo pairs exist. We then ortho-rectify all images of a location onto the respective DTM and co-register them to each other locally based on Enhanced Correlation Coefficient Maximization (ECC) [11] to reach subpixel accuracy.

To highlight the changes we first subtract the co-registered images of different times (Fig. 1). We then identify the block falls amongst all changes of the region by modelling them as bright objects accompanied by a shadow. We combine thresholding and BLOB detection with a Support Vector Machine (SVM) trained on Histogram of Oriented Gradients (HOG) [12] of thousands of blocks as well as other changes to recognise all the pairs of newly appeared blocks and shadows. We then refine their shape by combining edge detection with watershed and the volume of each block is estimated from an assumed ellipsoid around the long axis of a fitted ellipse to the shape of the block.

We also run the algorithm with the reverse order of the images to find the blocks that have disappeared. In some cases these have simply rolled further down or large blocks disintegrate into smaller pieces while moving downslope. In other cases blocks seem to sublimate over the years.

We validate our method by manually identifying block falls and comparing this to the result of the automated detection in several test areas. The validation shows a precision and sensitivity of over 70%.

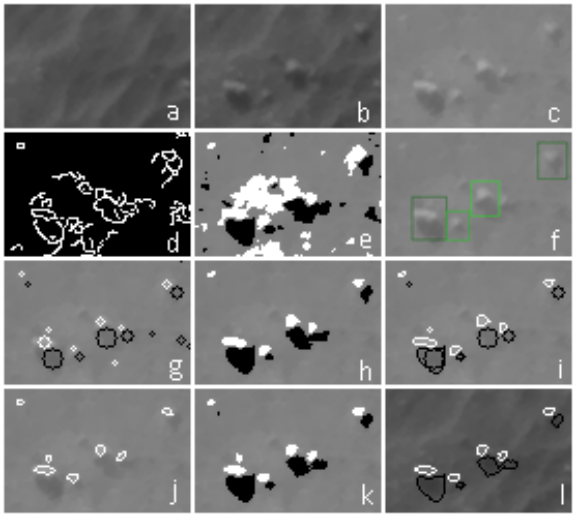

Figure 1: Change detection example. a) ”before” image, b) ”after” image, c) difference image, d) threshold image, e) edge detection, f) SVM-HOG detections, g) and h) BLOB bright and dark areas, i) candidate blocks and shadows, j) updated shape of candidate blocks from edges, k) shape of candidate blocks and shadows after watershed, l) final pairs of blocks and shadows.

3. Summary and Conclusions

Our study provides a systematic procedure for producing accurately co-registered HiRISE images and for detecting block falls between images of different times with a high confidence level. We apply this method to all scarps of the margin of the north polar ice cap where at least one HiRISE stereo pair exists to estimate the erosion rate of the steep icy scarps and we assess how and where erosion affects the current morphology of the north polar ice cap.

Acknowledgements

This work was co-funded by the European Union’s Seventh Framework Programme under iMars grant agreement n° 607379.

References

[1] Smith, I.B., Putzig, N.E., Holt, J.W. and Phillips, R.J.: An ice age recorded in the polar deposits of Mars, Science, 352, 1075–1078, 2016.

[2] Sori, M.M., Byrne, S., Hamilton, C.W. and Landis, M.E.: Viscous flow rates of icy topography on the north polar layered deposits of Mars, Geophysical Research Letters, 43, 541–549, 2015.

[3] Byrne, S., Sori, M.M., Russell, P., Pathare, A.V., Becerra, P., Molaro, J.L., Sutton, S., Mellon, M.T. and the HiRISE Team: Mars polar cliffs: stressed out and falling apart, European Planetary Science Congress. 11, EPSC2017-333, 2017.

[4] Herkenhoff, K.E., Byrne, S., Russell, P.S., Fishbaugh, K.E. and McEwen, A.S.: Meter-scale morphology of the north polar region of Mars, Science, 317, 1711–1715, 2007.

[5] Russell, P., Thomas, N., Byrne, S., Herkenhoff, K., Fishbaugh, K., Bridges, N., Okubo, C., Milazzo, M., Daubar, I., Hansen, C. and McEwen, A.: Seasonally active frost-dust avalanches on a north polar scarp of Mars captured by HiRISE, Geophys. Res. Lett. 35, L23204, 2008.

[6] Russell, P.S., Byrne, S., Herkenhoff, K.E., Fishbaugh, K.E., Thomas, N., McEwen, A.S. and the HiRISE Team: Active mass-wasting processes on Mars’ north polar scarps discovered by HiRISE, Lunar and Planetary Science Conference, March 1, 2008.

[7] Wagstaff, L., Panetta, J., Ansar, A., Bunte, M., Greeley, R. and Hoffer, M.P.: Change detection in Mars orbital images using dynamic landmarking, Kiri. 2, 2010.

[8] Di, K., Liu, Y., Hu, W., Yue, Z. and Liu, Z.: Mars surface change detection from multi-temporal orbital images. IOP Conf. Ser.: Earth Environ, Sci. 17, 012015, 2014.

[9] Xin, X., Di, K., Wang, Y., Wan, W. and Yue, Z.: Automated detection of new impact sites on Martian surface from HiRISE images, Advances in Space Research, 60, 1557–1569, 2017.

[10] Shean, D.E., Alexandrov, O., Moratto, Z.M., Smith, B.E., Joughin, I.R., Porter, C. and Morin, P.: An automated, open-source pipeline for mass production of digital elevation models (DEMs) from very-high-resolution commercial stereo satellite imagery, ISPRS Journal of Photogrammetry and Remote Sensing, 116, 101–117, 2016.

[11] Evangelidis, G.D. and Psarakis, E.Z.: Parametric image alignment using enhanced correlation coefficient maximization, IEEE Transactions on Pattern Analysis and Machine Intelligence, 30, 1858–1865, 2008.

[12] Dalal, N. and Triggs, B.: Histograms of oriented gradients for human detection, International Conference on Computer Vision & Pattern Recognition, June, 2005.